Stochastic investigation of the evolution of small-scale turbulence in the wake of a wind turbine exposed to different inflow conditions

Ingrid Neunaber

Von der Fakultät für Mathematik und Naturwissenschaften
der Carl von Ossietzky Universität Oldenburg
zur Erlangung des Grades und Titels eines

DOKTORS DER NATURWISSENSCHAFTEN
DR. RER. NAT.

angenommene Dissertation

von Frau Ingrid Neunaber
geboren am 20. November 1989 in Oldenburg

CARL VON OSSIETZKY universität OLDENBURG

Gutachter: Prof. Dr. Joachim Peinke

Zweitgutachter: Prof. Dr. Gerard Schepers

Tag der Abgabe: 23.11.2018

Tag der Disputation: 15.01.2019

Contents

Abstract

Wind turbines operate in the atmospheric boundary layer that is naturally turbulent. They are also usually clustered in wind farms. As a result, wind turbines are permanently exposed to turbulence, either within the wind, or, in case of a wind farm setup, when the downstream turbines are hit by the wakes of the front row turbines. As the wake of an upstream turbine determines how much power a downstream turbine can generate and which loads it experiences, the study and characterization of wind turbine wakes has become an important research area. This thesis aims to examine the evolution of turbulence, especially small-scale turbulence, in the wake downstream the turbine. In particular, an experimental approach is followed where wind tunnel experiments are carried out to investigate the influence of turbulence in the inflow on the wake development. For this, an actuator disc and a model wind turbine are exposed to different uniform, turbulent inflows, and the wake of a turbine within a wind farm setup is investigated. The data is examined stochastically using one and two point statistics. Different turbulence regions are identified in the wakes of the actuator disc and the model wind turbine by investigating the downstream evolution of the turbulence intensity. In the far wake, the wakes of both wake generating turbine models are similar. In this wake area, a core region with homogeneous isotropic turbulence can be identified. The results are independent on the inflow conditions, which is interpreted as the turbine imprinting its own turbulence onto the flow. Therefore, the main findings are summarized in an easy-to-use turbulence wake map.

Zusammenfassung

Windenergieanlagen (WEA) sind permanent Turbulenzen ausgesetzt, da sie in der bodennahen atmosphärischen Grenzschicht operieren, die turbulent ist. WEA werden meist in Windparks erbaut, sodass außerdem einige WEA im turbulenten Nachlauf, der sich hinter den vorderen Anlagen ausbildet, stehen. Da dieser Nachlauf bestimmt, wie viel Leistung die hintere Anlage generiert und welche Lasten sie erfährt, ist die Entwicklung von Nachläufen Thema aktueller Forschung. Diese Arbeit widmet sich speziell der Entwicklung der kleinskaligen Turbulenz im Nachlauf. Anhand von Windkanalversuchen wird der Einfluss der Turbulenz in der Einströmung auf die Turbulenz im Nachlauf untersucht. Ein statisches Rotormodell und eine Modell-WEA werden hierzu verschiedenen Strömungen, laminar und turbulent, ausgesetzt, und außerdem wird die Turbulenz im Nachlauf einer Windparkkonstellation untersucht. Die Daten werden stochastisch mithilfe von Ein- und Mehrpunktstatistiken analysiert. Anhand der Turbulenzintensität lässt sich der Nachlauf des statischen Rotormodells und der Modell-WEA in verschiedene Turbulenzregionen einteilen. Stromabwärts gleichen sich die Nachläufe beider Objekte, und es lässt sich ein Nachlaufkern identifizieren, der homogene, isotrope Turbulenz aufweist. Die Ergebnisse sind weitestgehend unabhängig von der Art der Einströmturbulenz, was bedeutet, dass die Modell-WEA der Strömung eine eigene Turbulenz aufprägt. Dies ermöglicht die Visualisierung von Turbulenzregionen in einem Nachlauf-Diagramm.

Nomenclature

Latin symbols

A	cross-section of the WGT
C_ε	dimensionless constant related to the energy dissipation
c_P	power coefficient
c_T	thrust coefficient
D	diameter of the WGT
$E(f)$	energy spectrum in frequency domain
$E(k)$	energy spectrum in wave number domain
exp	Exponent characterizing the turbulence decay in the inertial sub-range
F	flatness
f	frequency
f_T	rotational frequency of the turbine
k	frequency
$L^\star$	characteristic length scale
L	integral length
$p()$	probability density function
P_{wind}	power within the wind
P_T	mean converted by turbine
r	length scale
Re	Reynolds number
Re_λ	Taylor Reynolds number
T_T	thrust acting on the turbine
TI	turbulence intensity
u	mean stream-wise velocity
$u(t)$	flow velocity
u'	velocity fluctuations $u' = u(t) - u$
u_0	wind velocity
u_{disc}	mean stream-wise velocity at the rotor plane
u_{wake}	mean stream-wise velocity of the wake
X,Y,Z	Cartesian coordinates

Greek symbols

β, β_1, β_2	Decay exponent of the turbulence intensity
$\delta u(\tau)$	velocity increment on time scale τ
ε	Turbulent dissipation
λ^2, $\lambda^2(\tau)$	shape parameter
λ_T	Taylor length
μ	intermittency factor
ν	kinematic viscosity
ρ_{air}	Density of air
σ	Standard deviation of the mean velocity
σ_0	Median of the log-normal distribution
σ_τ	standard deviation of the time series of velocity increments
τ	Time scale of the velocity increment

Abbreviations

1D	One Dimensional
2D	Two Dimensional
ABL	Atmospheric Boundary Layer
ECN	Energy research Centre of the Netherlands
HIT	homogeneous isotropic turbulence
IEC	International Electrotechnical Commission
K41	referring to Kolmogorov's theory on turbulence from 1941
K62	referring to Kolmogorov's theory on turbulence from 1962
LDA	Laser Doppler Anemometer
LES	Large Eddy Simulation
OLWiT	Oldenburg's large wind tunnel
PIV	particle image velocimetry
PDF	probability density function
TSR	tip speed ratio
TWO	turbulence wind tunnel Oldenburg
WGT	Wake generating turbine model

1. Introduction

The consequences of global warming have been starting to show over the past years in sea level rise, droughts, floods, and other extreme weather events, making taking actions against CO_2 emissions more urgent than ever. As a transition from electricity generation based on fossil fuels to renewables helps to reduce CO_2 emissions, the share of renewables is increasing worldwide. In Germany, wind energy is the most important among the renewables as the resources of solar energy, hydro-electricity and others are more restricted. In total, 33.3% of the electricity consumed in Germany is currently provided by renewables, and 49% of the renewables, or 16.3% of total electricity, are delivered from wind energy, making wind energy crucial for the extension of renewables (BMWI (2018)). It is only natural that wind energy is also growing fastest among the renewables in Germany (Umweltbundesamt (2018)).

Both on- and offshore, the majority of wind turbines are installed in wind farms. This setup is the most economic and efficient one when it comes to planing, use of land and infrastructure, and maintenance. Figure 1.1 shows a photograph of the offshore wind farm Horns Rev that is located in the Danish North Sea. It illustrates the usual situation of a wind farm in operation: Wind turbines operate in the atmospheric boundary layer, being thus constantly exposed to non-uniform, turbulent inflow. As they convert a portion of the wind's kinetic energy to electrical energy, the wind velocity is reduced downstream the turbine. In addition, the turbine represents a rotating obstacle that induces turbulence to the flow. This *wake* evolving behind a turbine is visualized in figure 1.1 by fog. The fog is created during a rather rare atmospheric condition where supersaturated air condenses spontaneously downstream the turbine due to the pressure drop. This flow is considerably more complex than the initial atmospheric boundary layer inflow, as the turbulence of the inflow is now altered and partially superimposed with turbulence generated by a rotating obstacle. A downstream turbine exposed to this wake experiences a flow with lower velocity but higher turbulence. It converts less energy, and it was shown that wake effects can result in a reduction of the power production of around 10% (in extreme cases up to 50%) for the downstream turbines (cf. Barthelmie *et al.* (2007), Barthelmie *et al.* (2010)). At the same time, the turbine encounters higher fatigue loads due to the increased turbulence (e.g. Frandsen (2007), Lee *et al.* (2012)). Recently, Schwarz *et al.* (2018) showed that intermittency, i.e. the high probability of large velocity fluctuations at relatively small time intervals, increases fatigue loading. Intermittency is present both in the atmospheric flow (see Wächter *et al.* (2012))

Figure 1.1.: Visualization of wakes in the wind farm Horns Rev due to spontaneously condensed water vapor. Photographer: Christian Steiness (February 12th 2008), permission granted by courtesy of Vattenfall.

and the wake (see e.g. Bastine *et al.* (2015), Schottler *et al.* (2016a)). As it can only be detected using higher order statistics, this shows that an extension of the standard tools used for data analysis is important for a more thorough turbine design.

This exemplification shows how wake effects can dominate the inflow of downstream turbines within a wind farm. Therefore, profound knowledge of wakes can increase the energy yield by improving the layout with help of numerical tools such as WAsP (González *et al.* (2014), Chowdhury *et al.* (2012)). Additionally, the energy yield can be enhanced by using control mechanisms such as yawing (Fleming *et al.* (2014), Schottler *et al.* (2016b)) and the reduction of the upstream turbine's induction, which leads to higher flow velocities at the downstream turbine (Corten and Schaak (2003)). The former may also be used to reduce fatigue loads, and in combination with more specifically designed turbines, this can also reduce maintenance costs and frequency. But what do we know about wakes? And how can this knowledge be expanded? Over the last decades, the complexity of wind turbine wakes has been object to many analytical, numerical, and experimental (field and laboratory) studies. Because neither of the approaches is capable of delivering a complete picture of a full-scale turbine operating in the atmospheric boundary layer, all methods are needed to complement each other. As the flow field is highly turbulent, mainly statistical characteristics of the wake are studied. Among those, the evolution of the velocity deficit downstream a turbine is the most common subject of investigation, and wake models aim to capture it correctly. All studies naturally focus on selected details, and as there are only few reviews[i], the categorization of new results, especially regarding turbulence properties, into the framework of wake evolution does sometimes prove to be difficult. Generally, studies agree that the wake can roughly be divided into two regions, namely the *near wake*, where flow structures directly related to the blades, nacelle or tower are still identifiable, and the *far wake*, where a self-similar velocity profile is often assumed. The investigation of the transition between these regimes is listed as one long-term research challenge in wind energy by van Kuik *et al.* (2016). Further long-term research challenges include the interaction of the atmospheric boundary layer with the wake and the interaction between two or more wakes.

In order to examine these research questions within the framework of wake evolution, this thesis applies an experimental approach in a wind tunnel with reproducible inflows. Porous discs, also called actuator discs, are used in numerical simulations and experimental studies as simplified and cost-efficient substitutes for rotating turbine models. Therefore, one objective of this thesis is to compare the wake generated by a disc with radially varying blockage and the wake of a controlled model wind turbine. The turbulence properties will not only be examined by comparing the mean velocity and turbulence intensity profiles but also by comparing quantities such as energy spectral densities, the evolution of length scales, and two-point statistics, that allow conclusions to be drawn about the turbulence generation and the intermittency. Further, the influence of different properties of the inflow turbulence on the wake evolution will be explored. For this, uniform inflows with different types of turbulence with varying complexity will be generated, and the wakes of the two wage generating turbine models (WGTs) will be viewed. However, laboratory-generated turbulence differs from wake turbulence. Therefore, next, a turbine will be exposed to the wake of another turbine that is positioned upstream, and its wake will be examined. The results will be related to the results obtained in laboratory-generated turbulence. All measurements will be carried out with a high spacial resolution downstream to capture the transition from near wake to far wake. Then, all obtained results will be combined to pinpoint the transition from near wake to far wake by identifying different wake regions both in stream-wise and span-wise direction. The aim is to generate a simple but complete "map" of the wake that summarizes the main effects in a user-friendly and applicable manner thus helping to orient within the wake. Last, this work will concentrate on the recognition of turbulence patterns within the different regions to help to simplify turbulence wake models.

[i] e.g. Vermeer *et al.* (2003) - general overview; Sanderse (2009) - focus on computational fluid dynamics; Göçmen *et al.* (2016) - review of wake models developed at DTU

Structure of this thesis

To answer the proposed research items, in chapter 2, an introduction to turbulence with all used evaluation methods is given, and flow properties of the atmospheric boundary layer are discussed. Further, a summary on wind energy conversion and wind turbine wakes with focus on turbulence is included. The measurement methods, the disc and model wind turbine, and the setup will be introduced in chapter 3. In chapters 4 and 5, the results of two different setups are presented, and the results are discussed in chapter 6. Finally, this thesis closes with a summary and outlook in chapter 7.

2. Theory and Background

In the following, an introduction to turbulence and turbulence characterization will be given, followed by a brief overview of the nature of atmospheric turbulence, wind energy conversion, and wind turbine wakes with focus on turbulence in wind turbine wakes.

2.1. Turbulence

Turbulence is one of the big mysteries of our time[i]. Although research made it possible to shed light on more and more details of turbulence evolution, the overall knowledge is still unsatisfactory. Our picture of turbulence is to this day coined by R. L. Richardson's model of large eddies that bring energy into the system on large scales L, the so-called integral length scale. These vortices then decay into smaller and smaller vortices transporting kinetic energy down a cascade until the structures become so small that the influence of viscosity is noticeable. The approximate size of the vortices is then given by the so-called Taylor length scale λ_T. For vortices smaller than the Taylor length, dissipation becomes increasingly significant as energy is more and more transported by heat transfer and less by the cascade processes. Based on this assumption, A. N. Kolmogorov developed a theory for fully developed homogeneous, isotropic turbulence (HIT) in equilibrium in 1941, in the following called K41, or also Richardson-Kolmogorov phenomenology. A. N. Kolmogorov assumed that the turbulent dissipation rate ε from one scale to a smaller scale separated by a length scale r is constant within a certain range of scales and independent of the (kinematic) viscosity ν. Additionally, he assumed that the turbulence would generally evolve slowly while the small-scale movement ($r \ll L$) would in comparison be fast. The consequences are inter alia that the cascade only evolves from large scales to small scales and that the cascade is self-similar. Within this framework, A. N. Kolmogorov derived a scaling

[i] In this section, an overview of the concepts of turbulence description is given. It is based on standard textbooks like Hinze (1975), Frisch (1995), Pope (2000) and Davidson (2015), and the chapter on turbulence in Argyris *et al.* (2015), and the reader is referred to these sources for a more detailed introduction.

law for the turbulence energy spectrum in the corresponding range of scales between L and λ_T that is also called the inertial sub-range,

$$E(k) \propto k^{-5/3}, \tag{2.1}$$

where k is the wave number.
By means of Taylor's hypothesis of frozen turbulence[ii], the energy spectrum over wave number can be converged into the energy spectrum in the frequency domain, $E(f) = 2\pi \cdot E(k)/u$, where f denotes the frequency and u is the mean value of a velocity time series $u(t)$. The relation 2.1 holds also in the frequency domain, $E(f) \propto f^{-5/3}$.
It seems reasonable to suppose that L and λ_T can be estimated from the turbulence energy spectrum, as they can be referred to as the boundaries of the inertial sub-range. Hinze (1975) suggests this by means of the one-dimensional energy spectrum. The integral length can be estimated by calculating the limit of the energy spectrum in the frequency domain for f approaching 0,

$$L = \lim_{f \to 0} \left(\frac{E(f) \cdot u}{4\sigma^2} \right), \tag{2.2}$$

as illustrated in figure 2.1(a). σ is the standard deviation of the velocity time series $u(t)$. Note that here, only the frequency range where $E(f) \approx const$ just outside the inertial sub-range is used to determine L.
The Taylor length is defined as

$$\lambda_T = \left(\frac{\sigma^2}{\langle (\partial u'/\partial x)^2 \rangle} \right)^{1/2}, \tag{2.3}$$

where $u' = u(t) - u$ are the fluctuations of the velocity and $\langle \cdot \rangle$ denotes the ensemble average. The term $\langle (\partial u'/\partial x)^2 \rangle$ can be calculated from the energy spectrum in space domain (cf. figure 2.1(b)),

$$\left\langle \left(\frac{\partial u'(x)}{\partial x} \right)^2 \right\rangle = \int_{k_{min}}^{k_{max}} k^2 E(k) \mathrm{d}k. \tag{2.4}$$

Note that the pre-multiplied spectrum is, as indicated in figure 2.1(b), only integrated up to the local minimum at high wave numbers, k_{max}. For wave numbers larger than k_{max}, the turbulence spectrum does only contain artifacts but no flow events.

[ii] Considering a turbulent flow with a mean wind speed u and corresponding standard deviation σ, Taylor's hypothesis states that the turbulence patterns evolve slowly compared to the mean velocity, if $\sigma << u$. As a consequence, one can estimate the size of a structure, r_s, that passes a sensor in the time Δt_s or that is sampled with a sampling frequency f_s with $r_s = \frac{u}{f_s} = u \cdot \Delta t_s$.

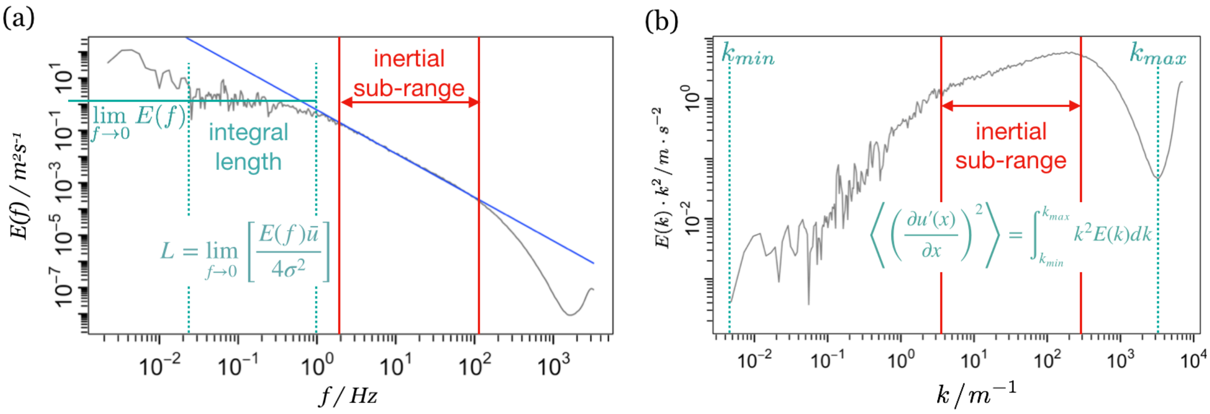

Figure 2.1.: Estimation of the integral length L (a) from the energy spectrum $E(f)$ and the Taylor length λ_T (b) from the pre-multiplied energy spectrum $E(k)\cdot k^2$. In (a), the blue line indicates a decay in the spectrum that corresponds to $E(f) \propto f^{-5/3}$. The inertial sub-range, where E(f) follows this decay, is marked.

As above-mentioned, the K41 theory holds for fully developed turbulent flows. In order to classify as such, the flow must fulfill the following condition: The inertial forces within a flow have to be much larger than the viscous forces. This condition is expressed by the Reynolds number

$$Re = \frac{u\cdot L^*}{\nu}. \tag{2.5}$$

L^* is a characteristic length scale of the setup. If $Re >> 1$, a flow is considered turbulent. In contrast, if $Re \approx 1$, the flow is laminar. The Reynolds number is not only used to classify flow states, but also to measure the similarity of two flows: Two similar flow conditions on different scales are assumed to behave similarly if they have the same Reynolds number[iii].

To categorize a flow with regard to turbulent flow properties, a second definition of the Reynolds number, the Taylor Reynolds number, is often used,

$$Re_\lambda = \frac{\lambda_T\cdot\sigma}{\nu}. \tag{2.6}$$

Fully developed turbulence is characterized by $Re_\lambda > 200$.
To complete the characterization of turbulence, a measure for the strength of turbulence fluctuations in the flow is given by the turbulence intensity $TI = \sigma/u$.

[iii] For example, a cylinder with diameter $d_c = 1\,$m exposed to an air flow of $u = 10\,$m/s and a cylinder with diameter $d_c = 0.001\,$m in a water flow with $u = 700\,$m/s share the same Reynolds number $Re \approx 700000$ and thus generate similar flows.

One major criticism in the K41 theory is the assumption that the turbulent dissipation rate ε is constant (see e.g. Argyris *et al.* (2015)). While it seems reasonable to assume fluctuations in ε in strongly turbulent flows, a constant dissipation rate prevents any variations of the energy transfer within the turbulent cascade. This becomes clear when looking into higher-order statistics: The temporal velocity increment for a time scale τ is defined as the difference of the velocities measured at two times $t-\tau/2$ and $t+\tau/2$, $\delta u(\tau) = u(t+\tau/2) - u(t-\tau/2)$, as illustrated in figure 2.2(a). The spacial velocity increment for a scale r is defined as the difference of two velocities measured at two points $\vec{x}$ and $\vec{x}+\vec{r}$, $\delta u(r) = u(\vec{x}+\vec{r}) - u(\vec{r})$ with $\langle \vec{r} \rangle = r$[iv]. As two velocities at different points in space or time are used, increments are part of two-point statistics. r and τ can be varied in a way that different scales are taken into account. The probability density functions of velocity increments $p(\delta u(\tau)/\sigma_\tau)$ and $p(\delta u(r)/\sigma_r)$, that are also called increment PDFs, are usually calculated for normalized velocity increments. The normalization is according to the standard deviation of the series of velocity increments, σ_τ or σ_r. Within the inertial sub-range, one can observe that the increment PDFs do not follow a Gaussian distribution $p(\delta u(\tau)) \propto (2\pi\sigma_\tau^2)^{-1/2} \cdot \exp\left\{-\delta u(\tau)^2/(2\sigma_\tau^2)\right\}$ which would be expected by K41. Rather, the probability density functions show a significantly higher probability of large fluctuations than expected by a Gaussian distribution (see also figure 2.2(b)). This phenomenon is often referred to as *intermittency*, and it is not accounted for by the K41 theory. To describe distributions that show the characteristic intermittent behavior, Castaing *et al.* (1990) proposed to superpose log-normally weighted Gaussian distributions with different standard deviations. In the following, only the formula for temporal velocity increments as proposed by e.g. Morales *et al.* (2011) is presented[v]; for spacial velocity increments, the formula is similar.

$$p(\delta u(\tau)/\sigma_\tau) = \frac{1}{2\pi\lambda(\tau)} \int_0^\infty \frac{\mathrm{d}\sigma}{\sigma^2} \exp\left\{-\frac{\delta u(\tau)^2}{2\sigma^2}\right\} \exp\left\{-\frac{\ln^2(\sigma/\sigma_0)}{2\lambda^2(\tau)}\right\}. \tag{2.7}$$

Two parameters control the form of the increment PDF, namely the shape parameter $\lambda^2(\tau)$ that determines the distribution's shape, and σ_0 that sets the median of the log-normal distribution (Morales *et al.* (2011)). The shape parameter can according to F. Chillà *et al.* (1996) be determined by

$$\lambda^2(\tau) = \frac{\ln(F(\delta u(\tau))/3)}{4}. \tag{2.8}$$

[iv] In case the spacial velocity increments are obtained from a time series by applying Taylor's hypothesis, one has to keep in mind to adjust the signs accordingly. As spacial increments are in this thesis calculated from time series measured simultaneously at two points in space, this is not relevant in this thesis.

[v] Here, a simplified version of the formula proposed by Castaing is used that does not include the skewness of the distribution.

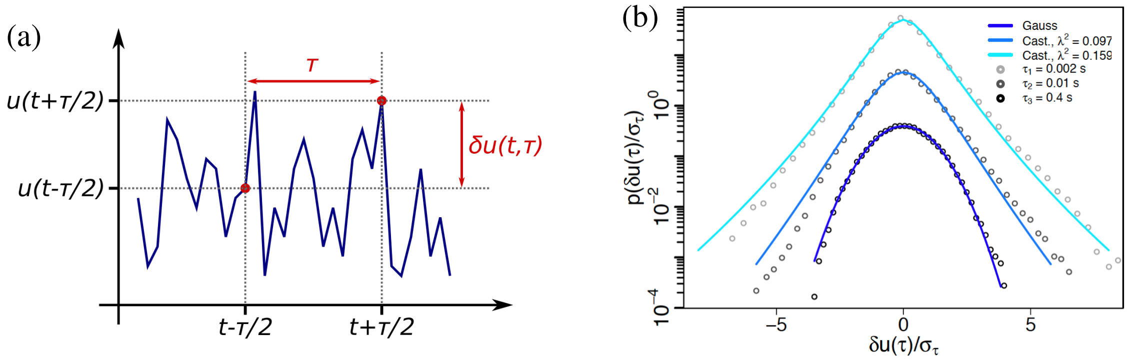

Figure 2.2.: Definition of the velocity increment at a time scale τ(a) and illustration of the probability density functions of temporal velocity increments for different time scales τ (b). The increment PDFs in (b) are shifted vertically for reasons of readability.

Here, $F(\delta u(\tau))$ is the flatness of the velocity increment time series at scale τ, and it is defined as

$$F(\delta u(\tau)) = \frac{\langle (\delta u(\tau))^4 \rangle}{\langle (\delta u(\tau))^2 \rangle^2}. \tag{2.9}$$

σ_0 can be obtained from

$$\sigma_0^2 = \langle \delta u(\tau)^2 \rangle \exp\left[-2\lambda^2(\tau)\right]. \tag{2.10}$$

A flow is considered intermittent at the scale τ if $\lambda^2(\tau) > 0$; if $\lambda^2(\tau) = 0$, the flow is not intermittent at the scale τ, and formula (2.7) turns into a Gaussian distribution.

As above-mentioned, intermittency can not be explained if a constant dissipation rate is assumed, or, to say this in another way, the energy fluctuations are related over λ^2 to the variance σ^2. In addition, the assumption of self-similarity is broken as the statistics are not identical for different scales. Thus, to take into account possible energy fluctuations and intermittency, A. N. Kolmogorov revised his initial theory together with A. M. Obukhov in 1962 by assuming ε to be log-normally distributed across the scales. This theory is known as K62.

One consequence of K62 is that the flatness scales in case of HIT with

$$F(\tau) \propto \tau^{-\frac{4}{9}\mu}, \tag{2.11}$$

where μ is generally referred to as the intermittency factor. In case of HIT, $\mu \approx 0.25 \pm 0.05$ is assumed to be realistic by Pope (2000).

2.2. Atmospheric turbulence

As wind turbines operate in the atmospheric boundary layer (ABL), knowledge of the prevailing wind conditions is important to design the turbines accordingly. For wind turbines, the standards are given in the norm IEC61400 (2005) of the International Electrotechnical Commission (IEC). The design requirements of turbines with regard to atmospheric wind can be found there. According to IEC61400 (2005), when characterizing a site, initially the distributions of wind speeds and wind directions are of interest. As the velocity increases with increasing height, the inflow is non-uniform. A power law profile is assumed close to the ground[vi], and it is influenced by the roughness of the surface. Additionally, the turbulence intensity is used to classify the strength of the fluctuations to account for possible fatigue loads. Turbulence fluctuations within a range of scales directly relevant for the turbine are primarily taken into account by modeling the energy spectrum in this regime, i.e. up to ≈ 10 min. The spectrum is assumed to have an inertial sub-range that follows $E(f) \propto f^{-5/3}$.
As explained in section 2.1, higher-order statistics reveal turbulent structures that are not captured with an analysis of the mean velocity, turbulence intensity and energy spectrum. Morales *et al.* (2011) showed that intermittency is present in the atmospheric boundary layer turbulence. Mücke *et al.* (2011) and Schottler *et al.* (2017) showed that intermittent wind fluctuations are transferred to the loads, torque and power output. Schwarz *et al.* (2018) could verify that intermittency leads to increased fatigue loads.

2.3. Wind energy conversion

This section will briefly introduce the concepts that underlie the conversion of electric energy from kinetic energy in the wind by a wind turbine[vii].
The power P_{wind} that is contained in the wind flowing through the rotor-swept area $A = \pi \cdot (D/2)^2$ of a turbine with diameter D is

$$P_{wind} = \frac{1}{2} \cdot \rho_{air} \cdot A \cdot u_0^3. \tag{2.12}$$

[vi] $u(h) = u(h_{hub}) \cdot (h/h_{hub})^{\alpha}$ with h being the respective height, $u(h)$ denoting the mean velocity at height h, h_{hub} being the hub height of the turbine and $\alpha \approx 0.2$ being the power law exponent

[vii] For further reading, the reader is referred to text books such as Gasch and Twele (2011) and Hau (2014).

ρ_{air} is the air density and u_0 the wind velocity. Formula 2.12 shows that the power is strongly dependent on the wind velocity, as P_{wind} grows cubically with u_0. The wind turbine converts the fraction

$$P_T = P_{wind} \cdot c_P \tag{2.13}$$

into electric power, where c_P is the power coefficient. The power coefficient expresses the efficiency of a turbine and includes all losses. Since not the complete power can be extracted from the wind, the question arises what the limit is. Albert Betz estimated this upper limit by assuming the turbine to be an actuator disc that converts energy from the flow. At the rotor, according to Betz' theory, the velocity is optimally reduced to $u_{disc} = 2/3 \cdot u_0$. In the wake, the velocity is then $u_{wake} = 1/3 \cdot u_0$, which yields the theoretical maximum power coefficient $c_{P,max} = 16/27 \approx 0.59$, where e.g. electric and aerodynamic losses, and physical limitations are not accounted for.

Another important quantity is the thrust acting on a turbine, T_T. The thrust indicates the momentum transfer between flow and turbine. A higher thrust results in stronger wake expansion and a higher velocity deficit in the wake; more kinetic energy in the wind is converted into turbulent motion, which can cause higher rotor loadings for a downstream turbine. For wake analysis, knowledge of the thrust is thus important. The thrust is characterized by the thrust coefficient that is defined as the ratio between the thrust acting on the turbine and the wind's force acting on a circular disc with area A, $c_T = T_T/(1/2 \cdot \rho_{air} \cdot A \cdot u_0^2)$. The corresponding thrust coefficient to $c_{P,max}$ is $c_T = 8/9$.

Of course, the disc concept used by Betz is just a simplified model of a real turbine that rotates with a frequency f_T. As the rotational speed of the turbine is in principle variable, the optimal point of operation is not necessarily met depending on the control settings. Therefore, the thrust can be varied which in turn influences the wake evolution. The rotational frequency is accounted for by calculating the tip speed ratio

$$TSR = \frac{2\pi \cdot f_T \cdot D/2}{u_0}, \tag{2.14}$$

that compares the speed of the rotor blade tip $2\pi \cdot f_T \cdot D/2$ and the inflow velocity.

2.4. Wind turbine wakes

Wind turbines do not only extract energy from the incoming flow but also interact with it actively. On the one side, the extraction of energy from the wind results in a velocity deficit downstream the turbine. On the other side, the turbine represents a rotating obstacle that induces vortices to

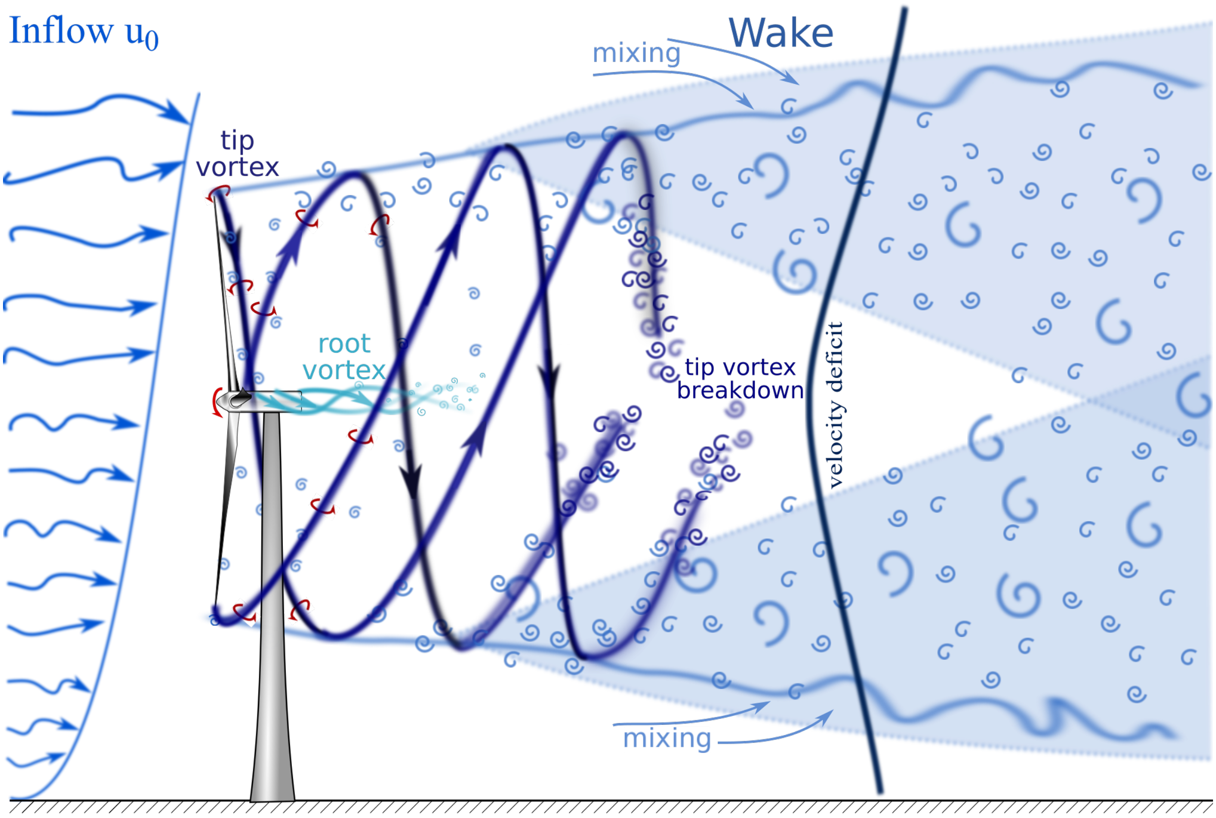

Figure 2.3.: Sketch of the wake downstream a turbine. Highlighted are the tip and root vortices, the shear layer between ABL and wake and the velocity deficit.

the flow. This combination of reduced velocity and increased turbulence downstream a wind turbine is called the *wake* of the turbine.

Wind turbine wakes have been subject to many studies since the 1970s. First, the focus was on modeling the development of the downstream velocity deficit to estimate power losses in a wind farm. One of the most famous models, that is still in use, dates back to 1983, when N. O. Jensen published a simplification based on momentum conservation that sees the wake as top-hat shaped deficit that expands linearly (Jensen (1983)). Since then, analysis and modeling of wind turbine wakes has been subject to investigations. Often, simplified non-rotating models, i.e. actuator discs, replace turbine models in both experimental and computational fluid dynamics wake studies for the sake of simplicity. However, the question arises to what extend this simplification is valid (e.g. Aubrun *et al.* (2013); Lignarolo *et al.* (2016)).

In figure 2.3, the evolution of the wake is sketched and some effects that influence the wake structure are indicated. The wake is characterized by a spin that is induced by the turbine's rotation. Due to conservation of momentum, this spin develops in counter-rotating direction (e.g. Hau (2014) and Sanderse (2009)). In addition, tip and root vortices are shed from the rotor blade's tip and root, respectively. Due to conservation of momentum, the tip and root vortices respectively rotate in opposite direction. The tip vortices are transported with the spinning wake, thus following a helical trajectory. Downstream, the wake widens and the tip and root vortices break down. A shear layer between ambient flow and wake develops, and when this shear layer reaches the wake's center, the phase of growing turbulence ends and in the following region, the turbulence evolution is characterized by turbulence decay.

Mean velocity in wind turbine wakes

The wind turbine extracts kinetic energy from the incoming wind. Thus, a velocity deficit is found behind the turbine. This deficit has approximately the cross-section of the rotor-swept area close to the turbine in the so-called near wake. The influence of the nacelle and the tower are still present. Moving downstream, the velocity decreases further at first (e.g. Hau (2014) and Sanderse (2009)). The reason for this velocity decrease is that the evolution of the mean velocity is linked to the pressure development around the turbine. The pressure increases upstream the turbine, drops at the rotor plane below ambient pressure and recovers downstream the rotor until it reaches ambient pressure again. At this point, the velocity is minimum, and now, the wake starts to recover (Keane *et al.* (2016)). The recovery is driven by re-entrainment of kinetic energy from the free flow around and especially above the turbine by turbulent mixing mechanisms (Lignarolo *et al.* (2014), Camp and Cal (2016)). The velocity deficit is largest in the central region and its profile can be approximated well by a Gaussian curve (Bastankhah and Porté-Agel (2014)). This velocity profile is often assumed to evolve self-similarly downstream the turbine if uniform inflow is considered.
The recovery rate of the mean velocity depends on the turbulence in the ambient flow: Higher ambient turbulence levels enhance the mixing between wake and ambient flow as the tip vortex breakdown is accelerated (Maeda *et al.* (2011); Lignarolo *et al.* (2014); Aubrun *et al.* (2013))[viii]. It could for example be shown that wind turbine wakes and even whole wind farm wakes are significantly extended in stable stratification of the atmospheric boundary layer as compared to turbulent atmospheric boundary layer states (see e.g. Platis *et al.* (2018)).

Turbulence in wind turbine wakes

While the velocity recovery in wakes has been subject to intensive studies, less studies focus on turbulence in wind turbine wakes. Often, the turbulence in the wake of a turbine is accounted for with the concept of *added turbulence*, where wake turbulence is a superposition of turbulence in the incoming flow and turbulence created by the turbine (Vermeer *et al.* (2003)). The latter can

[viii] Note that the turbine used in Lignarolo *et al.* (2014) is a two-bladed model.

be distributed into coherent periodic structures and random velocity fluctuations (Lignarolo *et al.* (2015)).

As a first parameter to describe turbulence, the turbulence intensity downstream a wind turbine is discussed here. The evolution of the turbulence intensity downstream a model wind turbine has for example been investigated experimentally in two different inflow situations by Chamorro and Porté-Agel (2010) up to $20D$ using hot-wire anemometry. An investigation in laminar inflow for a two-bladed turbine operating at two different tip-speed ratios can be found in Lignarolo *et al.* (2014) up to $5D$ using particle image velocimetry (PIV). A Large Eddy Simulation (LES) wake study that also discusses the influence of ambient turbulence on the evolution of the mean velocity and turbulence intensity was carried out in Kermani *et al.* (2013). It is evident from these studies that a wind turbine induces turbulence to the flow, as the turbulence intensity downstream the turbine in the wake is significantly higher than the inflow turbulence intensity. In case of non-uniform inflow, the maximum values are reached at the top tip position of the blade in the region close to the turbine where tip vortices are still present. At the wake centerline, the turbulence intensity first increases in a turbulence production region and reaches a maximum from where the turbulence intensity decreases due to turbulence decay. The stability of the tip vortices and thus also the position of the turbulence intensity maximum at the centerline correlate with the inflow turbulence intensity. The higher the ambient turbulence intensity, the faster/earlier the tip vortex breakdown, and thus the wake recovery by turbulent mixing, starts. Therefore, the centerline turbulence intensity maximum is also found closer to the rotor. Additionally, in accordance with the added turbulence concept, the turbulence intensity in the wake center increases with increasing ambient turbulence intensity.

The discussion of the evolution of turbulent length scales in the wake, above all the integral length scale, has also been subject to multiple studies (see e.g. Aubrun *et al.* (2013), Chamorro *et al.* (2013), Jin *et al.* (2016)). It has been found that the length scales in the near wake are increased in case of turbulent inflow compared to approximately laminar inflow, which can be interpreted as smaller structures from the inflow (i.e. $< D$) passing the rotor. Additionally, in case of turbulent inflow, a reduction of length scales downstream the rotor as compared to the length scales in the inflow is found and interpreted as the turbine chopping the incoming structures. A recovery of the scales takes place downstream the turbine.

Analyzing the turbulent structures in the wake is often done by investigating the energy spectra $E(f)$. On the one side, tip vortices and their breakdown can be evaluated, also with regard to the inflow turbulence. On the other side, energy spectra provide insight into the evolution of turbulence in the energy cascade and, if compared to the energy spectrum of the inflow, the interplay of flow and turbine.

In Maeda *et al.* (2011), Zhang *et al.* (2012), Aubrun *et al.* (2013), Al-Abadi *et al.* (2016), Barlas *et al.* (2016) and Eriksen and Åge Krogstad (2017), tip vortices are captured at outer radial positions around $R/D \approx 0.5$ in the near wake and up to $X/D \approx 2-3$, where R and X denote the radial and downstream position with respect to the center of the rotor. As above-mentioned, their breakdown indicates the start of the wake recovery. It has been found in e.g. Maeda *et al.* (2011), Aubrun *et al.* (2013), Al-Abadi *et al.* (2016) and Barlas *et al.* (2016), that tip vortices break down faster in higher ambient turbulence as the interaction between the wake and the surroundings is enhanced. Thus, the wake recovery is accelerated.

Chamorro *et al.* (2012), Chamorro *et al.* (2013), Singh *et al.* (2014), Bastine *et al.* (2015) and Jin *et al.* (2016) investigated the interaction between a turbine and the inflow. Chamorro *et al.* (2012), Chamorro *et al.* (2013) and Singh *et al.* (2014) examined the interaction between a fully developed boundary layer and the turbine[ix] and concluded that the turbine acts as an active filter that dampens turbulence structures larger than the rotor diameter and induces turbulence at scales smaller than the rotor diameter. In Jin *et al.* (2016), an active turbulence generator[x] is used to generate a uniform turbulent inflow with a turbulence intensity of $TI_{in} \approx 0.12$. It was shown that the turbine enhances the energy of low frequencies while damping the energy of high frequencies in this case.

Few studies exist that examine also intermittency in the wake of a turbine. Wessel (2008), Singh *et al.* (2014) and Bastine *et al.* (2015) investigate the intermittency with regard to the intermittency in the inflow, both in the laboratory and in the free field. They all agree that the turbine reduces intermittency in the flow. Bastine *et al.* (2015) finds signs of homogeneous isotropic turbulence in the center of the wake at one downstream position, which is supported by the findings of Ali *et al.* (2017). Schottler *et al.* (2018) investigated the intermittency by means of the shape parameter for time scales corresponding to the rotor diameter for yawed and non-yawed cases $6D$ downstream two different model wind turbines. A ring with high intermittency and a diameter of $2D$ surrounding the wake area with reduced velocity has been found. These findings extend the current definition of the wake width.

Comparison of actuator disc wake and wind turbine wake

As both experiments and - especially - simulations investigating fully rotating turbine models are complex and costly, the question remains whether and to what extend it is possible to use simplified, non-rotating turbine models, so-called actuator discs. The decay of the tip vortex is an important trigger for the turbulent mixing and, thus, the wake recovery. Therefore, it is of interest to know whether a wake can be modeled properly in the absence of the rotation-induced tip vortices. This problem was addressed experimentally e.g. by Aubrun *et al.* (2013), Lignarolo

[ix] In Chamorro *et al.* (2013), a bed-mounted axial-flow hydrokinetic turbine was used in a turbulent open channel flow.

[x] i.e. an active grid consisting of vertical and horizontal axes with flaps. The axes can be rotated by motors, and to create turbulent flows, the axes are rotated randomly.

et al. (2015), Lignarolo *et al.* (2016)[xi], and Camp and Cal (2016). In Aubrun *et al.* (2013), a disc consisting of an inner and an outer mesh with different blockages to model the nacelle and the rotor was designed to match the velocity deficit of a model wind turbine at $X/D = 0.5$. Two inflow conditions were used, namely decaying isotropic turbulence and an atmospheric boundary layer. Hot-wire measurements of horizontal profiles at $X/D = 0.5$ and $X/D = 3$ were analyzed regarding mean velocity, turbulence intensity, flatness, integral length scale and power spectra. It has been found that around $X/D = 3$ the above-mentioned quantities could be modeled using a disc with good agreement, especially under the more turbulent ABL inflow condition. Both Lignarolo *et al.* (2015), Lignarolo *et al.* (2016), and Camp and Cal (2016) investigated the wake downstream an actuator disc and a model wind turbine with similar c_T using PIV. The former two studies have used laminar inflow conditions, thus eliminating the beneficial influence of the inflow turbulence on the wake recovery. Therefore, the influence of the tip vortex development on the wake recovery can be compared to the mixing mechanisms created by a disc. Camp and Cal (2016) investigate the wake of the center model in the last row of a 3x4 model array which represents a more realistic setup.

Lignarolo *et al.* (2015) and Lignarolo *et al.* (2016) comment on the similarity of the velocity field, wake expansion and energy extraction downstream a disc and turbine. Anisotropic flow structures were found in the wakes of both models. The main difference is that downstream the turbine, the span-wise velocity component is significantly enhanced due to the rotation. Nevertheless, the present strong near wake flow fluctuations downstream the turbine do not enhance turbulent mixing. This result is also confirmed by Camp and Cal (2016). Turbulence intensities are found to be higher in the near wake of the turbine compared to the disc's near wake but they adapt downstream.

In conclusion, the studies agree that the wakes created by an actuator disc and a model wind turbine are astonishingly similar regarding the examined quantities despite the completely different mechanisms responsible for turbulent mixing.

[xi] Note that the turbine used in Lignarolo *et al.* (2015) and Lignarolo *et al.* (2016) is a two-bladed model.

3. Setup

In the following, details on the experimental realization of the wake studies are presented. First, the measurement methods and the two WGTs, i.e. the actuator disc and the model turbine, are introduced. Thereafter, two different experimental setups will be presented. The first one was designed to compare the wakes of an actuator disc and a turbine and to examine the influence of the inflow turbulence on the wake evolution. The second experiment was designed to investigate the evolution of a wake in a wind turbine array.

3.1. Measurement methods

In this section, a quick introduction to hot-wire anemometry is given, followed by an overview of how hot-wires were used in this thesis. Hot-wire anemometry is used as standard method to measure the velocity of air flows. For detailed information, the reader is referred to e.g. Bruun (1995).

All measurements presented in the main part of this thesis were carried out with hot-wires in air. Hot-wire anemometry was chosen because it is well suited to collect data for statistic analysis with a high temporal resolution. The measurement principle is based on the instantaneous and velocity-dependent cooling of a thin, heated wire exposed to a moving fluid. The cooling is caused by convective heat transfer. The resistance of the hot-wire changes due to its temperature dependence, and this resistance change can be measured. The usual setup intends to include the hot-wire in a Wheatstone bridge where the power needed to keep the wire's temperature constant, i.e. to keep the bridge in balance, is measured via the control voltage U_V. The hot-wire has to be calibrated to assign each velocity u a voltage U_V. The calibration follows the so-called *King's law*.

As the cooling of the wire is dependent on the angle between flow and wire, two or three wires with different tilt angles can be combined in a probe to design 2D and 3D hot-wires. These probes are capable of measuring additional flow components apart from the main flow direction, if a velocity calibration is combined with an angular calibration.

The thermal conductivity of the hot-wire is not only dependent on the flow velocity but also

on the difference between its temperature T_w and the ambient temperature T_a, $\Delta T = T_w - T_a$[i]. Thus, the calibration is only valid for the temperature of the fluid during the calibration. If the temperature varies in or during the measurement, the temperature has to be monitored during measurement and an additional temperature correction has to be applied. In this thesis, all data were corrected according to a procedure suggested in Hultmark and Smits (2010).
As hot-wires provide only single point measurements, several 1D hot-wire probes were combined in an array to scan the flow at multiple positions simultaneously. In figure 3.3 and 3.5, the arrays used in the two different setups are included. The first array included ten probes and was designed to scan the wake and the surrounding flow at multiple positions to obtain a horizontal flow profile at hub-height of the WGT and additional information on the flow at vertical positions. The second array included six probes and was designed to measure the wake expansion far downstream. Thus, the hot-wires were placed to measure a horizontal profile of half of the wake at hub height, and several sensors were placed outside the rotor-swept area.
The majority of measurements was performed with 1D hot-wire sensors operated by different systems from *Dantec Dynamics* and using A/D converters from *National Instruments*. A detailed description of the used equipment and the calibration procedure is included in appendix A.
To validate the results obtained from hot-wire anemometry, measurements have also been carried out with a 2D Laser Doppler Anemometer (LDA), a non-invasive optical measurement method, and some results can be found in appendix C.

3.2. Wake generating turbine models: actuator disc and model turbine

In the following, the two WGTs, i.e. the actuator disc (also referred to as disc) and the model wind turbine, are introduced.

Actuator disc

In figure 3.1, a photograph and the technical drawing of the disc are presented. The disc has a diameter of $D_D = 0.59\,\mathrm{m}$ and is cut from an aluminum plate of $5\,\mathrm{mm}$ thickness. Its blockage is $b_D \approx 53\%$. The disc is mounted on a tower with diameter $d_D = 3.6\,\mathrm{cm}$. The design differs from a more classical approach where a disc is modeled with fine uniform meshes (see e.g. Aubrun *et al.* (2013)), as it aims for fulfilling the following requirements:

[i] As the thermal conductivity is dependent on the fluid's density, a rather small dependence on changes in the ambient humidity and pressure is present.

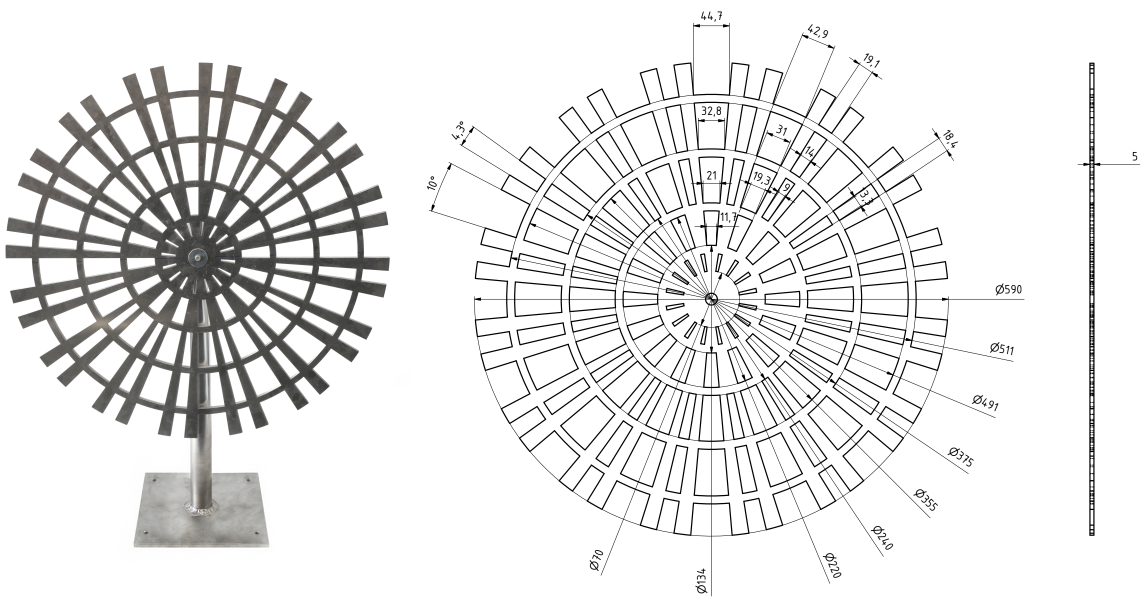

Figure 3.1.: Photograph (left) and technical drawing (right) of disc

- The local blockage should be 100% in the center where the nacelle is located in case of a turbine, and the blockage should vary radially similarly to a real turbine.
- The disc was designed to create high turbulent mixing on multiple scales due to its more fractal-like structure.
- The thrust of the disc needs to match the turbine's thrust at the desired inflow velocity to compare the results.

The measurement of the thrust force yields a thrust coefficient of $c_{T,D} = 0.96$ (cf. appendix D). The thrust coefficient is close to the ideal thrust coefficient of $c_T(c_{P,max}) = 8/9$ of a turbine.

Model turbines

In figure 3.2, a photograph and the technical drawing of the model turbine type are presented. The three-bladed model turbine has a rotor diameter of 0.58 m. It is controlled by varying the load on the generator, which results in the adaption of the turbine's rotational frequency $\omega_T = 2\pi \cdot f_T$ and thus its TSR. More details on the turbine can be found in Schottler *et al.* (2016a) and Schottler (2018).

During the measurements, two turbines of the above-described type, called *turbine 1* and *turbine 2*, were used. The blade pitch of $\psi \approx -1^\circ$ was the same for both turbines.

Two different control strategies were used in the measurements presented in this thesis.

For the measurements that were carried out in the *Turbulence Wind tunnel Oldenburg* (TWO),

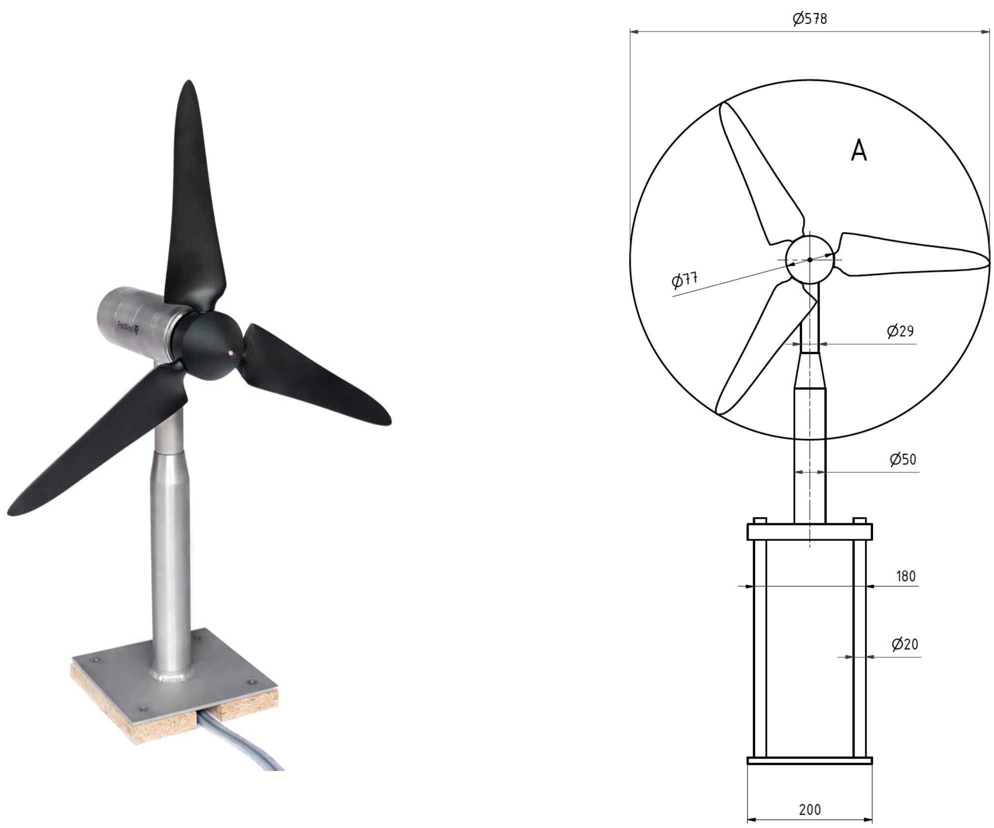

Figure 3.2.: Photograph (left) and technical drawing (right) of the model turbine. The technical drawing also includes the support structure that was used in some of the experiments.

the tip speed ratio was set to a fixed value. The turbine control acted to meet this TSR according to the velocity in front of the turbine. The velocity was measured by a 1D hot-wire mounted in a distance of $1/3D$ in front of the turbine at hub height[ii]. The control will be referred to as *control 1*. Details for this control can be found in Schottler (2018).
The measurements carried out in Oldenburg's new large wind tunnel (OLWiT) were performed with a new control that relies on the generator torque instead of a control hot-wire to find the respective operation point. An additional velocity measurement is thus not necessary anymore. However, the turbines need to be characterized before the measurement. This control will be referred to as *control 2*. For details regarding this control, see Petrović *et al.* (2018).

To characterize the turbines, their thrust was measured (cf. appendix D). The thrust was measured for turbine 1 and 2 operated with control 2, and additionally for turbine 2 operated with control 1. The values of the thrust coefficient can be found in table 3.1 in dependence of the respective control mode. The thrust acting on the two turbines is similar if they run with control

[ii] The compared to u_0 decelerated inflow at $1/3D$ upstream the rotor was accounted for during experiments when setting the TSR.

2. In case of turbine 2 operated with control 1, the TSR was calculated both using the decelerated measured velocity and the real inflow velocity u_0. The TSR and thrust are with regard to u_0 similar for both control algorithms. Compared to the ideal thrust coefficient, the thrust acting on the whole turbine is about 10% higher, however, the measured thrust is not corrected for the influence of the tower and nacelle. Also, the disc's thrust matches the turbine's thrust well.

3.3. Experimental setups

The aim of the measurements presented in this thesis is a structured investigation of the wind turbine wake. Therefore, in the following, two experimental setups that were used to investigate different aspects influencing the wake are described.

The first set of experiments was carried out in TWO. This wind tunnel has an outlet of $0.8\,\mathrm{m} \times 1.0\,\mathrm{m}$ (height $\times$ width) and an open test section of approximately 5 m length[iii]. As the blockage of the WGTs is comparatively high in this wind tunnel, the limitations of the setup are discussed in appendix C. Two goals were pursued during these experiments. First, the role of the turbine rotation in the wake recovery was to be investigated. To achieve this, the turbine was replaced by a disc to remove the impact of the rotation. Second, the influence of incoming turbulence on the evolution of turbulence in the wake was to be analyzed. For this, the inflow turbulence was varied by using different grids that were available for this wind tunnel.

The second set of experiments was carried out in OLWiT, a wind tunnel with an outlet of $3\,\mathrm{m} \times 3\,\mathrm{m}$ and a closed test section of 30 m length[iv]. Due to its significantly larger cross-section, this wind tunnel is more suitable for the WGTs used here. However, as it was finished in 2017, only a part of the measurements was carried out here. The aim of these measurements was to examine whether the results found in the first experiments can also be applied in a wind farm setup. Therefore, an array of two turbines was investigated, and an extended measurement range downstream was considered.

[iii] For more information on this wind tunnel, see Reinke (2017).
[iv] For more information on the wind tunnel, see Kröger *et al.* (2018)

Table 3.1.: Thrust coefficients for the disc and both turbines in both control modes as measured (cf. appendix D). The values in brackets in column 5 refer to the TSR and c_T obtained from the velocity measurement in front of the turbine.

	disc	**turbine 1** control 1	**turbine 2** control 1	**turbine 2** control 2
TSR	-	5.7	5.8	6.2 (7.3)
c_T	0.96	1.00	1.07	1.00 (1.40)

In the following, details on the respective setup are given. First, the setup will be described. Second, the inflow conditions are presented for the experiments carried out in TWO. Third, the measurement procedure is presented.

3.3.1. Experiments in TWO

The aim of this set of experiments is to examine the effect of different turbulent structures, i.e. vortices, in the inflow on the evolution of turbulence in the wake, and to explore how the presence of rotation induced by the turbine influences the wake. The setup for measurements downstream the disc and turbine [v] is presented in figure 3.3. In the open test section of the wind tunnel, the flow was investigated using ten 1D hot-wire probes (sensor length: 1.25 mm) mounted on an array. The probe positions are indicated in figure 3.3. At each position, $5 \cdot 10^6$ data points were collected with a sampling frequency of $f_s = 20\,\mathrm{kHz}$[vi]. As indicated, the WGT was placed $1.17D$ downstream the outlet. The center of the rotor position is used as origin of the coordinate system. Three inflow conditions were examined in the experiments:

1. The free flow of the wind tunnel, in the following called *no grid inflow* or *laminar inflow*
2. Uniform turbulent inflow generated by a regular square grid of mesh width 50 mm and blockage $\approx 23\%$, in the following called *regular grid inflow*
3. Turbulent inflow created by an active grid. The active grid can be used to imprint customized flow patterns onto the wind. If it is used as passive regular square grid, the mesh size and blockage are 110 mm and $\approx 5\%$. For the design, the reader is referred to Knebel *et al.* (2011) and Reinke (2017).
   Here, the active grid was used to re-create a time series measured in the free field. The motion protocol takes 68 s. The inflow will be called *active grid inflow*.

In order to characterize the flow field, the array was traversed downstream in a range $-0.31D - 3.31D$ in steps of $0.17D$, and additionally at $4.00D$ and $4.69D$. The main characteristics of the respective inflows at rotor position are summarized in table 3.2. An average value over the seven measurement positions within the rotor-swept area is given for the most relevant quantities. The integral length, Taylor length, Taylor Reynolds number, and shape parameter are not calculated for the laminar flow since the spectra show, as expected for laminar flows, no signs of turbulence. The mean wind speed is similar for all experiments whereas the turbulence intensity is lowest for the laminar inflow and highest for the active grid inflow. The Taylor Reynolds number mirrors this result as well. Additionally, the downstream evolution of the

[v] During all measurements carried out in TWO, *turbine 2* was used and the turbine was operated with *control 1*

[vi] For the statistic evaluation except calculation of mean velocity and standard deviation, the data was sampled down by taking every third data point, as some artifacts from the measurement system appeared in the spectra at frequencies $> 7\,\mathrm{kHz}$.

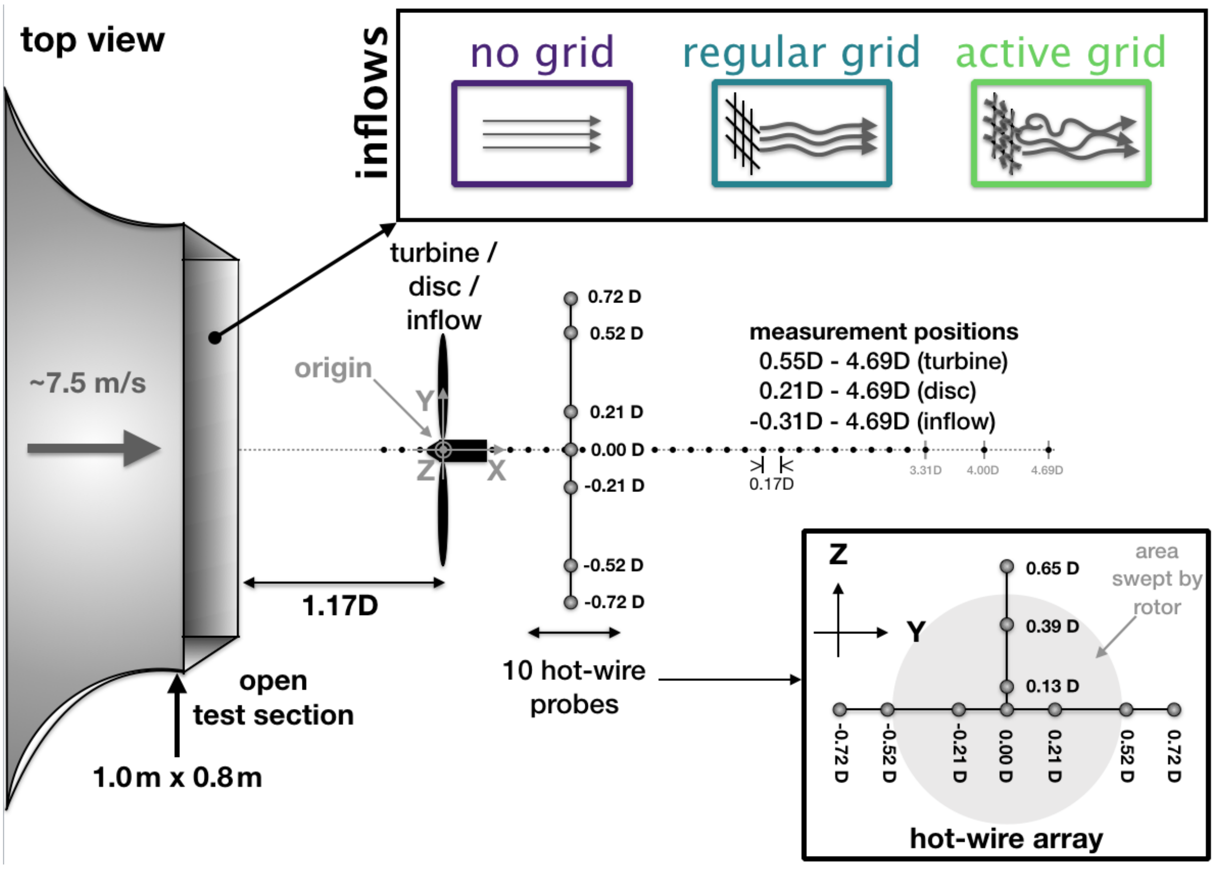

Figure 3.3.: Setup for measurements with disc and turbine in different inflow conditions in TWO.

mean velocity and the turbulence intensity can be found in figure 3.4 with regard to the turbine position. In case of laminar inflow, the flow field is even with low turbulence intensities close to the outlet. In the open test section, a shear layer evolves downstream, causing the velocity to drop in the outer regions of the flow field. Simultaneously, the turbulence intensity increases. The centerline is mostly unaffected in the measured region. Downstream the regular grid, the flow field is characterized by a stable core with medium turbulence intensity and an even flow field, while the shear layer affects the outer regions along the complete measurement field. The average mean velocity is higher than in laminar inflow. In case of the inflow generated by the active grid, the mean velocity and the turbulence intensity are highest. The flow field can again be separated into an inner region with even flow field and an outer region where the shear layer causes lower velocities and higher turbulence intensities.

The wake measurements were carried out downstream the disc and the turbine in the three inflow conditions introduced above (i.e. laminar, regular grid and active grid inflow).

The WGT, i.e. the disc or the turbine, is positioned 68 cm or $1.17D$ from the outlet, and the rotor is centered with regard to the wind tunnel outlet. All coordinates are given with respect to the

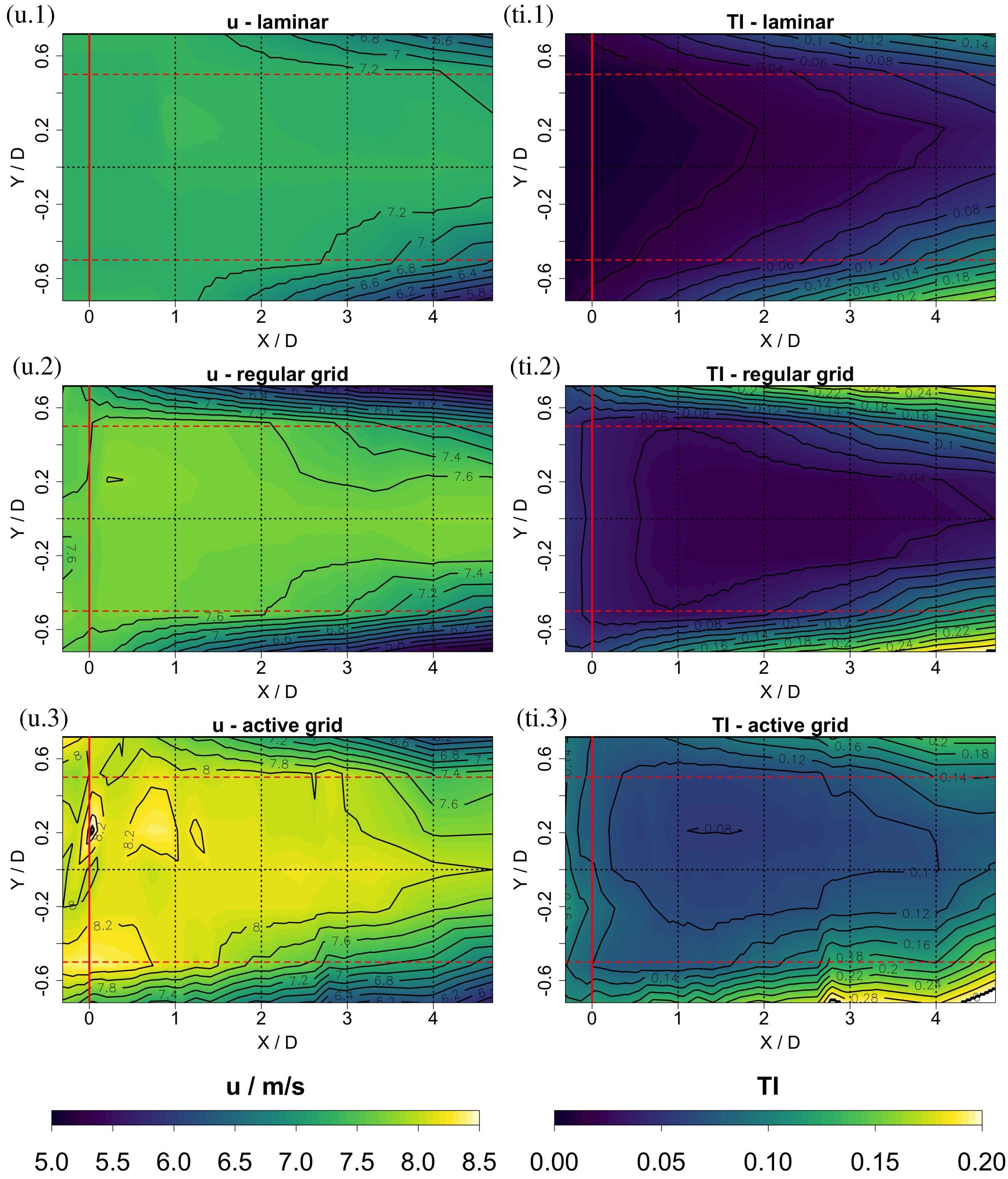

Figure 3.4.: Inflow conditions in TWO without WGT: Interpolated mean velocity (u.i) and turbulence intensity (ti.i) for the three inflow conditions, laminar (x.1), regular grid (x.2) and active grid (x.3). The red dashed lines mark the turbine radius, and the red line marks the rotor position.

Table 3.2.: Main characteristics of the three inflow conditions averaged over seven measurement positions across the rotor plane: mean velocities, turbulence intensities, approximate integral and Taylor lengths, Taylor Reynolds numbers and the shape parameter for a time scale corresponding to the rotor diameter are presented.

	laminar	**regular grid**	**active grid**
$u_0/\,\mathrm{m/s}$	7.26	7.63	8.06
$TI/\%$	0.3	7.1	10.3
$L/\,\mathrm{cm}$	-	2.4	1.5
$\lambda_T/\,\mathrm{mm}$	-	3.3	4.4
Re_λ	-	88	276
$\lambda^2(\tau \simeq D)$	-	0.00	0.13

center of the rotor.
The hot-wire array was traversed along the wake in a range of $0.55D - 3.31D$ downstream the turbine and $0.21D - 3.31D$ downstream the disc in steps of $0.17D$, and additionally at $4.00D$ and at $4.69D$.

3.3.2. Experiments in OLWiT

In the second set of experiments, the wake of a turbine exposed to another wake as inflow should be investigated. This setup is presented in figure 3.5. Here, experiments were carried out in OLWiT. Measurements were carried out in a closed test section in uniform laminar inflow. Both turbines were mounted on a support structure as indicated in the technical drawing in 3.2, and their hub height was 77 cm. The turbines were operated using control 2. Six 1D hot-wire sensors were mounted on a traverse to scan the wake. Their positions can be found in figure 3.5.
First, the wake of the front turbine (turbine 1) was measured, and turbine 2 was not present in the setup during this measurements. Turbine 1 was exposed to laminar, uniform inflow with $u_0 = 7.5\,\mathrm{m/s}$. The wake was measured in the region between $X/D = 0.55$ and $X/D = 12.62$ in steps of $0.17D$. For each point, $1.2 \cdot 10^6$ data points were collected with a sampling frequency of $f_s = 15\,\mathrm{kHz}$. Second, turbine 2 was positioned $5.17D$ downstream of turbine 1, thus being fully exposed to the wake of turbine 1. Third, turbine 2 was shifted $0.52D$ to the side to create a scenario where a turbine is hit by non-uniform, turbulent inflow. Downstream turbine 2, data was collected between $0.55D$ and $8.66D$ in steps of $0.17D$. $1.2 \cdot 10^6$ data points were collected with a sampling frequency of $f_s = 15\,\mathrm{kHz}$.

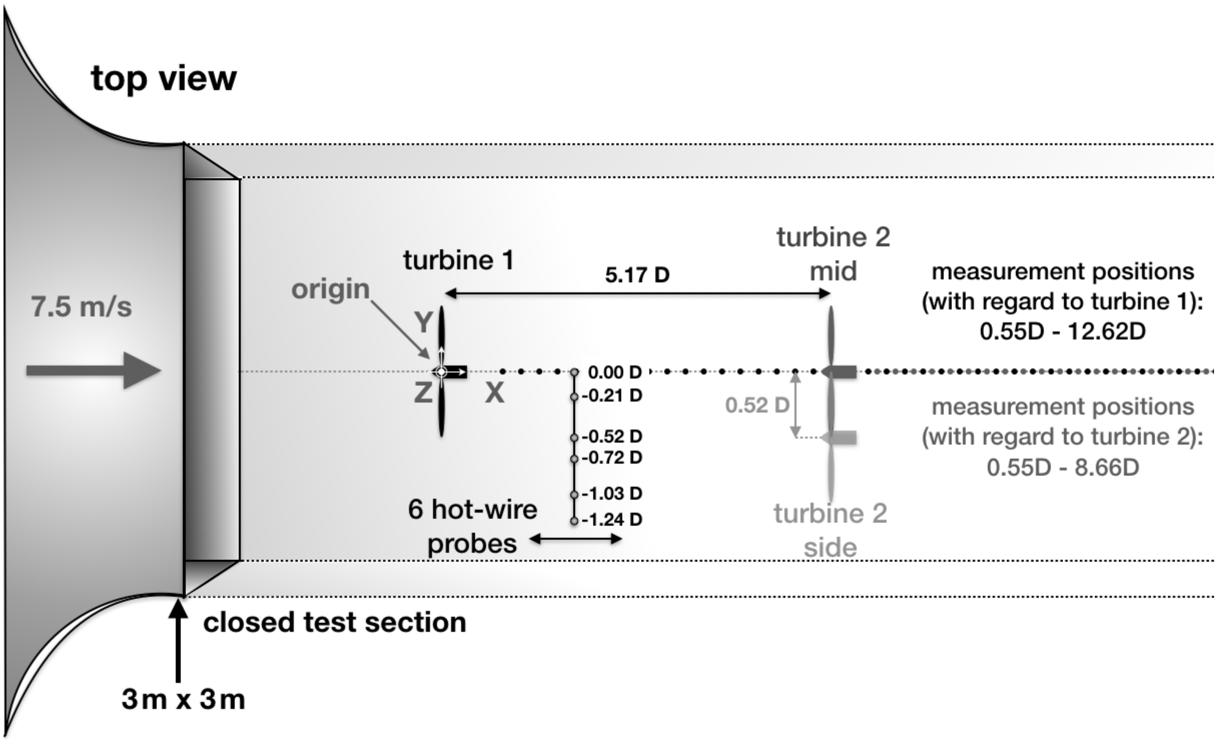

Figure 3.5.: Setup for measurements with turbine 1 and 2.

4. Results 1: Comparison of a disc and a turbine wake

In this chapter, the results of measurements carried out downstream the disc and the turbine in TWO are presented. Apart from the influence of the turbine's rotation, the impact of different uniform inflow conditions on the wake will be investigated. First, the data are examined with standard methods, i.e. mean velocities, turbulence intensities and characteristic length scales. In the second part, the evolution of energy spectra and probability density functions of temporal and spacial velocity increments is discussed. Additionally, the shape parameter is scrutinized to quantify non-Gaussian forms of the probability density function of velocity increments. The results are compared to results from other studies. This chapter is concluded by a comparison of the findings with results obtained from full-scale turbines.

The measurements that will be presented in the following can be organized into six different scenarios. These scenarios consist of the two WGTs, i.e.

(a) the *actuator disc*, also referred to as *disc*

(b) the *model wind turbine*, also referred to as *turbine*

and the three inflow conditions with different turbulence properties, i.e.

1. *no grid* inflow, also referred to as *laminar* inflow
2. *regular grid* inflow
3. *active grid* inflow.

The setup and properties of the different inflows can be examined in the preceding chapter 3, and the analysis methods can be read up in chapter 2.1.

4.1. Standard analysis of the wake flow

When investigating wakes, many studies focus based on applications on the velocity recovery and the downstream evolution of the turbulence intensity. In this section, the measurements are therefore surveyed within the framework of classical wake studies. First, the evolution of the mean velocity deficit is presented to give a first overview on the flow field downstream the turbine. The maximum velocity deficit and its position will be identified, and the flow recovery will be investigated. Next, the downstream development of the turbulence intensity is presented. It will be shown that - similar to the wake of a fractal grid - the turbulence intensity builds up first and decreases farther downstream. The decay of the turbulence will be discussed in analogy to the turbulence decay downstream a fractal grid. Afterwards, characteristic length scales are discussed to give an overview on the turbulence scales present in the wake and how they evolve downstream. All listed quantities are investigated in the following manner: First, interpolated contour plots give an overview of the whole measurement field. Afterwards, profiles at four downstream positions are depicted, and the centerline evolution of the respective quantity is plotted to allow for a direct comparison of the data. Error bars indicate the accuracy of the measurements; the error calculation is explained in appendix B. The results are then summarized and, where possible, compared to other studies. The especially in contrast to other studies high downstream resolution of measurement points enables a detailed description of the evolution of all quantities. Finally, this section concludes with a brief summary where the results are also viewed with regard to other studies.
A discussion of the results can be found in chapter 6 where all results obtained in this thesis are linked and summarized.

4.1.1. Downstream development of the normalized mean velocity

Figure 4.1 shows the evolution of the normalized mean velocity u/u_0 downstream the disc and the turbine for the three inflow conditions (cf. page 33) as interpolated contour plots. u_0 is the respective inflow velocity (cf. table 3.2).
Directly downstream the disc (plots (a.i)), the flow shows a strong velocity drop due to the local blockage. Beyond this velocity drop, the actual wake evolves. In the center of the wake, the velocity recovers after a local minimum around $X/D \approx 1.5$. The decrease of the normalized velocity outside the rotor plane with increasing downstream position indicates the wake expansion. An influence of the inflow conditions on the wake evolution downstream the disc is not visible.
Downstream the turbine (plots (b.i)), a strong decrease of the velocity is visible directly behind the rotor blades, while the velocity is not as much reduced under the nacelle's lee. The wake

evolves from there: First, the velocity decreases in the center of the wake. Then, the wake recovery starts around $X/D \approx 2$. The wake expansion can be identified by the decrease in velocity outside the rotor plane with increasing distance from the turbine. An influence of the inflow conditions is visible, although the overall behavior of the wake evolution is comparable for the different inflow conditions.

For a better direct comparison, figure 4.2 shows wake profiles at distances $X/D = 1.07, 2.10, 2.97, 4.00$ for the disc (a) and turbine (b). Downstream the disc, a strong profile evolves that flattens downstream. As already expected from the contour plots, the profiles downstream the disc show no dependence on the inflow condition.

In the wake of the turbine at $X/D = 1.07$, the influence of the nacelle is visible. A profile develops only farther downstream, and it flattens downstream. An influence of the inflow on the wake development is visible, although the qualitative evolution is comparable. With regard to laminar inflow, the average difference across the rotor varies between 7% at $X/D = 1.07$ and 29% at $X/D = 2.10$ for regular grid inflow, and between 12% at $X/D = 1.07$ and 19% at $X/D = 2.97$ for active grid inflow.

The centerline evolution of the normalized mean velocity is considered for all inflows in figure 4.3 for the disc (a) and turbine (b).

Looking at the development of the normalized mean velocity downstream the disc confirms its independence on the inflow condition. Quantitatively, the local minimum of $u/u_0 \approx 0.19$ at $X/D = 1.59$ can be seen as the start of the wake recovery. This point will be named $X^u_{a.i}$, and the results are also summarized in table 4.1. At $X/D = 4.69$, the wake has recovered to $u/u_0 \approx 0.63$.

In the wake of the turbine, differences due to the inflow conditions can be seen, although the overall behavior is comparable for the different inflow conditions. The wake recovery defined by the minimum velocity starts depending on the inflow at around $X/D \approx 2$, where the normalized centerline velocity is between $u/u_0 \approx 0.1$ and $u/u_0 \approx 0.2$. The precise positions $X^u_{b.i}$ can be found in tables 4.1 and also E.1. At the end of the test field, the wake has recovered to $u/u_0 \approx 0.53$. The difference between laminar inflow and inflow generated by a regular grid is 18%, and it is 1% in case of inflow generated by an active grid.

For a direct comparison of the wakes of the two WGTs, the average evolution of the normalized mean velocity downstream the disc is indicated in figure 4.3(b) where the centerline evolution of the normalized mean velocity downstream the turbine is shown.

In figures 4.1 and 4.2, a comparison of the wakes between disc and turbine shows that on the one side, the flow field looks differently in proximity to the WGT. On the other side, the flow fields look similar far downstream except for the slightly lower velocity downstream the turbine. The normalized velocity profiles and the centerline evolution of the normalized velocity pronounce both the different development of the wake close to the respective WGT and the wakes' adaption far away. The high downstream resolution of measurement points allows for a

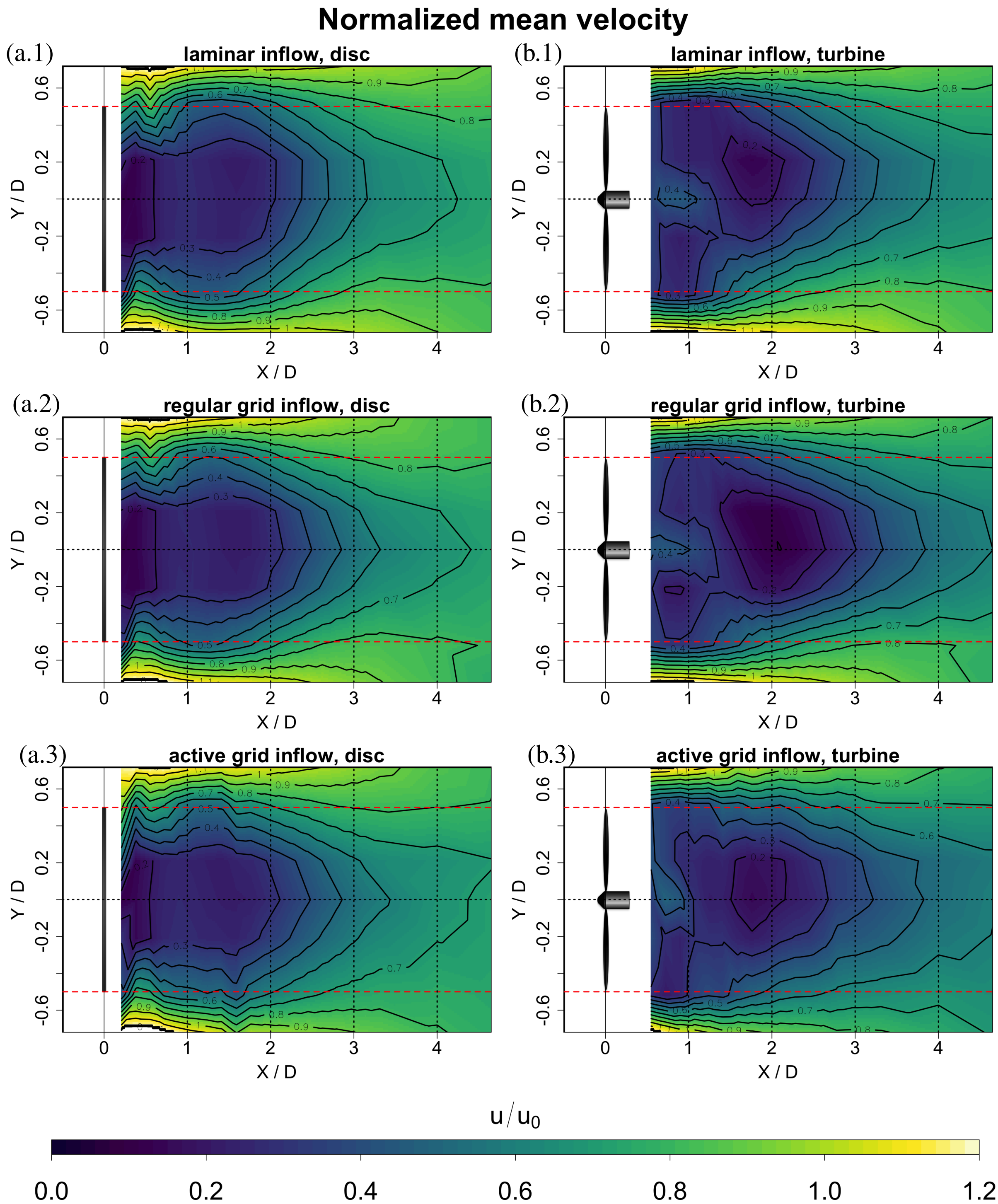

Figure 4.1.: Evolution of normalized mean velocity u/u_0: Surface plots downstream the disc (a.i) and the turbine (b.i) for laminar (x.1), regular grid (x.2) and active grid (x.3) inflow.

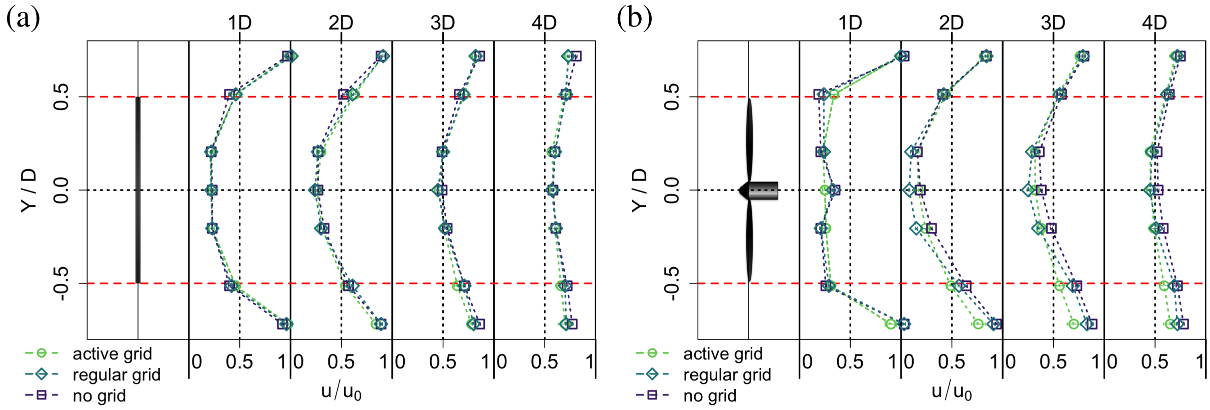

Figure 4.2.: Profiles of the normalized mean velocity downstream the disc (a) and the turbine (b) at $X/D = 1.07, 2.10, 2.97, 4.00$ for different inflow conditions. Error bars are included but may be within the symbols.

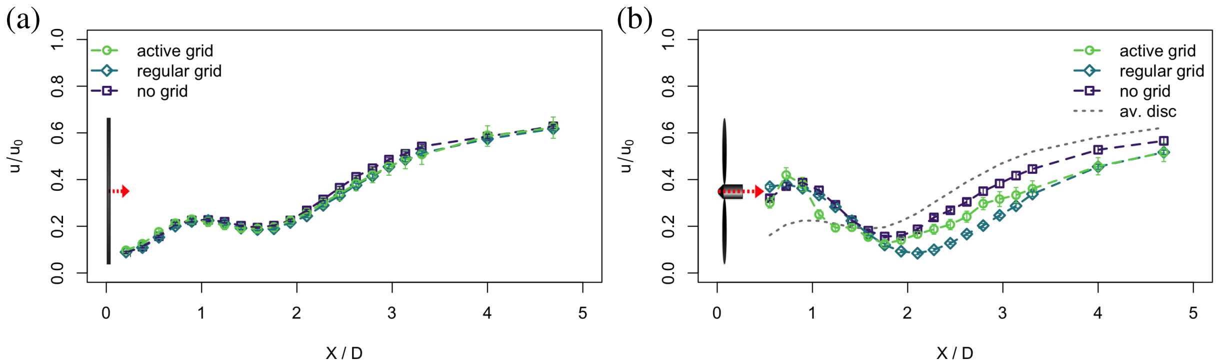

Figure 4.3.: Development of the normalized mean velocity downstream the disc (a) and the turbine (b) on the centerline for different inflow conditions. Error bars are included but may be within the symbols. In (b), the downstream evolution of the mean velocity averaged over all inflow conditions is plotted for comparison.

detailed investigation of the evolution of the mean velocity, and the downstream position where the wake recovery begins can be identified.

To summarize, the evolution of the mean velocity downstream the disc and the turbine shows the expected behavior. From the direct comparison of the centerline evolution of the mean velocity in figure 4.3(b), it could be shown that the wake of this disc is in the far field an adequate substitution of the wake of the turbine. This outcome is similar to the results found by Aubrun *et al.* (2013), Lignarolo *et al.* (2015), and Lignarolo *et al.* (2016). For example, the centerline velocity downstream both WGTs has recovered depending on the inflow turbulence to 55%-65% of the inflow velocity at $X/D = 3$ in Aubrun *et al.* (2013), matching the recovery at $X/D = 4.69$ obtained in this study. The differences may be explained by the lower TSR of

5.8 in Aubrun *et al.* (2013) and the adapted thrust of the disc. In Lignarolo *et al.* (2016), the centerline velocity is at $X/D = 2.2$ approximately 10% of the inflow downstream the turbine, and approximately 30% downstream the disc, which is in agreement with the results obtained in the here presented study. Also, the analysis of the mean velocity downstream the turbine shows a similar centerline evolution to Keane *et al.* (2016). Here, the wake recovery for a comparable inflow velocity of $7\,\mathrm{m/s}$ starts around $X/D \approx 2$, and at $X/D \approx 4.5$, the wake has recovered to approximately 65% of the inflow velocity.

Looking at the evolution from the near field to the far field, an influence of higher ambient turbulence levels on the wake recovery is not visible in case of the disc. However, as the break down of the tip vortex structure downstream the turbine is influenced by the ambient turbulence, differences can be identified in the wake of the turbine. The differences in the flow behavior close to the WGTs are caused by the fundamentally different turbulence mixing mechanisms.

In the next step, the evolution of the turbulence intensity is evaluated.

4.1.2. Downstream development of the normalized turbulence intensity

The evolution of the turbulence intensity is presented in a similar manner as the results of the normalized mean velocity. In figure 4.4, interpolated surface plots of the turbulence intensity development are presented for the wake of the disc (a) and the turbine (b) for the inflow conditions. To improve the comparability of all results, the turbulence intensity TI is normalized to the respective peak turbulence intensity[i] on the centerline, TI_{CLpeak}. The values can be found in table 4.2. A detailed discussion of the reliability of the measurements is included in appendix C considering the high measured turbulence intensities. LDA and 2D hot-wire measurements are used to validate the data.

Looking at the evolution of the normalized turbulence intensity downstream the disc (figure 4.4, plots (a.i)), one finds the highest values in direct vicinity to the disc in the center. They

[i] i.e. the local maximum around $X/D \approx 2$

Table 4.1.: Downstream positions X/D and values of the local velocity minima $u/u_{0,min}$ for the disc and the turbine for the three inflow conditions in TWO.

	disc			turbine		
	laminar	reg. grid	act. grid	laminar	reg. grid	act. grid
$u/u_{0,min}$	0.19	0.19	0.19	0.16	0.08	0.13
X/D	1.59	1.59	1.59	1.76	2.10	1.76

exceed the peak turbulence intensity TI_{CLpeak}. This is not discussed further here, as the behavior is assigned to be related to local structures rather than developed turbulence. After a brief decrease, the turbulence intensity increases from $X/D \approx 1$ to $X/D \approx 1.76$ as the turbulence builds up. Afterwards, the turbulence decays and the turbulence intensity decreases. Outside the rotor plane, the normalized turbulence intensity is small in vicinity of the rotor, but increases downstream where the wake expands. The influence of the inflow condition on the evolution of the normalized turbulence intensity is little.

Downstream the turbine (figure 4.4, plots (b.i)), the normalized turbulence intensity first builds up. Then, it reaches its maximum in the center of the wake around $X/D \approx 2$. Beyond the peak, the turbulence decays. In the near wake, a high turbulence intensity downstream the tips of the rotor blades is found, that is caused by the tip vortex structure. An influence of the inflow on the near wake structures is present. Far away from the turbine, the effect appears to be small.

For a more qualitative comparison, figure 4.5 shows profiles of the normalized turbulence intensity for all inflows downstream the disc (a) and turbine (b).

Downstream the disc, the normalized turbulence intensity develops a profile with high values in the center that decrease radially. The profile flattens with increasing distance from the disc. An influence of the inflow is with regard to the errors not present.

Close to the turbine at $X/D = 1.07$, a profile has not yet evolved. In the nacelle's lee in the wake center, the normalized turbulence intensity is smaller than at $Y/D = \pm 0.51$, where the tip vortices increase the turbulence level. Farther downstream in the region where the turbulence intensity decreases, a profile with high turbulence degrees in the center and low turbulence degrees at the outer radial positions is identifiable. This profile flattens with increasing downstream position. The inflow influences the evolution of the normalized turbulence intensity close to the turbine, but the influence diminishes downstream.

Next, the downstream evolution of the normalized turbulence intensity is compared by plotting TI/TI_{CLpeak} over X/D at $Y/D = 0$ for the disc (a) and the turbine (b) in figure 4.6.

Downstream the disc, the normalized turbulence intensity exhibits the highest values in close proximity to the WGT. After a drop, the normalized turbulence intensity increases, and the turbulence decays from $X/D = 1.76$. The precise positions can be found in table 4.3. At $X/D = 4.69$, the turbulence has decayed, and $TI/TI_{CLpeak} \approx 0.4$. An influence of the inflow is not present.

Table 4.2.: TI_{CLpeak} used for the normalization of the turbulence intensity for all scenarios.

	disc			**turbine**		
	laminar	reg. grid	act. grid	laminar	reg. grid	act. grid
TI	0.63	0.62	0.62	0.68	0.81	0.91
X/D	1.76	1.59	1.59	2.10	2.28	2.10

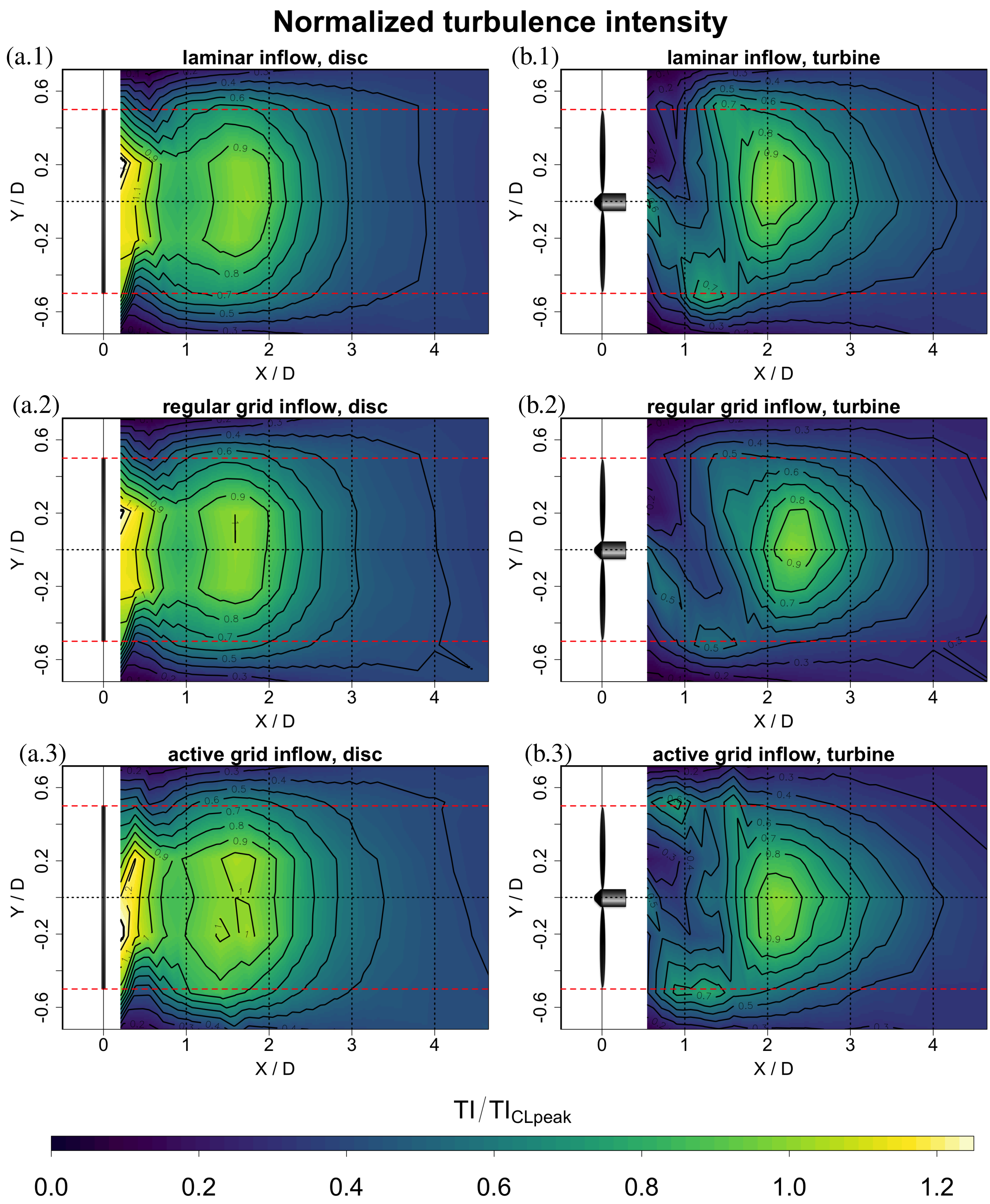

Figure 4.4.: Evolution of the normalized turbulence intensity TI/TI_{CLpeak}: Surface plots downstream the disc (a.i) and the turbine (b.i) for laminar (x.1), regular grid (x.2) and active grid (x.3) inflow.

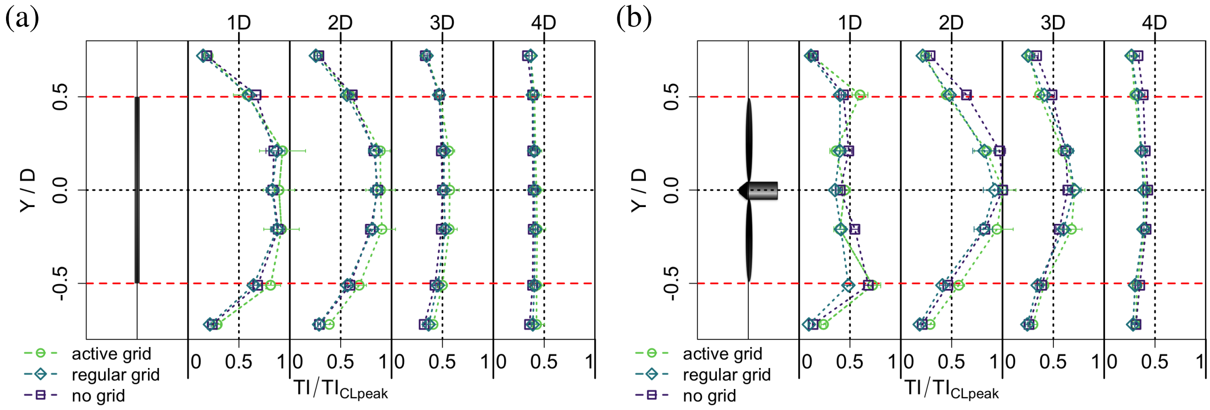

Figure 4.5.: Profiles of the normalized turbulence intensity TI/TI_{CLpeak} downstream the disc (a) and the turbine (b) AT $X/D = 1.07, 2.10, 2.97, 4.00$ for different inflow conditions. Error bars are included but may be within the symbols.

Downstream the turbine, the evolution of the normalized turbulence intensity is first influenced by the nacelle. The influence vanishes around $X/D \approx 1$ [ii] from where the turbulence builds up and the turbulence intensity increases. From $X/D \approx 2$, the turbulence intensity decreases. The precise positions o the local extrema can be found in table 4.3 and additionally in appendix E in table E.1. At $X/D = 4.69$, $TI/TI_{CLpeak} \approx 0.4$ similarly to the disc, which is also emphasized by the gray line in figure 4.6(b) that indicates the average evolution of TI/TI_{CLpeak} downstream the disc. In the region where the turbulence intensity decreases, a difference can not be seen with regard to the error bars.

Regions where the turbulence intensity decreases indicate a decay of the turbulence, that is in turbulence research often assumed to follow a power law (see e.g. Hurst and Vassilicos (2007)). Therefore, an investigation of this turbulence decay follows. In Neunaber *et al.* (2017), the decrease of the turbulence intensity has been fitted with good agreement to a power law. To further pursue this approach, the centerline evolution of the normalized turbulence intensity is

[ii] An investigation of the nacelle's influence on the data can be found in appendix C.

Table 4.3.: Downstream positions X/D and values of the local turbulence intensity extrema $TI/TI_{CLPeak,min}$ and $TI/TI_{CLPeak,max}$ for the disc and the turbine for the three inflow conditions in TWO.

	disc			**turbine**		
	laminar	reg. grid	act. grid	laminar	reg. grid	act. grid
$TI/TI_{CLPeak,min}$	0.19	0.19	0.19	0.16	0.08	0.13
X/D	0.90	0.90	0.90	1.07	1.07	0.90
$TI/TI_{CLPeak,max}$	1.00	1.00	1.00	1.00	1.00	1.00
X/D	1.76	1.59	1.59	2.10	2.28	2.10

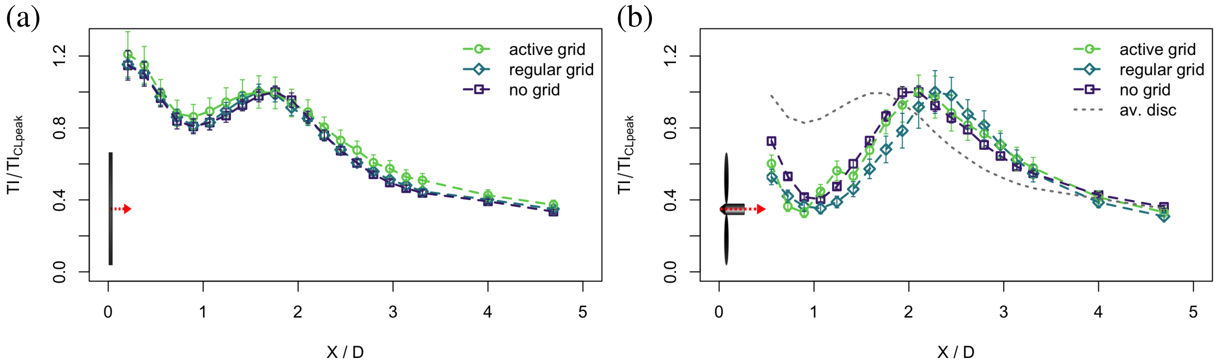

Figure 4.6.: Development of the normalized turbulence intensity TI/TI_{CLpeak} downstream the disc (a) and the turbine (b) on the centerline for different inflow conditions. Error bars are included but may be within the symbols.

plotted with logarithmic axes in figure 4.7 downstream the disc (a) and turbine (b). In addition, the turbulence decay region is fitted according to $TI/TI_{CLpeak} \propto \alpha \cdot (X/D)^{\beta}$. The slope appears to change around $X/D = 3$. Therefore, β_1 is fitted between $2 \lesssim X/D \lesssim 3$, and β_2 is fitted between $3 \lesssim X/D \lesssim 4.69$. Table 4.4 includes all values for β and their χ^2 errors. While β decreases downstream the disc, it increases downstream the turbine.

The decay exponent changes from one fit range to the other. This result is very interesting, as it takes up results obtained downstream regular grids where the decay process of turbulence also changes Hinze (1975).

To further investigate this change within the turbulence decay on the centerline, the variance σ^2 is plotted over X/D in figure 4.8 downstream the disc (a) and the turbine (b) for all inflow conditions.

Downstream the disc, the variance increases up to $X/D \approx 3$ and then starts to decrease. While the curves evolve similarly for laminar and regular grid inflow, higher values are reached in case of active grid inflow. Downstream the turbine, the variance first decreases close to the rotor and

Table 4.4.: Investigation of turbulence intensity decay: fit parameter β with fit error χ^2 for fit regions 1 and 2 downstream the disc and the turbine for all inflow conditions.

	β_1	$\chi^2(\beta_1)$	β_2	$\chi^2(\beta_2)$
disc, laminar	-1.53	0.03	-0.81	0.06
disc, reg. grid	-1.37	0.06	-0.80	0.07
disc, act. grid	-1.18	0.06	-0.93	0.05
turbine, laminar	-1.24	0.07	-1.28	0.05
turbine, reg. grid	-1.63	0.15	-1.88	0.10
turbine, act. grid	-1.17	0.04	-1.69	0.06

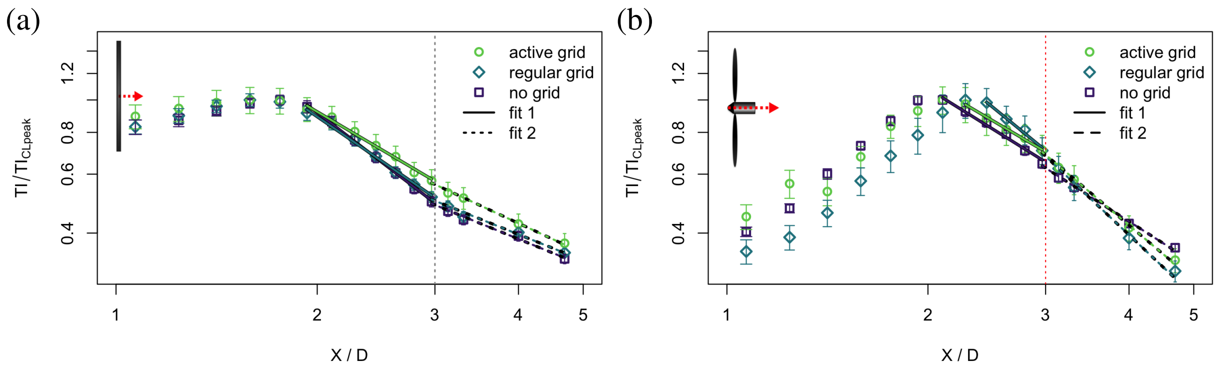

Figure 4.7.: Development of the normalized turbulence intensity TI/TI_{CLpeak} downstream the disc (a) and the turbine (b) on the centerline for different inflow conditions with logarithmic axes. The lines are fits that indicate a power law decay. Error bars are included but may be within the symbols.

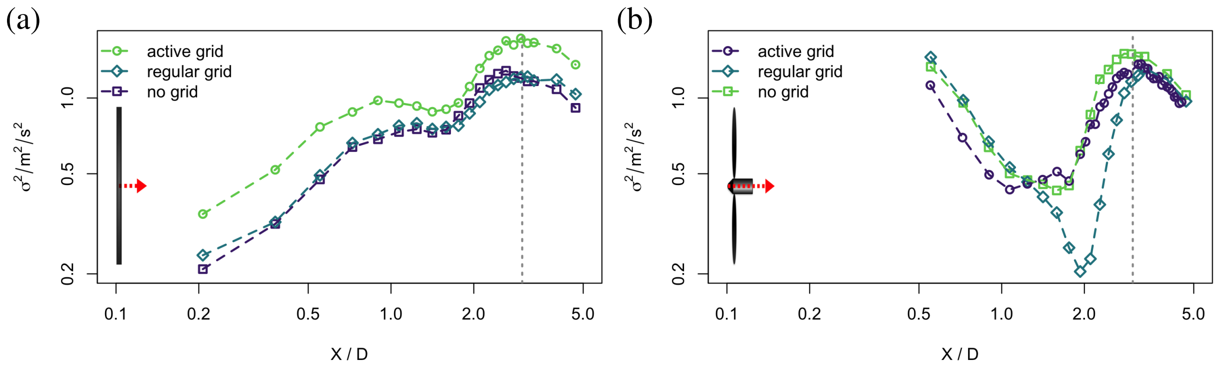

Figure 4.8.: Development of the variance σ^2 downstream the disc (a) and the turbine (b) on the centerline for different inflow conditions with logarithmic axes.

increases again between $X/D \approx 2$ and $X/D \approx 3$. Then, σ^2 starts to decrease.
This brief investigation shows that the change of the decay exponent around $X/D \approx 3$ is related to the decrease of the variance that starts after the decrease of the turbulence intensity.
Finally, comparing the evolution of the normalized turbulence intensity downstream the disc and the turbine reveals on the one side a different development close to either WGT. On the other side, beyond a local maximum that exists in both cases, the turbulence intensity decreases. Far downstream the WGTs, the normalized turbulence intensities are comparable. The influence of the inflow condition on the evolution of the normalized turbulence intensity is not perceptible in case of the disc, but visible in case of the turbine, especially in proximity of the rotor.

Overall, the normalized turbulence intensities downstream the disc and the turbine are comparable far downstream from $X/D \approx 4$. Upstream, the influence of the respective WGT is present due to fundamentally different turbulence production mechanisms (see Lignarolo *et al.* (2016)). Compared with results from the literature, e.g. Aubrun *et al.* (2013), where the turbulence intensity profiles collapse already at $X/D = 3$, the adaption of the wakes behind disc and turbine is shifted farther downstream. The development of the normalized centerline turbulence intensity appears to be qualitatively in accordance with Kermani *et al.* (2013)[iii]. In this study, though, the downstream position of TI_{CLpeak} cannot be related to the turbulence degree of the inflow condition. A higher turbulence intensity is captured downstream the tips of the rotor blades in the near wake of the turbine at $Y/D = -0.51$ and for active grid inflow also for $Y/D = 0.51$. This is in accordance with results from e.g. Chamorro and Porté-Agel (2010). Further downstream and in case of laminar and regular grid inflow at $Y/D = 0.51$, the effect is not captured anymore due to the wake expansion in combination with the coarse span-wise probe resolution. In summary, the results that are presented here are qualitatively in agreement with results from the literature. The main difference lays in the higher turbulence degrees found in this study, that appear to be specific for this setup (cf. appendix C). The compared to other studies significantly higher downstream resolution of measurement points additionally allows for a detailed view on the downstream evolution of the turbulence intensity. The decrease of the turbulence intensity is found to follow a power law, but depending on the downstream region, the exponent changes.

4.1.3. Downstream development of characteristic length scales

There are two characteristic length scales that indicate the range of correlated structures within turbulence, i.e. the integral length scale L and the Taylor length scale λ_T (cf. chapter 2). They are examined downstream the investigated objects for the different inflow conditions.

Integral length

The evolution of the integral length scale is shown in interpolated contour plots in figure 4.9 downstream the disc (a.i) and turbine (b.i) under laminar, regular grid and active grid inflow conditions. In direct vicinity to the disc, the integral length is for all inflow conditions $L \approx 0.02\,\mathrm{m}$. The integral length increases with increasing distance from the disc. In the center, L increases slower than in the flow outside the rotor plane. While the evolution appears to be similar for laminar and regular grid inflow, the active grid inflow causes a faster increase and overall larger values for L.

[iii] Note that they define the turbulence intensity as $TI^* := \sigma/u_0$, which is an according to the inflow velocity normalized standard deviation. A comparison of the evolution of the mean velocity deficit and TI^* in Kermani *et al.* (2013) with the evolution of the mean velocity (figure 4.3(b)) and the variance (figure 4.8) presented in this thesis leads to the conclusion that the results are similar.

Close to the turbine, the integral length has compared to the disc case similar values of $L \approx 0.02\,\mathrm{m}$, and L increases with increasing distance. Also, the integral length increases faster outside the rotor plane. While the evolution of L downstream the turbine is similar for laminar and regular grid inflow, L increases faster in case of active grid inflow.

In figure 4.10, profiles of the integral length downstream the disc (a) and turbine (b) are plotted for the three inflow conditions.

Downstream the disc, a profile with small integral length scales in the center and larger integral length scales at the sides evolves for all inflow conditions, as already indicated in the interpolated surface plots. Farther downstream, the profile begins to flatten, and an asymmetry can be seen. Whereas both laminar and regular grid inflow lead to a similar evolution of the integral length scale, the active grid inflow leads to a similar behavior close to the disc but generates higher integral length scales from $X/D \approx 3$ onwards.

Downstream the turbine, a clear profile does not evolve for any of the inflow conditions. An asymmetry is present for all inflow conditions. The integral length grows with increasing distance from the rotor. Again, in case of the active grid inflow, the integral length scales are largest and do strongly deviate from the integral length scales downstream the turbine in case of laminar and regular grid inflow from $X/D \approx 4$ onwards.

In figure 4.11, the centerline evolution of the integral length downstream the disc and the turbine is plotted both with absolute scales and normalized to the rotor diameter D.

Downstream the disc, the integral length increases for all inflow conditions similarly up to $X/D \approx 3$. Farther downstream, L increases similarly in case of laminar and regular grid inflow ($L(X/D = 4.69) \approx 0.10\,\mathrm{m}$), but stronger in case of active grid inflow ($L(X/D = 4.69) \approx 0.15\,\mathrm{m}$).

Downstream the turbine, the integral length also increases, but a higher sensitivity to the inflow is visible. At $X/D = 4.69$, the integral length has increased to $L \approx 0.10\,\mathrm{m}$ for laminar and regular grid inflow. In case of active grid inflow, it increases to $L \approx 0.20\,\mathrm{m}$.

Positions indicating changes in the development of L can be found in table E.1 in appendix E.

In comparison, the integral length evolves principally similarly downstream the disc and the turbine. However, a look at the evolution of the profiles shows differences downstream the disc and the turbine across the rotor plane. The values of L downstream the disc and the turbine are comparable. Close to the WGT, the size of the vortices is determined by the size of the bars in case of the disc ($\approx 2\,\mathrm{cm}$) and by the largest structures that could pass the gap between two rotor blades while the turbine is rotating ($\leq 5\,\mathrm{cm}$). In active grid inflow, the integral length far downstream is for both WGTs largest. The reason might be that due to stronger turbulent mixing larger structures created by either the active grid or the shear layer of the free stream are swept into the wake. Additionally, this might explain why in this scenario, the integral length is increasing, which would be unusual for decaying turbulence. The similarity of the results in

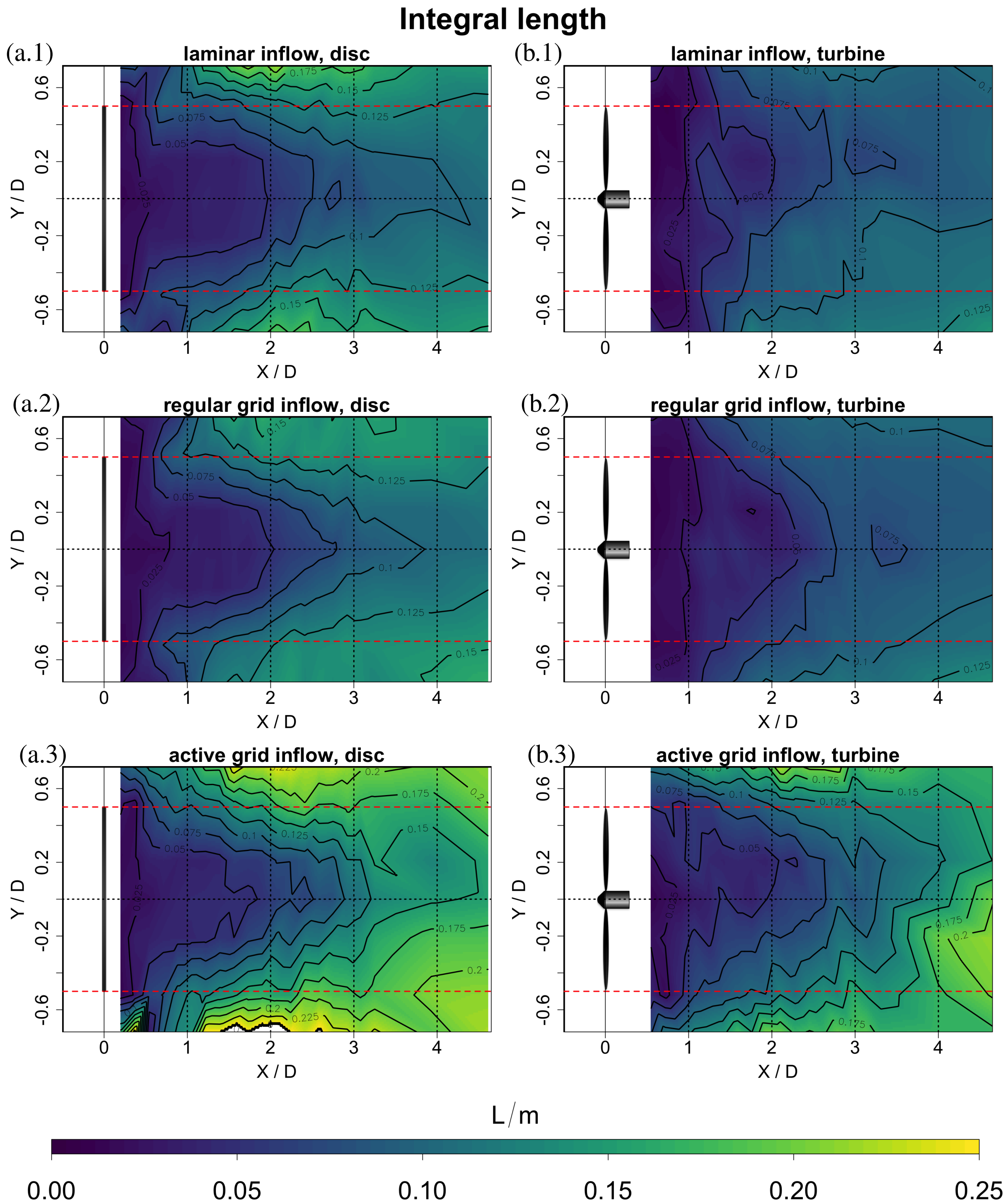

Figure 4.9.: Evolution of integral length: Surface plots downstream the disc (a.i) and the turbine (b.i) for laminar (x.1), regular grid (x.2) and active grid (x.3) inflow.

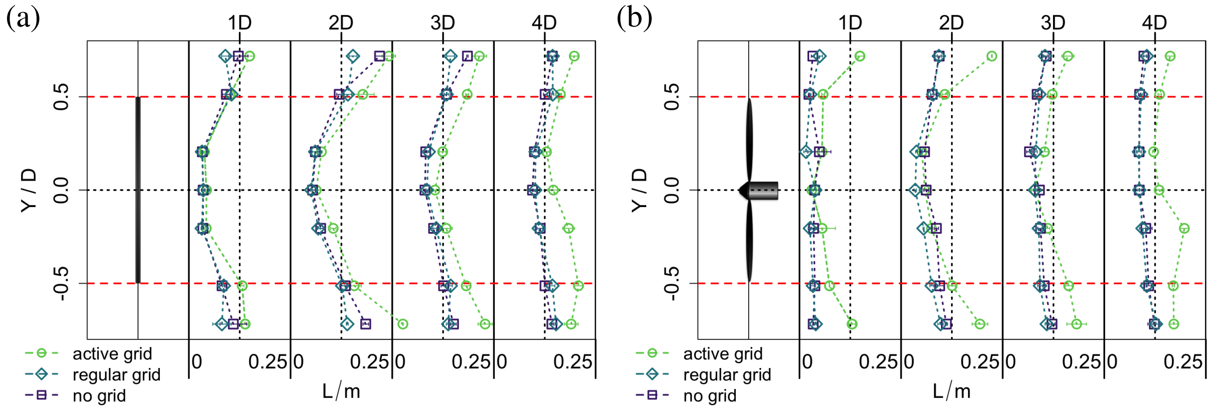

Figure 4.10.: Profiles of the integral length L downstream the disc (a) and the turbine (b) at $X/D = 1.07, 2.10, 2.97, 4.00$ for different inflow conditions. Error bars are included but may be within the symbols.

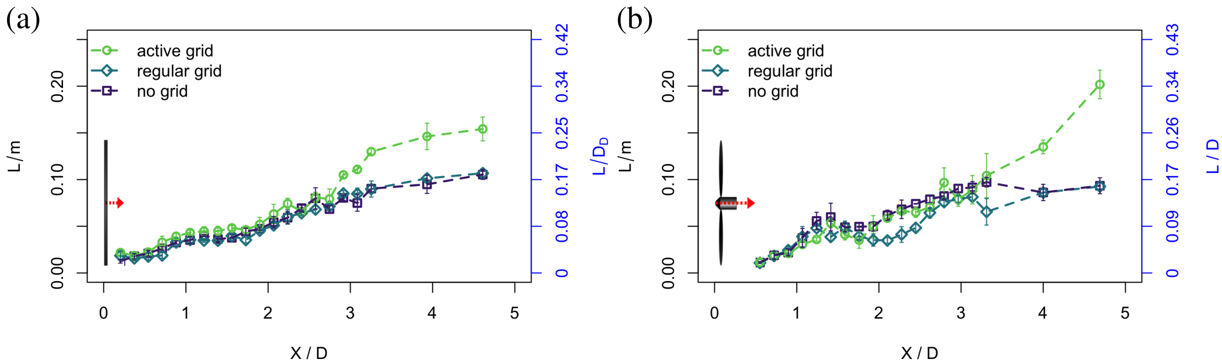

Figure 4.11.: Development of the integral length L downstream the disc (a) and the turbine (b) on the centerline for different inflow conditions. The blue ordinate on the right shows the value of L normalized to the rotor diameter D, L/D. Error bars are included but may be within the symbols.

laminar and regular grid inflow in contrast to the deviation of the results in active grid inflow indicates that the inflow turbulence plays a minor role in the creation of large flow structures compared to the intermittency.

Overall, the evolution of the integral length downstream the disc and the turbine is comparable far downstream. In Aubrun *et al.* (2013), similar measurements have been carried out at two downstream positions. In accordance with the results presented above, it was found that the complex inflow leads to higher integral length scales, that the integral length has similar magnitudes downstream the disc and the turbine, and that the integral length scale is small in close vicinity to the WGT. However, while in the near wake in Aubrun *et al.* (2013) the magnitude of the integral length scale is also determined by the inflow, this result could not be reproduced here. Also, the finding of Chamorro *et al.* (2013) that small vortices pass the rotor, which leads to differences in the evolution of the integral length depending on the structures present in the inflow, could not be verified.

Taylor length

Similarly, the evolution of the Taylor length scale downstream the disc and turbine is presented by means of interpolated contour plots (cf. figure 4.12) for the different inflow conditions. As the calculation of the Taylor length is sensitive, values that exceed the average Taylor length in the wake significantly are masked from the plot.

Downstream the disc, the Taylor length increases from $\lambda_T \approx 2\,\mathrm{mm}$ in close proximity to the disc. The highest values are found outside the rotor plane far downstream, similarly to the evolution of the integral length. An influence of the inflow is not apparent from these plots.

Downstream the turbine, the Taylor length first increases but then drops again around $X/D \approx 2$. Beyond $X/D \approx 2$, it increases. The highest values are as well found far downstream outside the rotor plane. While the Taylor length evolves comparably in laminar and regular grid inflow, higher values are reached in case of active grid inflow, especially far downstream.

Figure 4.13 shows profiles of the Taylor length downstream the disc (a) and turbine (b) that include error bars.

Downstream the disc, profiles evolve that flatten farther downstream. As for the integral length scale, the influence of the inflow is mainly present in case of the active grid inflow. Here, downstream from $X/D \approx 3D$ onwards, the Taylor length is significantly higher than for the other inflow conditions.

A profile only develops for laminar and regular grid inflow downstream the turbine. In case of active grid inflow, the span-wise profiles develop an asymmetry.

In figure 4.14, the evolution of the Taylor length at centerline is presented. As already indicated, the Taylor length increases downstream the disc for all inflow conditions similarly to the evolution of the integral length. Up to $X/D \approx 2.5$, the evolution is independent on the inflow. Beyond, the Taylor length increases almost identically for laminar and regular grid inflow to $\lambda_T \approx 7.5\,\mathrm{mm}$. In case of active grid inflow, the Taylor length increases stronger to $\lambda_T \approx 9.0\,\mathrm{mm}$.

Interestingly, the Taylor length evolves quite differently downstream the turbine. The Taylor length increases at first, drops after $X/D \approx 1.41$ and increases again starting from $X/D \approx 2.28$, where the turbulence intensity also starts to decrease. In contrast to the evolution of the integral length, a dependence on the inflow conditions is clearly visible. At $X/D = 4.69$, the Taylor length has increased to $\lambda_T \approx 7.0\,\mathrm{mm}$ for laminar inflow, $\lambda_T \approx 6.5\,\mathrm{mm}$ for regular grid inflow and $\lambda_T \approx 9.0\,\mathrm{mm}$ for active grid inflow.

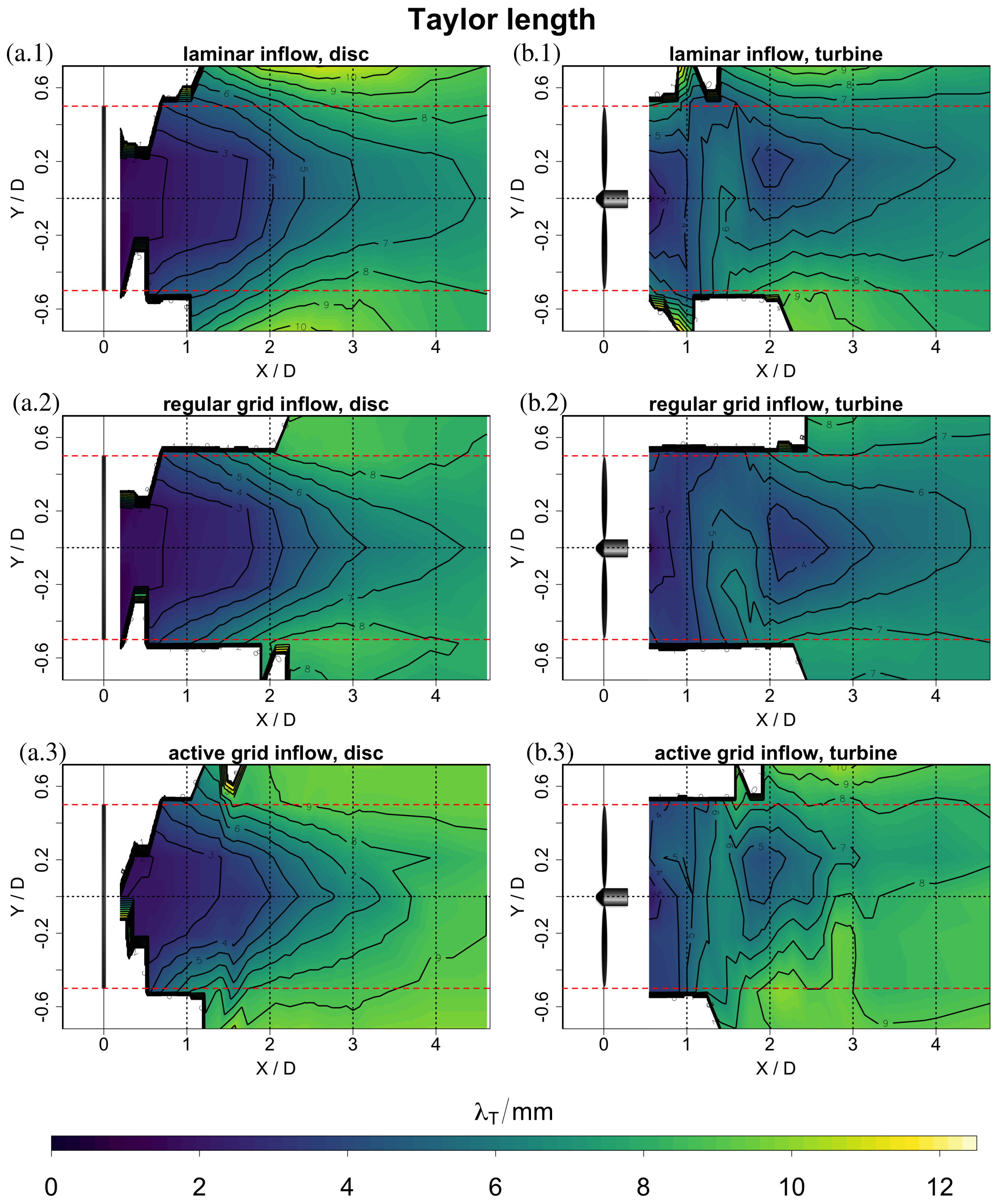

Figure 4.12.: Evolution of Taylor length: Surface plots downstream the disc (a.i) and the turbine (b.i) for laminar (x.1), regular grid (x.2) and active grid (x.3) inflow. As the calculation of the Taylor length is sensitive, values that exceed the average Taylor length in the wake significantly are masked from the plot.

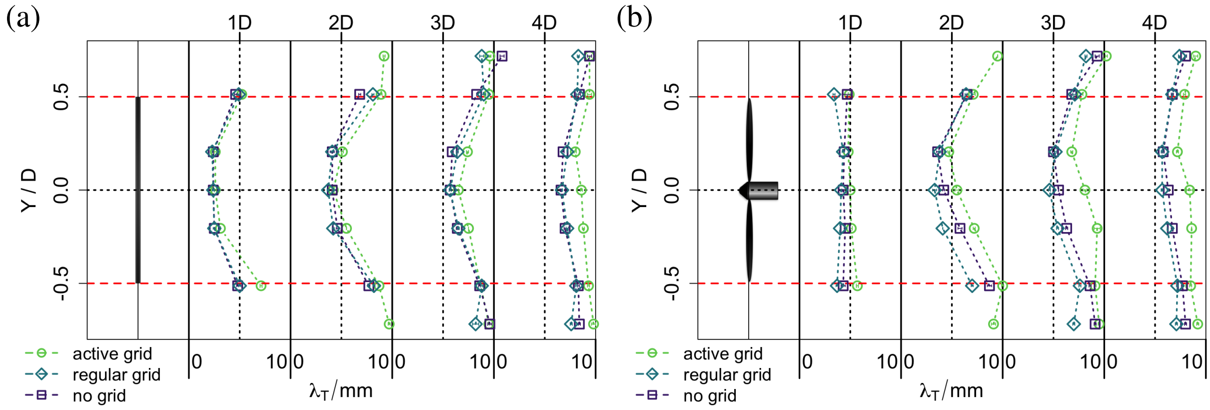

Figure 4.13.: Profiles of the Taylor length scale λ_T downstream the disc (a) and the turbine (b) at $X/D = 1.07, 2.10, 2.97, 4.00$ for different inflow conditions. Error bars are included but may be within the symbols.

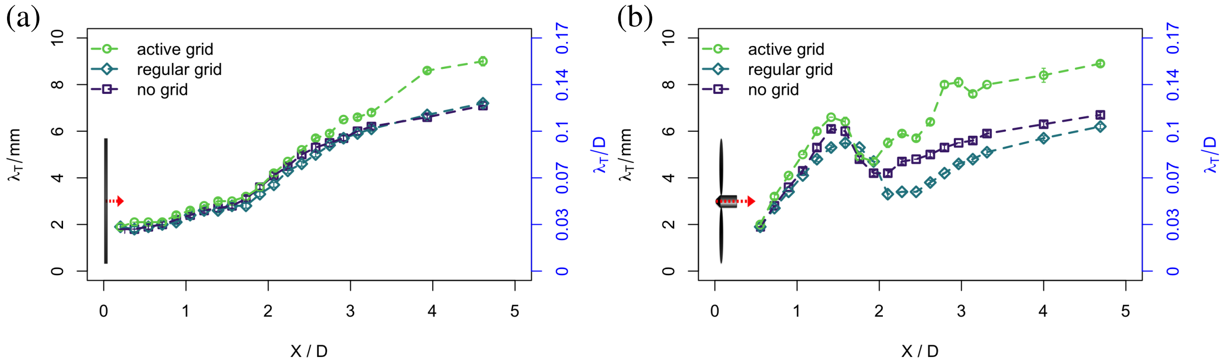

Figure 4.14.: Development of the Taylor length scale λ_T downstream the disc (a) and the turbine (b) on the centerline for different inflows. The blue ordinate on the right shows the value of λ_T normalized to the rotor diameter D, λ_T/D. Error bars are included but may be within the symbols.

Positions indicating changes in the development of λ_T can be found in table E.1 in appendix E.

In comparison, the evolution of the Taylor length downstream both WGTs is different close to the rotor but similar far downstream. While inflow generated by the active grid does have an influence on the evolution especially far downstream, the influence of laminar and regular grid generated inflow is not present downstream the disc and only small downstream the turbine. Thus, one may conclude that the turbulence degree of the inflow has a small impact on the evolution of the Taylor length in the wake while the presence of intermittency does alter the evolution.

Integral length over Taylor length and Taylor Reynolds number

Figure 4.15 shows the evolution of L/λ_T over X/D for the centerline of the wake downstream the disc (a) and turbine (b) for all inflow conditions. In the inertial sub-range where turbulence decays, the integral length and the Taylor length describe its beginning and the area where dissipation becomes relevant, respectively. Thus, the ratio is a measure of the extension of the inertial sub-range, or the range with turbulence dynamics.
As can be seen, in case of laminar and regular grid inflow, L/λ_T increases and saturates to the same constant value of $L/\lambda_T \approx 15$ both downstream the disc and the turbine. In case of the active grid inflow, downstream the disc, the saturation level is $L/\lambda_T \approx 20$. Therefore, the inertial subrange is larger compared to laminar and regular grid generated inflow. In case of active grid inflow downstream the turbine, L/λ_T and consequently the inertial sub-range increase.
To further quantify the degree of turbulence in the wake, the Taylor Reynolds number is calculated and presented in figure 4.16 for the three inflow conditions downstream the disc (a) and the turbine (b).
Downstream the disc, Re_λ increases for laminar and regular grid inflow up to $X/D \approx 3.3$ and saturates to $Re_\lambda \approx 450$. For active grid inflow, Re_λ saturates to $Re_\lambda \approx 690$ downstream the disc. Downstream the turbine, Re_λ increases from $X/D \approx 2$ and saturates from $X/D \approx 3.3$ to $Re_\lambda \approx 445$ (laminar inflow), $Re_\lambda \approx 400$ (regular grid inflow) and $Re_\lambda \approx 730$ (active grid inflow). Therefore, compared to the inflow, a significant increase in the Taylor Reynolds number is found. The downstream position from where Re_λ increases collapses with the position from where the turbulence intensity decreases.
In combination with the evolution of L/λ_T, one can conclude for laminar and regular grid generated inflow that far downstream, $L/\lambda_T \propto Re_\lambda$, which is expected within the Richardson-Kolmogorov phenomenology of turbulence (Vassilicos (2015)). The increase of L/λ_T and Re_λ indicates that turbulence evolves in a broader production region, similarly to the situation downstream a fractal grid (see e.g. Mazellier and Vassilicos (2010), Vassilicos (2015)): Here, the broad production region is caused by wakes of bars with different sizes that will interact at different distances downstream the grid. Therefore, it is concluded, that a comparable process could lead to a similar behavior in the wake of a turbine and a disc when different structures from the WGTs and the surrounding flow mix and reach the centerline. The saturation indicates that the range of the inertial subrange stays constant contrary to the decaying turbulence. Considering the evolution of the integral length and the Taylor length (cf. figure 4.11 and 4.14), this shows that both quantities increase similarly. In decaying turbulence, a decrease would be expected; however, the independence of L/λ_T on X/D can also be found downstream plane wakes.
However, in case of active grid inflow downstream the turbine, L, L/λ_T and consequently the inertial sub-range increases. As the integral length increases, the turbulence expands. This might as above-mentioned be caused by larger flow structures brought into the flow from the

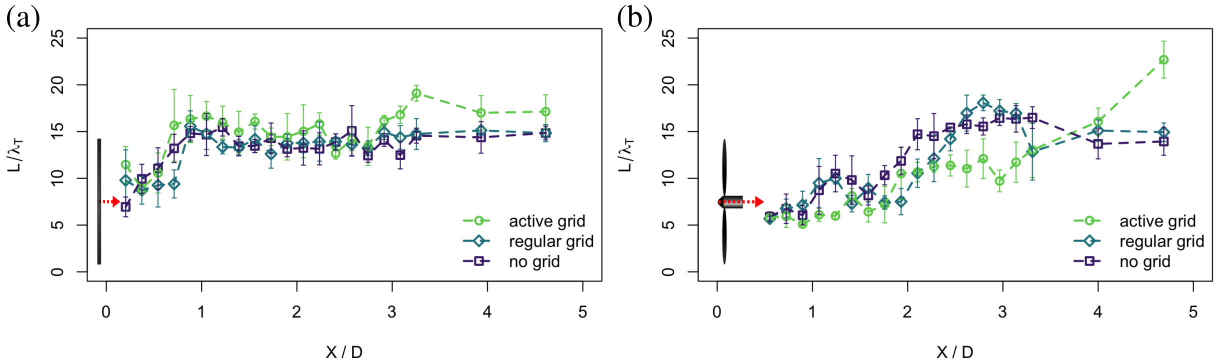

Figure 4.15.: Development of L/λ_T downstream the disc (a) and the turbine (b) on the centerline for different inflows. Error bars are included but may be within the symbols.

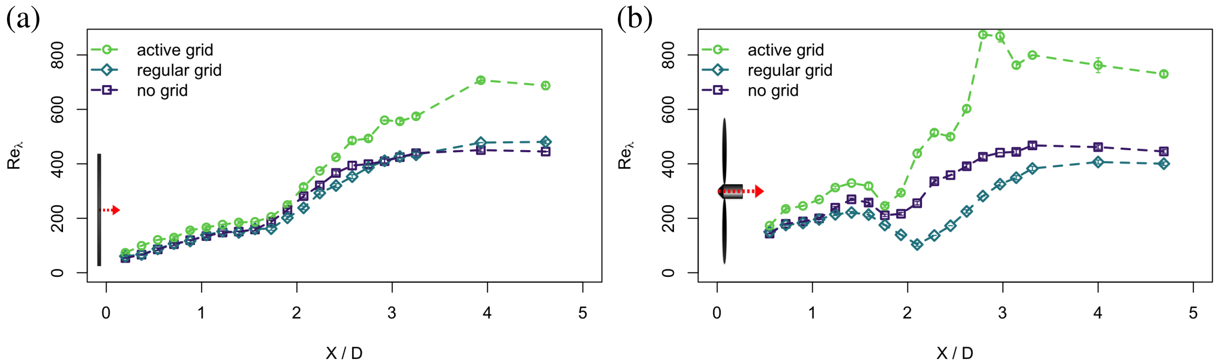

Figure 4.16.: Development of the Taylor-Reynolds number Re_λ downstream the disc (a) and the turbine (b) on the centerline for different inflow conditions. Error bars are included but may be within the symbols.

surrounding flow far downstream by turbulent mixing.Additionally, there appears to be the tendency that Re_λ is constant while L/λ_T increases. This indicates an abnormal behavior of the turbulence evolution. Overall, the magnitude of Re_λ found far downstream of the disc and the turbine are an indication of highly turbulent flow.

4.1.4. Summary

In conclusion, a comparison between the wakes downstream the disc and the turbine reveals that the wakes are for the investigated quantities similar far downstream, i.e. at $X/D \approx 4$. The evolution of the turbulence intensity allows to identify *four* instead of the usually identified three regions in the wake. They will be called the *near wake* up to the minimum of the mean velocity at $X/D \approx 1$, where strong influences of the rotor are still present, the *transition region* up to the peak of the turbulence intensity around $X/D \approx 2$, where the turbulence develops, the *turbulence decay region* where the turbulence decay starts, and finally, from $X/D = 3$ the *far wake*, where the slope of the decay changes. The positions of these regions are approximately given to provide a simplified wake description in terms of turbulence. In table E.1, the exact downstream positions of local minima and maxima and changes of the slope of different quantities are shown. The regions can also partially be identified within the evolution of λ_T, L and Re_λ. While these quantities change within the first three regions, they are (more or less) constant in the far wake. The results show that the use of the disc as a realistic WGT is limited to the decay and far wake region where the influence of fundamentally different turbulence mixing mechanisms vanishes. Within the transition region, the wake of the turbine is more sensitive to different inflow conditions than the wake of the disc, but in the far wake, the results are in good agreement with the results downstream the disc. Thus, a disc can be seen as a good substitution for wake examination in the far wake region.

The analysis of L/λ_T and Re_λ indicates that turbulence develops differently downstream the WGTs in the near wake. Nevertheless, in the far wake, the evolution of L/λ_T and Re_λ is similar for both WGTs and appears to be in agreement with the Richardson-Kolmogorov phenomenology. Additionally, L/λ_T and Re_λ are independent of X/D for laminar and regular grid inflow.

The results were compared to results from the literature where possible. They are in good agreement with the studies of Sandrine Aubrun (e.g. Aubrun *et al.* (2013)) who has as well validated the actuator disc principle at two downstream positions. Additionally, the centerline evolution of the normalized mean velocity downstream the turbine is comparable to results found in Keane *et al.* (2016) although the wake recovery is slower in this experiment due to the different setup. The evolution of the normalized turbulence intensity downstream the turbine appears to be qualitatively similar to the evolution presented in Kermani *et al.* (2013).

4.2. Investigation of the wake with extended stochastic methods

In section 4.1, the evolution of the wake downstream a disc and a turbine under different inflow conditions was scrutinized with standard methods characterizing the mean quantities of turbulence without a detailed investigation. This section aims to deepen the knowledge on the turbulent structures that evolve downstream the two investigated WGTs. First, to investigate the cascade-like structure of developed turbulence, the development of energy spectra is considered by discussing their evolution and the decay exponent in the inertial sub-range. Then, the turbulence dissipation is briefly discussed. Afterwards, the probability density functions

(PDFs) of velocity increments are examined, and the temporal and spacial shape parameter is analyzed. This will reveal the evolution of intermittency in the wakes in dependence of the inflow conditions.

4.2.1. Energy spectra

In the following, the evolution of energy spectra downstream the disc and the turbine is investigated. Energy spectra show the distribution of turbulent energy E over frequency f. Because the frequency can be related to a flow structure of size d by means of Taylor's hypothesis, $d = \langle u \rangle / f$, the energy spectrum gives information on the energy distribution over flow structures, i.e. vortices. In turbulence, these vortices are expected to decay in a vortex cascade in a certain range of frequencies called the inertial sub-range. The inertial sub-range is limited by the integral length, that indicates the largest structures where energy is brought into the system, and by the Taylor length that indicates when energy dissipation starts to play a significant role in the energy transfer process of the cascade. In the inertial sub-range, the energy spectrum is expected to decrease with $E(f) \propto f^{-5/3}$. To emphasize the starting point of this decay region, the energy spectra will be presented in pre-multiplied form, $f \cdot E(f)$. To directly relate frequencies to the size of the turbine, the frequency axis is scaled by $D/\langle u \rangle$.

Downstream evolution of energy spectra

In figure 4.17, the evolution of the pre-multiplied energy spectra $f \cdot E(f)$ downstream the disc (a.i) and turbine (b.i) in laminar inflow is presented for the span-wise positions $Y/D = 0, -0.21, -0.51$. A lighter color indicates a position further downstream. In dark red (dashed line), the reference spectrum of the respective inflow at central rotor plane position is plotted (i.e., $X/D = 0$, $Y/D = 0$). In red (small dashes), the reference spectrum of the respective inflow at the last downstream position is plotted (i.e., $X/D = 4.69$, $Y/D = 0$). The blue straight line indicates the $-5/3$-decay. The two dashed curves that indicate the inflow without any WGT show how the free-stream evolves downstream. Whereas the energy content at rotor plane is rather low, a significant increase is seen at $X/D = 4.69$, or 3.4 m downstream the outlet. Additionally, a peak appears at $f \cdot D/u_0 \approx 0.25$. The reason for the rise of energy is considered to be the following: The experiment was carried out in an open jet wind tunnel. Between the standing air in the lab and the flow, a shear layer develops, as known from jet experiments. When assuming an opening angle of 9° for the expansion of this shear layer, the shear layers of the bottom and top would reach the center of the flow around 2.5 m downstream the outlet[iv]. The peak is assumed to be caused by the vortex shedding at the wind tunnel outlet.

By looking at the evolution of the energy spectra downstream the disc and the turbine, it becomes clear that both WGTs induce turbulent energy to the flow on all scales as all spectra show a significant offset to the reference spectrum. Even in comparison to the downstream reference spectrum, the energy is significantly enhanced for all downstream positions. Additionally, the energy increases with increasing downstream position for frequencies up to $f \cdot D/u_0 \approx 0.3$.

The impact of vortex shedding at the wind tunnel outlet can also be observed for both WGTs at the outer positions $Y/D = -0.21$ and $Y/D = -0.51$ where a peak around $f \cdot D/u_0 \approx 0.2$ is visible. From $f \cdot D/u_0 \gtrsim 0.3$, the pre-multiplied energy spectra decrease with increasing frequency. Here, the turbulence decay in the inertial sub-range begins. Qualitatively, the downstream evolution of the energy spectra of all span-wise positions for both disc and turbine shows a comparable behavior: The energy distribution over frequency first decreases in the near wake, increases thereafter in the transition region and finally collapses in the far wake beyond $X/D = 2.58$. All collapsed spectra follow a $-5/3$-decay over several orders of magnitude in the frequency range $0.3 \lesssim f \cdot D/u_0 \lesssim 30$. Furthermore, downstream the turbine, the tip and root vortex structures were captured: At $Y/D = 0$ in 4.17(b.1), a peak at $X/D = 0.88$ at $f \approx 26\,\text{Hz}$ indicates the root vortex that rotates with the rotational frequency of the turbine and decays fast. In 4.17(b.3), at $Y/D = -0.51$, the tip vortex structure is captured up to $X/D = 0.88$ with the same frequency as the root vortex and its first harmonic. In the far wake, the spectra in the wake downstream disc and turbine are alike independently of the span-wise position.

Figure 4.18 represents the spectra for regular grid inflow in a similar manner. In contrast to the laminar inflow at rotor position and downstream, the inflow created by the regular grid is characterized by the introduction of vortices of a certain size to the flow. For high frequencies $f \cdot D/u_0 \gtrsim 0.8$, the energy content is higher in proximity to the outlet, but as the turbulence decays downstream, the energy content in this frequency range decreases. For frequencies $f \cdot D/u_0 \lesssim 0.8$, the two reference spectra show a similar behavior with exception of the peak around $f \cdot D/u_0 \approx 0.3$ that again corresponds to vortex shedding from the wind tunnel outlet. A $E(f) \propto f^{-5/3}$-decay is not present in the inflow.

The energy spectra downstream the disc and the turbine evolve similarly in this inflow condition with increasing distance despite the different, compared to the laminar flow more turbulent inflow created by the regular grid. The tip and root vortex structures can again be identified in the near wake downstream the turbine for a rotational frequency of $f \approx 26\,\text{Hz}$. In the far wake, the spectra for the disc and the turbine show only minor differences at low frequencies and collapse in the inertial sub-range while decaying with $E(f) \propto f^{-5/3}$. Overall, the additional turbulence does not seem to affect the evolution of the energy spectra with increasing distance.

[iv] From details given in Nieuwstadt *et al.* (2017), an opening angle of 12° was estimated for a turbulent jet under the assumption of a Gaussian self-similar profile.

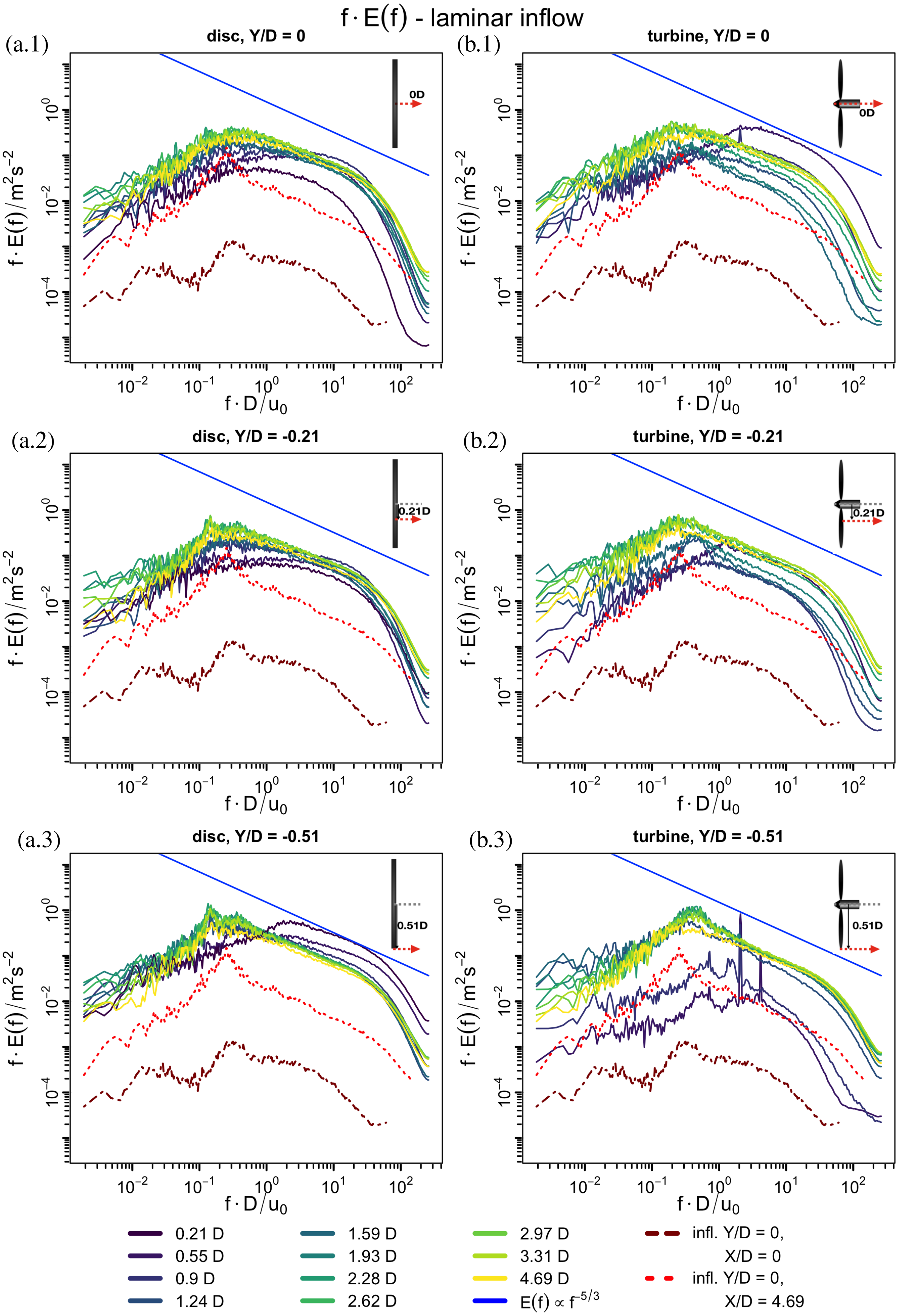

Figure 4.17.: Downstream evolution of energy spectra in the wake of disc (a.i) and turbine (b.i) in laminar inflow for span-wise positions $Y/D = 0$ (x.1), $Y/D = -0.21$ (x.2) and $Y/D = -0.51$ (x.3).

In figure 4.19, the evolution of energy spectra is shown for the active grid inflow in the same manner as the results presented for laminar and regular grid inflow. The inflow created by the active grid contains significantly higher turbulent energy than both laminar and regular grid inflow, especially in the low frequencies $f \cdot D/u_0 \lesssim 0.8$. Similarly to the regular grid inflow, the energy content is higher in proximity to the outlet for high frequencies $f \cdot D/u_0 \gtrsim 0.8$. As turbulence decays downstream, the energy content in this frequency range decreases. A frequency range where the spectra follow $E(f) \propto f^{-5/3}$ is not present in the inflow. Downstream, this inflow shows a higher energy content for frequencies $f \cdot D/u_0 \lesssim 0.3$. It is associated as before with vortex shedding from the wind tunnel outlet, here in combination with flow modulation and interaction due to the active grid.
Overall, the wake downstream the disc and the turbine evolves similarly compared to laminar and regular grid inflow. Nevertheless, the higher ambient turbulence level causes the tip vortices to decay earlier so that they are not captured. Compared to the reference spectrum, the WGTs lead to an increase of the energy at low frequencies $f \cdot D/u_0 \lesssim 0.3$, because the high energy in the inflow is transferred to the wake when the turbine reacts to the slow flow modulations by the active grid. Within the high-frequent structures $f \cdot D/u_0 \gtrsim 0.3$, the energy in the spectra downstream the disc and the turbine is reduced compared to the reference spectrum at $X/D = 0$, and a $E(f) \propto f^{-5/3}$ decay of the turbulence is present far downstream where the spectra collapse.

In summary, an increase of energy in the wake of the disc and the turbine in low frequencies up to $f \cdot D/u_0 \lesssim 0.3$ as compared to the laminar and regular grid inflow was seen. This indicates, that the respective WGT imprints structures to the flow that are larger than D. In addition, at far downstream positions, the interaction between the wake and large flow structures of the shear layer might add to this effect. Additionally, large-scale flow structures are transferred to the wake, as indicated by the higher energy in low frequencies up to $f \cdot D/u_0 \lesssim 0.3$ in active grid generated inflow. The energy spectra in the wake of the disc and the turbine become alike in the high frequency range far downstream beyond a region where the spectra vary. The result is both independent of the inflow and also to a great extent independent of the span-wise position. Thus, the turbulence generation process is solely determined by the WGT. The before identified wake regions seem to be identifiable, too. The transition region appears to be in agreement with the turbulence generation zone seen from the turbulence intensity. In the far wake, the spectra collapse and the turbulence appears to follow a $E(f) \propto f^{-5/3}$ decay although the inflow conditions do not show this behavior. This result is also consistent with the indication of Richardson-Kolmogorov turbulence drawn from L/λ_T and Re_λ.
This analysis of the energy spectra also enables to separate periodic shares from the turbulence spectrum. As the variance that represents the turbulence degree is directly related to the energy

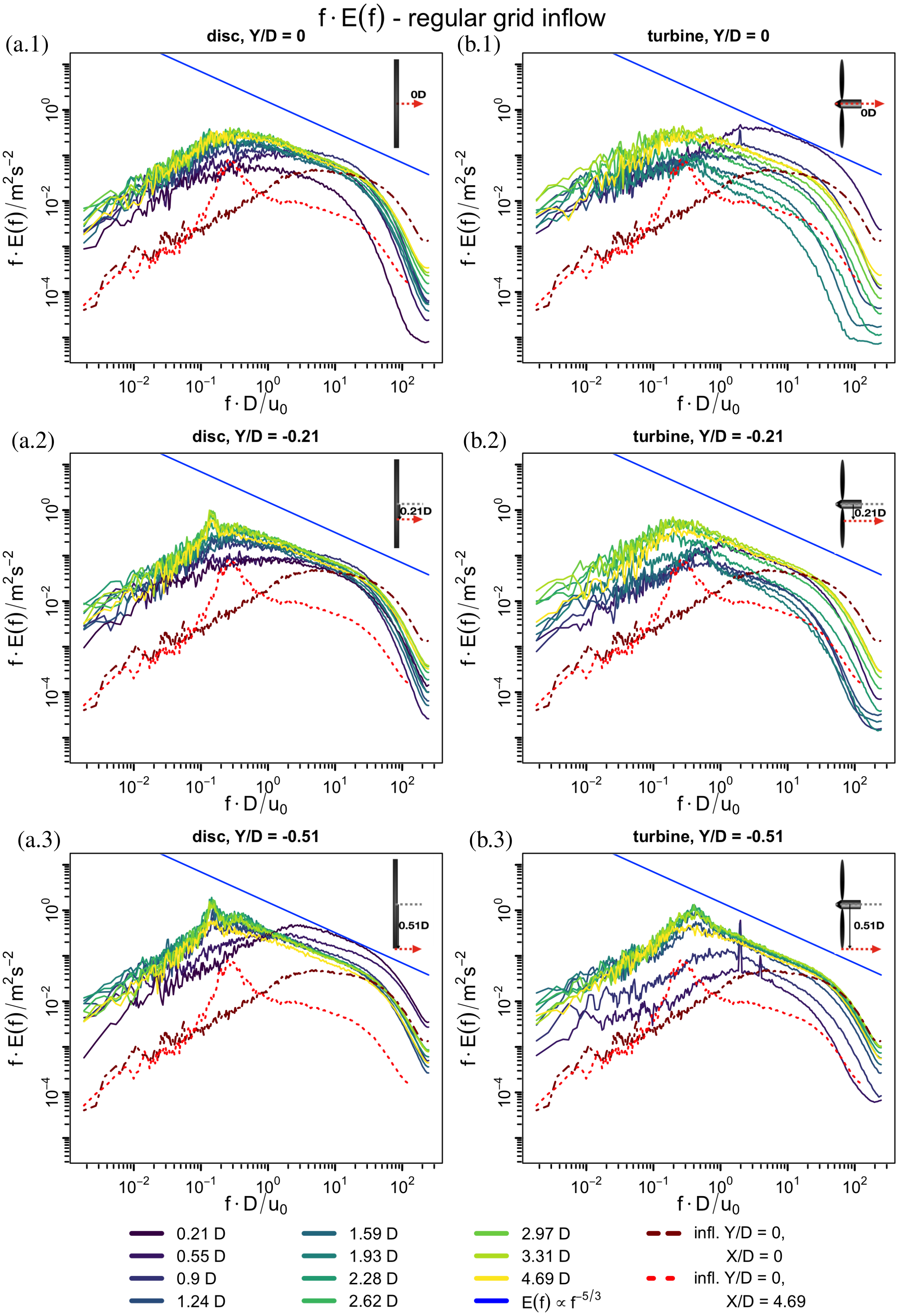

Figure 4.18.: Downstream evolution of energy spectra in the wake of disc (a.i) and turbine (b.i) in regular grid inflow for span-wise positions $Y/D = 0$ (x.1), $Y/D = -0.21$ (x.2) and $Y/D = -0.51$ (x.3).

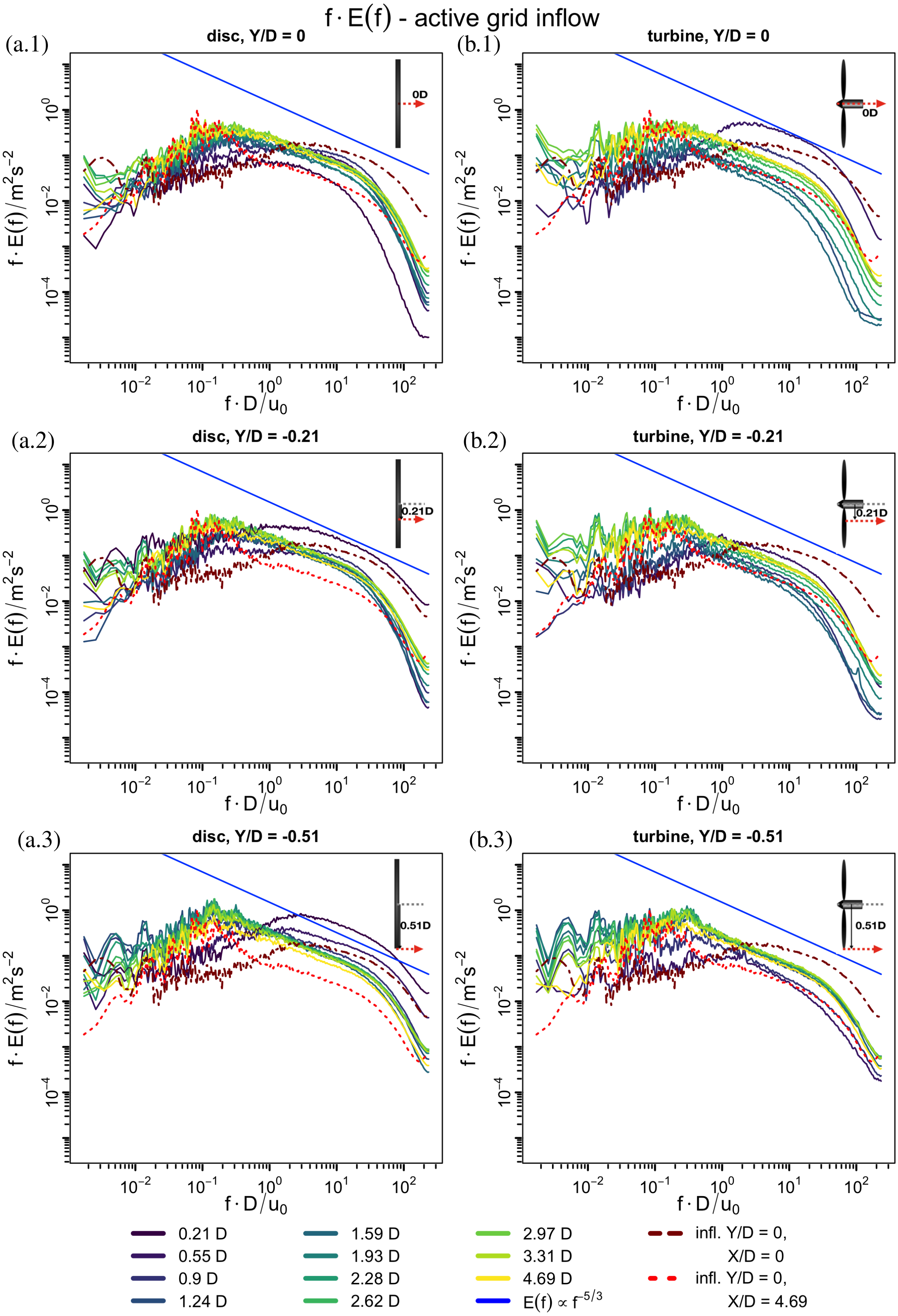

Figure 4.19.: Downstream evolution of energy spectra in the wake of disc (a.i) and turbine (b.i) in active grid inflow for span-wise positions $Y/D = 0$ (x.1), $Y/D = -0.21$ (x.2) and $Y/D = -0.51$ (x.3).

spectrum by Parseval's theorem, $\sigma^2 = \int_0^\infty E(f)\mathrm{d}f$ (see e.g. Pope (2000)), the spectrum analysis gives additionally an overview of the shares of the turbulence degree with periodic and turbulent origin. Overall, the evolution of energy spectra is consistent with the evolution of L/λ_T and Re_λ which becomes also clear looking at the downstream evolution of the variance in figure 4.8.

Compared to other studies that investigate the behavior of energy spectra downstream a disc and a turbine at single positions, similar results were found. Aubrun *et al.* (2013) showed that the spectra downstream the two different WGTs collapse in the far wake at $X/D = 3$. Additionally, one could interpret from their results that large-scale structures in the inflow conditions are also transferred to the wake. Jin *et al.* (2016) investigated the behavior of the energy spectra downstream a turbine with a similar setup using uniform inflows with different turbulence degrees. The findings of the here presented work are in accordance with their results that the turbine imprints large and small scale motions to the flow, but due to the high resolution of measurement points, the evolution of energy spectra reveals in which region the statement is valid. Additionally, they, too, found that in case of high inflow turbulence, the energy is enhanced at large scales. This is interpreted as a strong interaction between the inflow and the wake. Also, in case of high inflow turbulence, the turbine filters small scales similarly to the results presented in this work. A similar modulation of turbulent structures is found by Bastine *et al.* (2015) where a $E(f) \propto f^{-5/3}$ decay is reported in the wake at $X/D \approx 5$ but not in the inflow, and it is related to the occurring homogeneous isotropic turbulence in the wake of a turbine. Thus, to further pursue this idea, the decay exponent will be determined in the following.

Downstream evolution of the decay exponent

In the following, the decrease of the energy within the inertial sub-range will be quantified by fitting $E(f) \propto a \cdot f^{exp}$ to this region. If $exp = -5/3$, the turbulence decays in an equilibrium cascade while deviations indicate that additional mechanisms within the energy production or dissipation are present. The evolution of the decay exponent exp with increasing downstream position is presented for both WGTs, all inflow conditions and the three span-wise positions discussed above. In (a) the respective development downstream the disc is plotted and in (b), the development downstream the turbine is shown.
Figures 4.20 and 4.21 show the downstream evolution for the central positions $Y/D = 0$ and $Y/D = -0.21$, respectively. Downstream the disc in (a), the above-discussed wake regions can be identified: The decay exponent first increases as far as $X/D \approx 0.9$ in the near wake, decreases beyond in the transition region and remains constantly at $exp \approx -5/3$ from $X/D \approx 1.8$ in the turbulence decay region. The precise positions can be found in table E.1 in appendix E. The

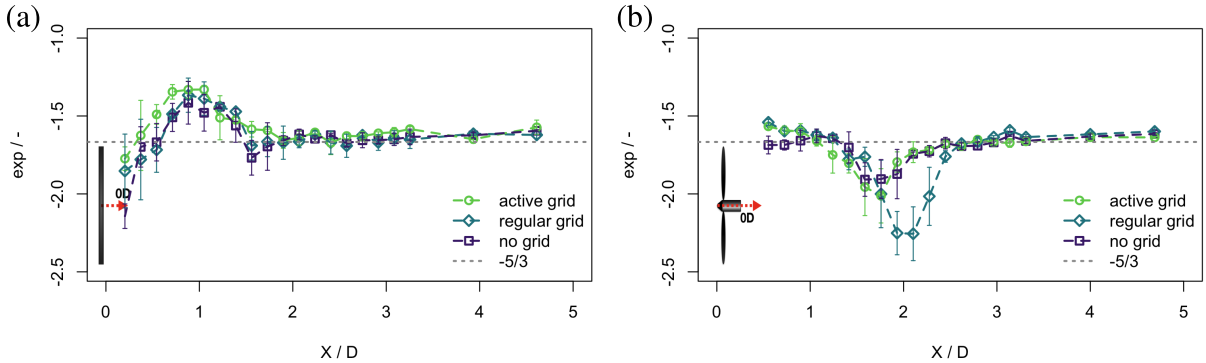

Figure 4.20.: Development of decay exponent downstream the disc (a) and the turbine (b) on the centerline for different inflows. Error bars are included but may be within the symbols.

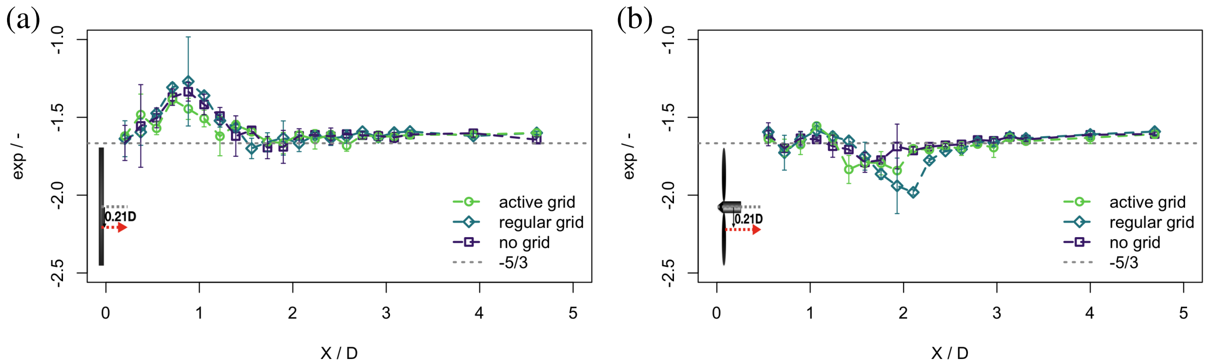

Figure 4.21.: Development of decay exponent downstream the disc (a) and the turbine (b) at $Y/D = -0.21$ for different inflows. Error bars are included but may be within the symbols.

turbulence decay region and the far wake are not distinguishable. An influence of the inflow condition is to a small extend visible in case of the active grid inflow.
Downstream the turbine in (b), the decay exponent is constant in the near wake. Then, it first decreases as far as $X/D \approx 2$ in the transition region and increases beyond in the turbulence decay region. The decay exponent saturates to $exp \approx -5/3$ from $X/D \approx 2.5$ in the far wake. Here, the inflow influences the magnitude of the decay exponent's variation up to $X/D \approx 2.5$, but beyond $X/D \approx 2.5$, the curves collapse. The precise positions can be found in table E.1 in appendix E. Thus, the before qualitatively described change of the spectra from near wake to far wake is now quantified by a changing slope of the spectra that saturates to $exp \approx -5/3$ (indicated by the gray dashed line). In the outer region $Y/D = -0.51$ in figure 4.22, changes of the decay exponent are present up to $X/D \approx 1.5$ for both WGTs, and further downstream, the inertial sub-range follows a $-5/3$-law for all inflow conditions.

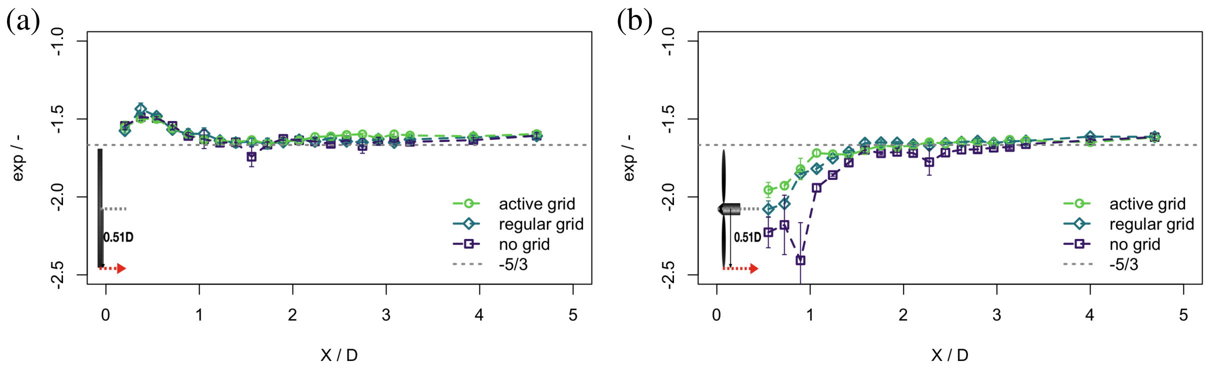

Figure 4.22.: Development of decay exponent downstream the disc (a) and the turbine (b) at $Y/D = -0.51$ for different inflows. Error bars are included but may be within the symbols.

Overall, it is shown that the decay region in the wake downstream the disc and the turbine show a similar behavior in the inner far wake region independently of the inflow condition. Additionally, the before introduced wake regions could be identified in the central wake. It appears as if three regions can be distinguished downstream the disc but four regions are identifiable downstream the turbine. The analysis of the decay exponent proves an inertial sub-range that decays with almost $-5/3$ independently of the inflow, the span-wise position and the WGT for the analyzed region in the far wake. Thus, a region exists in the wake where both the disc and the turbine imprint a new turbulence that first develops in the transition region and then remains stable within an inertial sub-range in the far wake. This is supported also by the downstream evolution of L/λ_T in figure 4.15 that is in case of laminar and regular grid inflow constant and roughly constant to slightly increasing for active grid inflow.
These results can further be interpreted as indication of homogeneous isotropic turbulence in the far wake.

Brief comment on the turbulent kinetic energy dissipation

As the investigation of the energy spectra and the decay exponent indicate that the turbulence in the wake downstream the disc and the turbine evolves towards homogeneous isotropic turbulence and follows the Kolmogorov phenomenology of an equilibrium cascade, the turbulent kinetic energy dissipation will be briefly discussed. For this, the dimensionless coefficient

$$C_\varepsilon = \frac{\varepsilon L}{\sigma^3} = \frac{15L}{Re_\lambda \lambda_T} \tag{4.1}$$

is introduced (e.g. Vassilicos (2015)). If the turbulence dissipation is in equilibrium, C_ε is, as proposed by Kolmogorov, constant Obligado *et al.* (2016). This means that C_ε is both

independent on the Reynolds number and the viscosity. However, if anomalies occur, a violation of this independence indicates non-equilibrium dissipation of the turbulence.
In figure 4.23, the centerline evolution of C_ε is plotted downstream the disc (a) and the turbine (b). Downstream the disc, C_ε decreases up to $X/D \approx 3$ and remains then constant at $C_\varepsilon \approx 0.5$. An influence of the inflow turbulence is scarcely visible. Downstream the turbine, C_ε is approximately constant up tp $X/D \approx 1.76$, increases and then decreases again. The evolution is differently pronounced depending on the inflow turbulence. In the far wake, $C_\varepsilon \approx 0.5$ for all inflow conditions.
To connect the downstream evolution of C_ε at the centerline with the dependence on the Taylor Reynolds number, C_ε is plotted over Re_λ in figure 4.24 for the disc (a) and the turbine (b). In case of the disc, C_ε decreases with increasing Re_λ for $100 \leq Re_\lambda \leq 300$ and remains constant for higher Taylor Reynolds numbers that are reached mostly in case of active grid inflow. In case of the turbine, C_ε is approximately independent of Re_λ for laminar and active grid inflow. For regular grid inflow, a decrease of C_ε for increasing Re_λ is found for $75 \leq Re_\lambda \leq 400$ for data within the downstream region $2 < X/D < 3$, i.e. the decay region.
To summarize these results, downstream the disc, C_ε varies in the near wake and shows in this region also a dependence on Re_λ. This might suggest non-equilibrium dissipation in this region; however, as the turbulence evolves in this region and $E(f) \not\propto f^{-5/3}$, the result has to be handled with care. Downstream the turbine, non-equilibrium dissipation appears to be present in case of regular grid inflow within the decay region, however, $E(f) \not\propto f^{-5/3}$ as well.
Overall, this analysis suggests that non-equilibrium dissipation can occur in turbulence created by a disc or a turbine.

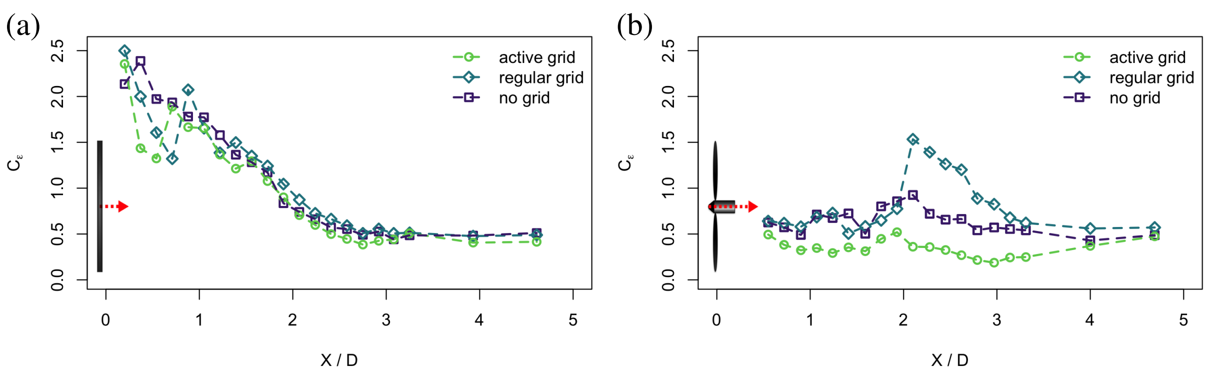

Figure 4.23.: Development of C_ε downstream the disc (a) and the turbine (b) on the centerline for different inflow conditions.

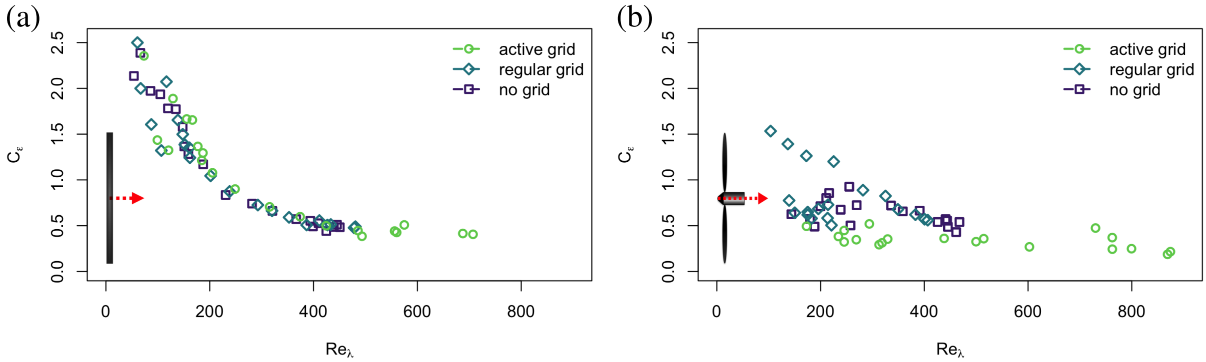

Figure 4.24.: Development of C_ε over the Taylor Reynolds number Re_λ downstream the disc (a) and the turbine (b) on the centerline for different inflow conditions.

4.2.2. Increment PDFs and shape parameter

To follow the above-developed idea of the disc and turbine being elements that imprint their own turbulence independently on the type of inflow, two-point statistics are scrutinized in the following. Here, the probability density functions of temporal and spacial velocity increments are plotted and the respective temporal and spacial shape parameter λ^2 are investigated. This will give further information on the evolution of turbulence structures on different scales, and intermittency can be identified if $\lambda^2 > 0.1$. Moreover, this analysis can be used to further back up the indication of homogeneous isotropic turbulence occurring far downstream in the wake.

Temporal increments and shape parameter

The probability density functions of velocity increments are in the following presented for a time scale τ that corresponds to the turbine diameter D, in the following also noted as $\tau \simeq D$. Two downstream positions, namely $X/D = 2.45$ and $X/D = 4.00$, were chosen to represent one location in the turbulence decay range where the spectra start to collapse, and one location where a stable state is exhibited. In addition, a curve corresponding to equation (2.7) as proposed by Castaing *et al.* (1990) is plotted if the shape parameter λ^2 that is calculated from the fourth structure function is positive. Here, the shape parameter is used as an indicator for the occurrence of intermittency in the wake.

In figure 4.25, the probability density function of velocity increments is presented for the position $X/D = 2.45$ downstream the disc (a) and the turbine (b).

At this position downstream the disc, the increment PDFs exhibit an almost Gaussian behavior independently of the inflow. The shape parameter λ^2 is similar for laminar and regular grid inflow, and about thrice as high for active grid inflow, as can be taken from table 4.5.

Downstream the turbine, a difference between laminar inflow and regular and active grid inflow

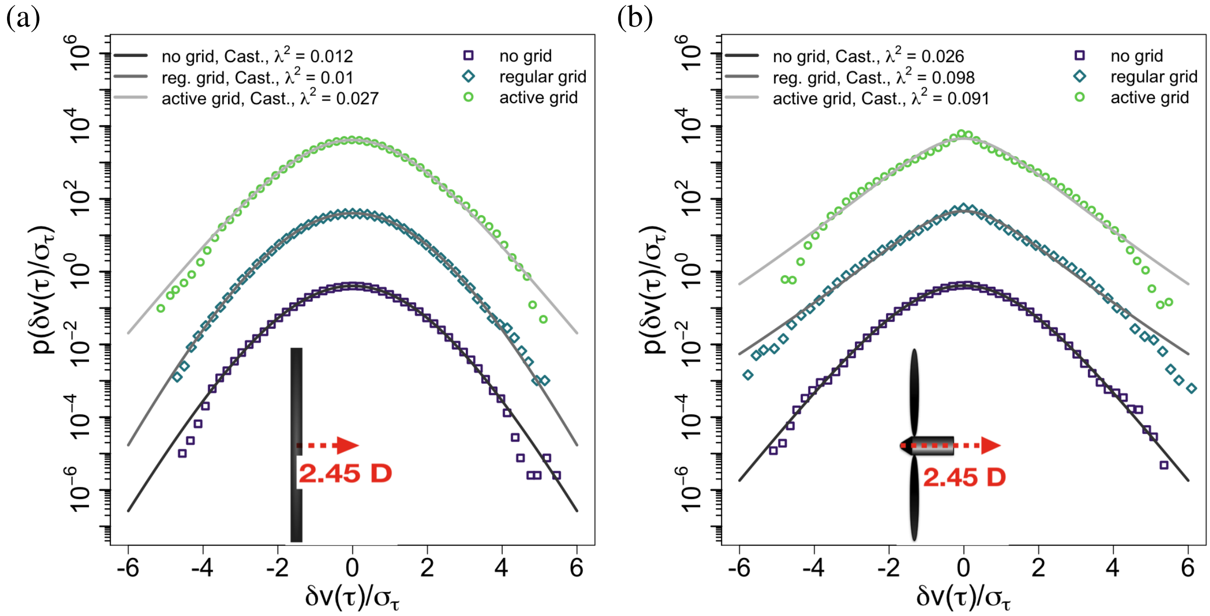

Figure 4.25.: Probability density function of velocity increments for time scale $\tau \simeq D$ at $X/D = 2.45$ on the centerline for disc (a) and turbine (b). If $\lambda^2 > 0$ as indicated in the top-left legend, a Castaing curve is plotted in addition. The curves are vertically shifted for better distinction.

is present. While the curves capture the behavior of the increment PDFs in the wake of the disc well, deviations are present in case of the turbine wake.

Overall, the wake downstream the turbine shows a more intermittent behavior as compared to the disc's wake. Figure 4.26 indicates that farther downstream at $X/D = 4.00$, the wakes of both disc and turbine exhibit Gaussian behavior for all inflow conditions which is indicated by $\lambda^2 \approx 0$.

It was shown that the intermittency that is indicated by the heavy-tailed probability density functions of velocity increments can be characterized by the shape parameter λ^2 calculated from

Table 4.5.: Shape parameter λ^2 downstream the disc and the turbine at $X/D = 2.45$ and $X/D = 4.00$ calculated from the kurtosis.

Downstream position	λ^2 lam.	λ^2 reg. grid	λ^2 act. grid
$X/D = 2.45$ - disc	0.01	0.01	0.03
$X/D = 4.00$ - disc	-0.01	0.00	-0.01
$X/D = 2.45$ - turbine	0.03	0.10	0.09
$X/D = 4.00$ - turbine	0.00	0.01	0.00

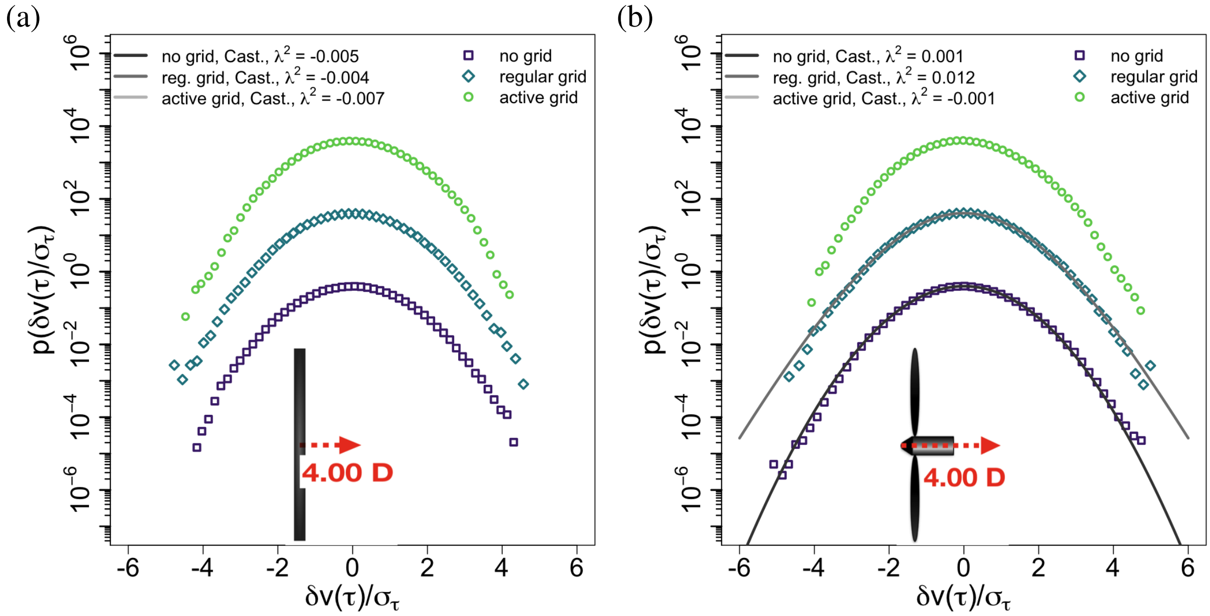

Figure 4.26.: Probability density function of spacial velocity increments for time scale $\tau \simeq D$ at $X/D = 4.00$ on the centerline for disc (a) and turbine (b). The different spacial increments are indicated in the sketches. If $\lambda^2 > 0$ as indicated in the top-left legend, a Castaing curve is plotted in addition. The curves are vertically shifted for better distinction.

the kurtosis. Therefore, the centerline evolution of the shape parameter for $\tau \simeq D$ is investigated next. Figure 4.27 shows the results downstream the disc (a) and turbine (b).
Downstream the disc, the values are overall small with an exception directly behind the disc, and the three regions (near wake, transition and turbulence decay region/far wake) can be identified. In case of the turbine, $\lambda^2 \approx 0$ in the near wake, increases up to $\lambda^2 \approx 0.15$ in the transition region and decreases to $\lambda^2 \approx 0$ in the turbulence decay region. Downstream from $X/D \approx 3$, in the far wake, $\lambda^2 \approx 0$. While the inflow turbulence does have an influence on the evolution of the intermittency in the transition and decay region, an influence on the evolution of the shape parameter is not present anymore in the far wake.

To investigate the intermittency in dependence on the scale in the far wake, the evolution of the shape parameter is plotted over τ in figure 4.28 at the centerline at $X/D = 4.00$. The scales were chosen to represent $\tau \simeq (0.01, 0.02, 0.03, 0.09, 0.17, 0.34, 0.51, 1.03, 1.54, 2.05, 3.08, 4.10, 5.13, 6.84, 8.55, 10.26)D$. For all inflow conditions and for both disc and turbine similarly, the shape parameter decreases from $\tau \simeq 0.01D$ to $\tau \simeq 0.5D$ and is afterwards approximately zero. Thus intermittency is not present in the far wake downstream both WGTs from scales that exhibit $0.5D$. To round off

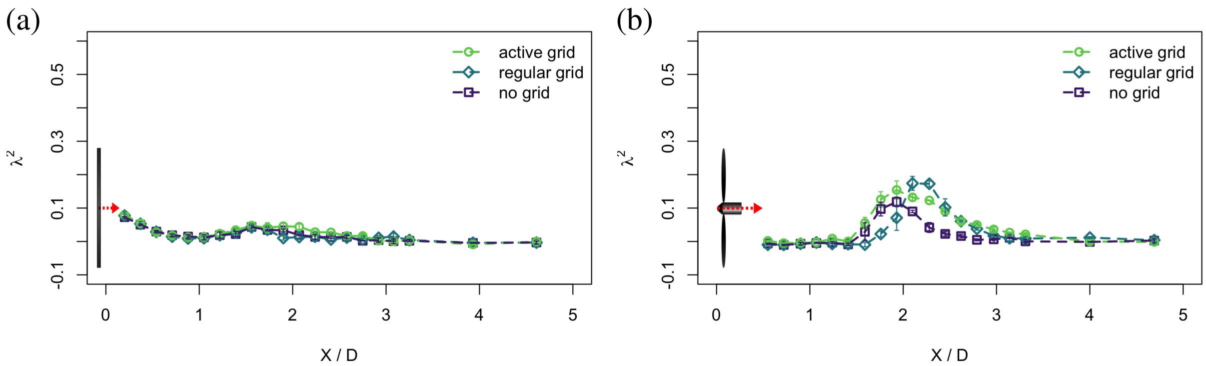

Figure 4.27.: Downstream evolution of the shape parameter for $\tau \approx D$ for disc (a) and turbine (b) at centerline.

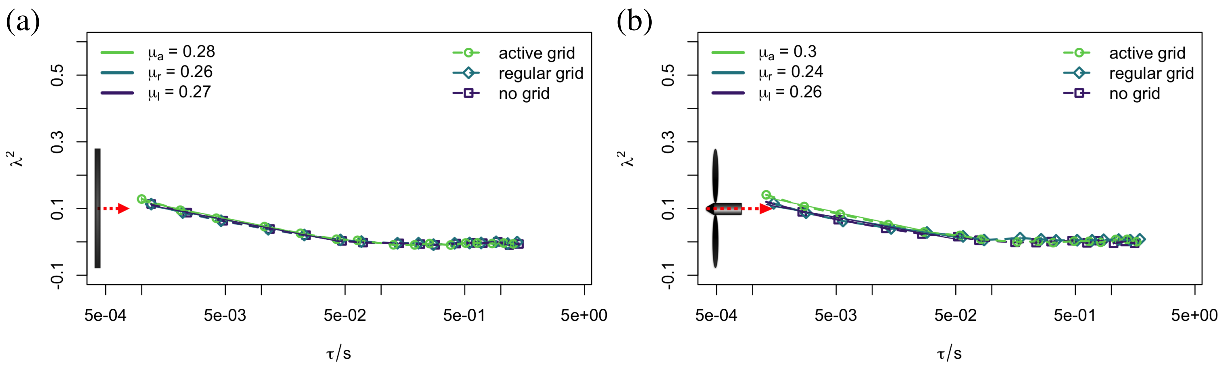

Figure 4.28.: Evolution of the shape parameter over τ at $X/D = 4.00$ for disc (a) and turbine (b) at centerline.

the analysis and to check for further signs of homogeneous isotropic turbulence, a fit is used to determine the intermittency parameter μ from the decreasing shape parameter:

$$F(\tau) \propto \tau^{-4/9 \cdot \mu} \tag{4.2}$$

$$\lambda^2 \simeq \frac{\ln F(\tau)}{4}, \tag{4.3}$$

This relation is born of Kolmogorov's K62 theory that assumes a certain scaling behavior of the structure functions in case fully developed turbulence. Therefore, this relation can be used to identify signs of homogeneous isotropic turbulence in the flow. μ has to be determined experimentally. For homogeneous isotropic turbulence, a value of $\mu \approx 0.25 \pm 0.05$ is assumed to be realistic by Pope (2000). The determined values can be found in table 4.6, and as they vary between $0.26 < \mu < 0.30$, the existence of homogeneous isotropic turbulence in the center of a wind turbine wake and an actuator disc wake is highly likely.

Overall, the findings of Wessel (2008), Bastine *et al.* (2015) and Singh *et al.* (2014), that a turbine reduces intermittency in the flow, and that indicators of homogeneous isotropic turbulence are present, could be verified. In this thesis, the analysis goes a step further. Due to the detailed investigation of the downstream evolution of λ^2, now a region in the wake can be assigned to these findings.

Next, an overview of the evolution of $\lambda^2(\tau \simeq D)$ in the measured plane is given.
Figure 4.29 presents the interpolated contour plots for the disc and the turbine for $\tau \simeq D$ for all inflow conditions. Overall, the influence of the inflow conditions on the evolution of the shape parameter is small for both disc and turbine. Directly downstream the disc, the shape parameter exceeds 0.1 but decreases fast farther downstream. Outside the rotor plane up to $X/D \approx 2.5$, higher values are found that might be caused by the shear layer of the expanding wake and the surrounding flow. Downstream the turbine, two different regimes with $\lambda^2 > 0.2$ are present. In the central region, the above described transition region is identified around $X/D \approx 2$ and $-0.21 < Y/D < 0.21$. Additionally, in the tip region at $Y/D = \pm 0.51$, high values of the shape parameter are found in proximity to the rotor. They have been reported first in Schottler *et al.* (2018) for two different turbine models where a high-intermittency ring was found to be present at $X/D = 6$. Due to the coarse span-wise spacing of the probes, this ring is not captured in this experiment further downstream.

Spacial increments and shape parameter

To complete the analysis of velocity increments, an investigation follows that uses the different sensor positions to calculate span-wise increments of the velocity measured in stream-wise direction. First, the probability density functions of spacial velocity increments are plotted at downstream positions $X/D = 2.45$ and $X/D = 4.00$ for the disc and turbine wake in active grid inflow. The respective orientation of the increments are indicated in sketches in the plot (upstream view). Increment PDFs are shown for $r_1 = 0.13D$, $r_2 = 0.21D$, $r_3 = 0.24D$, $r_4 = 0.25D$, $r_5 = 0.33D$ and $r_6 = 0.52D$. r_2 and r_6 are horizontally oriented, r_1 and r_4 vertically, and r_3 and r_5 diagonally. The scales were chosen to exemplary reproduce the main results while similar

Table 4.6.: Intermittency parameter μ downstream the disc and the turbine at $X/D = 4.00$.

	μ lam.	μ reg. grid	μ act. grid
Disc	0.27	0.26	0.28
turbine	0.26	0.24	0.30

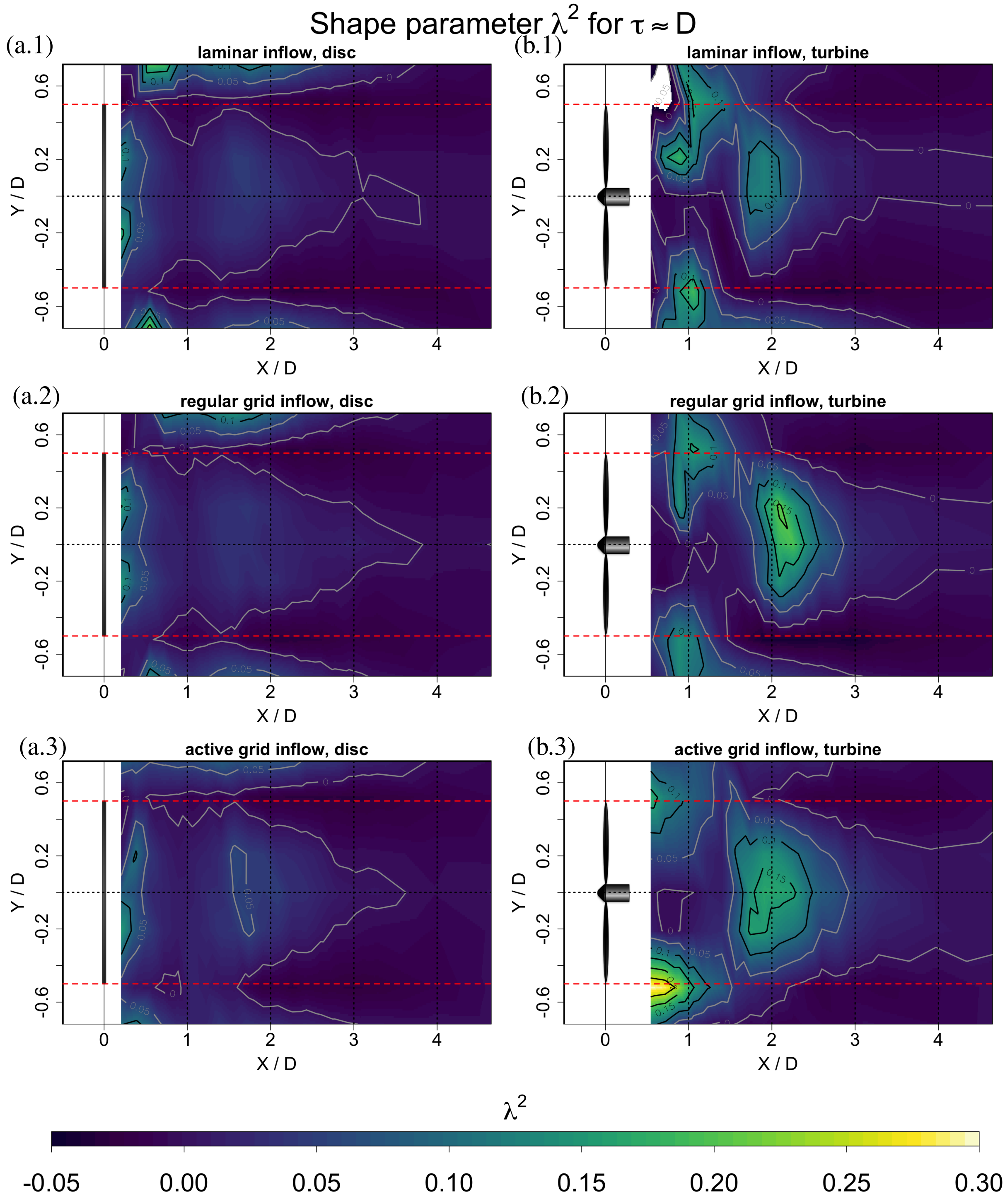

Figure 4.29.: Evolution of the shape parameter for $\tau \simeq 58\,\mathrm{cm}$: Surface plots downstream the disc (a.i) and the turbine (b.i)) for laminar (x.1), regular grid (x.2) and active grid (x.3) inflow. Grey contours indicate areas of Gaussian behavior of the velocity increments ($\lambda^2 < 0.05$) and black contour lines indicate intermittent behavior of the velocity increments ($\lambda^2 > 0.10$).

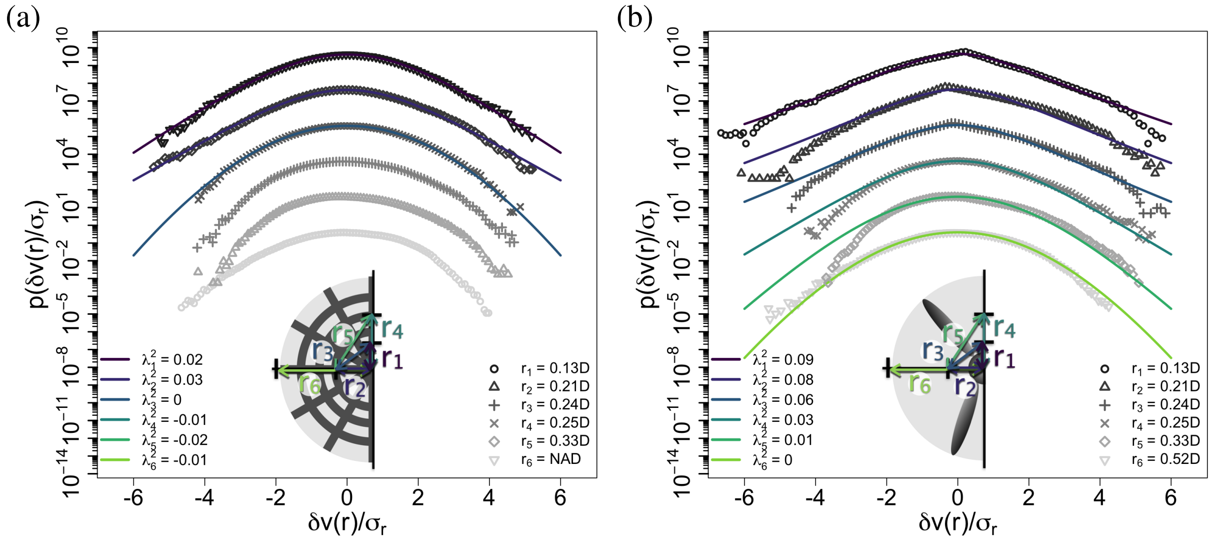

Figure 4.30.: Probability density function of spacial velocity increments at $X/D = 2.45$ for disc (a) and turbine (b). If $\lambda^2 > 0$ as indicated in the top-left legend, a Castaing curve is plotted in addition.

results have been found for other possible combinations and also for the other half of the rotor. A curve corresponding to equation (2.7) as proposed by Castaing *et al.* (1990) is plotted if $\lambda^2 > 0$. The values are shown in table 4.8; if λ^2 is slightly negative but $\lambda^2 \approx 0$, this is indicated with $\lambda^2 = -0.00$.

Figure 4.30 shows the results at $X/D = 2.45$. In case of the disc (a), only r_1 and r_2 sightly indicate intermittent behavior while the fluctuations are more or less Gaussian for the other scales. In case of the turbine (b), only the largest scale exhibits a Gaussian distribution for velocity fluctuations. The intermittency decreases with increasing scale, while the skewness increases. Further downstream at $X/D = 4.00$ (cf. figure 4.31), the spacial increment PDFs of velocity fluctuations are similar for disc and turbine. The distributions are approximately Gaussian for all scales with λ^2 being positive only for the smallest three scales. Overall, this is in agreement with the description of the temporal increments at $\tau \simeq D$.

In figure 4.32, the downstream evolution of the six presented scales $r_1 - r_6$ is shown for the disc and the turbine for all inflow conditions. In general, the evolution of the shape parameter downstream the disc is influenced only marginally by the inflow conditions. The curves for scales r_1, r_2 and r_3 are showing a decreasing shape parameter up to $X/D = 1$ in the near wake, followed by a small increase in the transition region. The curves decrease again and from $X/D = 2$, the value stays constant. The local maxima can be found in table 4.7. For scales r_4 and r_5, the curves collapse as well. A jump can be seen for laminar and regular grid inflow after $X/D = 0.37$. It is also present for active grid inflow, but less pronounced. It is assumed to be caused by a transition from an area that is blocked by the disc to an area where turbulent mixing sets in. For r_6, λ^2 is

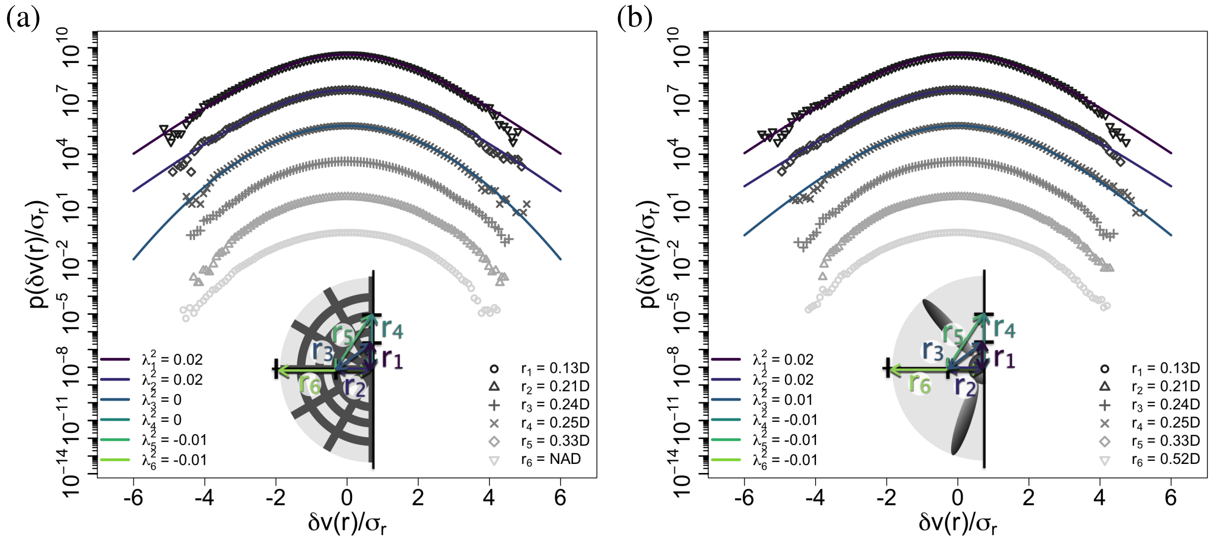

Figure 4.31.: Probability density function of spacial velocity increments at $X/D = 4.00$ for disc (a) and turbine (b). If $\lambda^2 > 0$ as indicated in the top-left legend, a Castaing curve is plotted in addition.

negative for most positions and thus indicating a sub-Gaussian behavior of the fluctuations. In the far wake, the curves of r_1 and r_2 collapse to $\lambda^2 \approx 0.02$, and the ones of r_3 - r_6 collapse to $\lambda^2 \approx 0$.

Downstream the turbine, the influence of the inflow conditions is present: While the above-mentioned curve-pairs can similarly be identified downstream the turbine, the evolution shows minor differences for the respective inflow. The curves of r_1 - r_3 are flat in the near wake and have a peak in the transition region at around $X/D = 2$ similarly to the temporal shape parameter. It is followed by a decrease until $X/D \approx 3$ in the turbulence decay region, and the shape parameter remains constantly $0 < \lambda^2 < 0.025$ further downstream in the far wake. For r_4 and r_5, the curves have roughly the same shape but with stronger deviations. The states used for the wake region identification seem to be shifted upstream. For r_6, a jump to higher λ^2 at the beginning, followed by a decrease to $\lambda^2 < 0$ and a convergence to $\lambda^2 \approx 0$ is found similar to the temporal analysis,

Table 4.7.: Spacial shape parameter λ^2 downstream the disc and the turbine at $X/D = 2.45$ and $X/D = 4.00$ calculated from the kurtosis for active grid inflow.

	r_1	r_2	r_3	r_4	r_5	r_6
$X/D = 2.45$ - disc	0.02	0.03	0.00	-0.00	-0.02	-0.01
$X/D = 4.00$ - disc	0.02	0.02	0.00	-0.00	-0.01	-0.01
$X/D = 2.45$ - turbine	0.09	0.08	0.07	0.03	0.01	0.00
$X/D = 4.00$ - turbine	0.02	0.03	0.01	-0.01	-0.01	-0.01

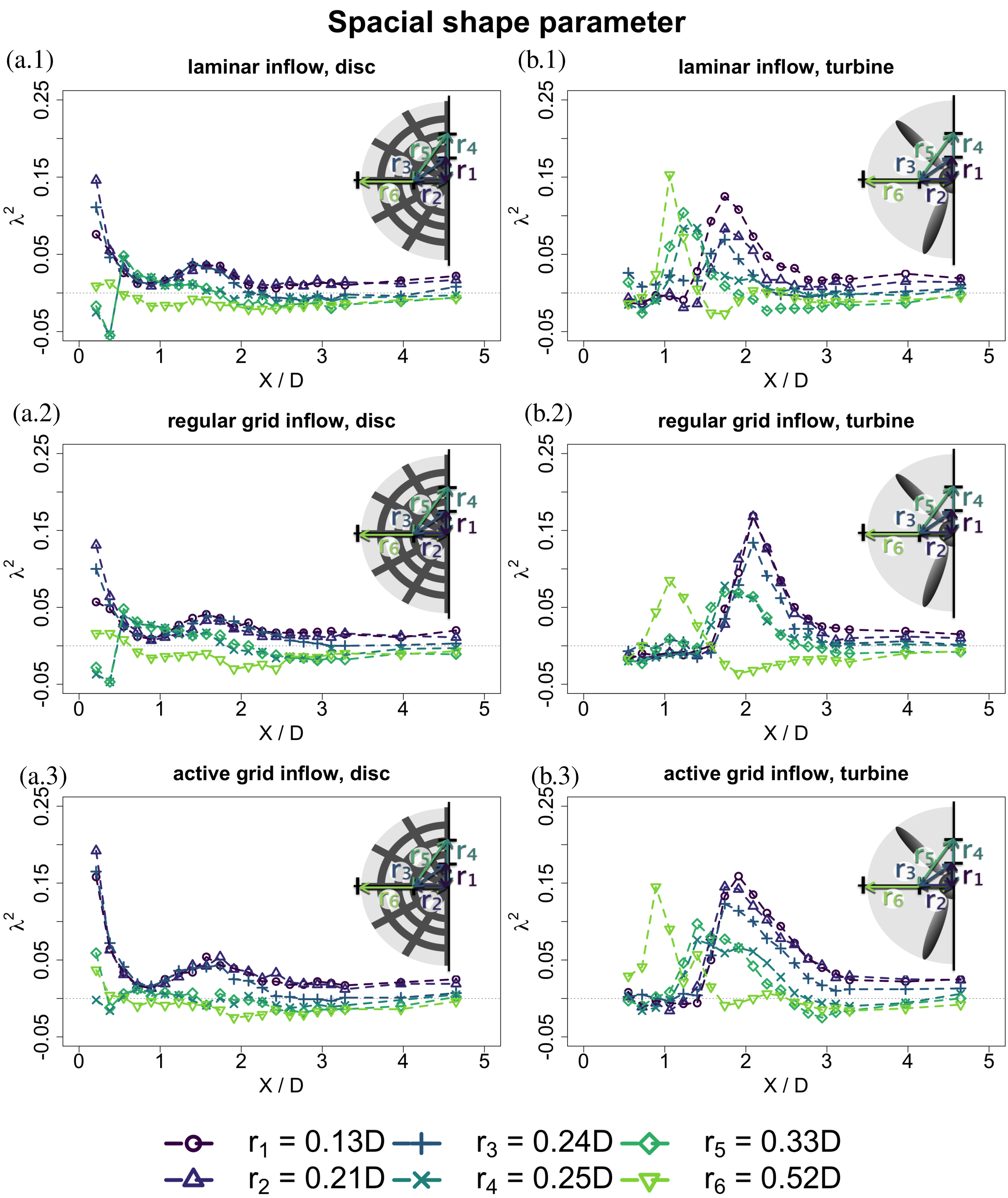

Figure 4.32.: Downstream evoltion of spacial increments downstream the disc (a.i) and the turbine (b.i) for laminar (x.1), regular grid (x.2) and active grid (x.3) inflow. The increments are indicated in the sketches top right.

Table 4.8.: Local maximum of the spacial shape parameter λ^2 downstream the disc and the turbine with respective downstream positions.

			r_1	r_2	r_3	r_4	r_5	r_6
laminar	disc	λ^2_{max}	0.04	0.04	0.04	0.02	0.02	-0.01
		X/D	1.40	1.57	1.40	1.23	1.40	1.40
	turb.	λ^2_{max}	0.12	0.08	0.08	0.08	0.10	0.15
		X/D	1.74	1.74	1.74	1.40	1.23	1.06
reg. grid	disc	λ^2_{max}	0.04	0.03	0.04	0.02	0.02	-0.01
		X/D	1.57	1.57	1.57	1.57	1.57	1.57
	turb.	λ^2_{max}	0.17	0.17	0.13	0.08	0.07	0.08
		X/D	2.09	2.09	2.09	1.74	1.74	1.06
act. grid	disc	λ^2_{max}	0.05	0.05	0.04	0.01	0.01	-0.00
		X/D	1.57	1.74	1.74	1.06	1.06	0.89
	turb.	λ^2_{max}	0.16	0.14	0.12	0.08	0.10	0.14
		X/D	1.91	1.74	1.74	1.40	1.40	0.89

and the wake regions appear to be shifted even farther upstream. The local maxima can be found in table 4.7.

Overall, this analysis shows that both temporal increments downstream the centerline and spacial increments in the inner wake close to the centerline (i.e. r_1 - r_3) evolve similarly downstream the WGTs. This can also be interpreted as Taylor's hypothesis holding for the analyzed data sets. The investigation of spacial increments additionally enables a localization of a central wake with the characteristic wake regions, and the downstream evolution changes from scales $r_1 - r_3$ to $r_4 - r_5$ to r_6.

The spacial increments indicate velocity differences across the rotor and are thus directly linked to the loads acting on the turbine. As the turbine spacing in wind farms decreases, knowledge of regions with intermittent flow is important to take into account higher loads.

Validating isotropy

By means of the decay exponent and μ, the occurrence of homogeneous isotropic turbulence downstream a turbine was indicated. To further investigate this evidence, 2D hot-wire measurements were carried out at the centerline downstream the turbine in active grid inflow. The 2D hot-wire probe was both aligned in X-Y-orientation and in X-Z-orientation to measure all three flow components. In figure 4.33, the ratios of the respective flow component's standard deviations σ_a/σ_b with $a,b \in X,Y,z;\ a \neq b$ are plotted. As isotropic flow is characterized by

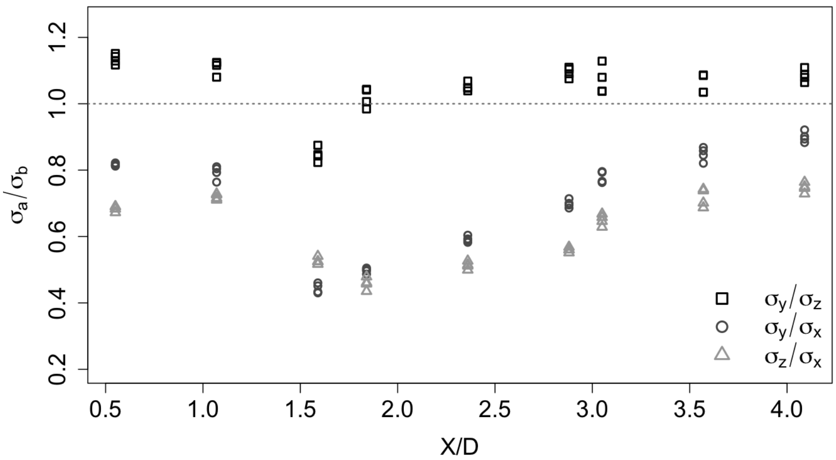

Figure 4.33.: Investigation of isotropy downstream the turbine: The respective ratios of standard deviations σ_a/σ_b ($a,b \in x,y,z$) of the flow components u_x, u_y and u_z are plotted.

similar fluctuations in all directions, $\sigma_a/\sigma_b = 1$ is expected to hold. For the Y and Z flow component, $\sigma_Y/\sigma_Z \approx 1$ for the whole measurement range. Compared to the fluctuations in main flow direction, the fluctuations in y and Z direction are smaller. In the region around $X/D \approx 2$, the fluctuations in X direction are double the fluctuations in Y and Z direction. Nevertheless, far away from the turbine, the ratio increases to $\sigma_Y/\sigma_X \approx 1$ and $\sigma_Y/\sigma_Z \approx 0.75$, respectively. Therefore, the flow shows strong signs of isotropy far away from the rotor.

Summary

Overall, the analysis of energy spectra, probability density functions of temporal and spacial velocity increments, and the temporal and spacial shape parameter revealed a turbulence transition region from near wake to far wake, where the turbulence structures are primarily influenced by the model and not by the inflow. The before introduced wake regions are identifiable for these quantities as well. The presented energy spectra show for the span-wise positions $Y/D = 0$ and $Y/D = -0.21$ a similar downstream evolution that varies from the evolution at $Y/D = -0.51$. For the spacial increments, looking at the scales in combination with the coordinates of the probes (see 3.3), it is found that the statistics for the inner positions agree. Moving outwards, it is shown that the intermediate positions start to vary from this statistics. The statistics of the outer position looks due to different turbulence production and mixing mechanisms differently. This leads to the conclusion that an inner wake region exists where a certain kind of turbulence is created. This turbulence is in proximity to the disc/turbine dependent on the WGT and the inflow. Farther downstream, it converges after a transition region to a region where the created turbulence is dominant and independent on the inflow and to some degree the WGT. Features of homogeneous, isotropic turbulence could be identified in this inner far wake region, which is also suggested by Bastine *et al.* (2015) for one downstream position. Also, it was demonstrated how the intermittency evolves in the wake and that a turbine and a disc reduce intermittency compared to the inflow. The latter was indicated by Wessel (2008), Singh *et al.* (2014) and Bastine *et al.* (2015) for the wake of a turbine at single downstream positions.

4.3. Investigation of field data

When carrying out laboratory experiments, the question remains whether and to what extend results can be applied to full-scale turbines operating in the atmospheric boundary layer. To view results from full-scale measurements, data provided by the Energy research Centre of the Netherlands (ECN; now ECN part of TNO) have been analyzed. These data come from a measurement campaign executed in the framework of the TKI Wind op Zee LAWINE project (see Boorsma *et al.* (2016)) partly subsidized by RVO.
Time series from three Nordex N80 2.5 MW turbines with 80 m rotor diameter and 80 m hub height are used. A met mast is positioned close to the three turbines. For the turbine position and the met mast, see Eecen and Verhoef (2007). Depending on the wind direction, the met mast stands in the wake of either turbine, and different downstream positions of the wake are measured. The wakes of the three wind turbines WT 05 ($3.5D$ from the met mast), WT 06 ($2.5D$ from the met mast) and WT 07 ($5.4D$ from the met mast) are investigated. For the wake data sets, time windows were chosen where the 10 minute average wind direction came from the respective direction $\pm 10°$ for at least 20 minutes. Additionally, the turbines were operating with a tip speed ratio $7.0 < TSR < 7.4$ in partial load range similar to the turbine. The sampling frequency of the sonic anemometer is 4 Hz. As no data of the incoming wind speed is available, the tip speed ratio was calculated with the inflow velocity from the 10 minute average power and the power curve from the data sheet. To compare the data with free inflow conditions, time series with the respective incoming velocity but with wind direction from west-south-west (Inflow WSW) are used. The amount of data that fits the criteria is rather small, as the met mast is not in the wake of either of the turbines if the wind comes from the main wind direction. Thus, the average results over all time series are presented here. In table 4.9, the mean velocities and turbulence intensities with the standard deviation of this average, and the number of data points are shown. As expected, the mean velocity in proximity to the wind turbine is lowest while the mean velocity at $3.5D$ and $5.4D$ is higher. A reason for the higher velocity at $3.5D$ compared to $5.4D$ is hard to identify since the data sets are from two different turbines and several different dates. The turbulence intensity decreases with increasing distance similar to the results from the laboratory experiment after the turbulence intensity peak.
In figure 4.34, the probability density functions of velocity increments are plotted for five scales

Table 4.9.: Summary of results from free field measurements. For the thee turbines, the mean velocities and turbulence intensities of all time series including their standard deviation and the total number of data points are presented.

	WT 05 - 3.5 D	**WT 06 - 2.5 D**	**WT 07 - 5.4 D**	**Inflow WSW**
$u/m/s$	7.52 ± 1.05	4.95 ± 1.85	7.09 ± 1.05	9.33 ± 0.67
$TI/\%$	20 ± 5	24 ± 1	18 ± 1	10 ± 2
no. of data points	79200	19200	52800	348000

Table 4.10.: Shape parameter λ^2 calculated from free field data in the wake and inflow for the five time scales that represent rotor-related scales $\tau_i \simeq (0.025/0.125/0.5/1/2)D$.

	WT 05 - 3.5 D	**WT 06 - 2.5 D**	**WT 07 - 5.4 D**	**Inflow WSW**
$\tau_1 \simeq 0.025D$	0.08	0.09	0.09	0.13
$\tau_2 \simeq 0.125D$	0.07	0.05	0.05	0.12
$\tau_3 \simeq 0.500D$	0.05	0.03	0.03	0.11
$\tau_4 \simeq 1.000D$	0.03	0.04	0.01	0.10
$\tau_5 \simeq 2.000D$	0.02	0.03	0.01	0.10

that relate to the turbine diameter as $\tau_i \simeq (0.025/0.125/0.5/1/2)D$ downstream the turbines in comparison with the inflow. In addition, a curve as proposed by Castaing *et al.* (1990) is added with λ^2 being listed in the plot legend and in table 4.10. The whole sets of time series have been used for the increment analysis: For each coherent time series, the increment time series were calculated, and the increment time series generated this way are catenated to single, long increment time series for each flow situation. To compare the wake time series to the inflow, the same amount of data points has been used between inflow and the respective flow situation. In addition, the influence of the number of data points on the result have been checked, and it is found that 19200 data points can already be used to calculate a reliable increment PDF.

As can be seen both by directly comparing the increment PDFs and looking at the shape parameter, the wake is on all scales less intermittent than the inflow. Further, larger scales show less intermittent behavior. For scales equal or larger than D, the shape parameter decreases downstream with increasing distance, while the values show no trend on scales $r < D$. Overall, the results agree with the findings in the laboratory that the turbine reduces intermittency in the wake and that the intermittency is eliminated for temporal scales corresponding to at least the rotor diameter.

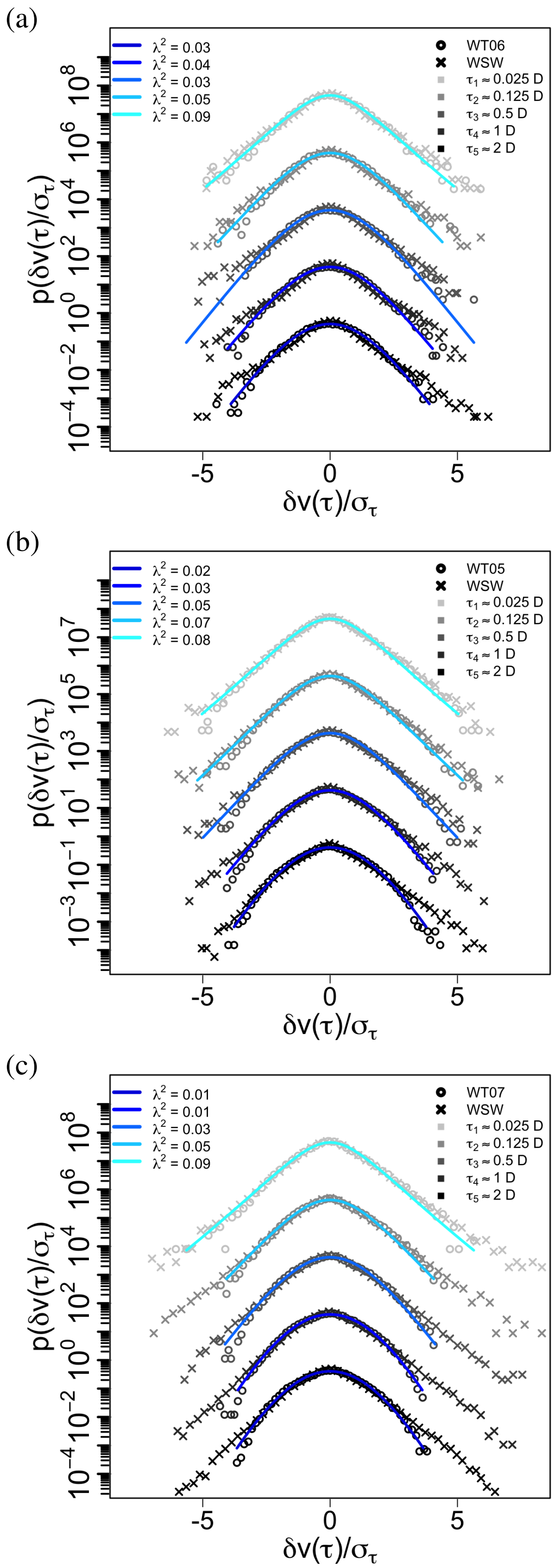

Figure 4.34.: Probability density functions of velocity increments from free field data at $X/D = 2.5$ (a), $X/D = 3.5$ (b) and $X/D = 5.4$ (c) for different, rotor-related time scales. If $\lambda^2 > 0$ as indicated in the top-left legend, a Castaing curve is plotted in addition.

5. Results 2: Wake of a turbine array

In the preceding chapter, it was shown that the behavior of certain quantities in the wake downstream a model turbine are independent on the inflow condition. It was also demonstrated that the model turbine imprints features of homogeneous isotropic turbulence onto the wake in the central wake of the turbine. As a deduction, similar findings are expected in the wake of a wind turbine array. This hypothesis is to be proven in this chapter. Therefore, measurements were carried out downstream a single model turbine in laminar inflow, and downstream an array of two model wind turbines. Two array setups were investigated, where the first turbine is exposed to laminar inflow and the second turbine is positioned in the full wake and the half wake of the first turbine. The turbines were controlled to perform optimally. This chapter is structured similarly to the preceding chapter: A presentation of the results obtained with standard methods is followed by the results from stochastic turbulence analysis.

In this section, wake measurements are presented that were carried out in OLWiT with an outlet of $3\,\mathrm{m} \times 3\,\mathrm{m}$ in laminar inflow at $u_0 = 7.5\,\mathrm{m/s}$. Three different scenarios have been used to evaluate the hypothesis that certain quantities evolve independently of the inflow so that homogeneous isotropic turbulence occurs in the wake center. These scenarios are:

1. Measurements downstream turbine 1 up to $X/D = 12.62$. Turbine 1 is exposed to laminar inflow; the scenario is referred to as *turbine 1*.
2. Measurements downstream turbine 2 that is aligned with turbine 1 and placed $5.21D$ downstream from turbine 1. It is thus exposed to a wake as sole inflow. This scenario is referred to as *turbine 2 mid*.
3. Measurements downstream turbine 2 that is shifted half a diameter sidewards from turbine 1. Turbine 2 is thus exposed to a sheared inflow consisting of wake center, wake boundary layer and laminar inflow. The turbine is placed $X/D = 5.21$ downstream of turbine 1. This scenario is referred to as *turbine 2 side*.

This chapter is structured as chapter 4. First, the measurements are evaluated with standard analysis methods and in the second part, an analysis with extended methods is applied.

5.1. Standard analysis of the wake flow

In this section, the measurements are presented in the same way as in the last chapter. First, the evolution of the mean velocity deficit is presented. Next, the downstream development of the turbulence intensity is shown. Afterwards, characteristic length scales are discussed. All listed quantities are investigated in the following manner: First, interpolated contour plots give an overview of the whole measurement field. Afterwards, profiles at several downstream positions are depicted, and the centerline evolution of the respective quantity is plotted to allow for a direct comparison of the data. Thereafter, the results are briefly discussed. This section closes with a summary.

5.1.1. Downstream development of the mean velocity

In figure 5.1, the normalized mean velocity u/u_0 in the wake is presented as interpolated contour plot downstream turbine 1 (a), turbine 2 mid (b) and turbine 2 side (c). In (a), the position of the second turbine's rotor at $X/D = 5.21$ is marked with a dashed red line. From the contour plots, a qualitative comparison between the three wakes can be obtained. Downstream turbine 1, the characteristic wake behavior with a near wake with strongly reduced mean wind speed is present. The wake starts to recover from $X/D \approx 5$ and also expands. Downstream turbine 2 mid, a similar behavior is visible, but the evolution is compressed and thus the wake recovery is accelerated. Downstream turbine 2 side, an asymmetry is present due to the strongly asymmetric inflow (indicated in figure 5.1(a) by the vertical dashed line). The wake recovery is similarly enhanced compared to the wake downstream turbine 1.

The comparison of normalized velocity profiles downstream turbine 1 and turbine 2 mid in figure 5.2 illustrate how the wake recovery is accelerated in turbulent inflow downstream turbine 2 mid across the rotor area. Due to the asymmetric inflow, the profiles downstream turbine 2 side vary from the profiles of turbine 2 mid.

Looking at the centerline evolution of the normalized velocity in figure 5.3 enables an additional quantitative comparison of the three wake situations. The development looks as expected from chapter 4 with a decrease in velocity downstream the turbine and a wake recovery that is in this experiment strongly dependent on the inflow. In the laminar inflow condition downstream turbine 1, the wake recovery starts at $X/D \approx 5$. At $X/D \approx 12.62$, the wake recovered to 70% of the free flow. Downstream turbine 2 (both positions), that is placed shortly behind the velocity

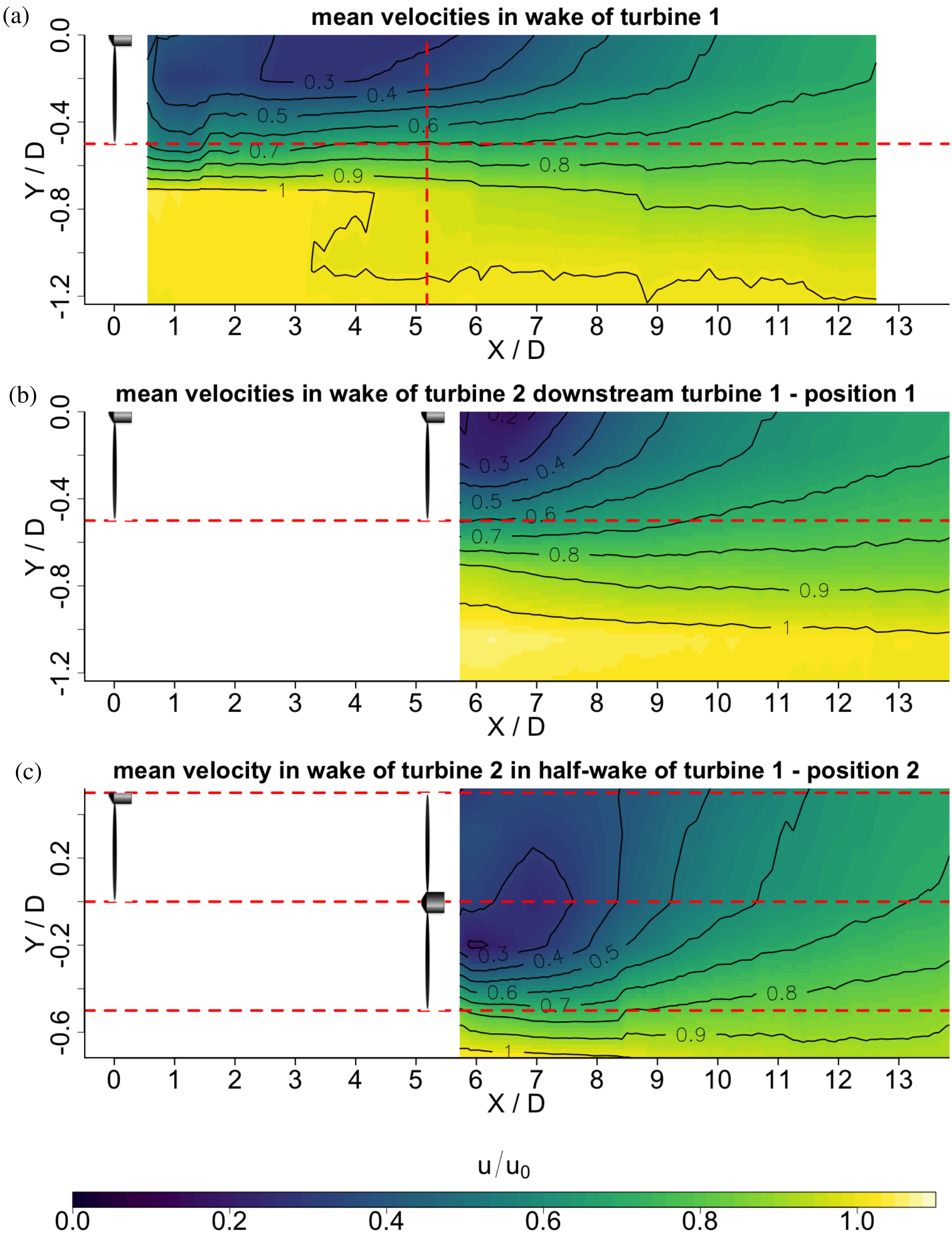

Figure 5.1.: Evolution of the normalized mean velocity downstream turbine 1 (a), turbine 2 mid (b) and turbine 2 side (c).

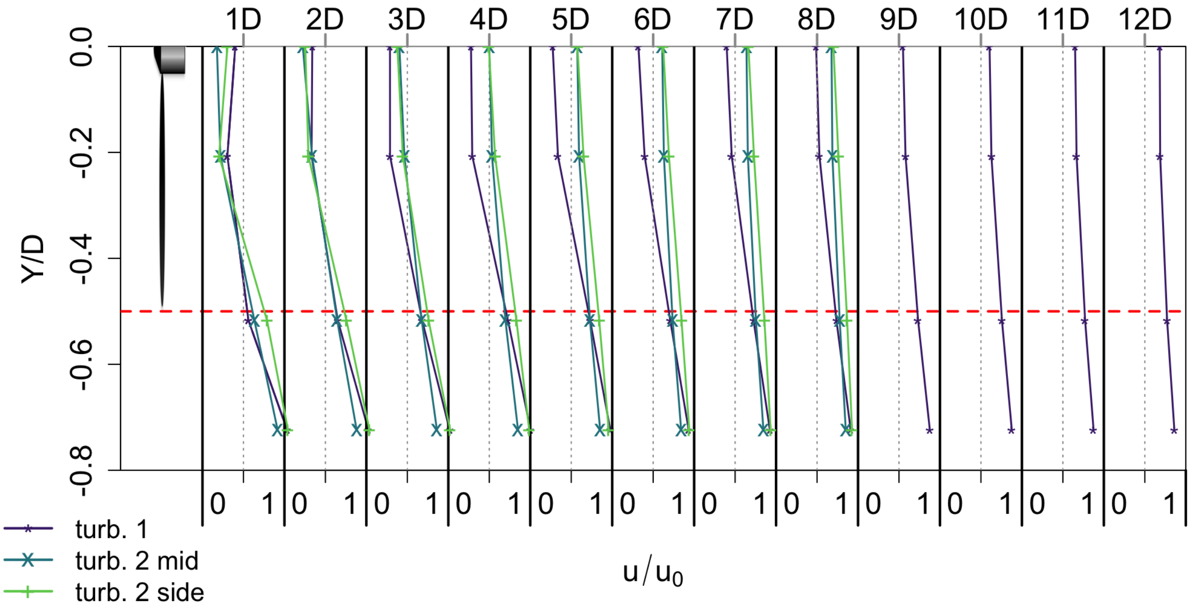

Figure 5.2.: Profile comparison of the to the inflow velocity $u_0 = 7.5\,\mathrm{m/s}$ normalized mean velocity downstream turbine 1 (purple *), turbine 2 mid (turquoise x) and turbine 2 side (green +). The Y-coordinate is with respect to the turbine center.

minimum downstream turbine 1, the recovery is significantly accelerated: The wake recovery starts already around $X/D \approx 2$, and at $X/D \approx 8.66$[i], the velocity is $\approx 70\%$ of the inflow. The precise position of the minima can be found in table E.2 in appendix E.

In conclusion, the evolution of the normalized mean velocity behaves characteristically and is quantitatively comparable to the results discussed in the preceding chapter. An asymmetry in the wake in case of asymmetric inflow downstream turbine 2 side is present. Due to the different setup in OLWiT, the positive influence of turbulence on the wake recovery as reported in e.g. Maeda *et al.* (2011), Aubrun *et al.* (2013) and Jin *et al.* (2016) could be verified. The results in turbulent inflow are in terms of the wake recovery similar to these studies. In Maeda *et al.* (2011), the centerline velocity recovered in turbulent inflow to approximately 65% of the inflow velocity at $X/D = 6$, and in Jin *et al.* (2016) to 70%, respectively, which is comparable to this study. However, the results obtained here in laminar inflow deviate. The evolution is significantly stretched with the recovery starting at $X/D \approx 5$ in case of laminar inflow. This is assigned to the very low blockage of 3% compared to the previous experiment: The wake is assumed to evolve slower as turbulent mixing is not reinforced by the surroundings (e.g. Jin *et al.* (2016)). In Lignarolo *et al.* (2014), a comparable experiment was carried out in laminar inflow with a two-bladed rotor and comparable TSR, and the centerline wake recovery starts from $X/D \approx 4.5$ with $u/u_0 \approx 0.2$, similarly to the results obtained in this thesis.

[i] This corresponds to $X/D = 13.87$ with regard to turbine 1.

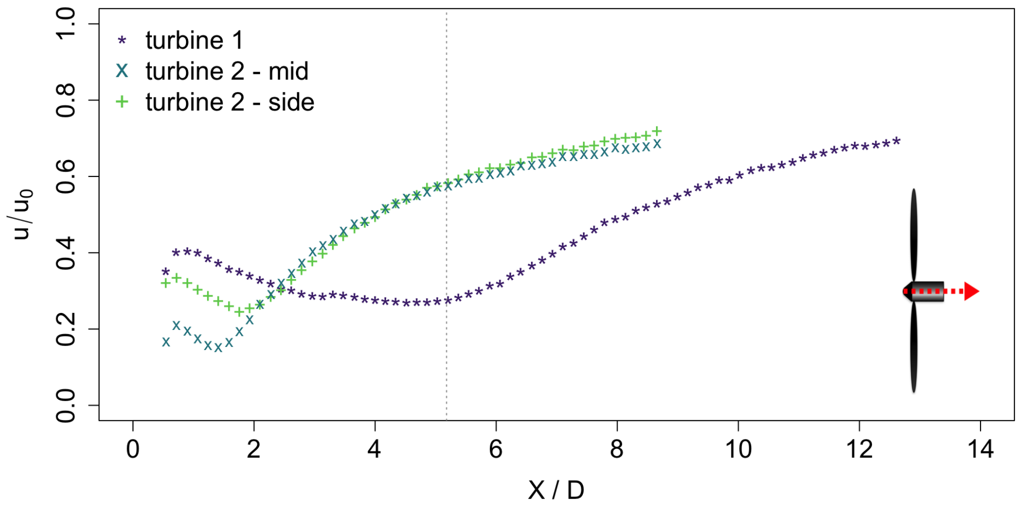

Figure 5.3.: Centerline evolution of the to the inflow velocity $u_0 = 7.5\,\mathrm{m/s}$ normalized mean velocity downstream turbine 1 (purple *), turbine 2 mid (turquoise x) and turbine 2 side (green +). The Y-coordinate is with respect to the turbine center.

5.1.2. Downstream development of the turbulence intensity

The evolution of the turbulence intensity is shown as interpolated contour plot in figure 5.4 downstream turbine 1 (a), turbine 2 mid (b) and turbine 2 side (c). The turbulence intensity is normalized to the respective peak turbulence intensity at the centerline, TI/TI_{CLpeak}, and the values can be found in table 5.1. As visualized in figure 5.4(a), the normalized turbulence intensity is strong directly downstream the rotor, especially under the nacelle's lee. Around $X/D \approx 5.5$ where the velocity minimum is located, a local maximum is also present. In this region, the turbulence intensity is not maximum at the centerline but around $Y/D = -0.21$ which causes an asymmetry. From the turbulence intensity peak around $X/D \approx 5.5$, the turbulence intensity decays. Downstream turbine 2 mid and side, the normalized turbulence intensity behaves similarly, but the ambient turbulent inflow leads to an earlier and faster decay of the turbulence intensity. In addition, the wake shows no asymmetry, and the peak turbulence intensity at centerline is the maximum turbulence intensity in that downstream area.

In figure 5.5, the downstream evolution of normalized turbulence intensity profiles is presented. Downstream turbine 1, a profile does develop only at the end of the measurement region.

Table 5.1.: TI_{CLpeak} used for the normalization of the turbulence intensity for all scenarios.

	turbine 1	**turbine 2 mid**	**turbine 2 side**
TI	0.21	0.49	0.40
X/D	6.24	1.76	2.45

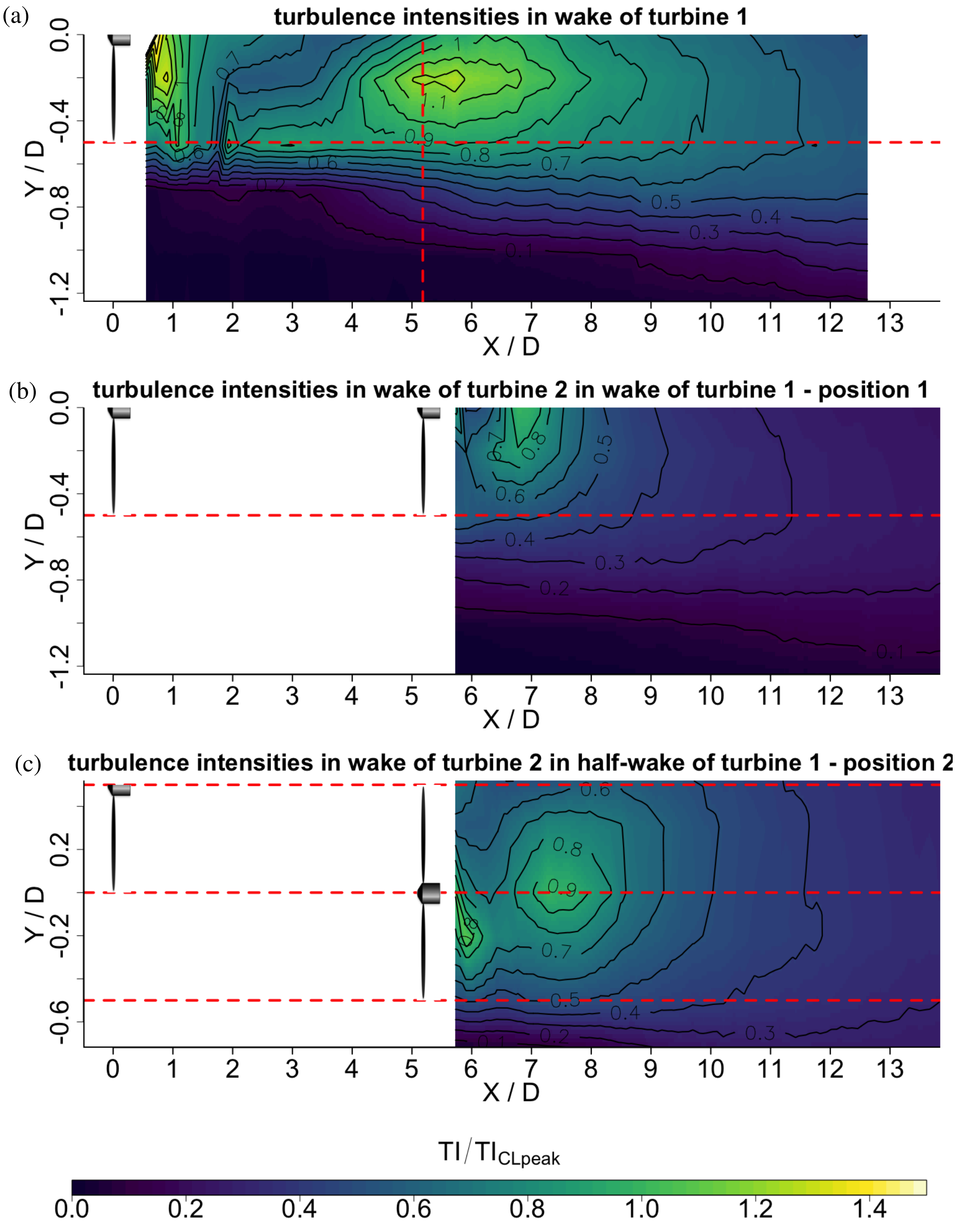

Figure 5.4.: Evolution of the to the maximum turbulence intensity normalized turbulence intensity downstream turbine 1 (a), turbine 2 mid (b) and turbine 2 side (c).

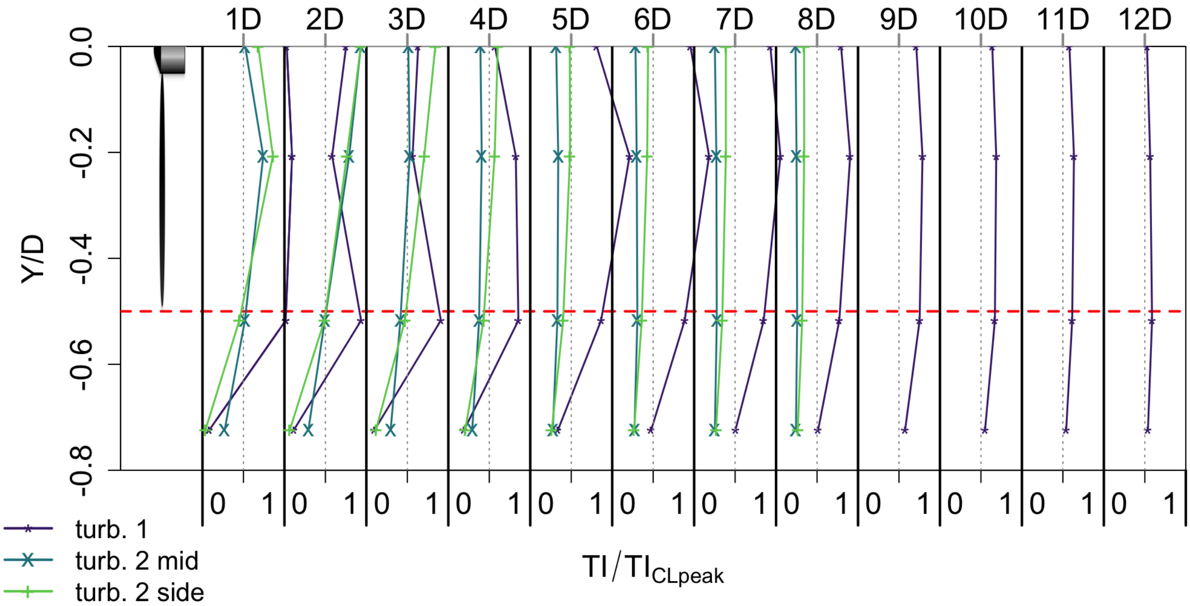

Figure 5.5.: Comparison of the to the turbulence intensity peak on the centerline normalized turbulence intensity downstream turbine 1 (purple *), turbine 2 mid (turquoise x) and turbine 2 side (green +). The Y-coordinate is with respect to the turbine center.

Closer to the turbine, different span-wise positions show a strong variation of the turbulence intensity evolution. An enhanced turbulence intensity at the rotor blade tip is for example visible up to approximately $4D$ in the near wake. Downstream turbine 2, a profile evolves already around $X/D \approx 2$. The influence of the different inflow situations is seen in the variation of the profile development. Downstream turbine 2 side, the profile shows close to the rotor a stronger curvature, as at the $Y/D = -0.72$ position, the sensor is exposed to the still laminar inflow. As the wake expands, the turbulence intensity increases downstream.

The centerline evolution of the normalized turbulence intensity shown in figure 5.6 enables a qualitative comparison with results from the preceding chapter and a quantitative comparison of the three scenarios investigated in this chapter. The curves develop similarly to the curves presented in the preceding chapter, and the four previously introduced wake regions can be identified. A drop under the lee of the nacelle characterizes the near wake and is followed by the transition region where the turbulence builds up. Finally, after the local maximum, the decay region starts. As the wake evolution is sensitive to the inflow turbulence in this setup, the regions are not fixed to certain downstream positions, but vary. For turbine 1, the measured maximum is located at $X/D = 6.24$, for turbine 2 mid at $X/D = 1.59$ and for turbine 2 side at $X/D = 2.10$. The precise positions can be found in table E.2 in appendix E. At the respective last measurement position, the normalized turbulence intensity has decayed to $TI_{end} \approx 0.50 \cdot TI_{CLpeak}$ downstream turbine 1, $TI_{end} \approx 0.22 \cdot TI_{CLpeak}$ downstream turbine 2

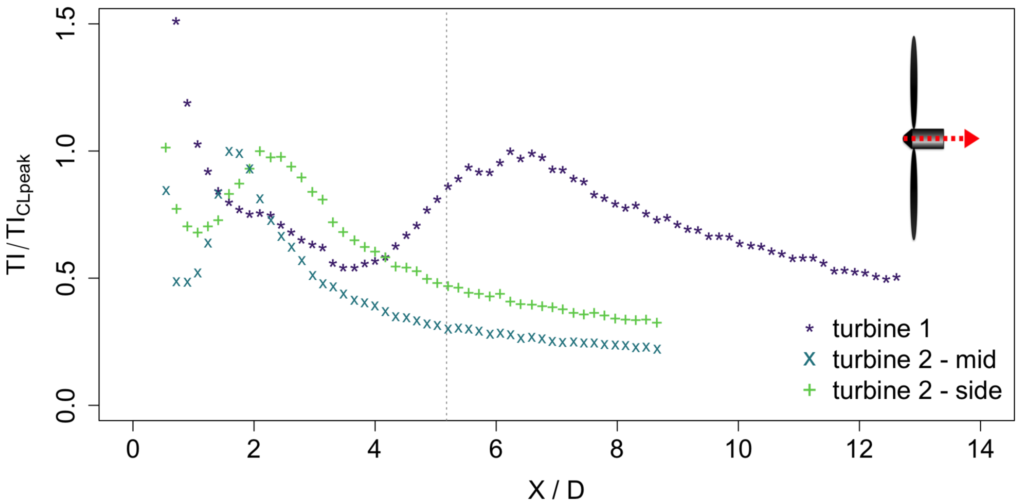

Figure 5.6.: Centerline evolution of the to the peak turbulence intensity normalized turbulence intensity downstream turbine 1 (purple *), turbine 2 mid (turquoise x) and turbine 2 side (green +). The Y-coordinate is with respect to the turbine center.

mid and $TI_{end} \approx 0.33 \cdot TI_{CLpeak}$ downstream turbine 2 side. To further investigate the decay of the normalized turbulence intensity, the centerline evolution of the normalized turbulence intensity is plotted with logarithmic axes in figure 5.7, and the decay region is fitted according to $TI/TI_{CLpeak} \propto \alpha \cdot (X/D)^{\beta}$. Again, the fitting range is split into two parts, as indicated by the dashed vertical lines. The fit regions and the exponent β can be found in table 5.2. $\beta_1 < \beta_2$ for all scenarios indicates that in the beginning, the turbulence decays faster. While β_1 and β_2 are quite similar for turbine 1, β_2 decreases by approximately 25% downstream turbine 2. This is equivalent to a less fast decay downstream turbine 2.
As already discussed in chapter 4, this change of the turbulence decay takes up results obtained downstream regular grids where the decay process of turbulence also changes [Hinze (1975)].

To relate the change of the decay exponent to the variance, the evolution of σ^2 is plotted in figure 5.8. The downstream positions where the decay exponent changes from β_1 to β_2 are marked with dashed lines for the respective wake. Close to the rotor, the variance decreases in

Table 5.2.: Investigation of turbulence intensity decay: fit parameter β with fit error χ^2 for fit regions 1 and 2 downstream the disc and the model turbine for all inflow conditions.

	β_1	$\chi^2(\beta_1)$	X/D	β_2	$\chi^2(\beta_2)$	X/D
turbine 1	-1.16	0.08	6.59 - 7.79	-1.03	0.02	7.97 - 12.62
turbine 2 mid	-1.27	0.04	1.76 - 3.14	-0.76	0.02	3.14 - 8.66
turbine 2 side	-1.04	0.05	2.45 - 4.00	-0.79	0.01	4.00 - 8.66

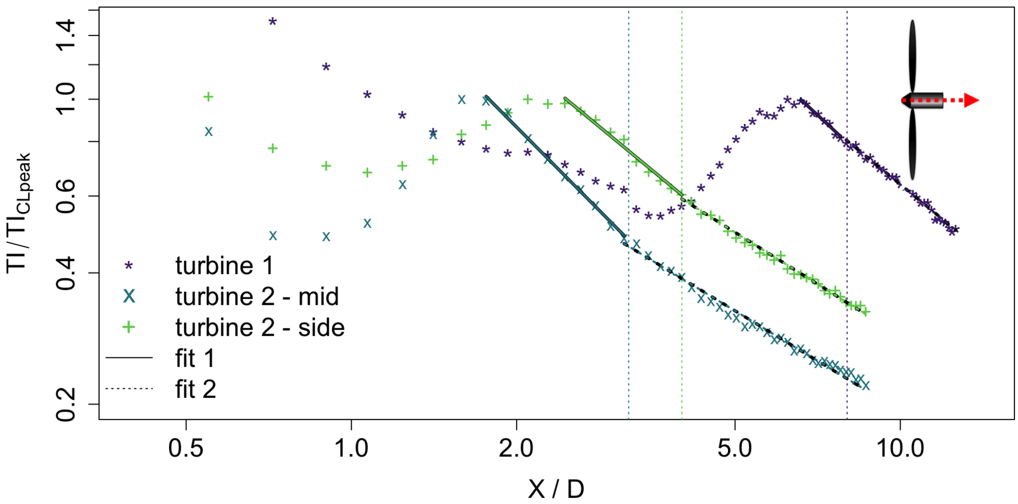

Figure 5.7.: Centerline evolution of the to the peak turbulence intensity normalized turbulence intensity downstream turbine 1 (purple *), turbine 2 mid (turquoise x) and turbine 2 side (green +) with fits within the decay region. The Y-coordinate is with respect to the turbine center.

all cases. After an increase, the variance starts to slowly decay after a local maximum. While downstream turbine 1, this decay starts around $X/D \approx 8.31$, it already starts at $X/D \approx 2.10$ in case of turbine 2 mid and $X/D \approx 3.14$ in case of turbine 2 side. Therefore, it can be concluded that the change of the decay exponent happens when the variance decreases.

Overall, the turbulence intensity evolves as expected from the experiments evaluated in the preceding chapter and also (qualitatively) as compared to e.g. Kermani *et al.* (2013). The positive influence of the inflow turbulence on the accelerated wake recovery could be shown. Here, the recovery does not only include the mean velocity upswing but also the turbulence intensity decay. The accelerated turbulence decay in case of turbulent inflow downstream turbine 2 was assigned to the extended fit region of β_1 downstream turbine 2 as compared to turbine 1: As $\beta_1 > \beta_2$, the decay of the turbulence intensity is thus accelerated. In combination with the above-mentioned downstream positions of TI_{peak}, the approximate downstream borders of the four wake regions can be identified for the three scenarios. The precise position of local

Table 5.3.: Identification of wake regions

	X/D near wake	X/D transition region	X/D decay region	X/D far wake
turbine 1	0.55 - 4.00	4.00 - 6.24	6.59 - 7.97	7.97 - 12.52
turbine 2 mid	0.55 - 0.90	0.90 - 1.76	1.76 - 3.14	3.14-8.66
turbine 2 side	0.55 - 1.07	1.07 - 2.45	2.45 - 4.00	4.00-8.66

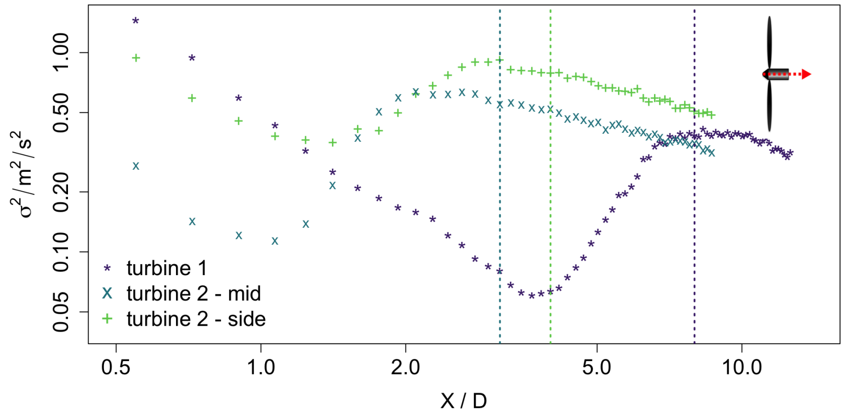

Figure 5.8.: Centerline evolution of the variance σ^2 downstream turbine 1 (purple *), turbine 2 mid (turquoise x) and turbine 2 side (green +). The Y-coordinate is with respect to the turbine center.

extrema and changes in the evolution can be found for different quantities in table 5.3. Thus, the existence of the before identified wake regions is confirmed.

5.1.3. Downstream development of characteristic length scales

Integral length

The development of the integral length downstream the turbine is plotted as contour plot for the three scenarios in figure 5.9. As the flow at the positions outside the rotor ($Y/D = -0.72, -1.03, 1.24$) in (a) is still laminar up to $X/D \approx 2.5$, the integral length is masked in this area. Downstream the rotor, an increase of the integral length is present for all scenarios. The highest values are found outside the wake close to the end of the scanned area. Turbine 2 is exposed to the wake of turbine 1 and thus to integral length scales around $5\,\text{cm} \lesssim L \lesssim 10\,\text{cm}$. It can be seen from the results downstream turbine 2, that the rotor first reduces the scale of the largest structures as compared to the inflow, and then the structures increase.

This behavior is also illustrated by the profiles plotted in figure 5.10.

The centerline evolution of the integral length scale in figure 5.11 also allows for a direct comparison. In the beginning, the integral length increases but appears to saturate for all inflow conditions towards $L \approx 12\,\text{cm} \simeq 0.2D$. The turbulent inflow accelerates the increase of the integral length so that the saturation region is reached closer to the rotor.

Compared to the results from the preceding chapter, similar values of the integral length were found. Considering laminar and regular grid inflow, the centerline evolution is also similar. In Aubrun *et al.* (2013), at the centerline at $X/D = 3$, an integral length of $L_{A,LT} \approx 0.1D$

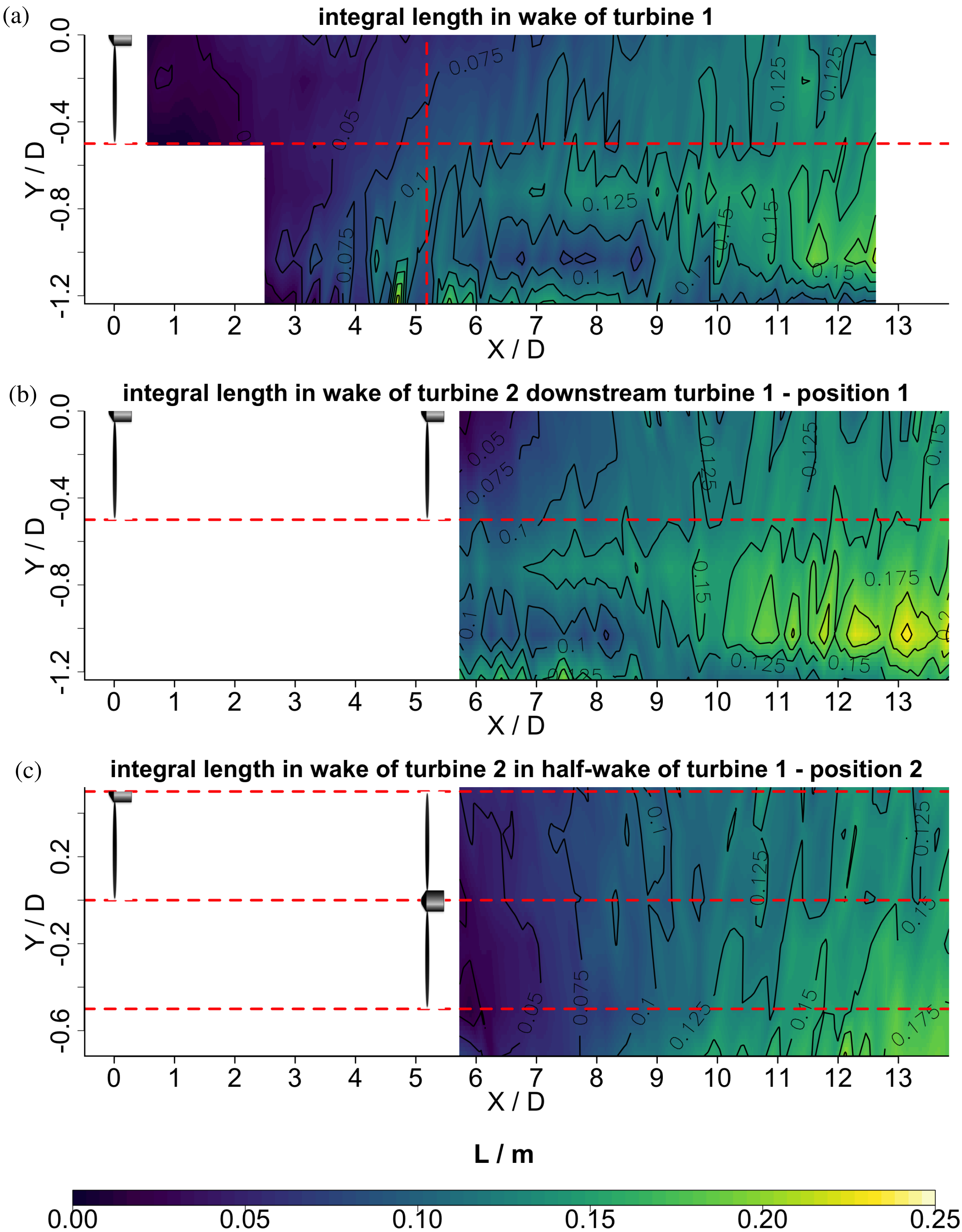

Figure 5.9.: Evolution of the integral length downstream turbine 1 (a), turbine 2 mid (b) and turbine 2 side (c).

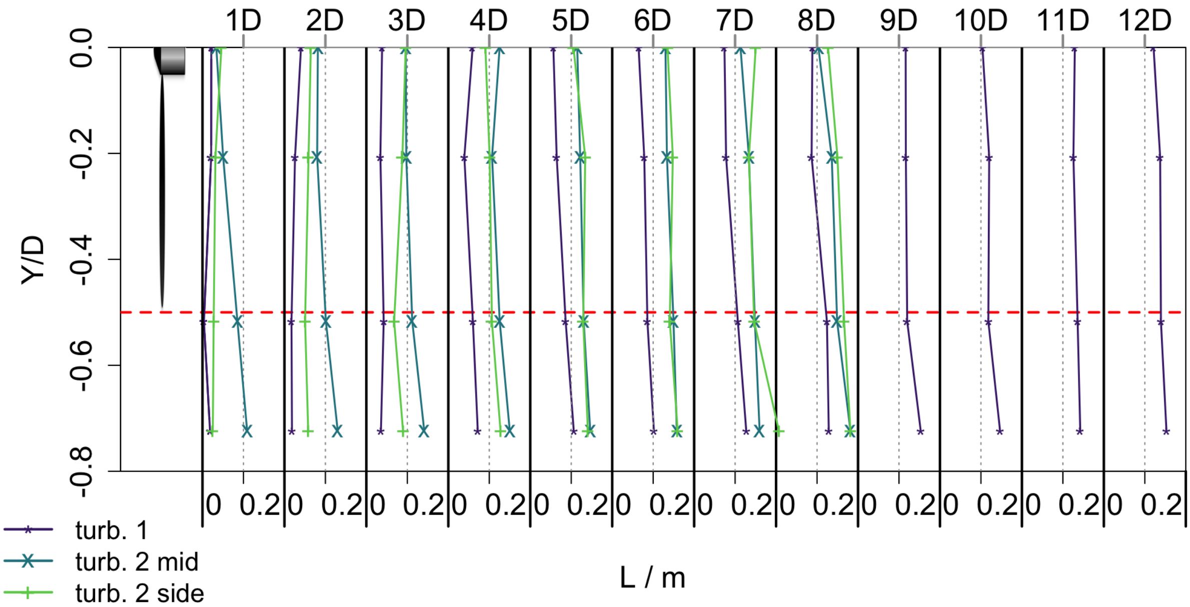

Figure 5.10.: Profile comparison of the integral length downstream turbine 1 (purple *), turbine 2 mid (turquoise x) and turbine 2 side (green +). The Y-coordinate is with respect to the turbine center.

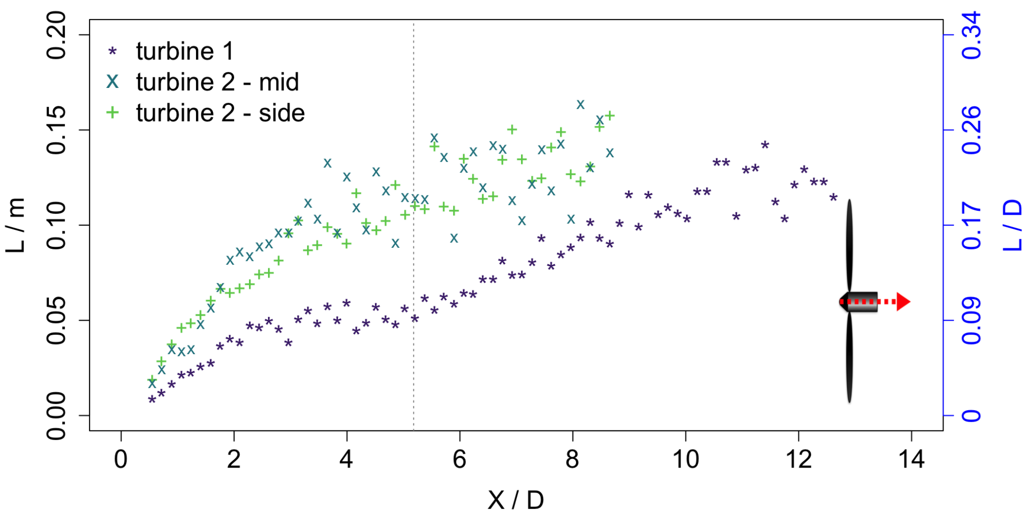

Figure 5.11.: Centerline evolution of the integral length downstream turbine 1 (purple *), turbine 2 mid (turquoise x) and turbine 2 side (green +). The Y-coordinate is with respect to the turbine center.

was found in case of lowly turbulent inflow, and $L_{A,HT} \approx 0.72D$ in case of highly turbulent inflow. They concluded that the integral length is determined by large flow structures from the inflow. The results from the previous chapter allow for this interpretation, too. However, the results obtained in this chapter also allow for a different interpretation, i.e. that the integral length is higher at the same downstream position in highly turbulent inflow because the fixed measurement region is assigned to a different wake region. This interpretation has consequences for wake research as the wake region may not be fixed during different experiments, and thus, results obtained from different turbulence regions within the wake are compared. Therefore, knowledge of the region downstream the WGT is of importance.

Taylor length

The evolution of the Taylor length is visualized as contour plot in figure 5.12 for the three scenarios in the wake region. Very high Taylor length values that occur naturally in the laminar flow are masked. Downstream the turbine, the Taylor length increases from $\lambda_T \approx 3-4\,\text{mm}$ under the nacelle's lee to $\lambda_T \approx 10\,\text{mm}$ at the end of the scanned plane. As the wake expands, the Taylor length is calculated for more span-wise positions. The highest values are found in the shear layer of the wake at the farthest measured downstream positions. Downstream turbine 2 side, the evolution is asymmetric due to the asymmetric inflow conditions.

The profiles in figure 5.13 show how the Taylor length evolves differently downstream turbine 1 and 2, and how the profiles of turbine 2 mid and side almost collapse downstream at $X/D \approx 8$ despite the different inflows at this rotor area.

A direct comparison of the evolution of the Taylor length at centerline for the three scenarios is given in figure 5.14. Downstream turbine 1, the Taylor length evolves similarly to the previous experiments, overall increasing but with a decrease between $4.34D - 6.41D$. While this development is also seen in case of turbine 2 mid, but closer to the rotor, the Taylor length only increases downstream turbine 2 side. Far downstream, the Taylor length is $\lambda_T \approx 9\,\text{mm}$.
Overall, compared to the results in the preceding chapter (cf. figure 4.14(b)), the evolution is similar in case of turbine 1 and turbine 2 mid, although the Taylor length is about 50% higher in these scenarios.

Integral length over Taylor length and Taylor Reynolds number

The centerline evolution of L/λ_T is plotted in figure 5.15 for the three scenarios. Downstream turbine 1, L/λ_T is constantly $L/\lambda_T \approx 5$ up to $X/D \approx 4$ in the near wake. Then, L/λ_T increases in the transition and turbulence decay region and saturates to $L/\lambda_T \approx 14$ at $X/D \approx 8$ in the far wake. Downstream turbine 2, the first region with constant L/λ_T is not found, but L/λ_T increases to

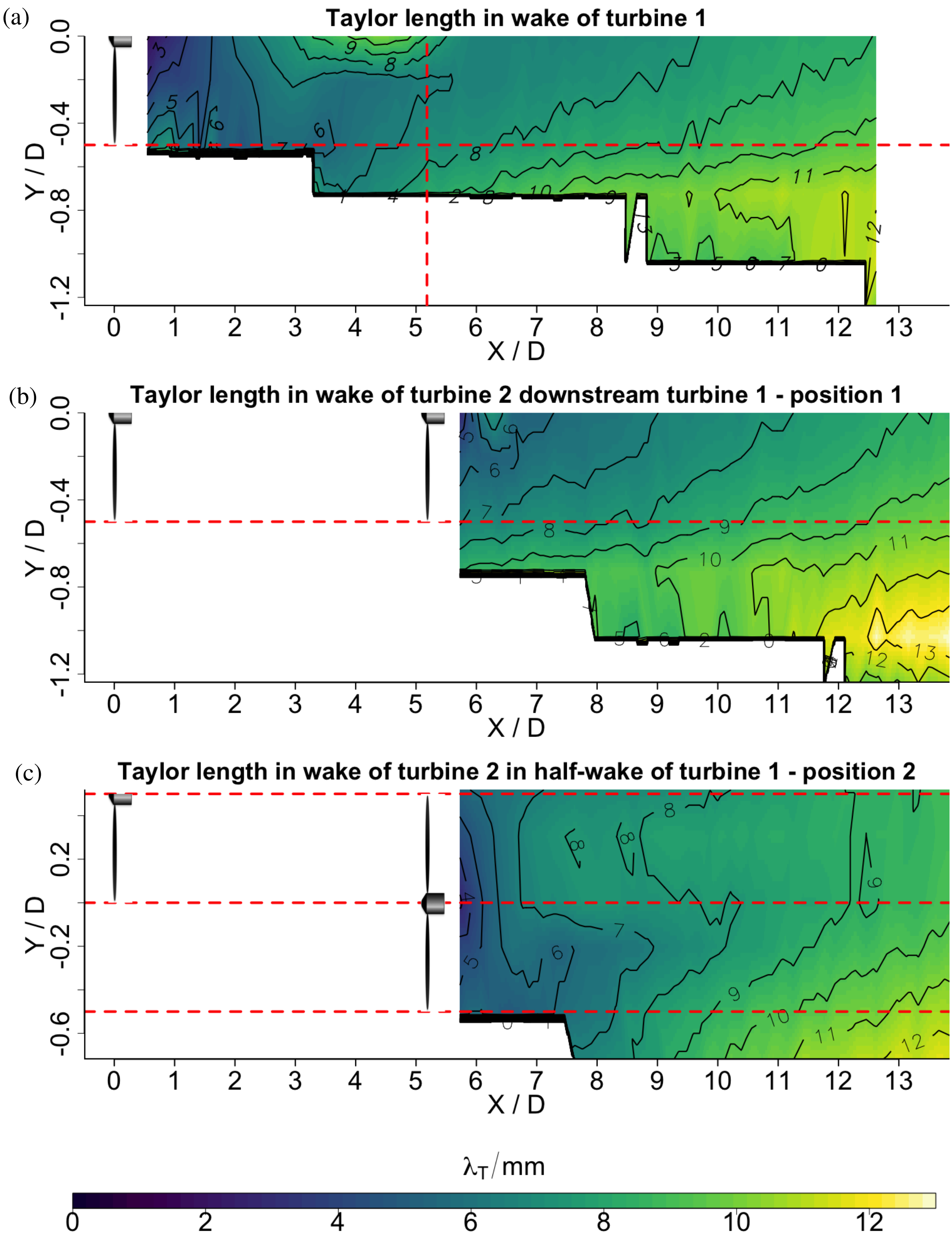

Figure 5.12.: Evolution of the taylor length downstream turbine 1 (a), turbine 2 mid (b) and turbine 2 side (c). Positions that are still influenced strongly by the ambient flow and do thus have extremely large Taylor length scales are masked to emphasize the influence of the model on the flow.

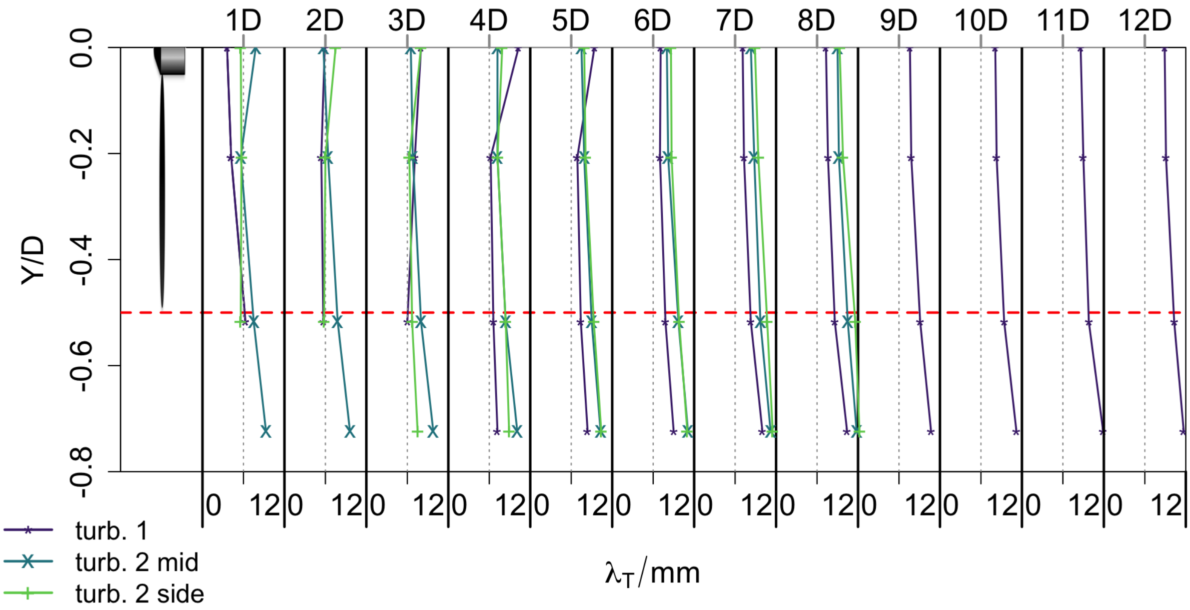

Figure 5.13.: Comparison of profiles of the Taylor length downstream turbine 1 (purple *), turbine 2 mid (turquoise x) and turbine 2 side (green +). Positions that are still influenced strongly by the ambient flow and do thus have extremely large Taylor length scales are masked to emphasize the influence of the model on the flow. The Y-coordinate is with respect to the turbine center.

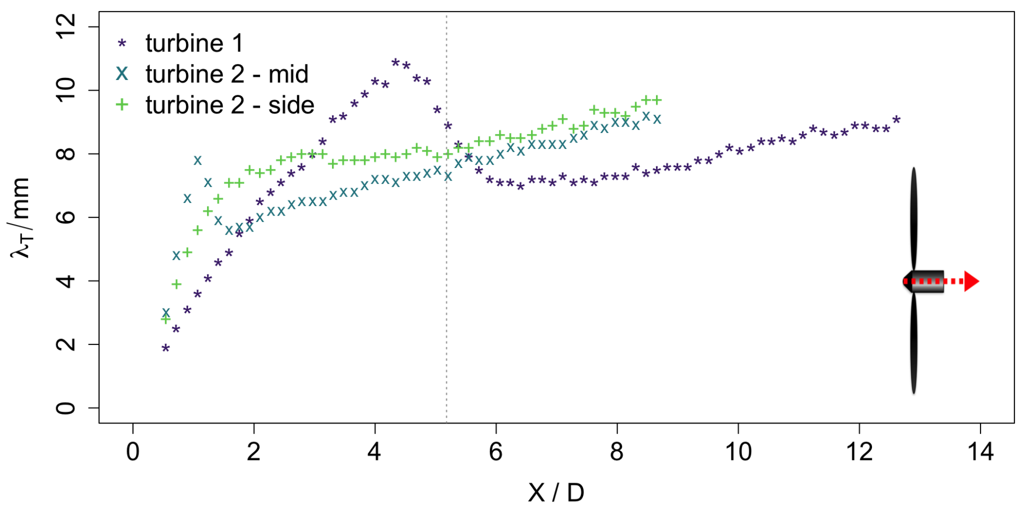

Figure 5.14.: Centerline evolution of the Taylor length downstream turbine 1 (purple *), turbine 2 mid (turquoise x) and turbine 2 side (green +). The Y-coordinate is with respect to the turbine center.

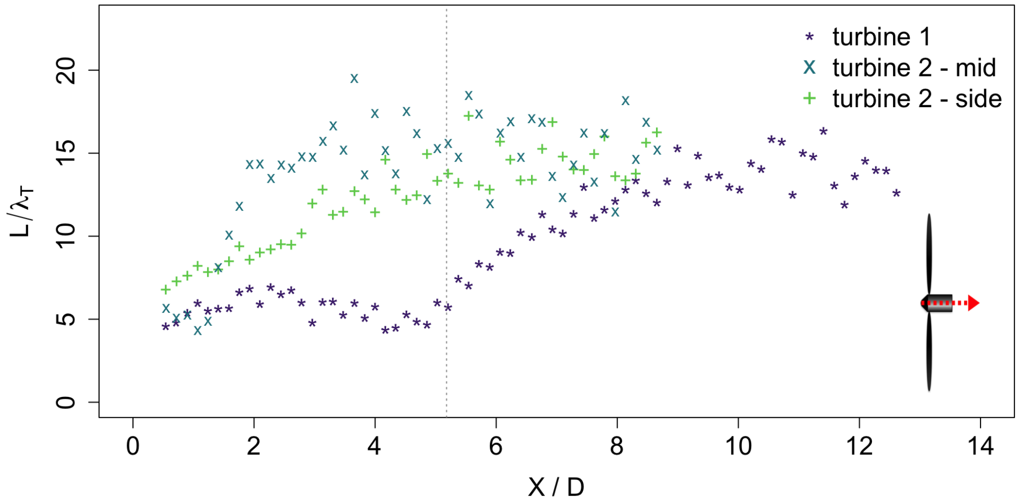

Figure 5.15.: Centerline evolution of L/λ_T downstream turbine 1 (purple *), turbine 2 mid (turquoise x) and turbine 2 side (green +). The Y-coordinate is with respect to the turbine center.

$L/\lambda_T \approx 15$ at $X/D \approx 4$ and saturates from there. The increase indicates that turbulence expands and evolves as large flow structures are brought into the wake as described briefly in chapter 4. The saturation indicates that the scales within the turbulence range are preserved in the far wake in an extended area even though the turbulence decays. The evolution of L/λ_T becomes independent of X/D, as indicated in the previous chapter. A dependence on the inflow velocity and thus the global Reynolds number is not visible.

In figure 5.16, the centerline evolution of the Taylor Reynolds number Re_λ is plotted. For all scenarios, Re_λ increases first and then saturates. While for turbine 1 and turbine 2 mid, the curves collapse to $Re_\lambda \approx 320$ at $X/D \approx 8$ and $X/D \approx 2$, respectively, downstream turbine 2 side, $Re_\lambda \approx 450$ from $X/D \approx 4$. These values indicate fully developed turbulent flows. The results are in accordance with the results from the preceding chapter where Re_λ also increased in a region and was constant with similar values for Re_λ further downstream. The wake regions can be distinguished in a similar manner as in the preceding chapter, although the transition region and the turbulence decay region melt together between the clearly identifiable near and far wake. In the far wake, $L/\lambda_T \approx const.$ and $Re_\lambda \approx const.$ This is again an indication for the validity of the Richardson-Kolmogorov phenomenology in that area. However, in the region where both quantities change, the conditions are not fulfilled, and this will be object to further study outside of this work. In addition, it can be noted that both for active grid generated inflow and in the sheared inflow of turbine 2, the highest Taylor Reynolds numbers are reached, and thus, the inflow turbulence does affect the wake turbulence in the far wake.

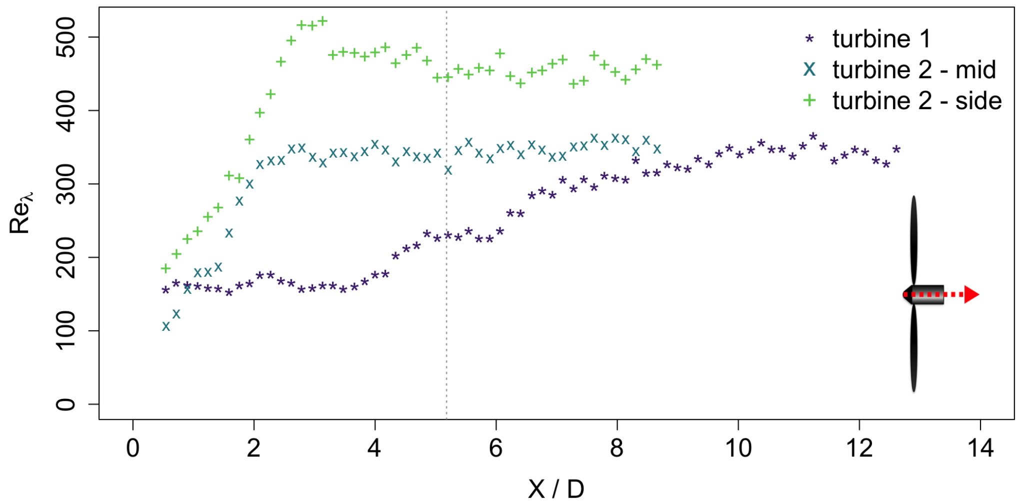

Figure 5.16.: Centerline evolution of the Taylor Reynolds number downstream turbine 1 (purple *), turbine 2 mid (turquoise x) and turbine 2 side (green +). The Y-coordinate is with respect to the turbine center.

5.2. Investigation of the wake with extended stochastic methods

In the following, the analysis of the wake for the three scenarios is completed with a more extensive investigation of the turbulence. This is achieved by investigating energy spectra qualitatively and additionally quantitatively by examining the decay exponent exp that indicates the decay in the inertial sub-range, $E(f) \propto f^{exp}$. A brief comment on the evolution of C_ε follows. Further, the probability density functions of temporal velocity increments and the evolution of the shape parameter downstream and over the time scale τ is discussed.

5.2.1. Energy spectra

In the following, the downstream evolution of the pre-multiplied energy spectra $f \cdot E(f)$ is plotted over the dimensionless frequency $f \cdot D/u_0$ for turbine 1, 2 mid and 2 side, respectively. The span-wise positions $Y/D = 0, -0.21, -0.51, -0.72$ are presented in sub-figures (a)-(d). The downstream position is indicated by the color with a lighter color indicating a position further downstream. A $E(f) \propto f^{-5/3}$ line (blue) is plotted for comparison.

First, the evolution of pre-multiplied energy spectra downstream turbine 1 in figure 5.17 is discussed. Turbine 1 is exposed to laminar inflow. The pre-multiplied energy spectra of the inner wake positions $Y/D = 0$ and $Y/D = -0.21$ in (a) and (b) evolve similarly: In the vicinity of the nacelle, they show the highest amount of energy in dimensionless frequencies

$1 \lesssim f \cdot D/u_0 \lesssim 300$. A peak at $f \cdot D/u_0 \approx 1.75$ indicates the root vortex, and its frequency $f \approx 22.5\,\mathrm{Hz}$ equals the rotational frequency of the turbine. With increasing downstream position up to $X/D \approx 4$, the energy in this range drops. Afterwards, the energy in the whole frequency range increase and the spectra collapse in the far wake from $X/D \approx 8.31$. This development can also be seen in the downstream evolution of the variance σ^2 in figure 5.8, as $\sigma^2 = \int_0^\infty E(f)\mathrm{d}f$. In the far wake, the spectra appear to follow a $-5/3$-law in the inertial sub-range. At the outer positions $Y/D = -0.51$ and $Y/D = -0.72$, the tip vortices are captured, as can be seen by the peaks in the spectrum at the turbine's rotational frequency $f \approx 22.5\,\mathrm{Hz}$, or $f \cdot D/u_0 \approx 1.75$, and its harmonics. In the laminar inflow, they are persistent up to $X/D \approx 3$. With increasing downstream position, the energy increases first for $Y/D = -0.51$, and from $X/D \approx 6.59$, the spectra start to collapse. A $-5/3$- decay in the inertial sub-range is present from here. At $Y/D = -0.72$, the spectra show close to the rotor the signs of laminar inflow with little energy distributed over frequencies. They are superimposed with the tip vortex signature. Downstream, the wake expands and the energy is enhanced for all frequencies while the tip vortex signature vanishes. From $X/D \approx 6.59$, the spectra collapse, and the inertial sub-range appears to follow the $-5/3$-decay.

Second, in figure 5.18, the evolution of pre-multiplied energy spectra downstream turbine 2 mid is shown. Additionally, the reference spectra of the inflow at rotor plane and at the last measurement position in the wake at centerline, i.e. spectra downstream turbine 1 at $X/D = 5.21$ and $X/D = 12.62$, are indicated by red dashed lines. At $Y/D = 0$ in (a), the energy first drops with increasing downstream position, then increases again, and from $X/D \approx 4$, the spectra collapse. This evolution is also consistent with the downstream evolution of the centerline variance in figure 5.8. At $Y/D = -0.21$ in (b), the energy increases up to $X/D \approx 3.14$ and then the spectra collapse. At $Y/D = -0.51$ (c) and $Y/D = -0.72$ (d), the energy decreases with increasing downstream position for the inertial sub-range that is located at dimensionless frequencies $2 \lesssim f \cdot D/u_0 \lesssim 30$. The spectra collapse and appear to follow a $-5/3$-decay in the inertial sub-range. Neither the tip nor the root vortex is captured, as the turbulent inflow causes a fast breakdown. Compared to the inflow at rotor plane, the energy of all spectra is enhanced over the whole frequency range, and compared to the evolved inflow, the energy is similar or slightly enhanced over the whole frequency range.

Third, the evolution of pre-multiplied energy spectra is investigated downstream turbine 2 side in figure 5.19. In red dashed lines, plotted are the spectra of the inflow at rotor plane and last measurement position at the center of turbine 2 side[ii]. Again, at $Y/D = 0$, plot (a), and $Y/D = -0.21$, plot (b), the energy drops first in the high frequency range. Afterwards, the energy increases in this frequency range and the spectra collapse from $X/D \approx 4$. For $Y/D = 0$, the result is consistent with the evolution of σ^2 in figure 5.8. Compared to the inflow at rotor plane,

[ii] i.e. $Y/D = -0.51$ for turbine 1

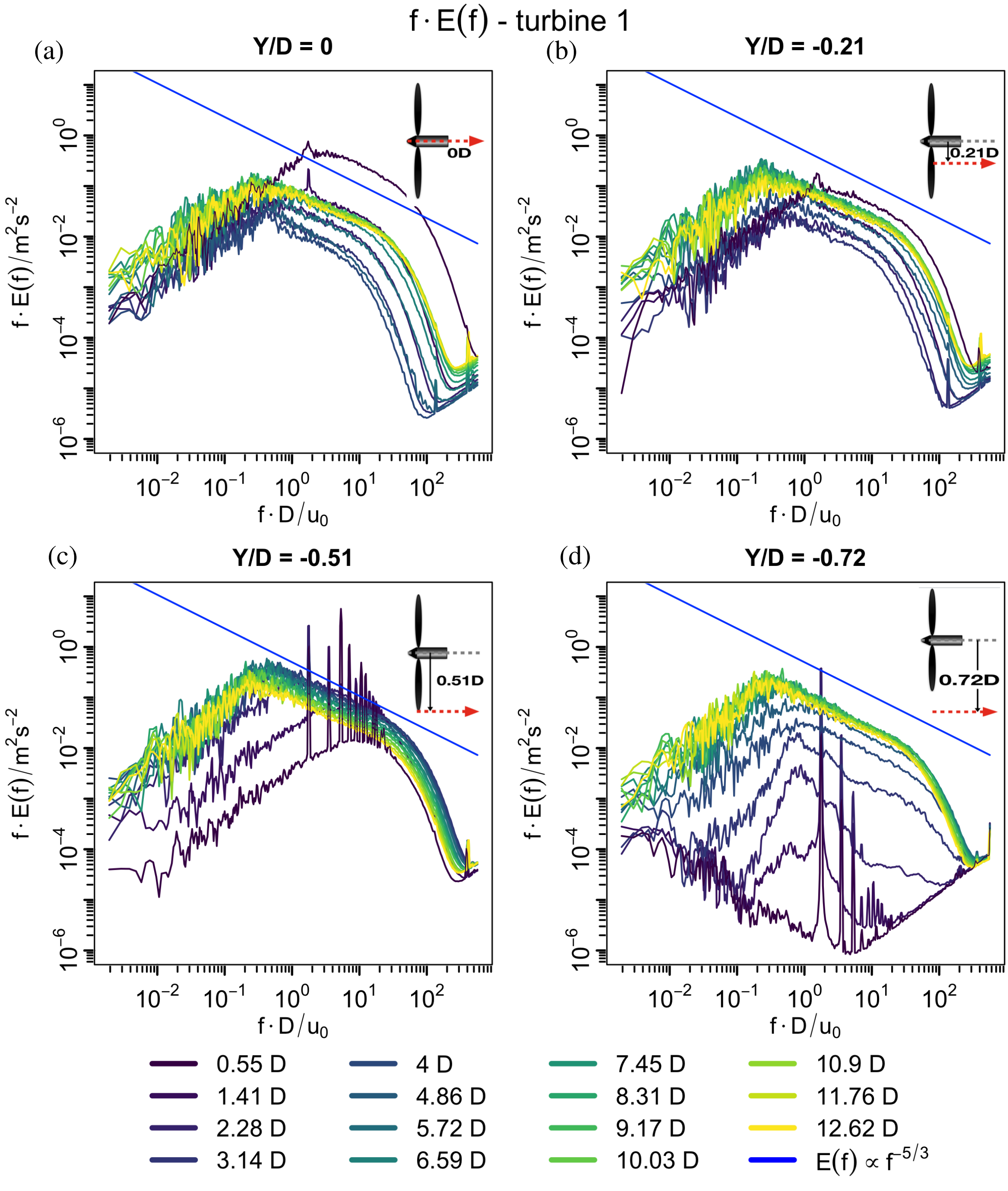

Figure 5.17.: Evolution of the pre-multiplied energy spectra downstream turbine 1 at $Y/D = 0$ (a), $Y/D = -0.21$ (b), $Y/D = -0.51$ (c), and $Y/D = -0.72$ (d).

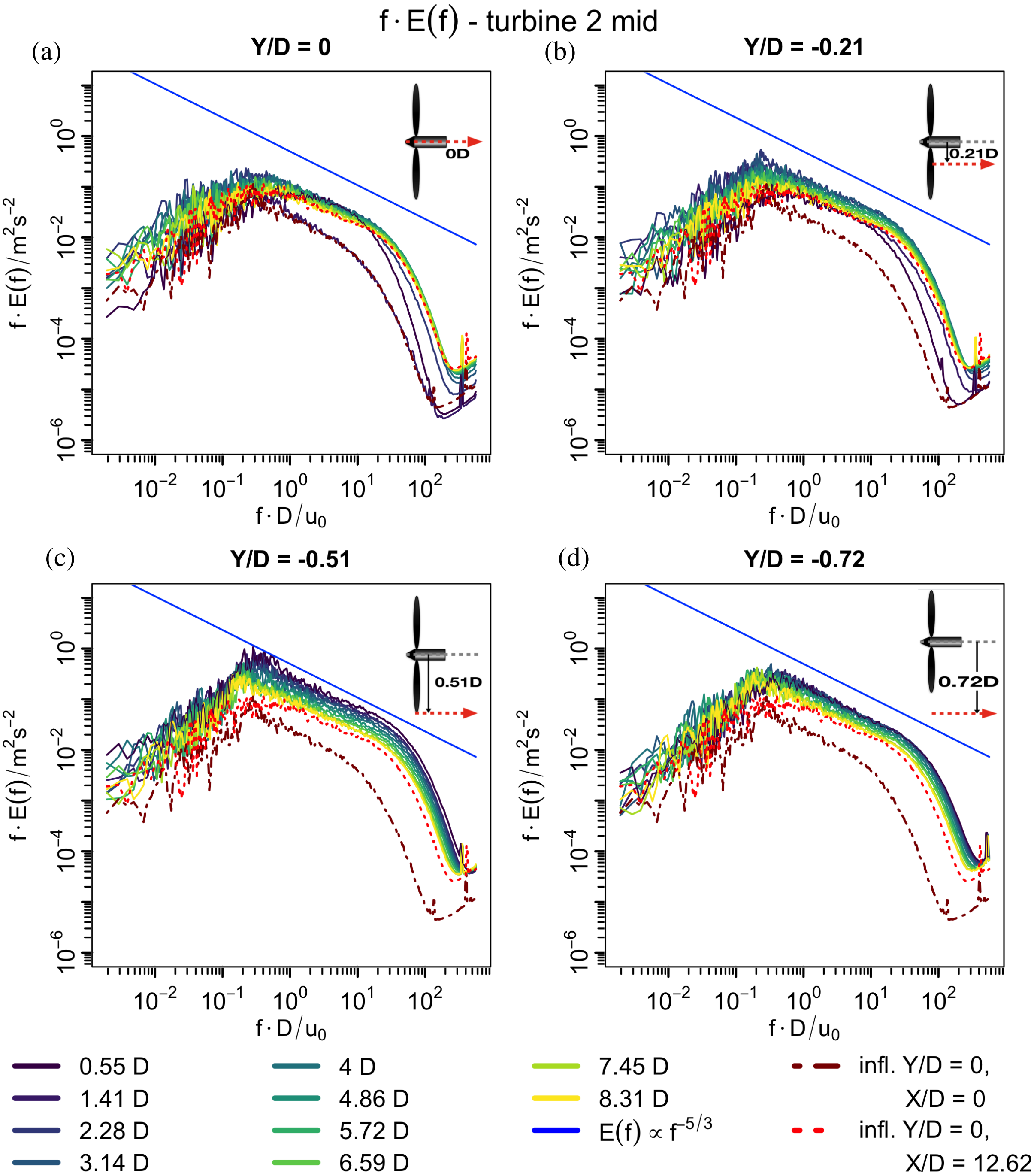

Figure 5.18.: Evolution of the pre-multiplied energy spectra downstream turbine 2 mid at $Y/D = 0$ (a), $Y/D = -0.21$ (b), $Y/D = -0.51$ (c), and $Y/D = -0.72$ (d). In addition, the energy spectrum of the inflow, i.e. the wake of turbine 1, is plotted at $X/D = 0$ (dark red dashed) and $X/D = 7.41$ (red dashed) at the center of turbine 2.

the energy is decreased for pre-multiplied frequencies $f \cdot D/u_0 \gtrsim 0.2$. Compared to the inflow at last measurement position, the spectra are similar in the far wake. At $Y/D = -0.51$, plot (c), the tip vortices are captured close to the rotor, but they decay quickly. At frequencies $f \cdot D/u_0 \gtrsim 1$, the energy is in proximity to the rotor higher than for downstream positions and compared to the inflow. In contrast, the energy is lower at frequencies $f \cdot D/u_0 \lesssim 1$. Moving downstream, the energy in frequencies $f \cdot D/u_0 \gtrsim 1$ decreases while it increases for frequencies $f \cdot D/u_0 \lesssim 1$. Compared to the inflow at rotor plane, the energy is decreased for frequencies $f \cdot D/u_0 \gtrsim 0.2$, but similar for lower frequencies. At $Y/D = -0.72$, plot (d), the influence of the laminar inflow is visible close to the rotor plane similarly to turbine 1 (cf. figure 5.17 (d)). The energy in the spectrum is low, but a superposition with the tip vortices is present. Moving downstream, the energy increases across all frequencies when the wake expands. The spectra collapse from $X/D \approx 4$ and appear to follow a $-5/3$ law in the inertial sub-range. For dimensionless frequencies $f \cdot D/u_0 \gtrsim 0.2$, the energy across frequencies is reduced compared to the inflow at rotor plane, but similar to the inflow at the last measurement position. For pre-multiplied frequencies $f \cdot D/u_0 \lesssim 0.2$, the spectra evolve similarly from $X/D \approx 4$ downstream.

In summary, the results obtained from these measurements are in accordance with the evolution of the turbulence intensity (cf. figure 5.6) that illustrates how the turbulence decay starts closer to the turbine in case of turbulent inflow. Depending on the position of turbine 2, the turbine is seen to either enhance (turbine 2 mid) or reduce (turbine 2 side) the energy content in the inertial sub-range compared to the inflow at rotor position for all span-wise positions. Still, the energy spectra downstream turbine 2 at $X/D = 8.31$ collapse in the central wake region, i.e. the sensor positions $Y/D = 0$ and $Y/D = -0.21$, with the evolved inflow spectrum from turbine 1 at $X/D = 12.62$. Thus, also the spectra downstream turbine 2 mid and side collapse. This supports the argument that the *turbine* coins the flow and an influence of the inflow on the turbulence creation is not, or scarcely, present. The inflow solely determines how far downstream the evolution takes place.
Additionally, the results are similar to the results from the preceding chapter (cf. e.g. figure 4.17) regarding the downstream evolution of the energy spectra.

Downstream evolution of the decay exponent

To investigate the decay region of the spectra, figure 5.20 shows the downstream evolution of the decay exponent *exp* for the three scenarios at the centerline. The decay exponent was determined by fitting $E(f) \propto a \cdot f^{exp}$ to the inertial sub-range. In addition, a dashed line indicates $exp = -5/3$. Downstream turbine 1, *exp* first decreases from $exp \approx -5/3$ at $X/D = 0.55$ to $exp \approx -2.4$ at $X/D \approx 4$, than increases to $exp \approx -1.59$ in the transition region and remains

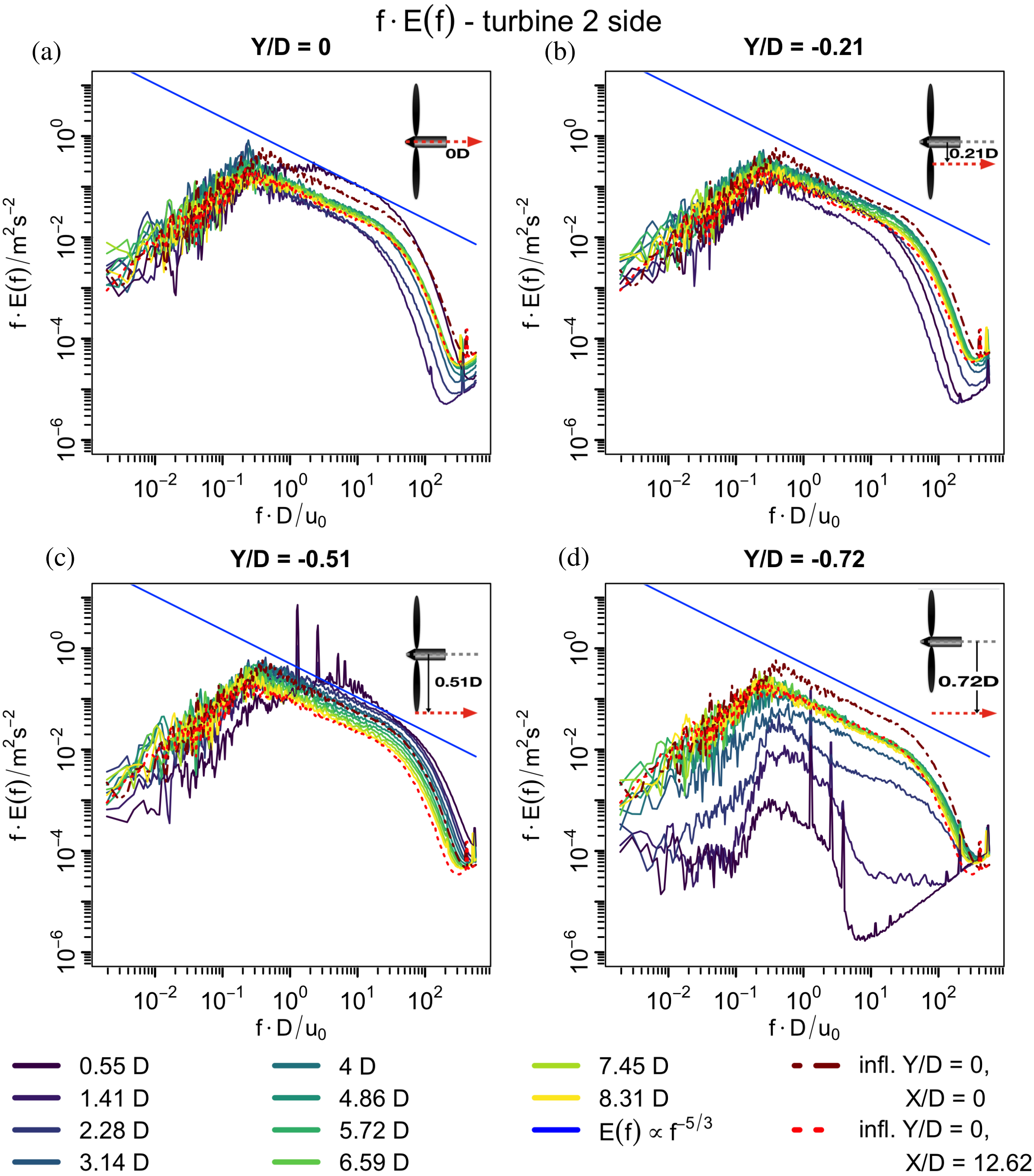

Figure 5.19.: Evolution of the pre-multiplied energy spectra downstream turbine 2 side at $Y/D = 0$ (a), $Y/D = -0.21$ (b), $Y/D = -0.51$ (c), and $Y/D = -0.72$ (d). In addition, the energy spectrum of the inflow, i.e. the wake of turbine 1, is plotted at $X/D = 0$ (dark red dashed) and $X/D = 7.41$ (red dashed) at the center of turbine 2.

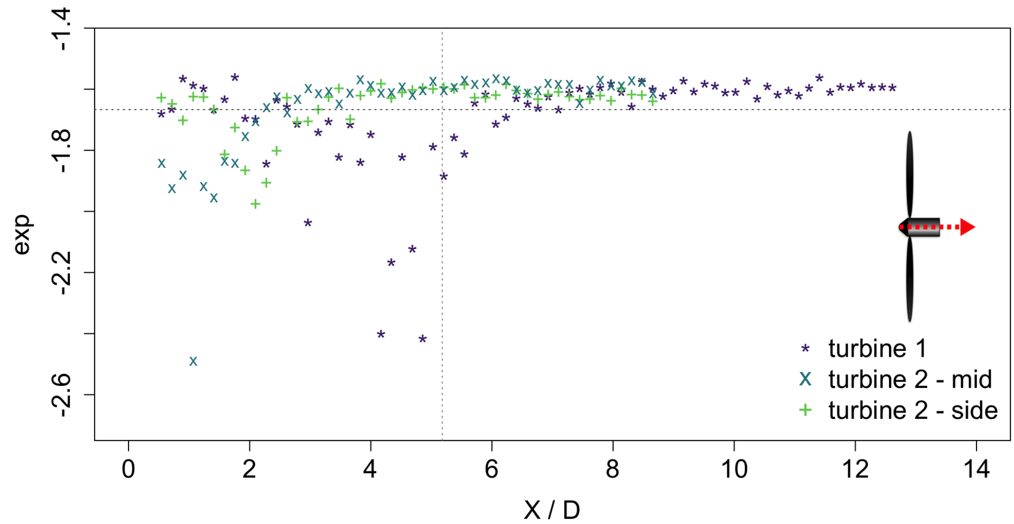

Figure 5.20.: Centerline evolution of the decay exponent downstream turbine 1 (purple *), turbine 2 mid (turquoise x) and turbine 2 side (green +).

constant from $X/D \approx 7$ in the turbulence decay region and the far wake. Similarly, *exp* evolves downstream turbine 2, with a drop, an increase and a saturation towards $exp \approx -1.59$ from $X/D \approx 3$.

Overall, the decay exponent of the energy spectrum in the inertial sub-range downstream the turbine collapses to $exp \approx -1.59$ for all scenarios. This value is very close to $-5/3$ and thus, the turbulence downstream the turbine exhibits features of homogeneous isotropic turbulence, which was already shown for different inflow conditions in the preceding chapter. Connecting the development to the evolution of the turbulence intensity reveals that the decay exponent varies approximately where the turbulence intensity builds in the transition region (see also table 5.1 in appendix E).

Brief comment on the turbulent kinetic energy dissipation

In the following, the behavior of C_ε over X/D and Re_λ is presented to draw conclusions about the dissipation of the turbulent kinetic energy. In figure 5.21, the evolution of C_ε is plotted over X/D downstream the centerline. Although the data points scatter, it can be seen that downstream turbine 1, $C_\varepsilon \approx 0.6$ is approximately constant in the near wake, and in the decay region and far wake but varies in the transition region. Downstream turbine 2 mid, a variation of C_ε within the transition region can also be seen, while $C_\varepsilon \approx 0.6$ in the decay region and the far wake. Downstream turbine 2 side, C_ε varies within the near wake, transition region, and decay region and is only constant in the far wake.

To relate C_ε and Re_λ, figure 5.22 shows C_ε plotted over Re_λ. In case of turbine 1, a dependency

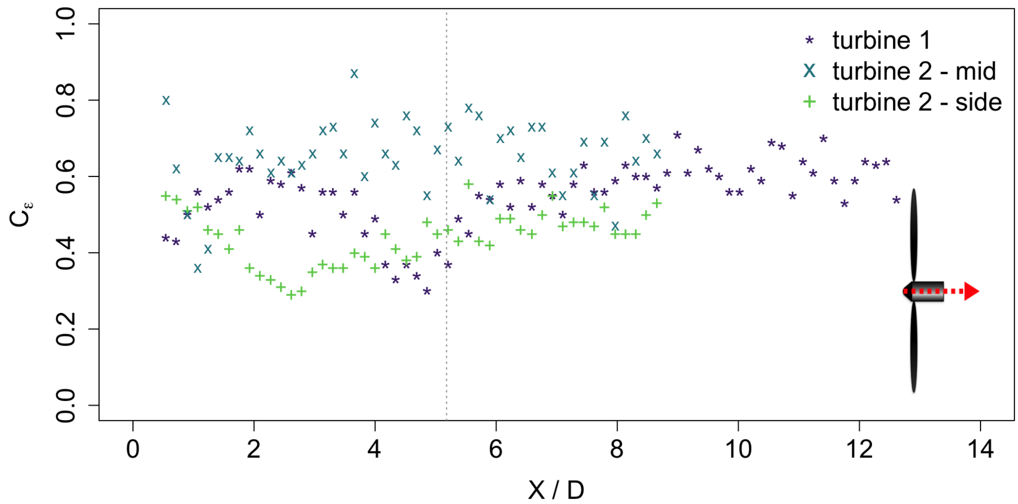

Figure 5.21.: Centerline evolution of C_ε downstream turbine 1 (purple *), turbine 2 mid (turquoise x) and turbine 2 side (green +).

of C_ε on Re_λ could be identified for $200 \leq Re_\lambda \leq 300$; the data points are assigned to downstream positions within the transition region. However, as the data points do scatter and $E(f) \not\propto f^{-5/3}$ within the transition region, the results have to be handled with care. In case of turbine 2 mid, a dependence of C_ε on Re_λ can not be identified. However, in case of turbine 2 side, a dependence of C_ε on Re_λ can be identified for $180 \leq Re_\lambda <\leq 500$. The corresponding downstream region is the near wake and transition region, where $E(f) \not\propto f^{-5/3}$ within the transition region. As the turbulence still evolves within this region, the results have to be handled carefully. Nevertheless, this analysis shows that the turbine creates turbulence that might - depending on the inflow turbulence - dissipate in some regions with a non-equilibrium law.

5.2.2. Increment PDFs and shape parameter

To expand the analysis of turbulence downstream the turbine for the three scenarios, another two-point analysis follows. First, the evolution of the temporal shape parameter λ^2 downstream the turbine is discussed for the three scenarios in figure 5.23 in interpolated contour plots. λ^2 is calculated on a time scale $\tau \simeq D$. In (a), the results for turbine 1 are presented. As turbine 1 is exposed to laminar inflow, no intermittency is present in the inflow [iii]. Downstream the rotor, $\lambda^2 \approx 0$ for most of the central wake except for a small area around $X/D \approx 4$ and $Y/D = -0.21$ where $\lambda^2 \approx 0.1$. Outside the rotor-swept area, the already mentioned intermittency ring is captured. Close to the rotor, it is found around $Y/D = -0.51$, then it disappears briefly due to the coarse spacing of the sensors, and as the wake expands, it is captured again by the next

[iii] The inflow turbulence intensity is $TI_{in} < 0.004$ and $\lambda^2(\tau \simeq D) \approx 0$.

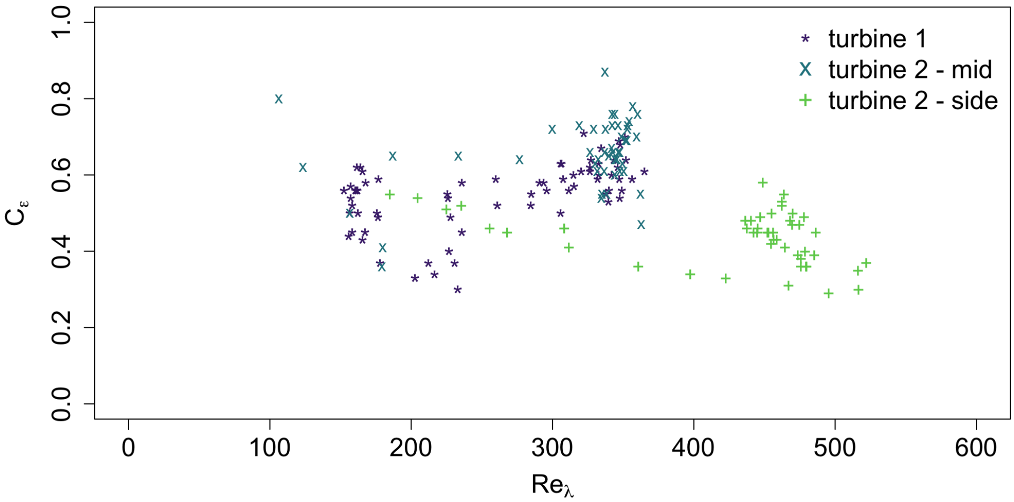

Figure 5.22.: Centerline evolution of C_ε over Re_λ downstream turbine 1 (purple *), turbine 2 mid (turquoise x) and turbine 2 side (green +).

probes. It can be seen, that it expands to have a diameter of over $2D$ around $X/D = 12.62$ in a region where the mean velocity and the turbulence intensity are only little influenced by the wake. Downstream turbine 2 mid (cf. figure 5.23(b)), the results are similar. The inflow, i.e. the wake of turbine 1, does not show strong intermittency where the turbine 2 mid is positioned, and downstream turbine 2 mid, the intermittency at the presented scale shows also little variation. The intermittency ring outside the rotor-swept area is captured again similarly. Turbine 2 side is hit by an asymmetric inflow situation also in terms of the intermittency: While one part of the rotor operates in the non-intermittent wake of turbine 1, the other part is exposed to the intermittency ring. Nevertheless, the wake downstream turbine 2 side does not show signs of intermittency. The intermittency ring downstream turbine 2 side is just captured at the side of the scanned area, before it disappears from the measurement area due to wake expansion.

For better comparison, the centerline evolution of the shape parameter calculated for time scales $\tau \simeq D$ is plotted in figure 5.24 for the three scenarios. Overall, the values of the shape parameter cover a comparatively small range of $-0.02 \lesssim \lambda^2 \lesssim 0.07$. Downstream turbine 1, λ^2 first increases from $\lambda^2 \approx 0$ in the near wake to $\lambda^2 = 0.067$ at $X/D = 5.21$ in the transition region and then decreases in the decay region to $\lambda^2 \approx 0$ around $X/D \approx 9$ from where on it remains constant in the far wake. Again, the region from where λ^2 decreases coincides with the peak turbulence intensity, and the defined wake regions are identifiable. Thus, similar results are expected for turbine 2, but in closer proximity to the rotor, and found.

In summary, it is shown that the turbine destroys intermittent structures in the inner wake region, as indicated already in the preceding chapter and by Bastine *et al.* (2015) and Singh *et al.* (2014). The decay process of turbulence that is also mirrored in the evolution of λ^2 is accelerated by turbulent or intermittent inflow. Additionally, the by Schottler *et al.* (2018)

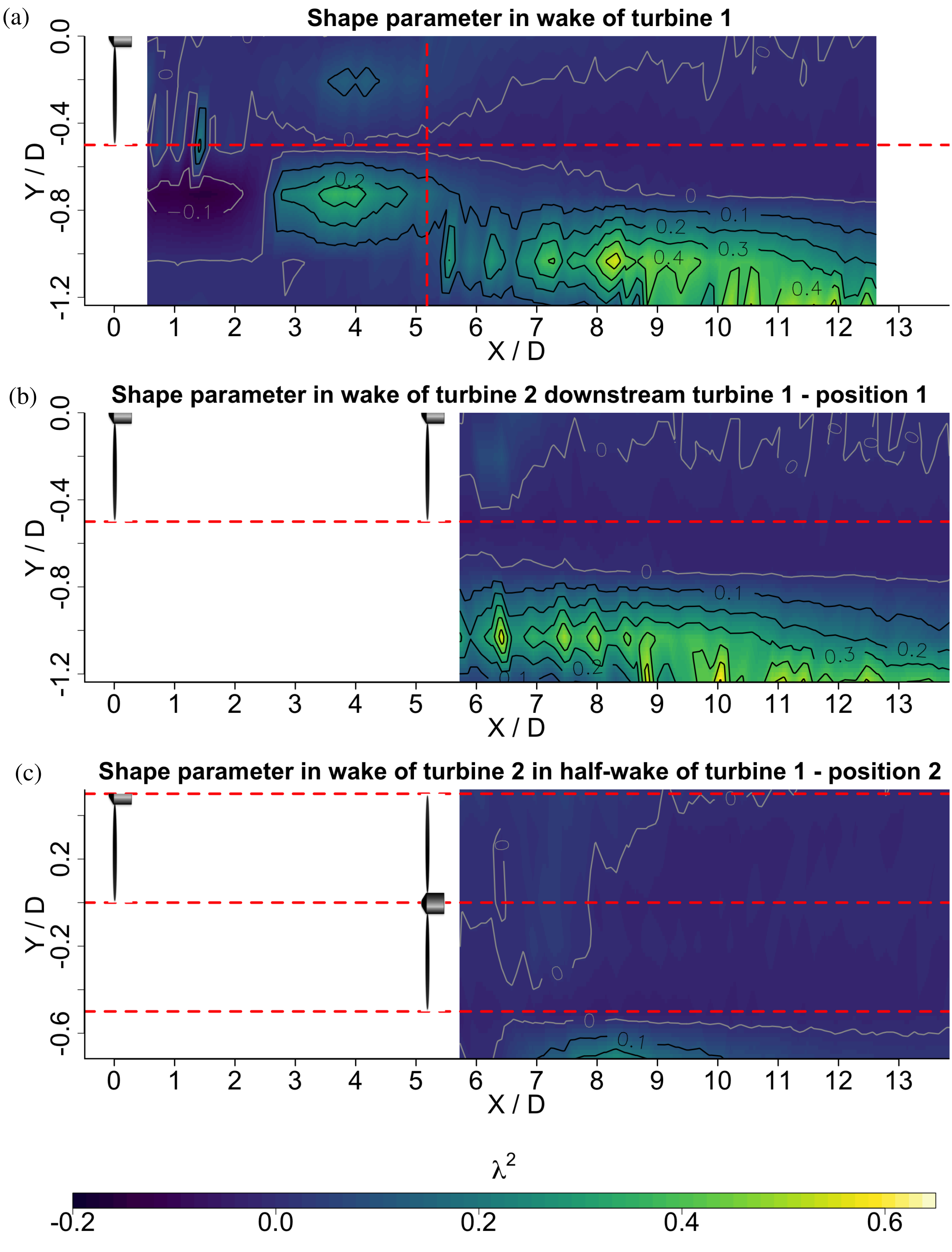

Figure 5.23.: Evolution of the shape parameter λ^2 downstream turbine 1 (a), turbine 2 mid (b) and turbine 2 side (c). Grey contour lines indicate Gaussian behavior of the fluctuations ($\lambda^2(D) < 0.05$) and black contour lines indicate intermittency on scales corresponding to the rotor diameter ($\lambda^2(D) > 0.10$).

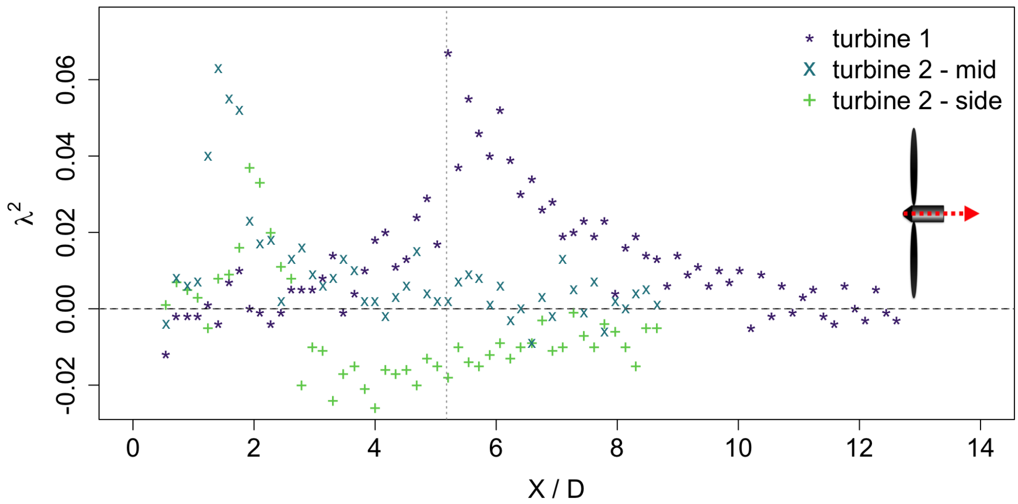

Figure 5.24.: Centerline evolution of the shape parameter for $\tau \simeq D$ downstream turbine 1 (purple *), turbine 2 mid (turquoise x) and turbine 2 side (green +).

reported intermittency ring is captured here, and its downstream evolution is observed.

As λ^2 is calculated from the kurtosis in this analysis, the question arises how well the respective curve corresponding to formula (2.7) as proposed by Castaing *et al.* (1990) fits the probability density function of velocity increments $p(\delta v(\tau \simeq D)/\sigma_\tau)$. Therefore, in figure 5.25(a) and (b), $p(\delta v(\tau \simeq D)/\sigma_\tau)$ is plotted for the transition region where λ^2 is maximal, and at the last measurement position for all three scenarios. From figure 5.25, it can be obtained that the Castaing curves estimated with a calculated λ^2 fit the data nicely. Thus, the statistical properties of the flow are well represented by λ^2. Also, it can be seen that the scenario with the highest inflow intermittency is the least heavy-tailed in the wake. Looking at the downstream position in figure 5.25, one can see that the intermittency is reduced compared to the upstream region, and that the shape of the probability density functions is Gaussian, as $\lambda^2 \approx 0$.

The investigation of $\lambda^2(\tau \simeq D)$ describes turbulence on scales related to the rotor diameter. As the energy spectra indicate the typical turbulence decay with $E(f) \propto f^{-5/3}$, the question arises whether $\lambda^2(\tau)$ does also evolve with a typical behavior for smaller scales. Thus, to further examine the turbulence in the wake, $\lambda^2(\tau)$ is plotted at the centerline in the respective transition region where $\lambda^2(\tau \simeq D)$ is maximum, and at last measured downstream position for the three scenarios. To estimate the slope of the in a semi-logarithmic representation linearly decreasing region of $\lambda^2(\tau)$, μ is fitted (cf. formula (4.3)). In the transition region (cf. figure 5.26), λ^2 behaves similarly for turbine 1 and turbine 2 with a decrease of λ^2 up to time scales $\tau \approx 0.2\,\mathrm{s}$ to $\lambda^2 \approx 0.06$. μ exhibits high values of $\mu_{t1} = 0.48$ for turbine 1, $\mu_{t2m} = 0.58$ for turbine 2 mid and $\mu_{t2s} = 0.37$ for turbine 2 side that are not associated with behavior according

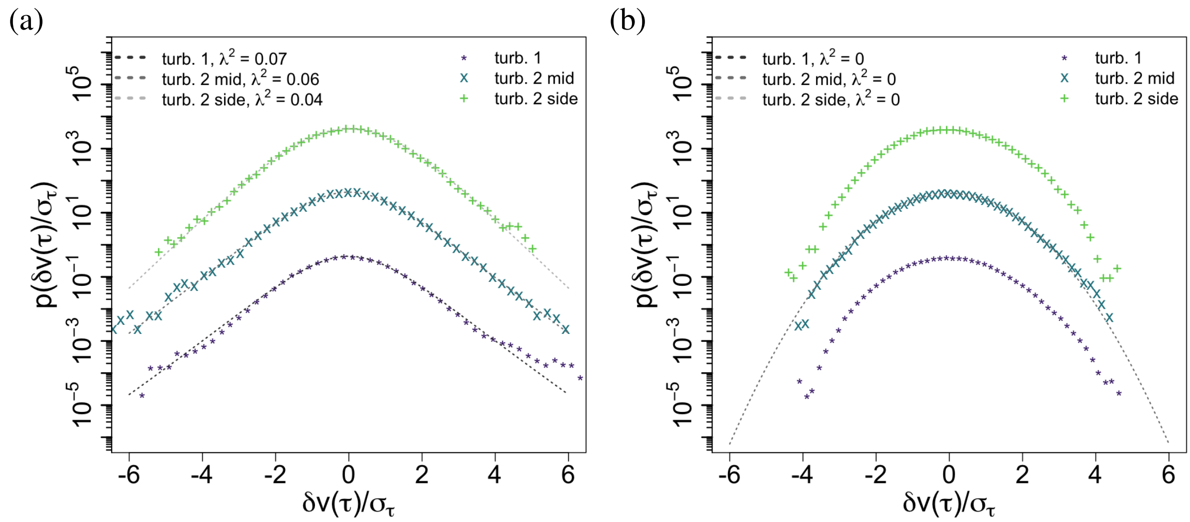

Figure 5.25.: Probability density function of velocity increments at centerline in transition region (a) and the far wake (b): data of turbine 1 (purple *, (a):$X/D = 5.21$, (b):$X/D = 12.62$), turbine 2 mid (turquoise x, (a):$X/D = 1.24$, (b):$X/D = 8.66$) and turbine 2 side (green +, (a):$X/D = 1.93$, (b):$X/D = 8.66$). In addition, the Castaing curves are plotted with λ^2 calculated from the kurtosis indicated in the top-left legend. The increment PDFs are shifted vertically for clearer visualization.

to K62.

At the farthest measured downstream position (cf. figure 5.27), all three scenarios show a similar development with a decrease up to $\tau \approx 0.05\,\mathrm{s}$ where $0.23 \leq \mu \leq 0.29$, and $\lambda^2 \approx 0$ for $\tau \gtrsim 0.05\,\mathrm{s}$. This $\lambda^2 \propto -\ln\tau$ behavior shows that the common ideal turbulence features of the K62 phenomenology, i.e. homogeneous isotropic turbulence, are given. Using Taylor's hypothesis, one finds that $\tau = 0.05\,\mathrm{s} \simeq 0.5D$. Thus, intermittency is induced by the turbine on scales less or equal the rotor blade length while it is reduced for larger scales in the far wake. To define the region in the wake where this claim holds, figure 5.28 and 5.29 show the evolution of $\lambda^2(\tau)$ for the three scenarios at last measurement position for $Y/D = -0.21$ and $Y/D = -0.51$, respectively. From figure 5.28 it becomes apparent, that the results are almost identical to those obtained at the centerline. In contrast, in figure 5.29 at $Y/D = -0.51$, μ changes, and $\lambda^2 < 0$ from $\tau > 0.05\,\mathrm{s}$. For turbine 1 and turbine 2 mid, the value of μ are characteristic for homogeneous isotropic turbulence, but they are higher than in the central wake region. For turbine 2 side, $\mu = 0.42$ indicates that the turbulence does not show this feature. Thus, the in chapter 4 identified inner wake region is confirmed.

Overall, this investigation of intermittency with the from the kurtosis obtained shape parameter reveals in the inner wake a transition from intermittency induced by the turbine to non-intermittent flow in the far wake. The results are independent of the characteristics of the

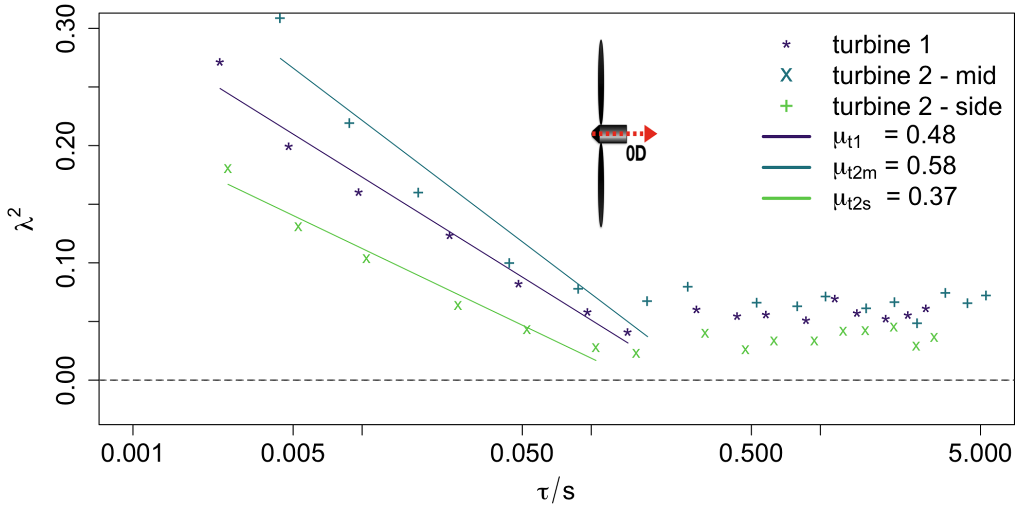

Figure 5.26.: Centerline evolution of $\lambda^2(\tau)$ for turbine 1 (purple *, at $X/D = 5.21$), turbine 2 mid (turquoise x, at $X/D = 1.24$) and turbine 2 side (green +, at $X/D = 1.93$) in the respective transition region.

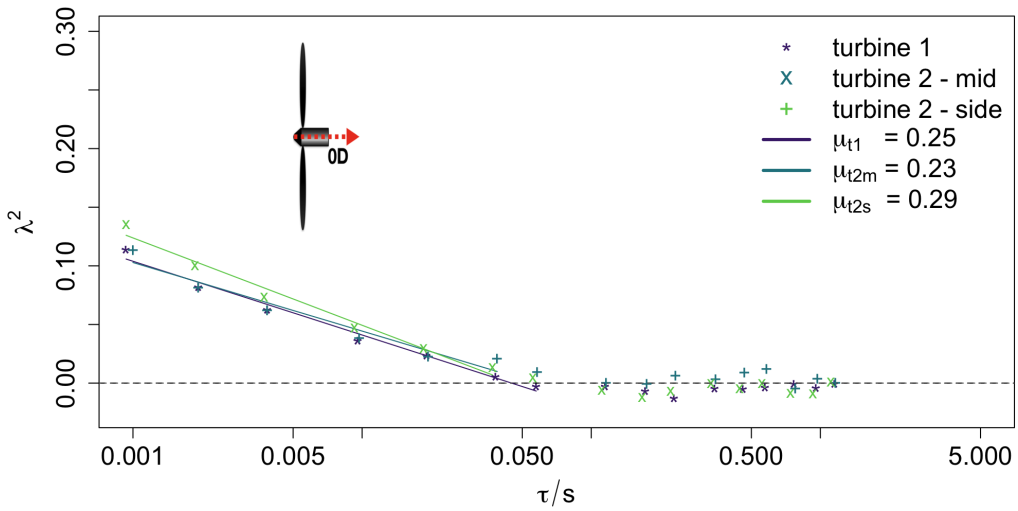

Figure 5.27.: Centerline evolution of $\lambda^2(\tau)$ for turbine 1 (purple *, at $X/D = 12.62$), turbine 2 mid (turquoise x, at $X/D = 8.66$) and turbine 2 side (green +, at $X/D = 8.66$) in the respective far wake at last measurement position.

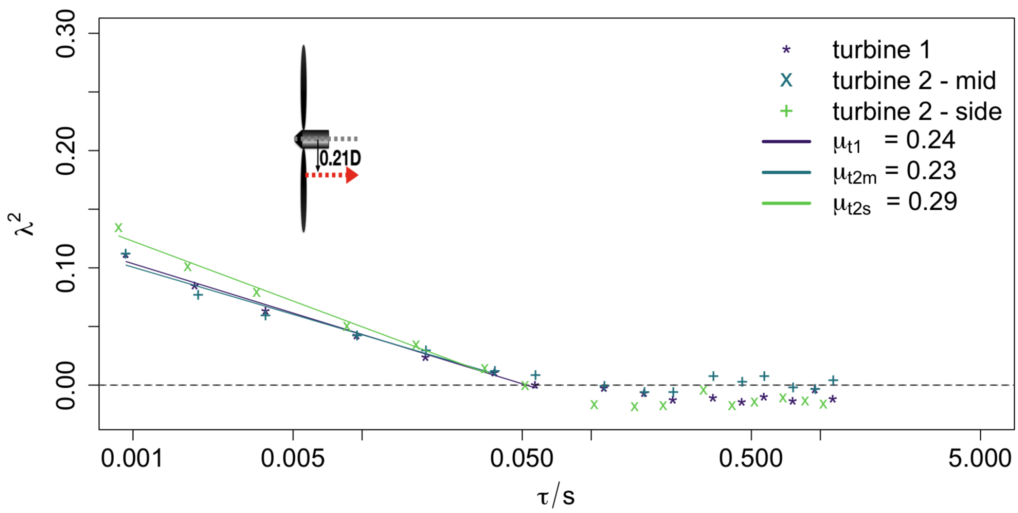

Figure 5.28.: Evolution of $\lambda^2(\tau)$ for turbine 1 (purple *), turbine 2 mid (turquoise x) and turbine 2 side (green +) in the respective far wake at last measurement position and $Y/D = -0.21$.

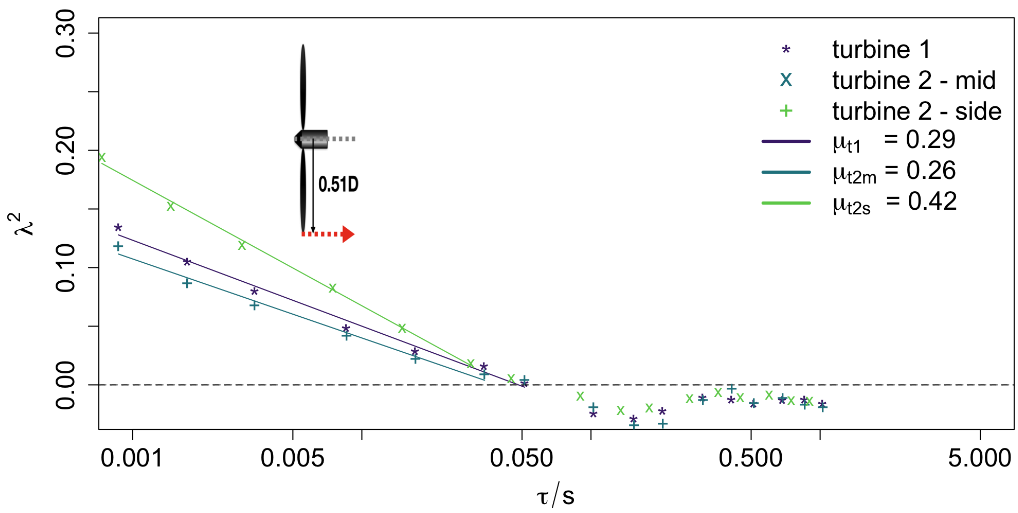

Figure 5.29.: Centerline evolution of $\lambda^2(\tau)$, turbine 2 mid (turquoise x) and turbine 2 side (green +) in the respective far wake at last measurement position and $Y/D = -0.51$. The Y-coordinate is with respect to the turbine center.

inflow, which also supports results from Singh *et al.* (2014) that intermittency is reduced by the turbine. The intermittency ring first captured by Schottler *et al.* (2018) is found and tracked downstream. An analysis of the variation of $\lambda^2(\tau)$ in the transition region and the far wake shows a change from multifractal scaling behavior without signs of homogeneous isotropic turbulence towards multifractal scaling behavior with signs of homogeneous isotropic turbulence in the far wake. The latter was also reported by Bastine *et al.* (2015) from Lidar measurements at one downstream position without describing the turbulence evolution process.

5.3. Summary

In this chapter, results from measurements in the wake of an array of two wind turbines were discussed. The aim was to prove the from results in chapter 4 deduced hypothesis, that the turbine imprints a certain kind of turbulence to the flow that evolves downstream in the far wake to homogeneous isotropic turbulence. It could be shown, that the identified wake regions can be found in all here investigated scenarios, and that a central wake region with a radius of $\leq 0.21D$ is distinguishable. Further, the investigation of L/λ_T, Re_λ, the decay exponent of the energy spectra and the intermittency parameter μ evidence the existence of homogeneous isotropic turbulence in the central far wake. The turbine creates intermittency on scales smaller than half the diameter, but filters intermittency from the inflow on larger scales. Overall, this analysis shows that the turbine creates turbulence that is for quantities used to identify homogeneous isotropic turbulence in the central far wake independent on the inflow conditions.

6. Discussion

In chapters 4 and 5, results from measurements obtained downstream a disc and a model WEC were presented and briefly discussed. The results obtained in this thesis can be assigned to the following objectives that will be discussed in the following:

1. to check with stochastic methods whether a disc is an adequate substitute for a rotating turbine, if not only the mean flow field and turbulence intensity but also the turbulence generation in the wake is considered
2. to thoroughly investigate the influence of different types of turbulent inflows on the wake generated by a disc and a model WEC
3. to evaluate the validity of the obtained results inside a wind farm
4. to identify different wake regions both in stream-wise and span-wise direction
5. to recognize turbulence patterns to help simplify turbulence wake models

In the following, the results are discussed within the framework of these objectives.

1. Comparison of the disc's and the turbine's wake

The first aim is discussed by re-evaluating the results from chapter 4 where measurements have been carried out downstream a disc and a model turbine. The disc was designed both to match the thrust force acting on the turbine and to roughly mimic the turbine's radially changing blockage while creating turbulence. The wakes downstream both WGTs are compared to show how well the rather simple, non-rotating disc reproduces the wake of a turbine.
The most frequently investigated quantity that the disc has to model correctly is the downstream mean velocity. It has been verified that the normalized mean flow fields downstream both WGTs evolve in a similar way and are comparable far downstream the obstacles. In the next step, the downstream evolution of the normalized turbulence intensity, the integral length L and the Taylor length λ_T have been investigated. Differences are visible in proximity to the WGTs due to different turbulence mixing mechanisms (cf. Lignarolo *et al.* (2016)). Nevertheless, these quantities evolve comparably far downstream the two objects. Overall, the results obtained from

an analysis with standard methods are in agreement with former experimental studies that also compared the evolution of a wake generated by an actuator disc with the wake generated by a turbine (see e.g. Aubrun *et al.* (2013), Lignarolo *et al.* (2015) and Lignarolo *et al.* (2016)).
Next, the evolution of turbulence both downstream and in span-wise direction was extended by analyzing the behavior of energy spectra and the intermittency. This detailed analysis of the turbulence development exceeds the investigation of turbulence in other works.
The span-wise and stream-wise evolution of energy spectra and their decay in the inertial sub-range have been examined for both WGTs. It has been confirmed that the turbulence mixing mechanisms are different for the disc and the turbine as the energy distribution over frequency evolves differently with increasing downstream position. Far downstream the rotor, the spectra collapse for all span-wise positions and both WGTs. The examination of the decay exponent exp in the energy spectra's inertial sub-range reveals that all spectra decay in the same way far downstream independently of the object and the span-wise position. This is also supported by the centerline evolution of L/λ_T that remains far downstream approximately constant, which in turn indicates a stable inertial sub-range, and the evolution of $C_\varepsilon \approx const$ in the far wake.
In the next step, the data has been analyzed using probability density functions of temporal and spacial velocity increments and the shape parameter λ^2. While differences exist close to the WGTs due to the different turbulence generation and mixing mechanisms, it has been found that the results are identical far downstream within the area covered by the rotor. Close to the turbine rotor, a ring of high values of the shape parameter for a temporal scale corresponding to the turbine's diameter D, in the following notated $\tau \simeq D$, appears to surround the wake. In the following, this ring will be called intermittency ring. It is not captured further downstream in this measurement but observed in the experiments carried out in OLWiT. This ring is not noticeable downstream the disc. Thus, it can be proposed that this ring is induced by the tip vortices.
Overall, the chosen disc design is suitable to substitute a rotating turbine model to carry out far wake studies, even if an analysis with two-point statistics is desired. This result expands the present knowledge that a disc is with regard to mean velocity, turbulence intensity, and energy spectra an adequate replacement for a turbine for far wake studies.

2. Influence of the inflow turbulence

In chapter 4, the disc and the model turbine were exposed to different turbulent inflows, varying from an (almost) laminar inflow with low turbulence intensity over turbulent inflow generated by a regular square grid to intermittent, atmospheric-like turbulence generated by an active grid. It has been shown that overall, the impact of the inflow on the wake both downstream the disc and the turbine is small. Downstream the disc, the wake develops almost independently from the inflow. Downstream the turbine, the inflow effects mainly the turbulence evolution close to the rotor. In contrast, far downstream, an influence of the inflow conditions is only noticeable on some quantities in case of inflow generated by the active grid: The creation of large-scale flow patterns by the active grid results in an increase of the energy in low frequencies. Additionally, both integral length L and Taylor length λ_T are increased by the active grid inflow, which is also in consistence with the higher Re_λ obtained in these measurements. From these results, it has been deduced that the inflow only influences the turbulence evolution process but not its decay both downstream the disc and downstream the turbine. Next, it needs to be verified that these results hold also in a wind farm layout where downstream turbines are exposed to the turbulence created by another turbine.

3. Verification of results in a wind farm setup

In order to transfer the findings obtained in different turbulent inflows under laboratory conditions to the more application-oriented wind farm setting, the turbine of investigation has been exposed to a wake flow of another turbine (cf. chapter 5). The wake of the upstream turbine (turbine 1) has been compared to the wake of the downstream turbine. The former was exposed to laminar inflow while the latter was either exposed fully to the wake of turbine 1 (turbine 2 mid), that is turbulent but not intermittent, or exposed to an inhomogeneous mixture of free inflow and wake (turbine 2 side) that is both turbulent and intermittent on scales related to the rotor diameter. It could be shown for the upstream turbine and the two different span-wise positions of the downstream turbine, that the results are consistent with the ones obtained before. The evolution of all presented quantities is qualitatively similar to the development of the wake in different turbulent inflows. In contrast to the previous setup, it was possible to identify a beneficial influence of turbulent inflow on the wake recovery in this setup: The development of all quantities is compressed and moved forward to the rotor in turbulent inflow (i.e. downstream turbine 2) compared to laminar inflow (i.e. downstream turbine 1). As a consequence, the wake recovers faster. Especially, the energy spectra of both turbines are identical far downstream for all span-wise positions. The intermittency ring that is only just indicated in the first experiment is captured here in the whole measurement range. The shape parameter for a temporal scale corresponding to the rotor diameter also evolves similarly far downstream. Overall, the turbulence properties are despite the decaying turbulence intensity persistent far downstream and the expansion of the inertial sub-range remains stable. Thus, apart from the downstream expansion, the findings from above do hold within a wind farm.

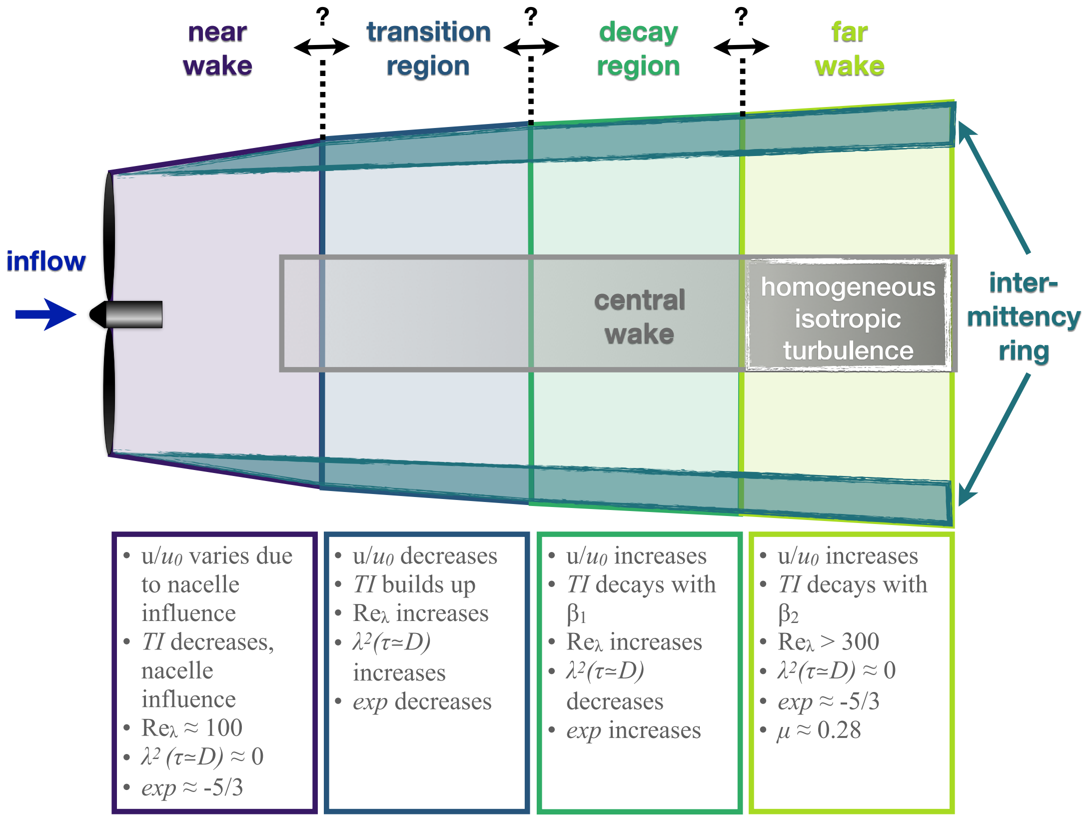

Figure 6.1.: Wake map: Sketch of the different wake regions that occur downstream a wind turbine. The central wake is additionally marked, and the intermittency ring and the region where homogeneous isotropic turbulence appears to exist are highlighted.

4. Identification of wake regions

While the previous sections 1-3 focused on the impact of the interaction between the inflow and the WGTs on the wake, this section and the following section 5 will focus on the analysis of the turbulence inside the wake. As mentioned in section 3, the wake evolution is on the one side independently of the setup qualitatively similar. On the other side, it is compressed or expanded in the different setups. A first step to describe this effect has been to identify similar downstream sections within these wakes. This was achieved by defining four downstream wake regions by means of the evolution of the normalized centerline turbulence intensity. The sketch in figure 6.1 gives an overview on the different downstream wake regions. As the downstream positions of the regions are not fixed, this variability is marked with "?" in the sketch. The *near wake* is characterized by still detectable structures from the investigated objects. Afterwards, the turbulence builds up in the *transition region*. From there, the turbulence decays according to a power law in the *decay region*. An alteration in the exponent indicates a change in the turbulence

decay. It is thus used to define the beginning of the *far wake*. These wake regions are identifiable both downstream the disc and downstream the turbine in all experiments, although the turbulence mixing mechanisms are different. The four regions can equally be identified in the downstream centerline evolution of the energy spectra's decay exponent *exp*, the shape parameter for the time scale $\tau \simeq D$ and the spacial shape parameter in the central wake. The main characteristics of these quantities are also summed up in the information boxes below each region in figure 6.1. Additionally, the near wake region and the far wake region are identifiable within the centerline downstream evolution of the integral length, the Taylor length and the Taylor Reynolds number while their transition and decay region are not clearly distinguishable from each other.
Looking at the downstream evolution of the energy spectra's decay exponent and the shape parameter in span-wise direction reveals additionally a change with increasing radial distance r from the center. Within the inner wake, i.e. $r \leq 0.21D$, the downstream wake regions are identifiable (sketched in figure 6.1 as *central wake*). Considering radial positions with increasing distance from the centerline (e.g. by means of the spacial shape parameter for increments r_4 and r_5) reveals that a span-wise turbulence transition region exists as well. In the outer radial positions, $r = 0.51D$ and $r = 0.72D$, the turbulent evolution of the energy spectra and the shape parameter is driven by the tip vortex development in the near wake, combined with the mixing shear layer between ambient flow and wake. The intermittency ring expands downstream and has a radius of $r \approx 1.2D$ in the far wake; it envelops the wake (see also figure 6.1).
In conclusion, it is possible to divide the wake into four downstream regions. Additionally, a wake core, a transition and an outer wake layer can be identified in span-wise direction. The downstream position of each region appears to depend on the inflow velocity, the inflow turbulence and the turbine thrust, but also on the setup and the wind tunnel.

5. Recognition of turbulence patterns

In the following, a detailed description of the turbulence regions presented in figure 6.1 will be given.
In the near wake, the turbulence has not yet evolved. The Taylor Reynolds number is small. The flow is characterized by the presence of the tip and root vortices (see e.g. figure 5.17). Due to the presence of these structures in the near wake, the results obtained from different turbulence analyses have to be viewed with care in this region. Intermittency on a scale D is present in the blade tip region where the intermittency ring is created. While the tip vortices' stability depends on the ambient turbulence, the intermittency ring does evolve independently.
With increasing distance from the rotor, the wake expands and the turbulence evolves in the transition and decay region. The length scales increase. The energy over frequency still alters and the turbulence decay in the inertial sub-range does not yet follow a $-5/3$-decay. Here,

intermittency is present downstream the turbine in the wake center, as can be identified both from the temporal shape parameter and the probability density functions of velocity increments for the time scale $\tau \simeq D$, and from the spacial shape parameters and probability density functions of velocity increments in the central region, r_1, r_2 and r_3.
In the far wake, the turbulence is finally fully evolved, which is indicated by the Taylor Reynolds number that exceeds 300 and remains independent of X/D. The far wake energy spectra collapse independently of the inflow, and the inertial sub-range follows a $-5/3$-decay over several orders of magnitude.[i] This is seen as an indication of homogeneous isotropic turbulence in the far wake. The similarity is also supported by the centerline evolution of L/λ_T that remains approximately constant far downstream: This indicates an inertial sub-range with a range that does not shrink despite the decaying turbulence; in combination with a constant Re_λ, this is an indication of the Richardson-Kolmogorov phenomenology (Vassilicos (2015)). Here, intermittency is not present anymore in the central wake for a time scale similar to the rotor diameter independently on the intermittency of the inflow. To include different scales in the investigation of the temporal shape parameter, $\lambda^2(\tau)$ has been calculated for different time scales in the range $0.01D \lesssim \tau \lesssim 10.26D$ in the far wake. Up to $\tau \simeq 0.5D$, the shape parameter decreases towards $\lambda^2 \approx 0$ and is constant for larger scales. The decrease of the shape parameter with $\lambda^2 \propto -\ln\tau$ up to $\tau \simeq D$ indicates the existence of homogeneous isotropic turbulence according to K62. This allows to determine the intermittency parameter $\mu \approx 0.27$, and the results matches results obtained in other studies. The fitted scales lay within the inertial sub-range of the energy spectra.
To further test for isotropy, 2D hot-wire measurements were carried out on the centerline downstream the turbine in order to measure the u and v velocity components and the u and w velocity components. In the far wake, the results indicate isotropic behavior of the turbulence. The results are confirmed by findings of Singh *et al.* (2014) and Bastine *et al.* (2015) regarding the reduction of intermittency on scales larger than D in the far central wake as compared to the inflow. Further, the strong indication of homogeneous isotropic turbulence in the far wake of a turbine is supported by results from Wessel (2008) and Bastine *et al.* (2015). However, this study is the first to precisely locate this region, put it into the framework of turbulence evolution and additionally prove an independence of the results on the inflow turbulence. Especially, it has to be pointed out, that the evolution of the energy spectra with increasing downstream position is not influenced by the different types of inflow conditions. While Chamorro *et al.* (2012), Singh *et al.* (2014) and Bastine *et al.* (2015) conclude that the turbine filters certain scales from the inflow while enhancing others, the obtained results give evidence to believe that the turbine is not acting as a filter but creates its own turbulence in scales $\lesssim 0.3f \cdot D/u_0$. Larger structures are found to be transferred to the wake.
It has to be drawn attention to the fact that the disc's wake shows similar results in the central far

[i]To be precise, the decay exponent $exp \approx -1.60$ matches even better the according to K62 corrected value of $exp \approx -1.64$ (if $\mu \approx 0.27$).

wake. This is an important result, as at least discs with the design used here are much simpler but adequate replacements for turbines for far wake modeling both in experiments and in simulations. It is concluded that an inner far wake region exists where both the turbine and the disc imprint turbulence with properties of homogeneous isotropic turbulence onto the flow. As has been shown, the turbulence evolves in the three upstream wake regions, where the mechanisms are different between disc and turbine. The central wake region appears to have a radius of $R_{CW} \approx 0.2D$, and the turbulence field varies radially. This is also in accordance with conclusions drawn from results from Schottler *et al.* (2018), where the turbulence kinetic energy is approximately constant and changes for $R > 0.2D$ in this region. Also, the ring with high intermittency on a time scale corresponding to the rotor diameter, that was first reported in Schottler *et al.* (2018), is captured. Here, the full downstream development is caught; the intermittency ring's radius increases with the wake expansion to $r \approx 1.2D$ in the far wake.
An analysis of the dissipation of the turbulent kinetic energy suggests that under some circumstances, regions with non-equilibrium turbulence dissipation occur in the wake of a turbine. This result shows again that the turbulence evolution within the wake of a turbine has strong parallels with the turbulence within wakes created by fractal objects.

Summary

In conclusion, the investigations planned to answer the defined problems were successfully carried out, and the presented analysis led to new conclusions. It has been found that the far wake of the here investigated disc is even with regard to energy spectra and intermittency an adequate alternative for a rotating turbine. The inflow turbulence was shown to have an influence on the transition and decay region in case of the turbine. Nevertheless, the far wake is independent on the inflow. Next, it has been proven that the results can be transferred to a wind farm. Thus, certain quantities do not build up within the wind farm but are similar downstream each turbine. Only the position of the different wake regions may depend on the inflow turbulence, but in addition to the inflow velocity and the turbine thrust. Last, the discussed quantities show that both the disc and the turbine destroy intermittency on scales of the rotor diameter and create an own flow with features of homogeneous isotropic turbulence in the central far wake. The turbine does not act as a filtering element for flow structures present in the inflow as proposed in e.g. Chamorro *et al.* (2012) but rather as a creator of a new turbulence on scales smaller the rotor diameter. Overall, these results enable the definition of a turbulence map of the wake that summarizes all measurement results in a simple but complete graphic. Furthermore, the strong indication of homogeneous isotropic turbulence in the central far wake redounds to a rather simple turbulence wake model.

7. Summary and Outlook

The evolution of small-scale turbulence in the wake of a wind turbine was studied in this thesis. Starting from research questions framed in van Kuik *et al.* (2016) regarding the transition region between near and far wake, the interaction between inflow and wake, and the interaction between two wakes, experiments were designed for a structured investigation. A disc as simplified turbine model and a model turbine were used as WGTs in the first part, and uniform inflow conditions with different turbulence properties were generated. The data were analyzed by means of the mean value, turbulence intensity, Taylor length scale and integral length scale, energy spectra, the shape parameter, and the intermittency parameter. While the wake of the disc was nearly unaffected by the different inflows, the turbine's wake showed some sensitivity towards the inflow within a certain region. Far downstream the turbine, the effect of the inflow turbulence diminished. Overall, it could be shown that this disc is a good substitute for the turbine far downstream, as all quantities behave similarly to the turbine's wake far downstream. The evolution of the centerline turbulence intensity was used to re-define the near and far wake. Additionally, two regions within the transition region, named transition and decay region, were identified by means of the turbulence intensity, where the turbulence builds up and starts to decay, respectively. The regions can be recognized downstream both WGTs, but with different characteristics within the near wake, transition and decay region. A comparison of the centerline evolution of the other investigated quantities confirms these regions. An investigation of different radial positions made it additionally possible to identify an inner wake core around the centerline where the findings hold. In the transition and decay region, the turbine was found to imprint intermittent structures of size of the turbine onto the flow that decays in the far wake. In the far wake core, strong evidence of homogeneous isotropic turbulence was found for both WGTs. Therefore, the disc is suited well as substitute for the turbine when executing far wake studies, even regarding higher-order statistics. As the findings are independent on the inflow conditions, it can be concluded that the turbine imprints independently on the inflow turbulence its own turbulence on the flow that develops and turns into homogeneous isotropic turbulence.
Following up on these results, the setup was further developed to test whether and to what extend the finding of the refined wake regions with homogeneous isotropic turbulence in the far wake core of a wind turbine holds in a wind farm. The finding could be confirmed for different constellations of two turbines. The beneficial influence of ambient turbulence on the

wake recovery downstream a turbine that was known from literature could also be confirmed, as well as the existence of a ring with high intermittency surrounding the wake. In high turbulence inflows, the tip vortices break down closer to the rotor, which can significantly compress the near wake, transition and decay region, leading to an earlier onset of the far wake.

For wake studies, this finding shows that obtaining measurements at fixed positions may lead to a comparison of results obtained in different wake regions. Therefore, knowledge of the position of the regions downstream the WGT is of importance.

A wake map was developed that sketches the different wake regions with their characteristics as a first, easy-to-use turbulence chart. This simplifies the categorization of new results, especially regarding turbulence properties, into the framework of wake evolution. However, this basic scheme has potential for refinement. First, measurements of all three flow components with high temporal resolution could be of interest to investigate the energy entry from the ambient flow into the wake within the framework of wake regions. Additionally, measurements with higher span-wise spacial resolution could be used to narrow down the wake core's location more precisely and to analyze the downstream evolution of mean flow profiles. The latter can be used to draw further conclusions on the turbulence state within the wake similarly to the work of e.g. Dairay *et al.* (2015) and Obligado *et al.* (2016) in the wake of irregular plates. They find that the turbulent kinetic energy is not necessarily dissipated with the energy cascade being in equilibrium, which leads to different scalings of the self-similar profiles downstream the irregular plate. Thus, an investigation of the profile scaling and the energy dissipation can be used to embed the wake of a turbine into classical turbulence theory. A first step in this direction was already done in this work when analyzing the evolution of C_ε.

Further, an investigation of the influence of the turbine spacing on the evolution of the downstream turbine's power generation, loads and wake is of interest. As above-mentioned, four turbulence regions can be distinguished in the wake. Investigating the turbine properties of a downstream turbine with regard to the wake region it is exposed to as inflow can help to optimize turbine spacing within a wind farm. This is especially important if the spacing of turbines within a wind farm is small and downstream turbines are thus operating in the turbulent and intermittent near wake and transition region.

The combined influence of ambient turbulence and turbine thrust on the position of the wake regions, especially the turbulence intensity maximum and the beginning of the far wake should be investigated. Combined with an investigation of the influence of different wake regions as inflow of a downstream turbine, this can be used to optimize wind farm control. If the wake could be scaled by adjusting the thrust, the downstream turbine's performance could be optimized. As the definition of wake regions by means of the turbulence intensity is a simple measure, it could also be imagined to place a nacelle LiDAR on the downstream turbine to identify the current wake region the turbine is operating in. If necessary, the control system could then adjust the upstream turbine's tip speed ratio.

Appendix

A. Measurement system and sensor calibration

All hot-wire measurements have been carried out with commercial systems from *Dantec Dynamics* using A/D converters from *National Instruments*. In total, three different systems have been used for the three measurement setups presented in chapter 3 in section 3.3.1 and 3.3.2 to collect the data presented in this thesis:

A.1. Experiments in TWO

A.1.1. I: Measurements with disc and turbine in different inflows

For measurements downstream the disc and the model WEC carried out in the Turbulence Wind tunnel Oldenburg (TWO), two *multichannelCTA 54N80* Systems were used to run 11 1D hot-wires of type 55P16 with 1.25 mm sensor length. A hardware low pass filter was set to a cut-off frequency of $f_{cut} = 10\,\mathrm{kHz}$, while the sampling frequency was $f_s = 20\,\mathrm{kHz}$. Data was collected with a *NI USB 6211* 16bit A/D converter with a temporal resolution of 250 kHz using LabView software. In addition, the flow temperature and the ambient pressure were measured. The probes were calibrated approximately every four hours, or at the beginning and end of each measurement. For this, the probes were placed in the center of the wind tunnel, approximately 1.1 m downstream of the outlet, and a pitot-static tube was connected to a pressure transducer to measure the velocity. The calibration was performed from $0\,\mathrm{m/s}$ to $15\,\mathrm{m/s}$ in steps of $1\,\mathrm{m/s}$. During experiments with the active grid, the calibration had to be performed with the active grid installed in the wind tunnel instead of in laminar inflow. To compensate for the higher turbulence, for each calibration velocity, 300000 data points were averaged. To calibrate the data, all calibrations from the respective day were averaged and the variation is used as measurement error. All data was, as above-mentioned corrected for temperature drift according to Hultmark and Smits (2010).
For the statistic evaluation except calculation of mean velocity and standard deviation, the data

was sampled down by taking every third data point, as some artifacts from the measurement system appeared in the spectra at frequencies $> 7\,\mathrm{kHz}$.

A.1.2. II: Measurements with a turbine in active grid inflow

Next, measurements with a higher spacial downstream resolution were carried out with the active grid in TWO. During these measurements, four 1D hot-wires (type 55P16, 1.25 mm) or two 1D hot-wires (55P16, 1 mm) and a 2D hot-wire (type 55P61) were operated by a Dantec Dynamics *StreamLine 90N10* frame with *90C10 CTA Modules* in combination with the belonging software StreamWare v6.0. The hardware low pass filter was set to $f_{cut} = 10\,\mathrm{kHz}$, and the sampling frequency was $f_s = 20\,\mathrm{kHz}$. Data was collected with a *NI PXI 6281* 18bit A/D converter. A temperature probe that is attached to the system was used to monitor the flow velocity during measurements, and in addition, the ambient pressure and humidity were measured. The sensors were calibrated from $0\,\mathrm{m/s}$ to $15\,\mathrm{m/s}$ in steps of $1\,\mathrm{m/s}$ with the *FlowUnit 90H02*, a calibration unit coming with the StreamLine system. When 2D hot-wire measurements were performed, not only a velocity calibration, but also a directional calibration was performed. The measured voltages were calibrated averaging over all velocity calibrations, and a temperature correction was applied according to Hultmark and Smits (2010). The velocity variation in the calibrations are used as measurement error.

A.2. Experiments in OLWiT

The last set of measurements was carried out in OLWiT using a *StreamLine 9091N0102* frame with *91C10 CTA Modules* run with *StreamWare v6.0* with six 1D hot-wire probes of type 55P16 (1.25 mm) and the system's temperature probe. Data was collected with a cDAQ system equipped with two 16bit A/D converter modules type NI 9215. The sampling frequency was $f_s = 15\,\mathrm{kHz}$, and the system's hardware low pass filter was set to $f_{cut} = 10\,\mathrm{kHz}$. The sensors were calibrated from $0\,\mathrm{m/s}$ to $15\,\mathrm{m/s}$ in steps of $1\,\mathrm{m/s}$ to the wind tunnel velocity[i] that is measured in the settling chamber and corrected to ambient temperature, humidity and pressure. The ambient humidity and pressure from these sensors was also used as reference for the measurement. The raw voltage data was calibrated using the average calibration over one day, and a temperature correction according to Hultmark and Smits (2010) was applied.

[i] A measurement showed that the laminar flow has a turbulence intensity of $TI \approx 0.4\%$.

B. Error Propagation

In the following, the procedure used here to derive errors for different quantities is explained. For all quantities $y(x_1, x_2, ...)$ derived from multiple variables x_i, the classical estimation of the influence of each variable's error Δx_i on the result, Δy,via Taylor expansion is used:

$$\Delta y = \left|\frac{\partial y}{\partial x_1}\right| \cdot \Delta x_1 + \left|\frac{\partial y}{\partial x_2}\right| \cdot \Delta x_2 + ... \qquad \text{(B.1)}$$

B.1. Measurements in TWO with MultiChannel CTA

B.1.1. Normalized mean velocity

As error of the mean velocity $\langle u \rangle$, the maximum deviation between the average calibration curve and all measured calibrations at the velocity $\langle u \rangle$ was taken.
In case of the inflow velocity $\langle u_0 \rangle$, that is the average value over all probes in the rotor plane, the standard deviation σ_0 between all points is used as error Δu_0.
Applying B.1 to the normalized mean velocity u/u_0 yields

$$\Delta \frac{u}{u_0} = \frac{1}{u_0} \cdot \Delta u + \frac{u}{u_0^2} \cdot \Delta u_0 \qquad \text{(B.2)}$$

B.1.2. Normalized turbulence intensity

The error of the turbulence intensity, ΔTI, is calculated inserting the error of the mean velocity, Δu, to formula B.1:

$$\Delta TI = \frac{\sigma}{u^2} \cdot \Delta u \qquad \text{(B.3)}$$

Thus, the error of the normalized turbulence intensity TI/TI_{max} is

$$\Delta \frac{TI}{TI_{max}} = \frac{1}{TI_{max}} \cdot \Delta TI + \frac{TI}{TI_{max}^2} \cdot \Delta TI_{max} \qquad \text{(B.4)}$$

with $\Delta TI_{max} = \left|\frac{\sigma}{u^2}\right|_{max} \cdot \Delta u$

B.1.3. Integral Length Scale and Taylor Microscale

To estimate the error of the integral length scale and the Taylor microscale for the data sets measured in TWO, the following procedure is used: First, the time series is divided into three segments of 84 s. These segments match with three of three and a half protocol runs of the active grid within the measurement time of five minutes and were applied to all inflow conditions for comparability. Second, each of the time series segments was down-sampled using only every third data point, as the temporal resolution of the measurement system corresponds to this sampling frequency. Starting at the first, second and third sample of each time series fragment yields three independent time series for the same time span. For each of the nine time series fragments, the integral length scale and Taylor microscale were calculated according to formulas 2.2 and 2.3, and an average and the root-mean-square deviation are calculated. Similarly, the error of the decay exponent is estimated by fitting the inertial sub-range for each of the nine time series fragments. The latter is represents a measure for the spreading and is used as error estimate.

B.2. Measurements in TWO with StreamLine

In this measurement campaign, measurements were carried in active grid inflow out using the StreamLine with a 10 kHz low pass filter. As the protocol was run depending on the measurement at least three times, the error for the respective quantity comes from averaging over the respective calculated quantities of each measurement and using the standard deviation as error.

C. Setup validation

In the following, experiments that were designed to validate the measurements carried out in TWO are presented. The wind tunnel outlet is in comparison to the diameter of the disc and the turbine rather small. Additionally, an open test section is used which causes the development of a turbulent shear layer between standing air in the laboratory and the jet. Thus, the correctness of the results has to be guaranteed. First, experiments with the disc and two scaled down disc models are compared. Second, the turbine is placed at different stream-wise and span-wise positions. Additionally, the influence of the comparatively large nacelle is investigated by adding an aerodynamic cap. Last, 2D hot-wire measurements are compared to measurements carried out with a 2D Laser Doppler Anemometer (LDA).

C.1. Experiments with scaled discs

In this section, the wake of the original disc, called disc 1 in the following, is compared to the wake of two scaled disc models, disc 2 and disc 3; details can be found in table C.1. The discs were mounted on scaled towers and centered in the wind tunnel. Inflow generated by the active grid was used. The setup can be seen in figure C.1. Measurements were carried out with four 1D hot-wires with the measurement system described in appendix A.1.2. The positions can be found in figure C.1.

In figure C.2, the centerline evolution downstream the three discs is shown for the mean velocity (a) and turbulence intensity (b). Error bars are calculated according to appendix B.2. In case of the mean velocity, the near wake evolves comparably, but from $X/D \approx 3.5$, the wake recovery is reduced in case of disc 1 while it is similar for disc 2 and 3. A comparison of the turbulence

Table C.1.: Diameter, thickness and blockage of the three different discs.

	diameter D/D_D	thickness	blockage
disc 1	$D_D = 59\,\mathrm{cm}$	5 mm	$\approx 22\%$
disc 2	$D_2 = 3/5\ D_D$	3 mm	$\approx 13\%$
disc 3	$D_3 = 1/5 D_D$	1 mm	$\approx 4\%$

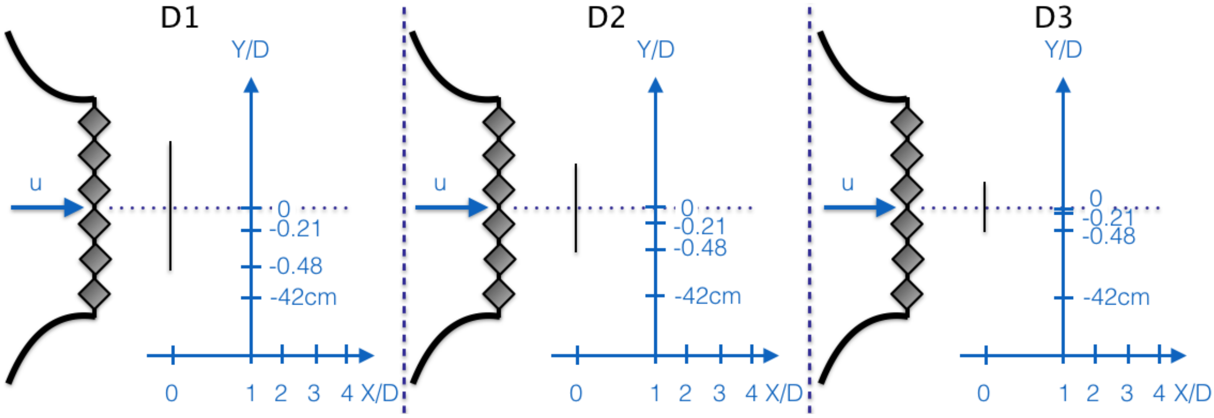

Figure C.1.: Setup: Experiment with scaled discs; the inflow is generated by the active grid.

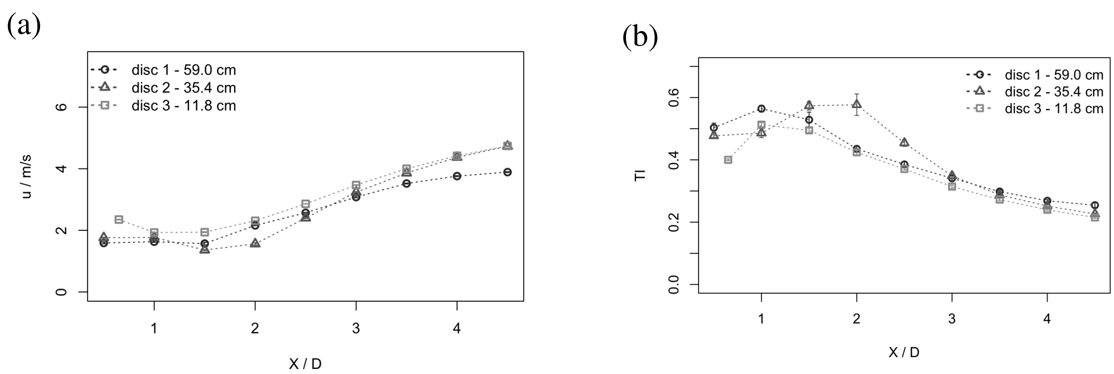

Figure C.2.: Centerline comparison of the mean velocity (a) and turbulence intensity (b) in the wake downstream three scaled discs, $D_D = 59\,\text{cm}$, $D_2 = 3D_D/5 = 36.4\,\text{cm}$, $D_3 = D_D/5 = 11.8\,\text{cm}$.

intensity in (b) shows differences between discs 1 and 3, and disc 2 in the near wake, but the turbulence intensity is similar from $X/D \approx 3$. This shows that the wake recovery downstream a large obstacle is dampened. Nevertheless, the turbulence decay is not affected by this.

In figure C.3, the downstream evolution of the flow measured at $Y/D = 42\,\text{cm} = 0.71D_D$ is shown. Presented are the mean velocity (a) and turbulence intensity (b). The mean velocity and the turbulence intensity evolve in case of disc 2 and 3 similar and at this position, an effect of the obstacle in the flow is not identifiable. In case of disc 1, the mean velocity is significantly decreased in the shear layer while the turbulence intensity is increased.

In conclusion, the central wake is in terms of turbulence generation not affected by the object's size, but the wake recovery is decreased for large objects. An influence of the object's size can also be found in the flow outside the rotor plane.

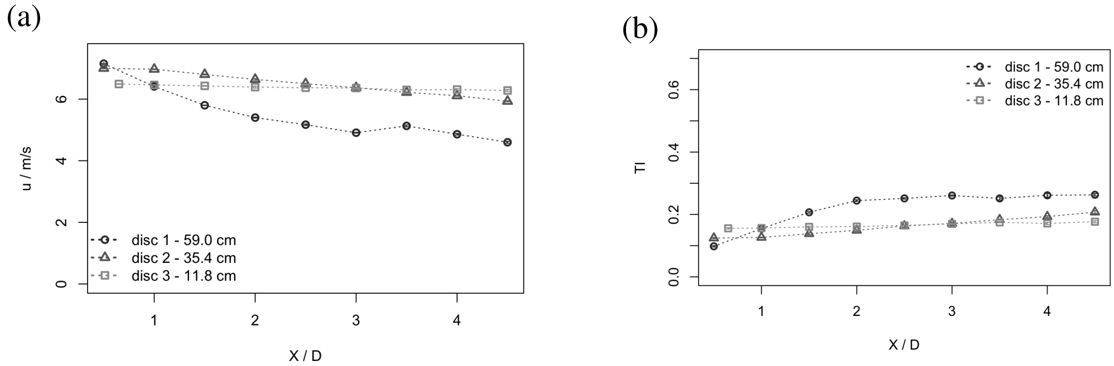

Figure C.3.: Comparison of the mean velocity (a) and turbulence intensity (b) in the wake downstream three scaled discs, $D_D = 59\,\mathrm{cm}$, $D_2 = 3D_D/5 = 36.4\,\mathrm{cm}$, $D_3 = D_D/5 = 11.8\,\mathrm{cm}$. The span-wise position is $Y/D_D = -0.72$.

C.2. Experiments with a relocated turbine

In the following, the position of the turbine is altered to investigate yet again the influence of the turbine's size and thus the blockage of the wind tunnel on the results. For all experiments, turbine 2 was used and operated with control 1.

C.2.1. Variation of downstream position

In this experiment the wake of the turbine in the regular setup is compared to a setup where the turbine is placed 155 cm, or $2.67D$ downstream the outlet. This position is referred to as turbine position 2 whereas the regular position is referred to as turbine position 1. A sketch of the setup can be found in figure C.4. The active grid generated inflow is used, and as the inflow conditions for the shifted turbine is different due to the different downstream position, details are given in table C.2. 1D hot-wire measurements were carried out according to appendix A.1.2, and the error calculation is introduced in appendix B.2.

In figure C.5, the mean velocity (a) and turbulence intensity (b) are plotted downstream the turbine along the centerline. The results obtained from measurements downstream the turbine at position 2 are compared to the measurements presented in chapter 3.3.1-II where the turbine is at

Table C.2.: Diameter, thickness and blockage of the three different discs.

	$u_{infty}/\mathrm{m/s}$	TI	λ/mm	L/cm
68 cm	8.06	0.12	85.7	6.5
155 cm	7.98	0.10	13.0	30.8

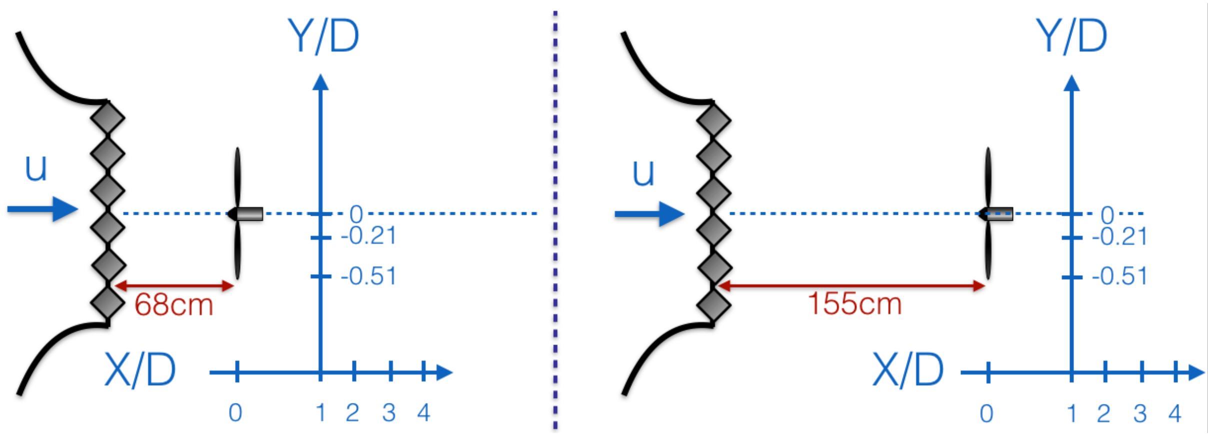

Figure C.4.: Setup: Experiment with the turbine shifted further downstream to 155 cm from the wind tunnel outlet. As inflow, active grid generated turbulence is used.

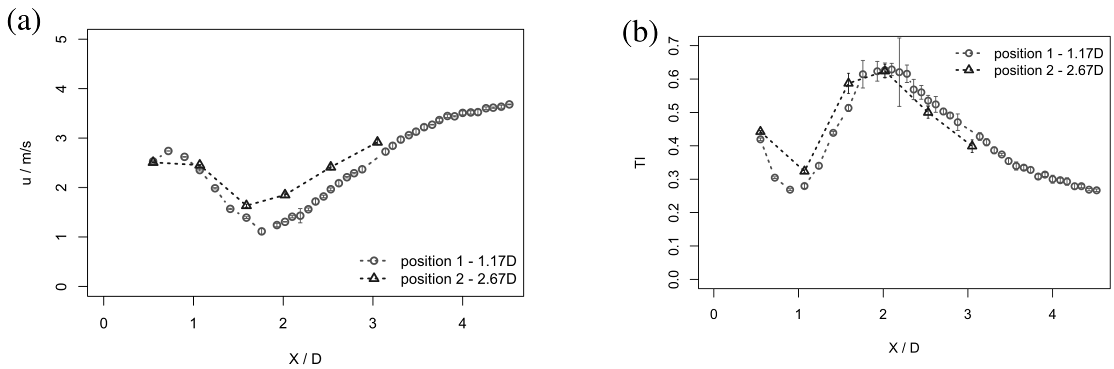

Figure C.5.: Comparison of the mean velocity (a) and turbulence intensity (b) at the centerline downstream the turbine mounted at 68 cm or 1.17D downstream the outlet and 155 cm, or 2.67D downstream the outlet.

position 1. The evolution of both quantities is overall similar for both turbine positions, although the wake recovers faster downstream the turbine in position 2. This effect may be addressed to the at position 2 more turbulence shear layer that is accelerating recovery effects by enhancing turbulent mixing. Nevertheless, this experiment shows that the results are not altered by blockage effects.

An investigation of the energy spectra with increasing downstream position in figure C.6 reflects this as well. Plotted are the spectra downstream the turbine in position 2 at the centerline at $X/D = 1.59$ and $X/D = 2.88$. The spectra are compared to the spectra at the centerline downstream the turbine in position 1 at $X/D = 1.59$, $X/D = 2.88$ and $X/D = 3.48$ (dashed lines). While the spectra differ at $X/D = 1.59$, they are similar at $X/D = 2.88$. Comparing the spectrum downstream the turbine at position 2 at $X/D = 2.88$ with the spectrum downstream the turbine at position 1 at $X/D = 3.48$ shows, that they collapse. Thus, this emphasizes that the

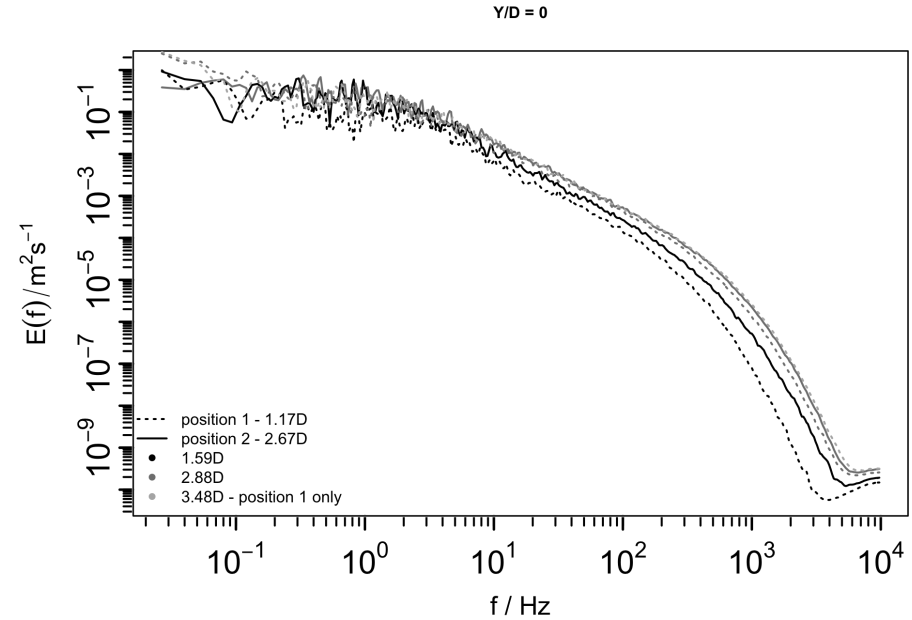

Figure C.6.: Comparison of the energy spectra downstream the turbine mounted at 68 cm or 1.17D downstream the outlet and 155 cm, or 2.67D downstream the outlet at $Y/D = 0$.

evolution is accelerated downstream the turbine in position 2 but apart from that not altered by blockage effects.

C.2.2. Variation of the turbine's span-wise position

To additionally investigate how the results are altered when the turbine is not placed in the center of the wind tunnel, in the next experiment, turbine 2 is exposed to laminar inflow and shifted 0.17D to the left and to the right from the center. The setup is shown in figure C.7. The turbine is placed at the usual position, position 1, and it is operated with control 1. 1D hot-wire measurements are obtained at span-wise positions $Y/D = 0$ and $Y/D = 0.34$; the measurement equipment is described in appendix A.1.2, and $1.2 \cdot 10^6$ data points were collected at each position with a sampling frequency of $f_s = 20\,\text{kHz}$.

In figure C.8, the mean velocity (a) and turbulence intensity (b) are plotted downstream the centerline for the three span-wise turbine positions (left/centered/right). Overall, the evolution is similar.

In figure C.9, the mean velocity (a) and turbulence intensity (b) are plotted at $Y/D = 0.34$ downstream for the three span-wise turbine positions (left/centered/right). The evolution is similar for the three positions, and also comparable to the centerline evolution.

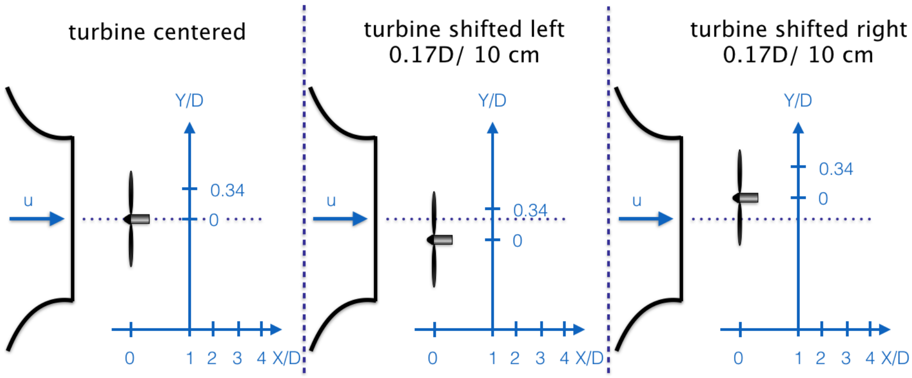

Figure C.7.: Setup: Experiment with the turbine shifted in span-wise direction $\pm 0.17D$ from the center. Laminar inflow is used.

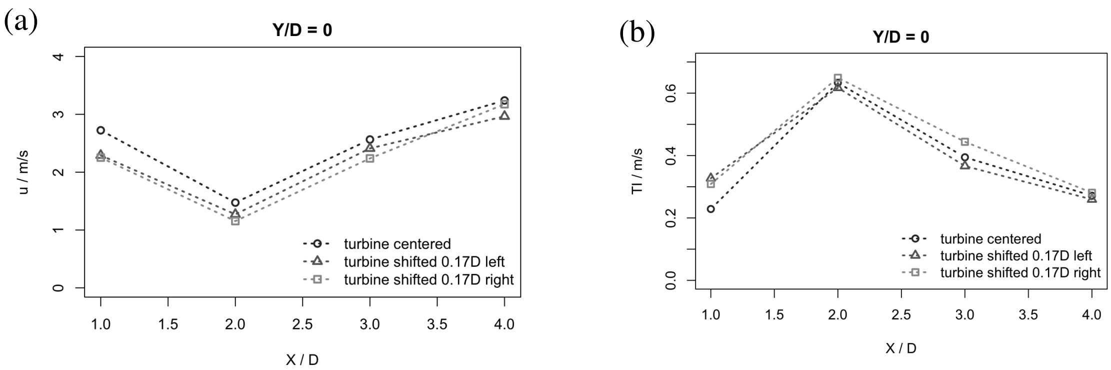

Figure C.8.: Comparison of the mean velocity (a) and turbulence intensity (b) in the wake downstream the turbine positioned at the wind tunnel center, shifted $0.17D$ to the left and $0.17D$ to the right. Centerline data is presented.

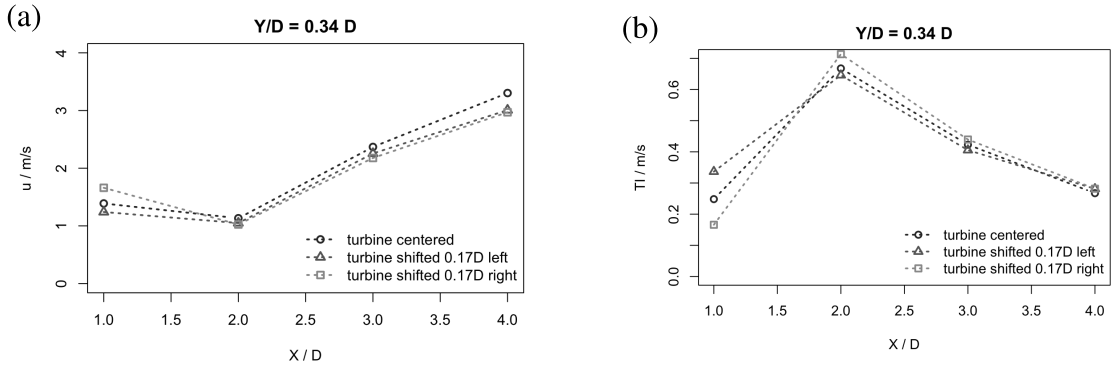

Figure C.9.: Comparison of the mean velocity (a) and turbulence intensity (b) in the wake downstream the turbine positioned at the wind tunnel center, shifted $0.17D$ to the left and $0.17D$ to the right. Data is presented for the span-wise probe position $Y/D = 0.34$.

In figure C.10, the energy spectra downstream the turbine are shown at $X/D = 2$ and $X/D = 4$ for the three span-wise turbine positions. While the spectra do not collapse perfectly, the development of the energy over frequency is very similar for the three span-wise positions.
In conclusion, this experiment shows that the wake center evolves similarly even if the turbine position is altered. This supports that the results are not adulterated by the setup.

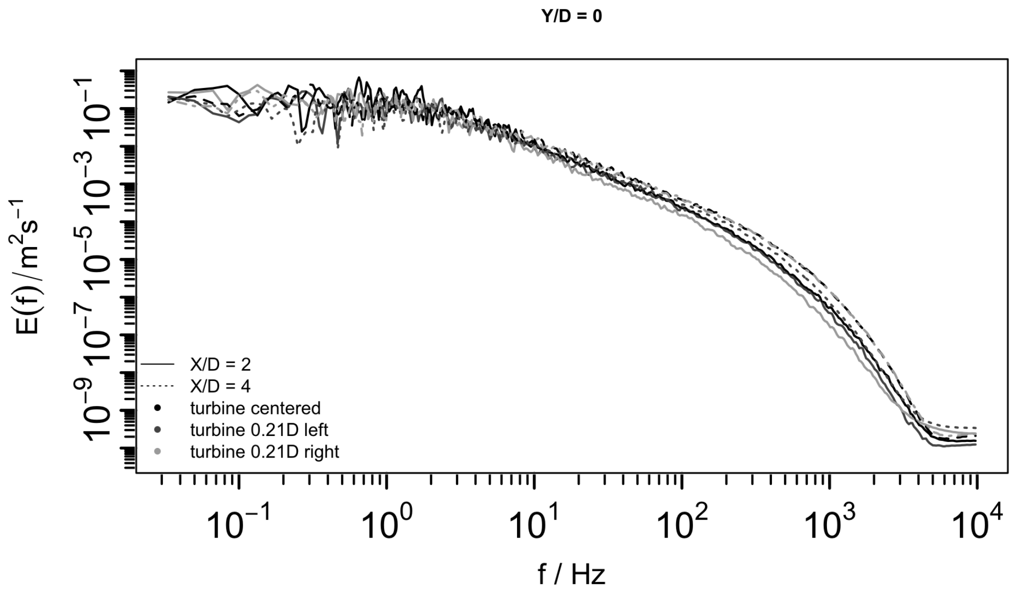

Figure C.10.: Comparison of the energy spectra in the wake downstream the span-wisely shifted turbine (diff. shades of gray) at $2D$ and $4D$ (dashed lines).

Figure C.11.: Aerodynamic cap as cover of the turbine's nacelle.

C.2.3. Experiments with cap

As the nacelle is in comparison to the rotor quite large, the question arises whether its high blockage influences the wake evolution. Therefore, an aerodynamic cap is used to cover at the nacelle's back, as shown in figure C.11. 1D hot-wire measurements were than carried out at the centerline in active grid generated inflow as described in appendix A.1.2. The results are compared to the results obtained downstream the un-covered nacelle, and the mean velocity and turbulence intensity are shown in figure C.12 (a) and (b). Overall, small deviations can be found in the near wake, and the curves collapse from $X/D \approx 2$. Thus, an influence of the nacelle on the turbulence evolution is not present.

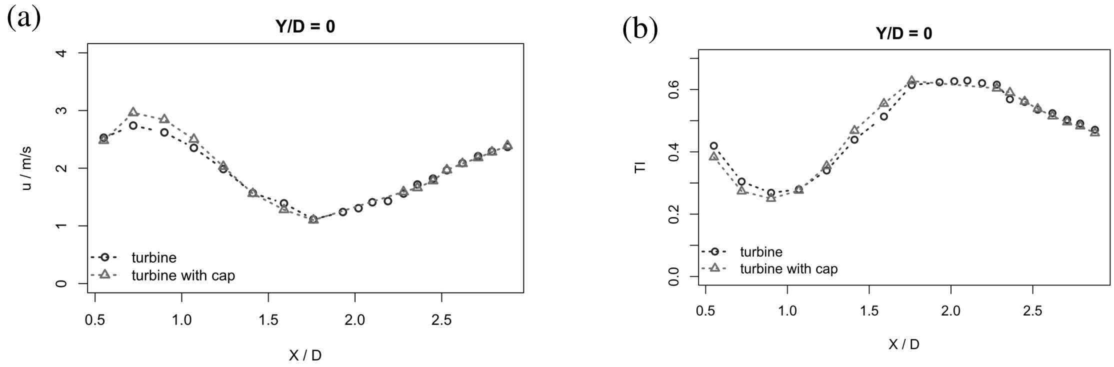

Figure C.12.: Comparison of the mean velocity (a) and turbulence intensity (b) in the wake downstream the turbine in the normal setting and with an aerodynamic cap covering the nacelle back.

C.3. Comparison between 2D hot-wire and 2D LDA measurements

The last experiment is a comparison of the evolution of the centerline mean velocity and turbulence intensity downstream the turbine measured with a 2D Laser Doppler Anemometer (LDA) with 1D and 2D hot-wire measurements. The LDA is a non-invasive, optical anemometer that is in contrast to a hot-wire also capable of measuring backflows, and therefore, it can be used to validate the very high turbulence intensities measured with the hot-wire. For an introduction to the measuring principle, the reader is referred to e.g. Ruck (1987). The experiment was carried out in the acoustic wind tunnel in Oldenburg in laminar inflow in an open test section. The 2D LDA was mounted on a traverse device and was aligned to measure the u_X and u_Z flow components. A sketch of the setup can be found in figure C.13.

Additionally, measurements were carried out similar to the description in chapter 3.3.1 with the system described in appendix A.1.2. Hot-wire measurements were carried out downstream the turbine in active grid inflow along the centerline in steps of $0.17D$ in the region between $X/D = 0.55$ and $X/D = 1.93$, and in steps of $0.09D$ for downstream positions between $X/D = 2.02$ and $X/D = 4.52$. The motion protocol of the active grid was repeated three times at each position, and each run was measured. The sampling frequency of the $1.25\,\mathrm{mm}$ 1D hot-wire was $f_s = 20\,\mathrm{kHz}$, and $1.5 \cdot 10^6$ data points were collected.

Additionally, 2D hot-wire measurements (sensor length: $1\,\mathrm{mm}$) were carried out in a similar manner at the centerline at 9 downstream positions between $X/D = 0.55$ and $X/D = 4.52$ with a sampling frequency of $f_s = 20\,\mathrm{kHz}$.

The mean velocity evolution downstream the turbine is presented in figure C.14. Data obtained with the 2D LDA in laminar inflow is compared to the 1D and 2D hot-wire measurements obtained in active grid inflow in TWO. The 2D hot-wire is aligned to measure the u_X and u_Z

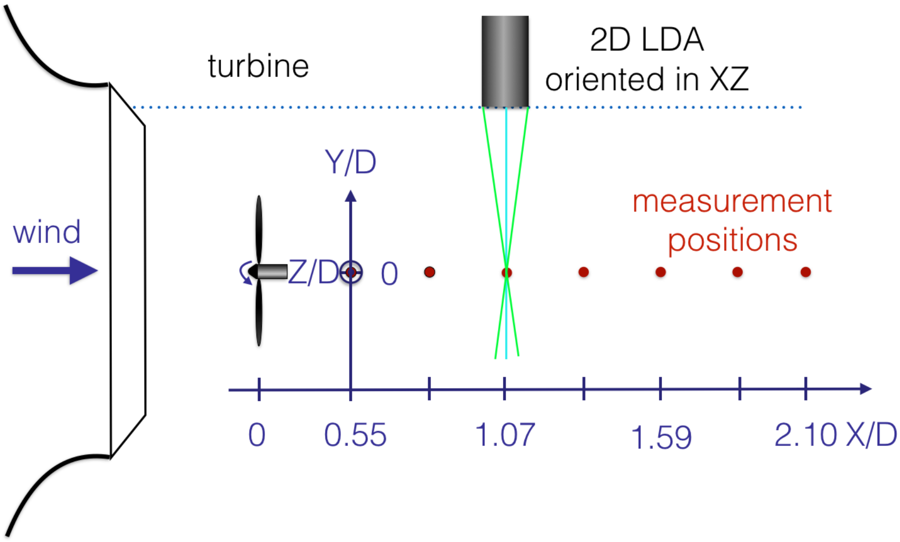

Figure C.13.: Setup: Wake measurements carried out with a 2D LDA in laminar inflow.

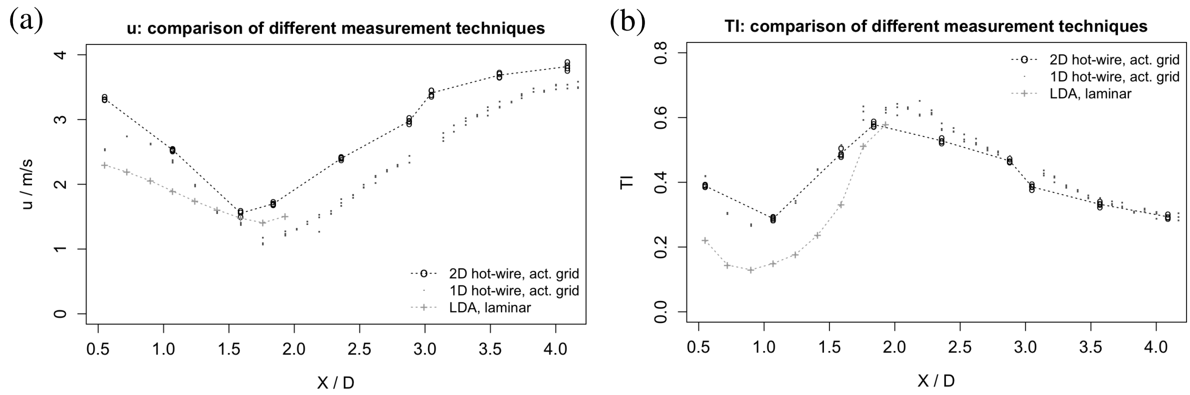

Figure C.14.: Comparison of the mean velocity (a) and turbulence intensity (b) on the centerline for data sets measured with 2D LDA, 2D hot-wire and 1D hot-wire.

flow components, like the 2D LDA. While the evolution of the mean velocity is similar for both hot-wire measurements, the flow velocity measured by the 2D hot-wire is higher. The 2D LDA measures a lower velocity compared to the hot-wires directly downstream the turbine, but the velocity also decreases up to $X/D = 1.76$ and starts to recover at $X/D = 1.93$.

The turbulence intensity is shown in figure C.14. The two hot-wire measurements evolve similarly with a maximum turbulence intensity $TI_{max} \approx 0.6$ around $X/D \approx 2$. The turbulence intensity obtained from LDA data is close to the rotor lower compared to the TI obtained from hot-wire data, but it increases to similar values of $TI \approx 0.6$ at $X/D = 1.93$.

Therefore, the measurements obtained with 1D hot-wire data are reliable for statistic turbulence analysis despite the very high turbulence intensities.

In comparison to the turbulence intensities obtained during the main measurements, the values are here lower in case of active grid inflow. Reasons may be that the inflow did vary despite careful checking or that a different calibration procedure and a different measurement system were used.

C.4. Summary

In this chapter, different measurements were shown to validate the setup in TWO and the measurements obtained with 1D hot-wire anemometry. It could be shown, that the data is reliable and only to a small degree influenced by the setup.

D. Thrust measurements

In the following, experiments are presented that were carried out to measure the thrust acting on the disc and the two turbines. All measurements were carried out using a Kistler force balance of type 9255C in combination with a Kistler charge amplifier of type 5080A. As this device is designed to measure fluctuating forces, the offset was measured at the beginning and the end of each measurement cycle, and the a linear offset compensation was afterwards applied to the data. The term *measurement cycle* denotes the increase of the velocity at first followed by a decrease to compensate for hysteresis effects. The inflow velocity is determined automatically from pitot tubes in the wind tunnel and sensors that capture the ambient temperature, pressure and humidity.

D.1. Thrust force acting on disc

In figure D.1, a measurement of the thrust force acting on the disc is presented. Two measurement cycles were carried out. All data were used to fit a curve $T \propto a \cdot u^2$ to the disc's thrust T_D, making a the fit parameter. From $a = 0.15$, the thrust coefficient $c_{T,D}$ of the turbine can easily be calculated with the total thrust in the wind, $T_{wind} = 1/2 \cdot \rho_{air} \cdot A \cdot u^2$[i], $c_{T,D} = T_D/T_{wind} = 0.96$.

D.2. Thrust force acting on turbine 1 and 2

In the following, the thrust measurements for both turbines are presented. In case of turbine 2, measurements for both controls, 1 and 2, are shown. In addition, the thrust force acting solely on the tower and nacelle will be presented.

In figure D.2, the thrust forces acting on turbine 1 and 2 are presented. The turbines were operated with control 2, and the average tip speed ratios were $TSR_{T1} \approx 5.7$ and $TSR_{T2} \approx 5.8$. The complete sets of measurements are included in the fit according to $T_{Ti} \propto a_i \cdot u^2$ with the fitting parameter a_i, where $i \in 1,2$ represents the turbine number. The thrust acting on turbine 1

[i] $\rho = 1.20\,\mathrm{kg/m^3}$, $A_D = 0.26\,\mathrm{m^2}$

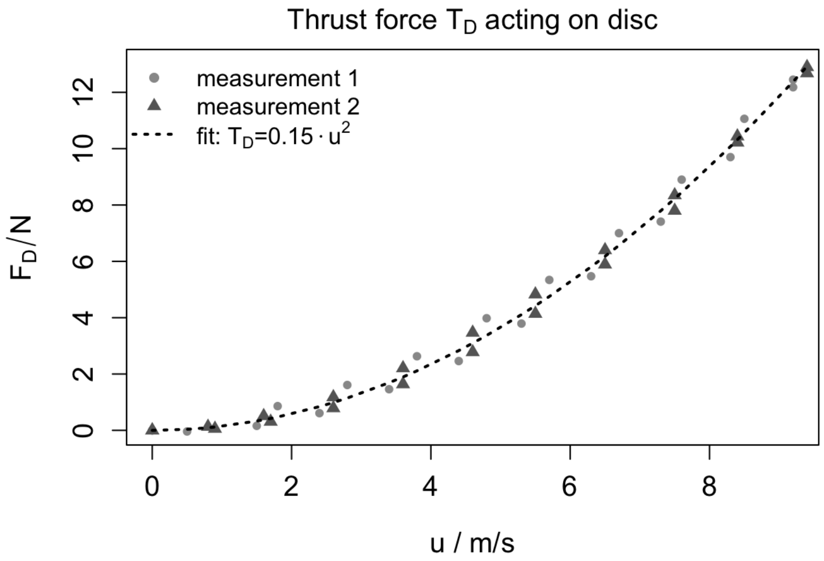

Figure D.1.: Thrust force acting on the disc in dependence on the inflow velocity. The data of the two measurements is fitted according to $T \propto a \cdot u^2$, and the fit parameter is printed in the legend.

is slightly smaller than the thrust acting on turbine 2, $a_1 = 0.15 < a_2 = 0.16$. With the slightly smaller surface of the turbine compared to the disc ($A_T = 0.25\,\mathrm{m}^2$), the thrust coefficients are $c_{T,T1} = 1.00$ and $c_{T,T2} = 1.07$.

In addition, the thrust acting on the turbine's nacelle and tower was determined by dismounting the rotor blades to get an impression of the impact of the tower and nacelle on the turbine thrust. The result is presented in figure D.3. The fit parameter $a = 0.02$ indicates a significantly smaller thrust than the one acting on the turbine, and an estimation of the thrust coefficient gives $c_{T,Tow} =\approx 0.17$.

Further, the thrust acting on turbine 2 is measured for a tip speed ratio of 7.2 with regard to the control hot-wire to know also the thrust for measurements operating with control 1 in this TSR. Here, only one cycle was measured. The control was switched off and the turbine was controlled manually to match the TSR. In figure D.4, the results are presented. The thrust T_{T2} is plotted over both the wind tunnel speed and the wind speed measured by the hot-wire. A significant decrease of the measured velocity in front of the turbine compared to the inflow is assigned to the velocity drop upstream an obstacle. This effect naturally leads to a higher *calculated* TSR (7.3 on average) as compared to the TSR with regard to the inflow velocity (6.2). Similarly, the thrust acting on the turbine is overestimated, as the thrust coefficient with regard to the inflow velocity yields $c_{T,WT} = 1.00$ while the thrust coefficient with regard to the measured velocity yields $c_{T,HW} = 1.40$.

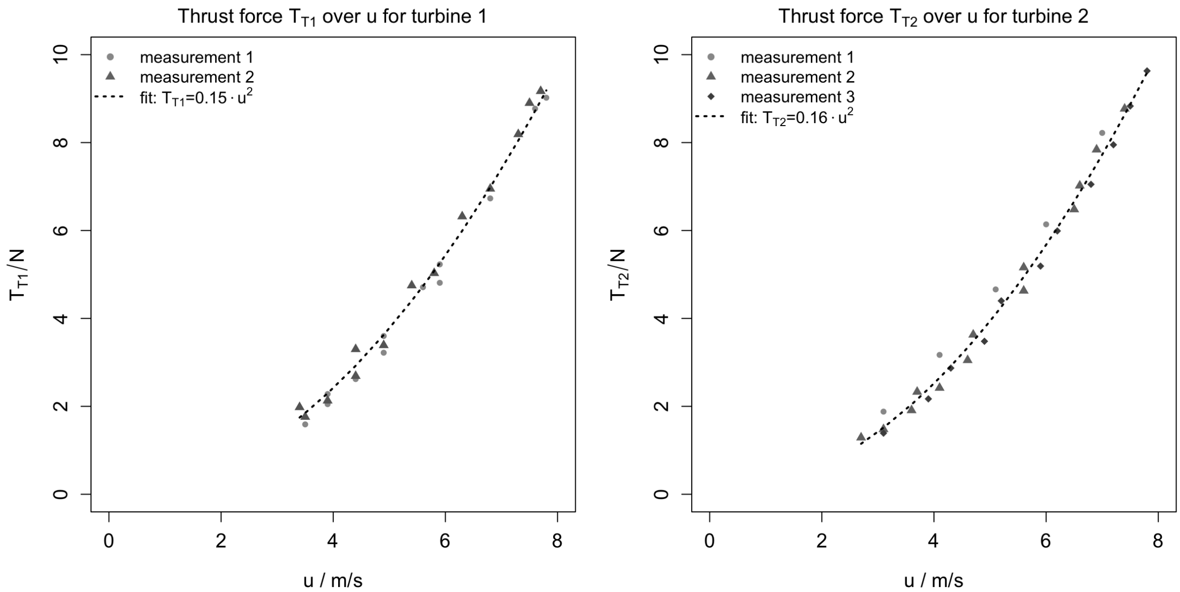

Figure D.2.: Thrust force acting on turbine 1 (left) and turbine 2 (right) plotted over the inflow velocity. The data of all measurements is included to obtain the fit parameter a in $T \propto a \cdot u^2$.

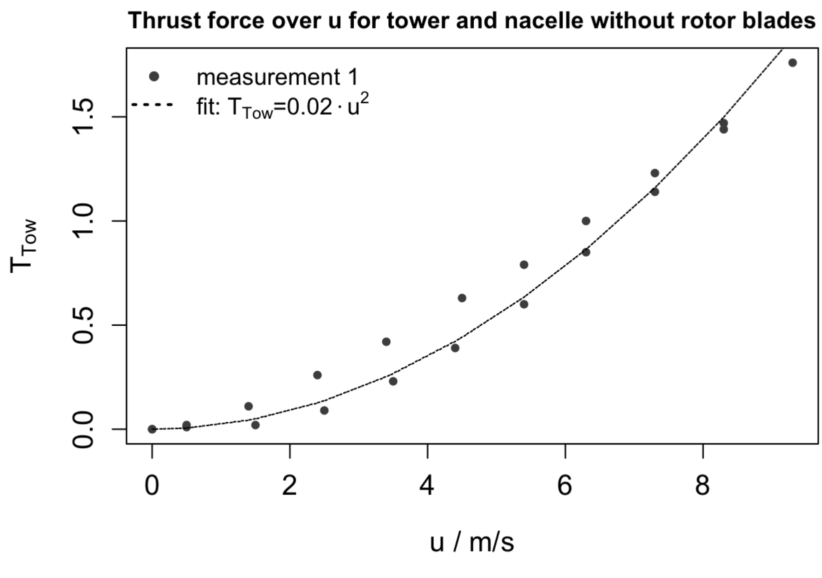

Figure D.3.: Thrust force acting on the tower and nacelle of the turbine body without rotor blades in dependence on the inflow velocity. The data of the measurement is fitted according to $T \propto a \cdot u^2$, and the fit parameter is printed in the legend.

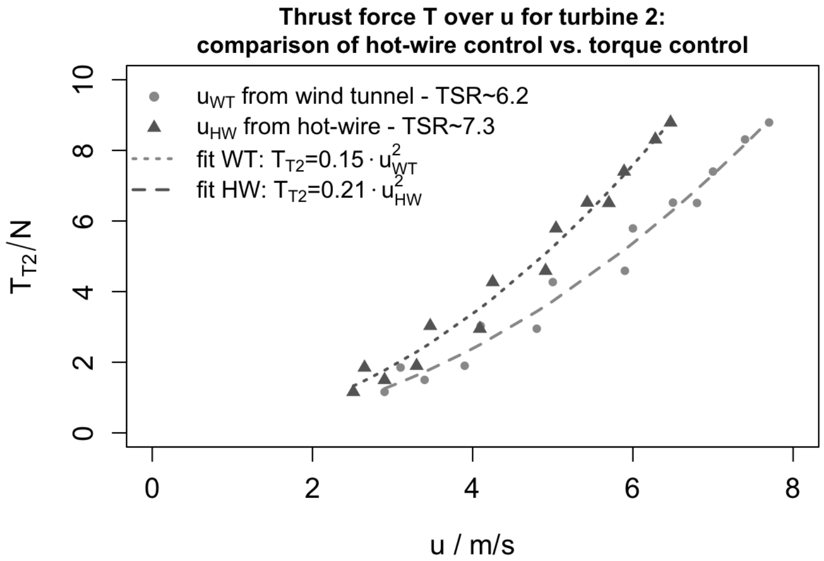

Figure D.4.: Thrust force acting on turbine 2 in dependence on the inflow velocity. Here, the turbine was controlled according to the velocity measured 20 cm upstream the turbine with a hot-wire. The thrust force is both plotted over the wind tunnel velocity and the velocity measured by the control hot-wire. The data of the two measurements is fitted according to $T \propto a \cdot u^2$, and the fit parameter is printed in the legend.

E. Exact downstream positions

Table E.1.: Downstream positions X/D of the local extrema and changes in the graphs of different quantities x for the disc (denoted with subscript a.i) and the turbine (denoted with subscript b.i) for the three inflow conditions in TWO.

x		**disc**			**turbine**	
	$X^x_{a.1}$	$X^x_{a.2}$	$X^x_{a.3}$	$X^x_{b.1}$	$X^x_{b.2}$	$X^x_{b.3}$
u_{max}	1.07	1.07	0.90	0.90	0.72	0.72
u_{min}	1.59	1.59	1.59	1.76	2.10	1.76
TI_{min}	0.90	0.90	0.90	1.07	1.07	0.90
TI_{Peak}	1.76	1.59	1.59	2.10	2.28	2.10
TI_2	2.97	2.97	2.97	2.97	2.97	2.97
σ_1^2	1.24	1.24	0.90	-	-	-
σ_2^2	1.41	1.41	1.41	1.59	1.93	1.76
σ_3^2	2.62	3.14	2.97	2.79	3.31	3.22
L_1	1.24	0.90	1.07	1.41	1.59	1.59
L_2	1.76	1.76	1.76	1.59	2.10	1.76
L_3	3.31	3.31	3.31	3.14	3.14	-
λ_{max1}	-	-	-	1.41	1.59	1.41
λ_{min}	1.76	1.76	1.93	1.93	2.10	1.93
exp_1	-	-	-	1.41	1.24	1.24
exp_2	0.90	0.90	0.90	1.59	2.10	1.59
exp_3	1.93	1.76	1.93	2.45	2.97	2.45

Table E.2.: Downstream positions X/D of the local extrema and changes in the graphs of different quantities x for the three turbine scenarios in OLWiT.

x	**turbine 1** X^x_{t1}	**turbine 2 mid** X^x_{t2m}	**turbine 2 side** X^x_{t2s}
u_{max}	0.90	0.72	0.72
u_{min}	4.52	1.41	1.76
TI_{min}	3.66	0.90	1.07
TI_{Peak}	6.24	1.76	2.45
TI_2	7.97	3.14	4.00
σ_1^2	-	-	-
σ_2^2	3.66	1.07	1.41
σ_3^2	8.31	2.10	3.14
L_1	2.10	-	-
L_2	6.07	-	-
L_3	8.83	4.00	4.00
λ_{max1}	4.34	1.07	-
λ_{min}	6.41	1.59	2.10
exp_1	2.97	-	1.59
exp_2	4.86	1.07	2.10
exp_3	6.76	2.28	4.00

Bibliography

Al-Abadi A, Kim YJ, Ertunç Ö, Delgado A (2016). "Turbulence Impact on Wind Turbines: Experimental Investigations on a Wind Turbine Model." *Journal of Physics: Conference Series*, **753**. URL `http://stacks.iop.org/1742-6596/753/i=3/a=032046`.

Ali N, Aseyev AS, Melius MS, Tutkun M, Cal RB (2017). "Evaluation of Higher Order Moments and Isotropy in the Wake of a Wind Turbine Array." In A Pollard, L Castillo, L Danaila, M Glauser (eds.), *Whither Turbulence and Big Data in the 21st Century?* Springer International Publishing. ISBN 978-3-319-41217-7. URL `https://doi.org/10.1007/978-3-319-41217-7_15`.

Argyris J, Faust G, Haase M, Friedrich R (2015). *An Exploration of Dynamical Systems and Chaos - Completely Revised and Enlarged Second Edition*. Springer-Verlag Berlin Heidelberg. ISBN 978-3-662-46042-9. doi:10.1007/978-3-662-46042-9.

Aubrun S, Loyer S, Hancock P, Hayden P (2013). "Wind turbine wake properties: Comparison between a non-rotating simplified wind turbine model and a rotating model." *Journal of Wind Engineering and Industrial Aerodynamics*, **120**, 1 – 8. URL `http://www.sciencedirect.com/science/article/pii/S0167610513001220`.

Barlas E, Buckingham S, van Beeck J (2016). "Roughness Effects on Wind-Turbine Wake Dynamics in a Boundary-Layer Wind Tunnel." *Boundary-Layer Meteorology*, **158**. URL `https://doi.org/10.1007/s10546-015-0083-z`.

Barthelmie RJ, Frandsen ST, Nielsen MN, Pryor SC, Rethore PE, Jørgensen HE (2007). "Modelling and measurements of power losses and turbulence intensity in wind turbine wakes at Middelgrunden offshore wind farm." *Wind Energy*, **10**. URL `https://onlinelibrary.wiley.com/doi/abs/10.1002/we.238`.

Barthelmie RJ, Pryor SC, Frandsen ST, Hansen KS, Schepers JG, Rados K, Schlez W, Neubert A, Jensen LE, Neckelmann S (2010). "Quantifying the Impact of Wind Turbine Wakes on Power Output at Offshore Wind Farms." *Journal of Atmospheric and Oceanic Technology*, **27**. URL `https://doi.org/10.1175/2010JTECHA1398.1`.

Bastankhah M, Porté-Agel F (2014). “A new analytical model for wind-turbine wakes.” *Renewable Energy*, **70**. URL http://www.sciencedirect.com/science/article/pii/S0960148114000317.

Bastine D, Wächter M, Peinke J, Trabucchi D, Kühn M (2015). “Characterizing Wake Turbulence with Staring Lidar Measurements.” *Journal of Physics: Conference Series*, **625**. URL http://stacks.iop.org/1742-6596/625/i=1/a=012006.

BMWI (2018). “Erneuerbare Energien.” https://www.bmwi.de/Redaktion/DE/Dossier/erneuerbare-energien.html. [online; accessed 25-July-2018].

Boorsma K, Wagenaar JW, Savenjie FJ, Boquet M, Bierbooms WAAM, Giyanani A, Rutterman R (2016). “LiDAR Application for WInd Energy Efficiency.” *Technical report*, Energy research Centre of the Netherlands. https://www.ecn.nl/publicaties/PdfFetch.aspx?nr=ECN-E--16-044.

Bruun H (1995). *Hot-wire Anemometry: Principles and Signal Analysis*. Oxford science publications. Oxford University Press. ISBN 9780198563426.

Camp EH, Cal RB (2016). “Mean kinetic energy transport and event classification in a model wind turbine array versus an array of porous disks: Energy budget and octant analysis.” *Phys. Rev. Fluids*, **1**. URL https://link.aps.org/doi/10.1103/PhysRevFluids.1.044404.

Castaing B, Gagne Y, Hopfinger E (1990). “Velocity probability density functions of high Reynolds number turbulence.” *Physica D: Nonlinear Phenomena*, **46**. URL http://www.sciencedirect.com/science/article/pii/016727899090035N.

Chamorro LP, Guala M, Arndt R, Sotiropoulos F (2012). “On the evolution of turbulent scales in the wake of a wind turbine model.” *Journal of Turbulence*, **13**. URL https://doi.org/10.1080/14685248.2012.697169.

Chamorro LP, Hill C, Morton S, Ellis C, Arndt REA, Sotiropoulos F (2013). “On the interaction between a turbulent open channel flow and an axial-flow turbine.” *Journal of Fluid Mechanics*, **716**.

Chamorro LP, Porté-Agel F (2010). “Effects of Thermal Stability and Incoming Boundary-Layer Flow Characteristics on Wind-Turbine Wakes: A Wind-Tunnel Study.” *Boundary-Layer Meteorology*, **136**. URL https://doi.org/10.1007/s10546-010-9512-1.

Chowdhury S, Zhang J, Messac A, Castillo L (2012). “Unrestricted wind farm layout optimization (UWFLO): Investigating key factors influencing the maximum power generation.” *Renewable Energy*, **38**. URL http://www.sciencedirect.com/science/article/pii/S0960148111003260.

Corten GP, Schaak P (2003). "Increase of Wind Farm Production by Reduction of the Axial Induction." In *Proceedings - 2003 European Wind Energy Conference and Exhibition : [16 - 19 June, Madrid, Spain] - EWEA, Spanish Renewable Energy Association*. European Wind Energy Association.

Dairay T, Obligado M, Vassilicos JC (2015). "Non-equilibrium scaling laws in axisymmetric turbulent wakes." *Journal of Fluid Mechanics*, **781**. doi:10.1017/jfm.2015.493.

Davidson PA (2015). *Turbulence - an introduction for engineers and scientists*. 2 edition. Oxford University Press. ISBN 978-0-19-872259.

Eecen PJ, Verhoef JP (2007). "EWTW Meteorological data base - Description June 2003-May 2007." *Technical report*, Energy research Centre of the Netherlands.

Eriksen PE, Åge Krogstad P (2017). "Development of coherent motion in the wake of a model wind turbine." *Renewable Energy*, **108**. URL `http://www.sciencedirect.com/science/article/pii/S0960148117301179`.

F Chillà, J Peinke, B Castaing (1996). "Multiplicative Process in Turbulent Velocity Statistics: A Simplified Analysis." *J. Phys. II France*, **6**. URL `https://doi.org/10.1051/jp2:1996191`.

Fleming PA, Gebraad PM, Lee S, van Wingerden JW, Johnson K, Churchfield M, Michalakes J, Spalart P, Moriarty P (2014). "Evaluating techniques for redirecting turbine wakes using SOWFA." *Renewable Energy*, **70**. URL `http://www.sciencedirect.com/science/article/pii/S0960148114000950`.

Frandsen S (2007). *Turbulence and turbulence generated structural loading in wind turbine clusters*. Ph.D. thesis, DTU - Risø National Laboratory.

Frisch U (1995). *Turbulence - The legacy of A. AN. Kolmogorov*. Cambridge University Press. ISBN 0-521-45103-5.

Gasch R, Twele J (eds.) (2011). *Windkraftanlagen*. McGraw-Hill classic textbook reissue series, 7 edition. Vieweg+Teubner Verlag. ISBN 978-3-8348-1460-9.

Göçmen T, van der Laan P, Réthoré PE, na Diaz AP, Larsen GC, Ott S (2016). "Wind turbine wake models developed at the technical university of Denmark: A review." *Renewable and Sustainable Energy Reviews*, **60**. URL `http://www.sciencedirect.com/science/article/pii/S136403211600143X`.

González JS, Payán MB, Santos JMR, González-Longatt F (2014). "A review and recent developments in the optimal wind-turbine micro-siting problem." *Renewable and Sustain-*

able Energy Reviews, **30**. URL http://www.sciencedirect.com/science/article/pii/S1364032113006989.

Hau E (2014). *Windkraftanlagen: Grundlagen, Technik, Einsatz, Wirtschaftlichkeit*. 5 edition. Springer Vieweg. ISBN 978-3-642-28877-7.

Hinze J (1975). *Turbulence*. McGraw-Hill classic textbook reissue series. McGraw-Hill. ISBN 9780070290372.

Hultmark M, Smits AJ (2010). "Temperature corrections for constant temperature and constant current hot-wire anemometers." *Measurement Science and Technology*, **21**, 105404. URL http://stacks.iop.org/0957-0233/21/i=10/a=105404.

Hurst D, Vassilicos J (2007). "Scalings and decay of fractal-generated turbulence." *Physics of Fluids*, **19**. URL https://aip.scitation.org/doi/10.1063/1.2676448#.

IEC61400 (2005). "IEC 61400-1: Wind turbines." *Technical report*, International Electrotechnical Commission - IEC.

Jensen NO (1983). "A Note On Wind Generator Interaction." *Risø-M-2411*. URL http://www.orbit.dtu.dk/fedora/objects/orbit:88807/datastreams/file_3494b4b2-1dae-4442-941a-f2e628673f31/content.

Jin Y, Liu H, Aggarwal R, Singh A, Chamorro LP (2016). "Effects of Freestream Turbulence in a Model Wind Turbine Wake." *Energies*, **9**. URL http://www.mdpi.com/1996-1073/9/10/830.

Keane A, Aguirre PEO, Ferchland H, Clive P, Gallacher D (2016). "An analytical model for a full wind turbine wake." *Journal of Physics: Conference Series*, **753**. URL http://stacks.iop.org/1742-6596/753/i=3/a=032039.

Kermani NA, Andersen SJ, Sørensen JN, Shen WZ (2013). "Analysis of turbulent wake behind a wind turbine." *Proceedings of the 2013 International Conference on Aerodynamics of Offshore Wind Energy Systems and Wakes (icowes2013)*. URL http://orbit.dtu.dk/ws/files/66105667/Analysis_of_turbulent_wake_behind.pdf.

Knebel P, Kittel A, Peinke J (2011). "Atmospheric wind field conditions generated by active grids." *Experiments in Fluids*, **51**. URL https://doi.org/10.1007/s00348-011-1056-8.

Kröger L, Frederik J, van Wingerden JW, Peinke J, Hölling M (2018). "Generation of user defined turbulent inflow conditions by an active grid for validation experiments." *Journal of Physics: Conference Series*, **1037**. URL http://stacks.iop.org/1742-6596/1037/i=5/a=052002.

Lee S, Churchfield M, Moriarty P, Jonkman J, Michalakes J (2012). "Atmospheric and Wake Turbulence Impacts on Wind Turbine Fatigue Loadings." *50th AIAA Aerospace Sciences Meeting including the New Horizons Forum and Aerospace Exposition, Aerospace Sciences Meetings*, **AIAA 2012-0540**. URL https://www.nrel.gov/docs/fy12osti/53567.pdf.

Lignarolo L, Ragni D, ao Ferreira CS, van Bussel G (2015). "Wind turbine and actuator disc wake: two experimental campaigns." *Proceedings of the 14th International Conference on Wind Engineering, ICWE14, Porto Alegre (Brasil), June 21-26, 2015*. URL uuid:7b6b95d2-076e-4f38-b167-879253805263.

Lignarolo L, Ragni D, Krishnaswami C, Chen Q, ao Ferreira CS, van Bussel G (2014). "Experimental analysis of the wake of a horizontal-axis wind-turbine model." *Renewable Energy*, **70**. Special issue on aerodynamics of offshore wind energy systems and wakes, URL http://www.sciencedirect.com/science/article/pii/S0960148114000494.

Lignarolo LEM, Ragni D, Ferreira CJ, van Bussel GJW (2016). "Experimental comparison of a wind-turbine and of an actuator-disc near wake." *Journal of Renewable and Sustainable Energy*, **8**. URL https://doi.org/10.1063/1.4941926.

Maeda T, Kamada Y, Murata J, Yonekura S, Ito T, Okawa A, Kogaki T (2011). "Wind tunnel study on wind and turbulence intensity profiles in wind turbine wake." *Journal of Thermal Science*, **20**. URL https://doi.org/10.1007/s11630-011-0446-9.

Mazellier N, Vassilicos JC (2010). "Turbulence without Richardson–Kolmogorov cascade." *Physics of Fluids*, **22**. URL https://doi.org/10.1063/1.3453708.

Morales A, Wächter M, Peinke J (2011). "Characterization of wind turbulence by higher-order statistics." *Wind Energy*, **15**. URL https://onlinelibrary.wiley.com/doi/abs/10.1002/we.478.

Mücke T, Kleinhans D, Peinke J (2011). "Atmospheric turbulence and its influence on the alternating loads on wind turbines." *Wind Energy*, **14**. URL https://onlinelibrary.wiley.com/doi/abs/10.1002/we.422.

Neunaber I, Schottler J, Peinke J, Hölling M (2017). "Comparison of the Development of a Wind Turbine Wake Under Different Inflow Conditions." In R Örlü, A Talamelli, M Oberlack, J Peinke (eds.), *Progress in Turbulence VII*. Springer International Publishing.

Nieuwstadt FT, Westerweel J, Boersma BJ (2017). *Turbulence - Introduction to Theory and Applications of Turbulent Flows*. 1 edition. Springer International Publishing. ISBN 978-3-319-31599-7. doi:10.1007/978-3-319-31599-7.

Obligado M, Dairay T, Vassilicos JC (2016). "Nonequilibrium scalings of turbulent wakes." *Phys. Rev. Fluids*, **1**. URL `https://link.aps.org/doi/10.1103/PhysRevFluids.1.044409`.

Petrović V, Schottler J, Neunaber I, Hölling M, Kühn M (2018). "Wind tunnel validation of a closed loop active power control for wind farms." *Journal of Physics: Conference Series*, **1037**. URL `http://stacks.iop.org/1742-6596/1037/i=3/a=032020`.

Platis A, Siedersleben SK, Bange J, Lampert A, Bärfuss K, Hankers R, nadillas BC, Foreman R, Schulz-Stellenfleth J, Djath B, Neumann T, Emeis S (2018). "First in situ evidence of wakes in the far field behind offshore wind farms." *Scientific Reports*, **8**(2163). URL `https://www.nature.com/articles/s41598-018-20389-y`.

Pope SB (2000). *Turbulent Flows*. Cambridge University Press. doi:10.1017/CBO9780511840531.

Reinke N (2017). *Application, Generation and Stochastic Analysis of Turbulent Flows*. Ph.D. thesis, University of Oldenburg, Faculty of Mathematics and Natural Sciences.

Ruck B (1987). "Laser Doppler Anemometry - A non-intrusive optical meauring technique for fluid velocity." *Particle & Particle Systems Characterization*.

Sanderse B (2009). "Aerodynamics of wind turbine wakes." *Technical report*, Energy research Centre of the Netherlands - ECN. URL `https://www.ecn.nl/docs/library/report/2009/e09016.pdf`.

Schottler J (2018). *Experimental Investigation of Wind Farm Effects using Model Wind Turbines*. Ph.D. thesis, University of Oldenburg, Faculty of Mathematics and Natural Sciences.

Schottler J, Bartl J, Mühle F, Sætran L, Peinke J, Hölling M (2018). "Wind tunnel experiments on wind turbine wakes in yaw: redefining the wake width." *Wind Energy Science*, **3**. URL `https://www.wind-energ-sci.net/3/257/2018/`.

Schottler J, Hölling A, Peinke J, Hölling M (2016a). "Design and implementation of a controllable model wind turbine for experimental studies." *Journal of Physics: Conference Series*, **753**. URL `http://stacks.iop.org/1742-6596/753/i=7/a=072030`.

Schottler J, Hölling A, Peinke J, Hölling M (2016b). "Wind tunnel tests on controllable model wind turbines in yaw." *AIAA SciTech Forum - 34th Wind Energy Symposium*. URL `https://doi.org/10.2514/6.2016-1523`.

Schottler J, Reinke N, Hölling A, Whale J, Peinke J, Hölling M (2017). "On the impact of non-Gaussian wind statistics on wind turbines – an experimental approach." *Wind Energy Science*, **2**. URL `https://www.wind-energ-sci.net/2/1/2017/`.

Schwarz CM, Ehrich S, Martín R, Peinke J (2018). "Fatigue load estimations of intermittent wind dynamics based on a Blade Element Momentum method." *Journal of Physics: Conference Series*, **1037**. URL http://stacks.iop.org/1742-6596/1037/i=7/a=072040.

Singh A, Howard KB, Guala M (2014). "On the homogenization of turbulent flow structures in the wake of a model wind turbine." *Physics of Fluids*, **26**. URL https://doi.org/10.1063/1.4863983.

Umweltbundesamt (2018). "Erneuerbare Energien in Zahlen." https://www.umweltbundesamt.de/themen/klima-energie/erneuerbare-energien/erneuerbare-energien-in-zahlen. [Online; accessed 29-July-2018].

van Kuik GAM, Peinke J, Nijssen R, Lekou D, Mann J, Sørensen JN, Ferreira C, van Wingerden JW, Schlipf D, Gebraad P, Polinder H, Abrahamsen A, van Bussel GJW, Sørensen JD, Tavner P, Bottasso CL, Muskulus M, Matha D, Lindeboom HJ, Degraer S, Kramer O, Lehnhoff S, Sonnenschein M, Sørensen PE, Künneke RW, Morthorst PE, Skytte K (2016). "Long-term research challenges in wind energy - a research agenda by the European Academy of Wind Energy." *Wind Energy Science*, **1**. URL https://www.wind-energ-sci.net/1/1/2016/.

Vassilicos JC (2015). "Dissipation in Turbulent Flows." *Annual Review of Fluid Mechanics*, **47**. URL https://doi.org/10.1146/annurev-fluid-010814-014637.

Vermeer L, Sørensen J, Crespo A (2003). "Wind turbine wake aerodynamics." *Progress in Aerospace Sciences*, **39**. URL http://www.sciencedirect.com/science/article/pii/S0376042103000782.

Wächter M, Heißelmann H, Hölling M, Morales A, Milan P, Mücke T, Peinke J, Reinke N, Rinn P (2012). "The turbulent nature of the atmospheric boundary layer and its impact on the wind energy conversion process." *Journal of Turbulence*, **13**. URL https://doi.org/10.1080/14685248.2012.696118.

Wessel A (2008). *Development of a physical model for calculation of the turbulence inside wind farms*. Ph.D. thesis, University of Oldenburg, Faculty of Mathematics and Natural Sciences.

Zhang W, Markfort CD, Porté-Agel F (2012). "Near-wake flow structure downwind of a wind turbine in a turbulent boundary layer." *Experiments in Fluids*, **52**. URL https://doi.org/10.1007/s00348-011-1250-8.

Acknowledgements

The TWiSt group deserves my heartfelt gratitude for welcoming me warmly. It has been six years by now since I started writing my master thesis in this group, lured here by the excitement with which the fluid dynamics and wind energy lectures were given (I originally planned to specialize in solar energy... how absurd!), and the people have always been eager to help and discuss any problem.
However, there are some people who deserve my special recognition.
In the beginning, I would like to thank Prof. Dr. Joachim Peinke for his support and for giving me the opportunity to work on this thesis. His enthusiasm and his way of thinking outside the box have always been motivating, and they have been the origin of many constructive discussions. I am also grateful for the opportunities I encountered during conference visits and international research exchanges.
Dr. Jaroslaw Puczylowski deserves my special recognition. Our cooperation has been lasting for quite some time now, as he took me in as student research assistant and supervised my master thesis. Since then, he has been a highly valued partner in many discussions and I can always count on him when I am in need of advice and help.
Dr. Michael Hölling has also been a valuable partner for discussions and for setting me back on track whenever I was close to drowning in all the data.
Further, I would like to thank Tom Wester, André Fuchs, Matthias Wächter and Gerrit Kampers for the input I got whenever I asked for advice.
For taking the time to be second examiner of this thesis, I would also like to thank Prof. Dr. Gerard Schepers.
Last, I would like to thank Prof. Dr. Martin Kühn for his support and for being my third examiner.

Ich möchte mich außerdem ganz herzlich bei meinen Eltern und meiner Schwester bedanken. Sie haben mich immer unterstützt und holten mich zurück auf den Boden, wenn ich mal wieder im Dreieck sprang...

I would like to thank and acknowledge the Energy research Centre of the Netherlands (ECN, now ECN part of TNO) for providing field data to validate the laboratory results and for their support during a research stay.

In the end, I want to thank the Deutsche Bundesstiftung Umwelt (German Federal Environmental Foundation) for their financial and idealistic support that gave me the freedom to carry out this research project.

Curriculum

Personal Information

Name	Ingrid Neunaber
Date of birth	November 20th, 1989
Place of birth	Oldenburg
Citizenship	German

Education

10/2008 – 09/2011	B.Sc. Physics, Philipps University Marburg
10/2011 – 09/2013	M.Sc. Engineering Physics, C.v.O. University of Oldenburg

Scientific Experience

10/2013 – 11/2014	Research associate (Project: Inflow Noise) AG TWiSt of Prof. Dr. Joachim Peinke C.v.O. University of Oldenburg
12/2014 – 12/2018	Doctoral student AG TWiSt of Prof. Dr. Joachim Peinke C.v.O University of Oldenburg
12/2014 – 11/2017	Doctoral scholarship Deutsche Bundesstiftung Umwelt
12/2014 – 09/2016	Research associate (Project: Inflow Noise; part-time) AG TWiSt of Prof. Dr. Joachim Peinke C.v.O. University of Oldenburg

List of Publications

Peer-reviewed journals: under submission

ALI N, FUCHS A, NEUNABER I, PEINKE J, AND CAL RB: *Multi-Scale/Fractal Process in the Wake of a Wind Turbine Array Boundary Layer*. Journal of Turbulence (2018). *Under submission.*

Conference proceedings

NEUNABER I, SCHOTTLER J, PEINKE J, HÖLLING M: *Comparison of the Development of a Wind Turbine Wake under Different Inflow Conditions*. Progress in turbulence VII: Proceedings of the iTi Conference in Turbulence 2016 (2017).

PETROVIĆ V, SCHOTTLER J, NEUNABER I, HÖLLING M, KÜHN M: *Wind tunnel validation of a closed loop active power control for wind farms*. Journal of Physics: Conference Series (2018).

Erklärung

Ich erkläre hiermit, dass

(a) eine Promotion zum Dr. rer. nat. angestrebt wird,

(b) ich diese Arbeit selbständig verfasst und nur die angegebenen Hilfsmittel benutzt habe und dass die Arbeit in Teilen bereits veröffentlicht wurde,

(c) die Leitlinien guter wissenschaftlicher Praxis an der Carl von Ossietzky Universität Oldenburg befolgt worden sind,

(d) im Zusammenhang mit dem Promotionsvorhaben keine kommerziellen Vermittlungs- oder Beratungsdienste (Promotionsberatung) in Anspruch genommen worden sind,

(e) diese Dissertation weder in ihrer Gesamtheit noch in Teilen einer anderen Hochschule zur Begutachtung in einem Promotionsverfahren vorgelegen hat.

Oldenburg, den 23. November 2018

....

(Ingrid Neunaber)